DECEMBER 2017 Ph.D. in CIVIL ENGINEERING FARID H. MAHAMMED

UNIVERSITY OF GAZİANTEP

GRADUATE SCHOOL OF

NATURAL & APPLIED SCIENCES

BEHAVIOR OF CONCENTRIC FLAT PLATE-COLUMN ASSEMBLY EXPOSED TO AMBIENT AND HIGH TEMPERATURE CONDITIONS

Ph.D. THESIS

IN

CIVIL ENGINEERING

BY

FARID H. MAHAMMED

DECEMBER 2017

Behavior of Concentric Flat Plate-Column Assemblies Exposed to Ambient and High Temperature Condition

Ph.D. Thesis

In

Civil Engineering

University of Gaziantep

Supervisor

Prof. Dr. Mustafa ÖZAKÇA

Co-supervisor

Assist. Prof. Dr. Sallal R. Abid

By

Farid H. MAHAMMED

December 2017

REPUBLIC OF TURKEY
UNIVERSITY OF GAZİANTEP
GRADUATE SCHOOL OF NATURAL & APPLIED SCIENCES
CIVIL ENGINEERING DEPARTMENT

Name of the thesis: Behavior of Concentric Flat Plate-Column Assembly Exposed to Ambient and High Temperature Condition

Name of the student: Farid H. MAHAMMED

Exam date: December 25, 2017

Approval of the Graduate School of Natural and Applied Sciences

Prof. Dr. Ahmet Necmeddin YAZICI
Director

I certify that this thesis satisfies all the requirements as a thesis for the degree of Doctor of Philosophy.

Prof. Dr. Abdulkadir ÇEVİK
Head of Department

This is to certify that we have read this thesis and that in our opinion it is fully adequate, in scope and quality, as a thesis for the degree of Doctor of Philosophy.

Assist Prof. Dr. Sallal R. ABID
Co-Supervisor

Prof. Dr. Mustafa ÖZAKÇA
Supervisor

Examining Committee Members;	Signature
Prof. Dr. Beytullah TEMEL	…………………
Prof. Dr. Mustafa ÖZAKÇA	…………………
Assoc. Prof. Dr. Hamza TANRIKULU	…………………
Assoc. Prof. Dr. Nildem TAYŞİ	…………………
Assist. Prof. Dr. Talha EKMEKYAPAR	…………………

I hereby declare that all information in this document has been obtained and presented in accordance with academic rules and ethical conduct. I also declare that, as required by these rules and conduct, I have fully cited and referenced all material and results that are not original to this work.

Farid H. MAHAMMED

ABSTRACT

BEHAVIOR OF CONCENTRIC FLAT PLATE-COLUMN ASSEMBLIES EXPOSED TO AMBIENT AND HIGH TEMPERATURE CONDITIONS

MAHAMMED, Farid H.

Ph.D. Thesis in Civil Engineering

Supervisor: Prof. Dr. Mustafa ÖZAKÇA

Co-supervisor: Assist Prof. Dr. Sallal R. ABID

December 2017, 267 pages

Flat plate-column connection is one of structural joint that is widely used worldwide, because of its low cost compared to other slab types. However, this type of connection is under significant risk of brittleness in punching shear failure, which is incompetently understood as the flexural behavior. The problem is aggravated when the structure exposed to high temperature. One of the commonly suggested solutions to the minimize the brittleness effect of the punching shear is using fibrous concrete. The shear failure of the slab-column connection under fire conditions depends mainly on the degradation of the material properties in addition to the indirect structural effect. This thesis aims to investigate the behavior of flat plate-column assembly, made from plain and fibrous concrete under ambient and fire conditions. The experimental work is divided into two main stages. In the first stage, twenty one slabs made from ECC of different types of synthetic fibers (NM, PVA, and PP) were compared with slabs made from plain concrete and steel fiber reinforced concrete. Moreover, in three other slabs, the critical D-zone was poured with ECC-NM, while plain concrete was used outside the zone. The results showed that the addition of steel fiber provides high improvement in the slab behavior. Therefore, the steel fiber reinforced concrete was used in the second stage. Twenty slabs were constructed and tested to investigate the residual punching shear strength of high-strength steel-fiber reinforced concrete flat plates after exposure to high temperatures. Four levels of high temperatures of 150, 300, 450, and 550 °C were adopted and three fiber contents of 0.75, 1, and 1.25% by volume of concrete were used. The experimental results were discussed and compared with results from previous works and existing formulas of some international codes of practice. In addition, regression formulas based on the current research's experimental results were suggested. Although extensive literature is available on the punching shear strength of fibrous concrete at ambient conditions, to the best of the authors' knowledge, there is no experimental work on the residual punching shear strength of steel-fiber reinforced concrete after high temperature exposure.

Finally, the heat transfer and the mechanical behavior of the specimens in the second stage were simulated in sequentially analysis process using the general purposes finite element software ABAQUS 6.14-1.

Key Words: Slab, Punching shear, Fire, Steel fiber, Flat plate - column connection

ÖZET

KONFERANSLI DÜZLÜ PLAK-KOLON AĞLARI VE KONFERANSLI ORTAMLARA DAVRANIŞ

MAHAMMED, Farid H.

İnşaat Mühendisliği Doktora Tezi

Danışman: Prof. Dr. Mustafa ÖZAKÇA

Yardımcı Danışman: Yrd. Doç. Dr. Sallal R. ABID

Aralık 2017, 267 Sayfa

Düz levha kolon bağlantısı, diğer döşeme tiplerine kıyasla düşük maliyeti nedeniyle dünya çapında yaygın olarak kullanılan yapısal bağlantılardan biridir. Bununla birlikte, bu tip bağlantı kesme başarısızlığında önemli bir kırılma riski altındadır ve bu da eğilme davranışı olarak yetersiz olarak anlaşılır. Yapı, yüksek sıcaklığa maruz kaldığında sorun ağırlaşıyor. Zımbalama makasının kırılganlık etkisini en aza indirgemek için yaygın olarak önerilen çözümlerden biri, lifli beton kullanmaktır. Yangın şartlarında döşeme sütun bağlantısının kayma başarısızlığı esas olarak dolaylı yapısal etkiye ek olarak malzeme özelliklerinin bozulmasına bağlıdır. Bu tez, düz ve elyaflı betondan çevre ve yangın koşullarında yapılan düz plaka-sütun montajının davranışını araştırmayı amaçlamaktadır. Deneysel çalışma iki ana aşamaya ayrılmıştır. İlk aşamada, ECC'den farklı sentetik elyaflardan (NM, PVA ve PP) oluşan yirmi bir plakalar, düz beton ve çelik telle güçlendirilmiş betonlardan yapılmış döşeme levhaları ile karşılaştırıldı. Ayrıca, diğer üç plakada, kritik D-bölgesi ECC-NM ile dökülürken, düz beton bölge dışında kullanıldı. Sonuçlar, çelik lif ilavesinin döşeme davranışında yüksek iyileşme sağladığını gösterdi. Bu nedenle ikinci aşamada çelik tel takviyeli beton kullanıldı. Yüksek sıcaklığa maruz kaldıktan sonra, yüksek mukavemetli çelik telle güçlendirilmiş beton levhaların kalıcı delinme kayma mukavemetini araştırmak için, toplam 30 levha inşa edildi ve test edildi. 150, 300, 450 ve 550 ° C'lik dört yüksek sıcaklık derecesi benimsenmiş ve hacim olarak 0.75, 1 ve 1.25 hacimdeki üç fiber içeriği kullanılmıştır. Deney sonuçları tartışılmış ve önceki çalışmaların sonuçları ve bazı uluslararası uygulama kurallarının mevcut formülleri ile karşılaştırılmıştır. Buna ek olarak, mevcut araştırmanın deneysel sonuçlarına dayanan regresyon formülleri önerildi. Ortam koşullarında lifli betonun zımbalama mukavemeti hakkında kapsamlı literatür bulunsa da, yazarların bildiği kadarıyla, yüksek sıcaklığa maruz kaldıktan sonra çelik telle güçlendirilmiş betonun kalıcı delme makaslama dayanımı hakkında deneysel bir çalışma bulunmamaktadır.

Son olarak, ikinci aşamadaki numunelerin ısı transferi ve mekanik davranışı, ABAQUS 6.14-1 genel amaçlı sonlu elemanlar yazılımı kullanılarak sıralı analiz prosesinde simüle edildi.

Anahtar Kelimeler: Döşeme, Zımbalama makası, Ateş, Çelik fiber, Sade koltuk bağlantısı

To

The Sultan of the Age (A.J.)

....My Parents...

....My Brothers, Sisters, and Wife ...

....My Little Angel....

ACKNOWLEDGEMENTS

To my life-coach, eternal cheerleader, my Father: because I owe it all to you.

I am grateful to my supervisor Prof. Dr Mustafa ÖZAKÇA and the Co-supervisor Assist. Prof. Dr Sallal R. ABID, who have provided me through educational, moral and emotional support along the way. With a special mention to my colleagues Ahmmad, Hayder, Abualtemen, and the structural engineering team, in general. It was fantastic to have the opportunity to work majority of my research with you.

A very special gratitude to my guardian angels (Mother and Daughter): both of you was always keen to know what I was doing and how I was proceeding, although it is likely that you have never grasped what it was all about! I will miss Mayyar's screams of joy whenever a significant momentous was reached and also just her general impudence.

And finally, last but by no means least, also to everyone in the university staff… it was great support and wonderful time with all of you during last four years.

Thanks for all your encouragement!

TABLE OF CONTENTS

Page

LIST OF FIGURES

Page

LIST OF TABLES

Page

LIST OF SYMBOLS

a	Slab length in mm
B	Slab perimeter in mm
b	Slab Width in mm
b_1	Distance from half ball support to the nearest slab edge
b_2	Distance between two adjacent half balls support
b_o	Perimeter at specified distance from the edge of column in mm.
c	Length or width of column or loaded area in mm
c_p	Concrete specific heat in J/Kg ^oK
D^{el}	Concrete elastic stiffness
D_o^{el}	Initial elastic stiffness
D_u	A displacement that corresponds to the maximum load
D_y	Effective yield displacement
D_f	Diameter of fiber in mm
h_c	Coefficient of heat transfer by convection in $W/m^2.K$
d	Effective depth (Distance from extreme compression fiber to centroid of longitudinal tension reinforcements) in mm
d_a	Maximum size of aggregate in mm
E	Young's modulus
E_c	Modulus of elasticity of concrete in MPa
E_s	Modulus of elasticity of steel in MPa
f_{co}	Initial uniaxial yield stresses under compression in MPa
f_{bo}	Initial biaxial yield stresses under compression in MPa

f'_c	Cylinder compressive strength of concrete at 28 days in MPa
f_{ck}	Caractrestic compressive strength of concrete at 28 days in MPa
f_{cm}	Mean compressive strength
f_{cu}	Uniaxial cube (compressive) strength of concrete in MPa
f_{ct}	Tensile Stress of concrete in MPa
f_{sp}	Splitting tensile stress of concrete in MPa
f_y	Yield Stress of Steel in MPa
G_f	Fracture Energy
h	Total thickness of slab in mm
k_c	Concrete thermal conductivity in W/m.ºK
K^e	Stiffness matrix of the element
l_{cri}	Critical distance from column face in mm
l_f	Length of fiber in mm
m	Flexural capacity of concrete section N.m
P_{cr}	Cracking load in kN
P_u	Ultimate load resistance in kN
P_y	Yielding load in kN
P_{flex}	Structure flexural capacity in kN
$\tilde{p}$	Effective hydrostatic pressure
Q	Gesund suggested failure criterion
$\tilde{q}$	von-Mises (equivalent effective) stress
r_o	Radius of column
r_q	Radius of the load point
r_s	Radius of the equivalent circular slab
μ	Displacement ductility
V_u	Ultimate shear capacity in kN
V_c	Punching shear strength provided by concrete in kN

V_n	Nominal Punching Shear Capacity in kN
V_f	Fiber volume fraction
w_c	Plain concrete unit weight.
x_{pu}	Compression zone depth
δ	Slab displacement in mm
ρ	Flexural reinforcement ratio
ε	Total Strain (mm/mm)
ε_c	Emissivity of the member surface
ε_{cr}	Crack strain (mm/mm)
ε^{el}	Elastic Strain (mm/mm)
ε^{pl}	Plastic Strain (mm/mm)
$\dot{\varepsilon}^{pl}$	The rate of the plastic strain
$\tilde{\varepsilon}^{pl}$	Equivalent plastic strain
σ	Total Stress in MPa
τ_c	Strength effect in code's provision
ϕ	Safety factor
φ	Drucker-Prager hyperbolic function
ψ	Rotation of the structural member in Rad
υ	Poisson’s ratio
ν_c	Punching shear stress provided by concrete in kN
ξ (d)	Size effect in code's provision in term of effective depth

LIST OF ABREVIATIONS

ACI	American Concrete Institute (code of practice ACI318)
AS	Australian Standard (code of practice AS-3600)
CDP	Concrete Damages Plasticity
CSA	Canadian Standard (code of practice CSA A23.3)
DIN	Germany standard (code of practice DIN1045)
EAC	Energy Absorption Capacity
EC2	Eurocode 2 (EN 1992-1-1 or 2)
ECC	Engineered Cementitious Composites
FE	Finite Element
IS	Indian Standard S456
MC	Model Code 2010
NM	Nylon Monofilament
PP	Polypropylene
PVA	PolyVinyl Alcohol
RC	Reinforced Concrete
SF	Steel Fiber
SFRC	Steel Fiber Reinforced Concrete
TS	Turkish Standard

CHAPTER 1

INTRODUCTION

1.1 General

Slabs without drop panels and supported by a system of columns without column capitals are known as flat plates [1], these structural systems provide functional and economic advantages. Figure 1.1 shows an example of the two way slab types.

Active and easier way to assess the behavior of a structure is by investigating the critical elements and the connections between them. Among various critical connections in most structures is the flat plate, which is widely used worldwide because of its importance from economy view, however, this type of connection is under significant risk of brittleness in punching shear failure. Many engineers had designed and constructed this type of structures since 1900, but the invention of this system is attributed to the Swiss engineer Robert Maillart [2]. Moreover, a vast number of experiments have been conducted on the slab-column connection behavior (about 512 tests were list in databank [3]), but there are still many points on the table for discussion such as:

- The punching problem is still so complex to understand, and there is no agreed design mechanical model confirmed by the codes of practice.
- Most codes of practice still introduce the provision of the punching design based on semi empirical formulae based on laboratory experiments for small specimens under monotonic short-time loading, in which the creep effects are neglected.
- Other codes introduce modified shear strength of beams, by fitting the critical section perimeter with uniform distribution of shear force around this perimeter. Whereas, the shear varies markedly and accompanied by torsion. Moreover, there are clear differences between the punching fracture mode

and the shear failure of beams, the former occurs due to high biaxial compression strains, while the latter occurs due to tensile strains.

- There is no appropriate attention has been devoted to evaluate the behavior of flat plates under fire conditions.

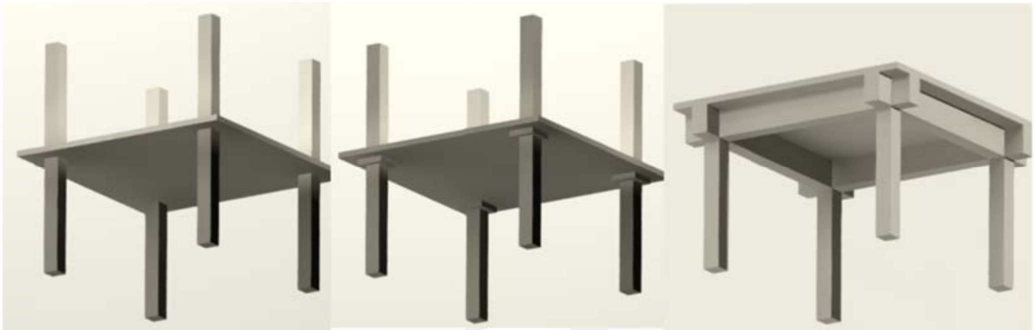

(a) (b) (c)

Figure 1.1 Two way slab system (a) Flat plate (b) Flat slab (c) Slab with beams

Flat plate-column assembly has a complex loading behavior that generally appears in the critical local zone (D-zone), where the flexural and punching are interacted in a complex behavior. The high stresses in (compression at the slab connection and tension on the opposite face of the slab) lead to forming an inclined crack around the column. The cone like punching failure is finally separate from the slab in a brittle failure type. The strength of the flat plate is often governed by the two-way shear design (punching), which is supposed to interact with yielding the flexural reinforcements. This requires a good understanding of the flexural and shear behaviors and the relation between them.

Many researches were conducted using different types of shear reinforcement in order to increase the slab punching capacity, for instance, bent bars and studs distributed in orthogonal and radial patterns within the critical section. However, few researches had investigated the improving of the ductility of the concrete. Over the past century, there has been a dramatic increase in researches on the influence of fibers on concrete properties to provide suitable answers to the designers on the behavior and effect of Fiber Reinforced Concrete (FRC) in different structural members. Flat slab is one of the structural systems that attracted the researchers' attention. Although, flat plate is widely used, the punching shear failure still takes place from time to time, and became the most important limitation of this particular structural element due to its brittleness nature, which causes catastrophic problems that should be avoided. Moreover, the gravity loads initially carried by the connection that fails in punching would be transferred to other supports.

Several investigations had been conducted in order to improve both strength and ductility of slab-column connections where the punching shear is the main problem. Many researchers had observed that fibers could provide a significant strength enhancement and minimize the brittleness of the concrete slab. Fibers can improve the post cracking behavior by bridge cracks depending on bonding strength, fiber fraction and the pull out strength of the cracked concrete The latter would improve the ductility of slabs through preventing the sudden failure that characterizes the shear behavior. Since 1960s, many types of fibers were investigated depending on the materials and shapes of fibers, where the friction between fibers and concrete is the main bond source. Therefore, the main concern was to increase the surface area by increasing the sides of the cross section, or increasing the aspect ratio of the fiber to get more bond strength.

Effect of fibers also depends on the type of stresses affecting the studies member as fibers are highly effective to improve tensile strength while almost insignificant where compression stresses are dominant. Therefore, any research on such area (punching shear) have to consider two major themes. The first is the investigation of the punching shear strength of an isolate member for the derivation and analysis and design formulas. On the other hand, the second theme is the considering of the effect of fibers on the behavior of the whole structure and the modifying of the proposed formulas to adopt with these new materials.

1.2 Punching Shear Failure

It was shown that the failure of flat plat column connection depends on many external and internal factors. External factors such as the shape, relative size of the column and slab, types, direction and distribution of the loads, and edge constraints. On the other hand, the internal factors are related to the rebars and aggregate interlock, membrane action, the bond between concrete and reinforcement, and type of the concrete and its ability to deform. Many mechanical models were proposed since 1960s when Kinnunen and Nylander [4] proposed their model, which inspired many other researchers. The model assumes rigid radial sectors of sectorial angle outside the tangential shear crack bounded by two radial cracks (see Figure 1.2). This sector rotates around a line located below the root of shear crack. The theory was based on the assumption that the punching resistance related to critical rotation and this strength can be calculate by equilibrium of the forces acting on the connection of the circular column to circular ring reinforced slab.

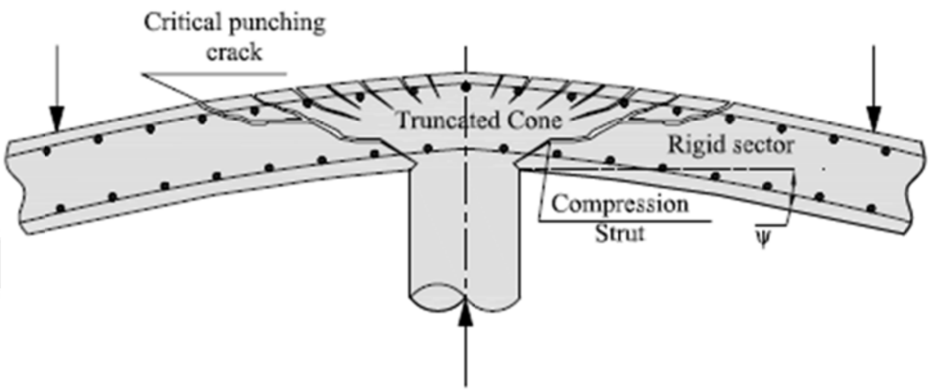

Figure 1.2 Failure model according to equilibrium forces approaches

Based on the test results and the flexural capacity of the slab, Kuang and Morley [5] recognized four types of failure in isolated interior slab-column system at ambient condition, which are:

(a) Pure flexural failure, $P_{u,test}/P_{u,flex} > 1.15$

(b) Flexural punching shear failure, $0.95 < P_{u,test}/P_{u,flex} < 1.15$

(c) Brittle punching, $P_{u,test}/P_{u,flex} < 0.95$

(d) Bond between steel bars and concrete,

The pure flexural failure (failure type a) is due to the formation of yield-lines. These lines depend on the supports' configuration, as will be discussed in Section 2.2.1 and 2.4.1. The flexural and the brittle punching shear failures (failure types b and c) form within the discontinuity region of high slab stress at the connection with the column. Finally, failure type (d) occurs when the reinforcement bars slide due to poor bonding with the surrounding concrete. This failure can be prevented by bonding carefully when using deformed bars.

It is worth to mention here, that the above failures affect each other, hence, significant formulae had been conducted since the previous century on the analysis of the bending moment, shear, and on the interaction relationship between them. These models generally differ in approaches, consideration of the mechanism, and in the failure criterion. However, none of these attempts to predict the punching strength with the same accuracy of the purely empirical methods.

1.3 Effect of Fire on Flat Plates

In most codes, the fire resistance provisions is limited and expressed by controlling the minimum slab thickness, for example ACI318 advice to use slab with 125 mm for 2 hours endurance time and 170 mm for 4 hours. This could be real for the isolated slabs in experimental work. However, for the whole structural system, the global structural behavior significantly affects the slab strength. Slabs commonly heated from one side undergo significant thermal curvatures, resulting in deflections and rotation. The carried load is redistributed away to the adjacent supports of less temperature represented in terms of extra hogging moments of the slab over a fixed support. As a result, the load equilibrium action increases the axial loads on the column [6,7], which can reach as high as 40-50% of the service load [8,9]. This increasing in the axial load discontinues after reaching the plastic capacity. Therefore, the amount of this load depends on the slab bending capacity [10].

1.4 Problem Statement

Based on the discussion in the previous section, it is obvious that the concentric punching shear behavior of the slabs without shear reinforcement is brittle with low load resistance and low deformation capacity that lead to catastrophic collapsing. Thus, using fibrous matrix to increase the strength of the slab is not the only objective, but also the increasing of the slab ability to deform under multi-loads level. Different types of fibers and different dosages lead to different performances, which are mainly depending on the fiber physical properties and the bond with the matrix. These properties tend to more gaining or decay when exposed to high temperatures. Such a type of investigations includes different challenges that could be summarized as follows,

- The punching shear behavior is still complex to understand and the code provisions do not apply a mechanical mechanism of failure for normal concrete. In addition, the mechanism of failure for fibrous concrete is also disagreed among the researchers.

- The fibrous concrete has different behaviors than those of normal concrete in both ambient and high temperature.

- Exposing to high temperatures changes the correlation between the standard specimens and the slab test because of the shape effect. Therefore, the provision of the current equations at ambient conditions cannot be used for fire conditions.

1.5 Objectives and Thesis Scope

The research presented herein aims to study the behavior of concentric interior flat plat-column joint made from different types and dosages of fiber reinforced concrete and Engineering Cementitous Composite (ECC). All flat plates are of the same size without any special shear reinforcement. The objectives of the research can be summarized as follows,

- Comparisons among many types of synthetic fibers cast and tested under ambient conditions.

- The fiber type that shows the best behavior under ambient conditions is investigated under many levels of high temperatures.

- Modifying the present mechanical models to employ for fibrous concrete flat plate-column connection.

- Nonlinear finite element simulation of the best slab behavior under ambient and fire conditions (includes simulation of the residual strength).

In order to achieve the above goals, five types of fibers with deferent dosages and configurations are used to produce the tested specimens. Moreover, Steel Fiber Reinforced Concrete (SFRC) slabs with different fiber volume fractions are exposed to four levels of high temperatures and the residual strength are investigated.

1.6 Thesis Layout

The current research aims to contribute a better understanding of punching shear strength of concrete materials incorporating various types of fibers. The residual strength of the best behavior of fibrous concrete flat plate at ambient conditions is then investigated under high temperature levels.

The current work covers many themes related to punching shear behavior of concentric flat plate-column joint. Figure 1.3 shows the flowchart of the themes that are covered in the current research.

In addition to this chapter which provides a general introduction to the problem under investigation, this thesis contains seven chapters. Chapter 2 includes a review of the previous works of the same scopes. Three parts are covered in this chapter, namely, (a) the mechanical models at ambient conditions, (b) behavior of flat plate-column connection under high temperature conditions, this is includes the fire scenario, the effect of high temperatures on the material properties, and the thermo-mechanical models proposed, and (c) collection of 47 test results from 6 references available, the collection includes a comparison among them.

Chapter 3 introduces the design details of testing specimens based on the numerical analysis of a virtual complete structure where the results of the analysis are compared with the models found in literature. The details of the experimental works are also introduced in this chapter.

Chapter 4 presents and discusses the results of the 21 tested flat plates divided into six groups. These groups were designed to investigate many parameters including the effect of reinforcement ratio, slab thickness, and the effect of three types, configuration, and dosage. The results are compared with predicted punching shear strength values of six codes for slabs having the same properties of the experimental specimens. Moreover, empirical model is proposed for the best slab results, in which the judgments are based on the load resistance, ductility, energy absorption, and load-deflection behavior.

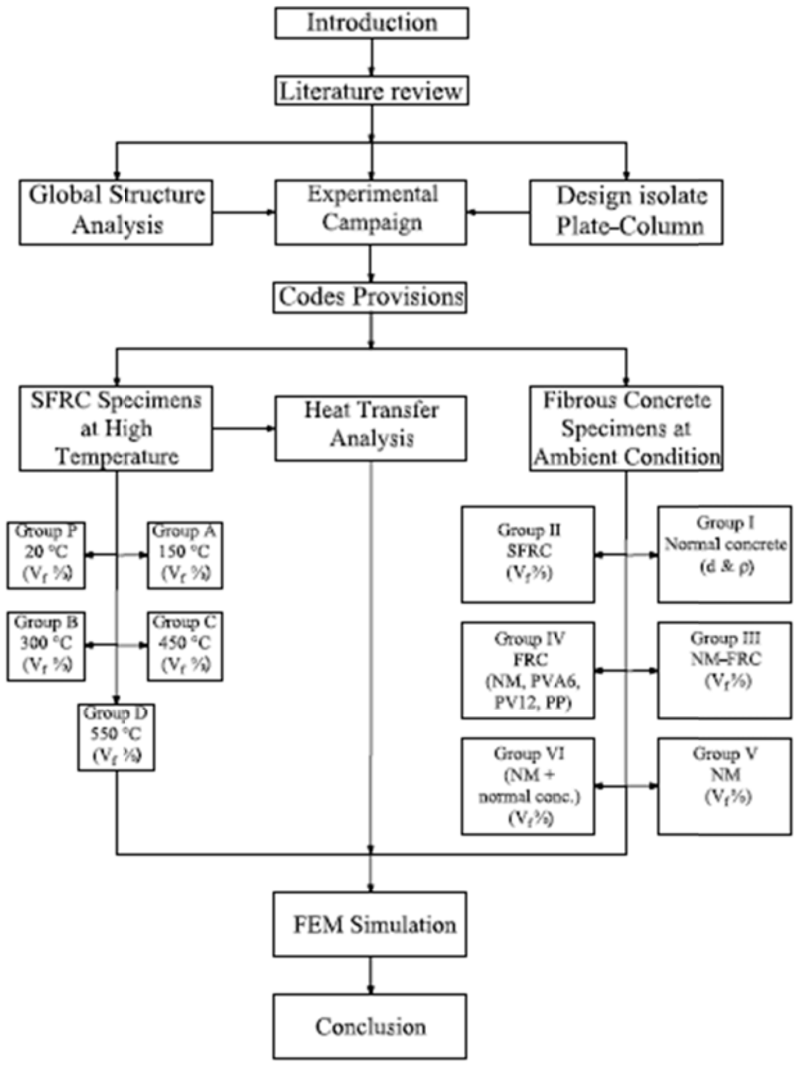

Figure 1.3 A flowchart of the research work presented in this thesis

Chapter 5 presents and discusses the results of the heat transfer through the slabs exposed to 550 º C temperatures. In order to compare the different proposed decay behaviors in the material properties, heat transfer of the current work and other specimens found in literature are then simulated. New technique for simulation of slab-column exposed to high temperatures is proposed.

In Chapter 6, the results of the residual strength of the SFRC exposed to four levels of high temperatures are presented. The effect of the high temperature on the mechanical properties of the concrete is discussed and suitable correlations are proposed.

In Chapter 7, the heated slabs that introduced in Chapter 6 are simulated, where the residual strength is simulated as a composed layers in different compressive strength, the chosen layers are based on the maximum temperature reached during the heating processes.

Finally, the conclusion driven from the presented results and discussion of the previous chapters are introduced in Chapter 9, in which, the most required future studies are also suggested.

CHAPTER 2

BACKGROUND AND LITERATURE REVIEW

2.1 General

The behaviors of flat plat column connection cannot be understood without establishing the main themes at ambient and fire conditions. This chapter covers four main subjects, these are, the mechanical models of the slabs at ambient condition and under monotonic increasing load up to failure, mechanical and thermal properties of plain concrete, heat transfer, and thermo-mechanical structural behaviors of slabs. Finally, results of an extensive review of research on punching shear behavior at high temperature conditions are presented.

2.2 Mechanical Models of Punching Shear Failure under Ambient Condition

Compared to the semi-empirical formulae, the structural behavior of the uniaxial flat plate-column assembly had been taking a little attention. This is because of the complexity of the interaction between flexural and shear transfer mechanisms, which have different ductility indexes, where the brittleness of the shear behavior may take place without yielding the reinforcement bars.

Many researchers had conducted significant formulae since the previous century. These models generally differ in approaches, consideration of the mechanism, and in the failure criterion. Following are some important approaches with their significant modifications.

2.2.1 Flexural capacity approach

In most cases, the tension reinforcement yields prior to failure along the yield line. This indicates that the ultimate load does not differ significantly from flexural capacity. However, in some cases, the yielding load is greater than the ultimate load.

Since 1943, many researchers [11-16] assumed that there is the full or partial relationship between punching and flexural strength. For example, Ramdane [11] used the simplified rectangular compressive stress that confirmed by BS8110 to determine the flexural capacity P_{test} / P_{flex}, where $P_{flex} = k \times M_u$, (k is the geometry and support condition factor), and $M_u = (0.67f_{cu})(0.9x)(d \times 0.45x)$, where x is the compression zone depth. Ramdane [11] found that, if $P_{test} / P_{flex} < 1$ the specimen fails in punching shear. However, for $P_{test} / P_{flex} > 1$, the specimen fails in flexure, and both failures can occur when $P_{test} / P_{flex} \approx 1$, where P_{flex} is the ultimate failure load. Figure 2.1 shows the most isolate column-slab connection used in laboratory tests and its general predicted flexural failure patterns. Table 2.1 lists the ultimate flexural failure loads for these cases.

In the same manner, Gesund [12] assumed that the failure would depend on the relative strengths in both shear and bending $\left[\rho \times f_y \times d^2 / (\sqrt{f'_c} \times b \times d)\right]$, where b is the perimeter of the column. By empirical establishing of the loading criterion as ρd / B, where B is slab perimeter, Gesund [12] suggested a failure criterion (Q) by combining the relative strength and loading criteria as follow,

$$Q = \frac{\rho^2 \times f_y \times d^2}{\sqrt{f'_c} \times b \times B} \times 10^4 \qquad (2.1)$$

Gesund [12] found that Q > 4 means that the specimen failure is due to shear, while the failure due to the formation of the bending yield line occurs in the case of Q < 2. Finally, both failures are expected if Q is in between 2 and 4.

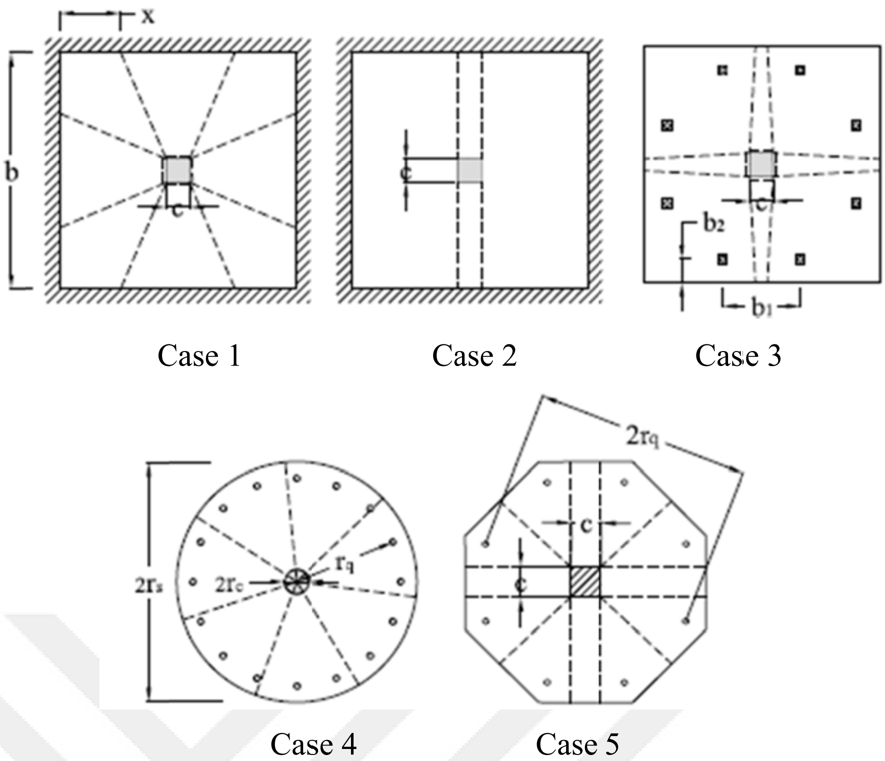

Figure 2.1 Cases for most tests configuration and their expected crack patterns

Table 2.1 Ultimate flexural failure P_{flex} for cases shown in Figure 2.1

Cases	Ultimate flexural failure load, $(P_{flex})^{\dagger}$
Case 1	$8m\left(\frac{1}{1-\ c/b}\ -\ 3+2\sqrt{2}\right)$
Case 2	$\frac{8m}{1-\ c/b}$
Case 3	$\frac{4\ m}{r_q(\cos(\pi/8)+\sin(\pi/8))\ -c}\times\frac{b^2\ -(b\times c)\ -(c^2/4)}{b\ -c}$
Case 4	$\frac{2\pi\times m\times r_s}{r_q-r_c}$
Case 5	$\frac{2\pi\times m\times r_q}{r_q-r_c/\pi}$

† all parameters are shown in Figure 2.1, and

$$m=\rho\times d^2\times f_y\times\left(1-0.59\ \rho\times{}^{f_y}\!/_{f'_c}\right)$$

2.2.2 Equilibrium of forces acting approach

This approach may considered as the first proposed mechanical model, it was recommended by the Swedish code in 1963, based on the finding of Kinnunen and Naylander [4], which was originally developed for axisymmetric loading. The theory based on the assumption that the punching resistance is related to the critical rotation ψ, and this strength can be calculated by the equilibrium of the forces acting on the connection of the circular column to the circular ring of the reinforced slab.

Kinnunen/Naylander's approach had become an inspiration to many other researchers during the last four decades. The model assumes rigid radial sectors of sectorial angle outside the tangential shear crack bounded by two radial cracks. This sector rotates around a line located below the root of shear cracks. It assumes that there are two different angles of inclination in tangential crack, which are 45degree for the compression zone that transfers the shear force to the column and α for tension zone. The failure criterion is limited by the concrete ultimate shear expansion ($\varepsilon_c = -0.00196$) at the tension face of the slab.

Based on the of Kinnuen/Naylander approach, Shehata [17] applied his model with modifications in sector shape and the radial net force inclination (to be 10degree), which acts normal to the projection area so that the load is ranging between 0.5 to 0.7 times the ultimate load (V_u). The observed shear crack inclination was 20degree (see Figure 2.2). According to his method, the rigid segment rotates around a line located on the face of column and at the level of the neutral axis (x) of the segment (see Figure 2.2). The proposed equation assumes three critical states. First, splitting of concrete occurs when the inclination of the compression force reaches 20degree. Second, crushing of concrete occurs when the radial strain on the compressed face reaches a value of 0.0035. Third, crushing of concrete occurs when the tangential strain on the compressed face reaches a value of 0.0035,

$$V_u = 1.76 r_o \times d \times \rho^{1/2} \times f'_c \left(\frac{E_s}{E_c}\right)^{1/2} \times \left(\frac{d}{r_o}\right)^{1/2} \times \left(\frac{500}{d}\right)^{1/3} \qquad (2.2)$$

where, r_o is the radius of column, and other parameters as in common.

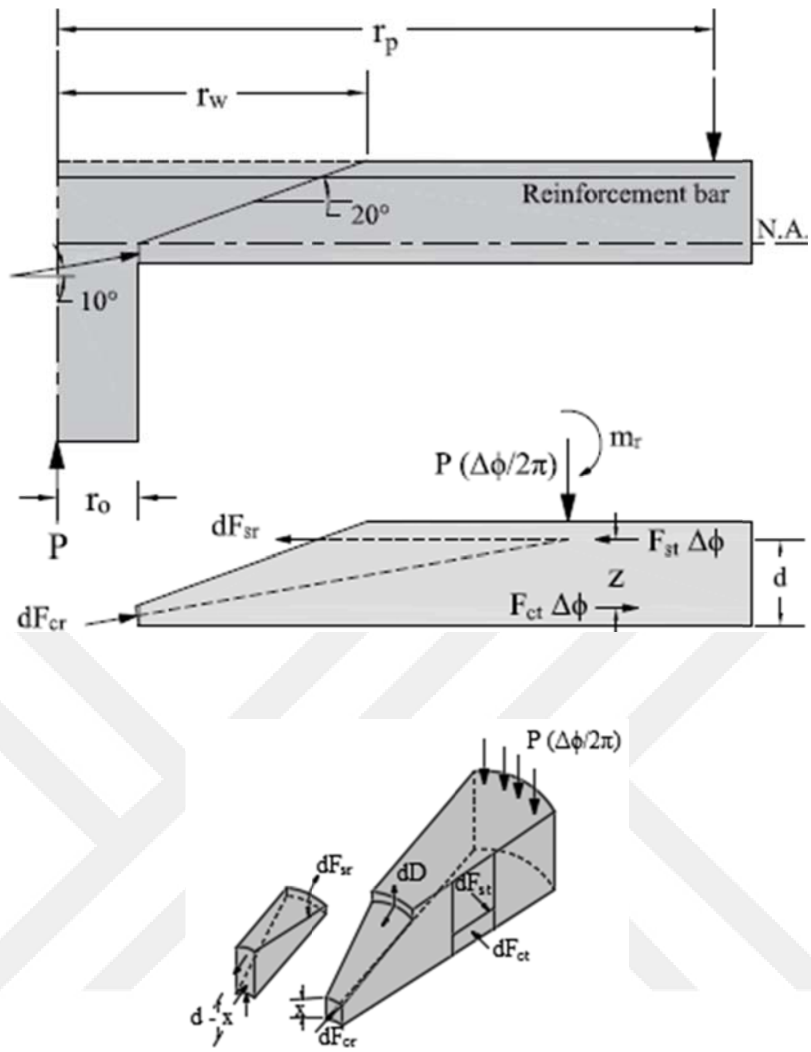

(a)

(b)

(c)

Figure 2.2 Mechanical punching model reproduced from [17] (a) stresses region, (b) forces acting on radial plane, (c) force acting on the segment

Broms [18] used same fictitious internal column capital of Kinnunen/Naylander model. He introduced his method and specified the different height of compression block by direct calculation based on the properties of materials. He defined the tangential strain based on the stress - strain relation in uniaxial compression cylinder. According to his assumption, the failure occurs when the tangential compression strain (V_{ε}) (see Figure 2.3a) in slab at the column edge exceeds 0.001, or when a radial compression stress (V_{σ}) (see Figure 2.3b) in the imaginary internal column capital reaches 1.2 times the concrete compressive strength. For the tangential compression strain (V_{ε}), the predicted punching shear is varied according to the failure modes. For the first mode, the stress in the reinforcement does not reach the yielding strength (f_y) (Equation 2.3a). In the second mode, the reinforcement is yielding and the punching failure distance r_y is less than the radius of the circular slab. In the third mode, V_ε is calculated when r_y lays within the slab radius.

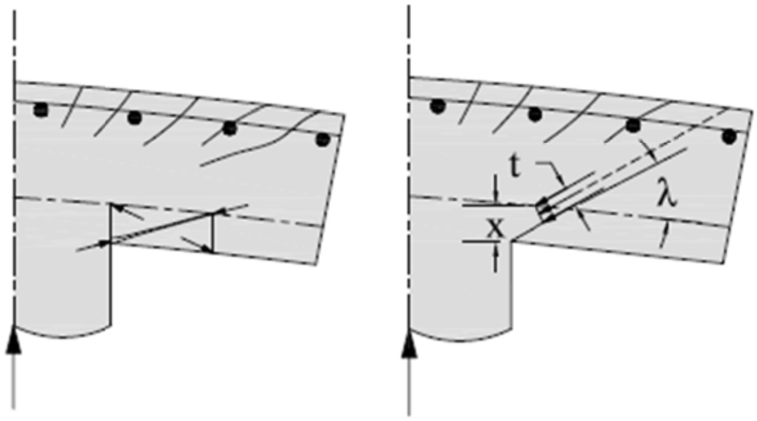

(a) (b)

Figure 2.3 Failure modes according to [18] (a) tangential compression strain V_ε (b) radial compression stress V_σ

The predicted punching capacity is the lesser of the Equation 2.3 and 2.4;

$$V_\varepsilon = m_\varepsilon \times \frac{8\pi}{2\ln\frac{b}{2r_o}+1-\frac{(2r_o)^2}{b^2}} \quad \text{if } \sigma_s < f_y \qquad (2.3a)$$

where, r_o is the radius of the circular column, b is the diameter of the circular slab, and,

$$m_\varepsilon = \frac{V}{8\pi}\left[2\ln\frac{b}{2r_o}+1-\frac{(2r_o)^2}{b^2}\right]$$

$$V_\varepsilon = m_y \times \frac{2\pi}{1-\frac{2r_o}{b}} \quad \text{if } \sigma_s \geq f_y \text{ and } r_y \geq \frac{b}{2} \qquad (2.3b)$$

where, $m_y = \rho \times d^2 \times f_y(1 - \frac{x}{3d})$

If $\sigma_s \geq f_y$ and $r_y < \frac{b}{2}$ Then

$$V_\varepsilon = \frac{V_{y2}}{m_y\frac{b}{2}}\left[m_y r_y + \int_{r_u}^{b/2}\left(\frac{V_{y1}}{8\pi}\left(2\ln\frac{b}{2r}+2-\frac{(2r_o)^2}{4r^2}-\frac{(2r_o)^2}{b^2}\right)+\Delta f'' EI\frac{2r_o}{2r}\right)dr\right] \qquad (2.3c)$$

where, r is a varied radius of the punching crack, $\Delta f''$ is the ultimate tangential curvature, V_{y2} equals to V_ε in Equation 2.3b, and

$$V_{y1} = m_y \times \frac{8\pi}{2\ln\frac{b}{2r_o} + 1 - \frac{(2r_o)^2}{b^2}}$$

The radial compression stress (V_σ) is obtained as follows,

$$V_{\sigma,\ max} = 1.2\, f'_c \times t \times \sin(25) \times u \times \left(\frac{0.15}{t}\right)^{\frac{1}{3}} \times 10^3 \qquad (2.4)$$

where, t is the depth of the compression strut equal to $\left(\frac{x}{2\cos\lambda}\right)$ (see Figure 2.3b) and λ is not less than 25degree.

2.2.3 Truss analogy model

The model of strut-and-tie considers the load transfer in slabs same as a space truss, where the reinforcement represents the tension tie and the inclined concrete represents the compression struts connecting at nodes. ACI318 [19] recommends that the angle of inclined compression struts α have to be at least 25degree in order to mitigate cracking and to provide compatibility due to the expansion ties and shortening struts. Related to slab column connection Alexander and his fellow researchers [20] introduced a lower bond prediction model by combining the strut-and-tie model featuring the concept of a limited shear stress assuming inclined arch compression strut (see Figure 2.4). The model consists of four orthogonal radial strips of the same column's width that act as cantilever beams holding the loads from four panels of the slab. Therefore, the curvature of the arch is affected by the beam's shear action normal to the arch face. The shear force is transferred from the slab to the column through the arch vertical component, whereas the horizontal component is in equilibrium with the flexural reinforcement. The plate maintains moment gradient through force gradient in reinforcement that is governed by the bond capacity in addition to yielding. According to this method, the punching resistance for square simply supported isolated slab-column connection is as follows:

$$V_u = 8 \times \sqrt{0.17\sqrt{f'_c} \times c \times d^3 \times \rho \times f_y \times \left(1 - \frac{\rho \times f_y}{1.7 f'_c}\right)} \qquad (2.5)$$

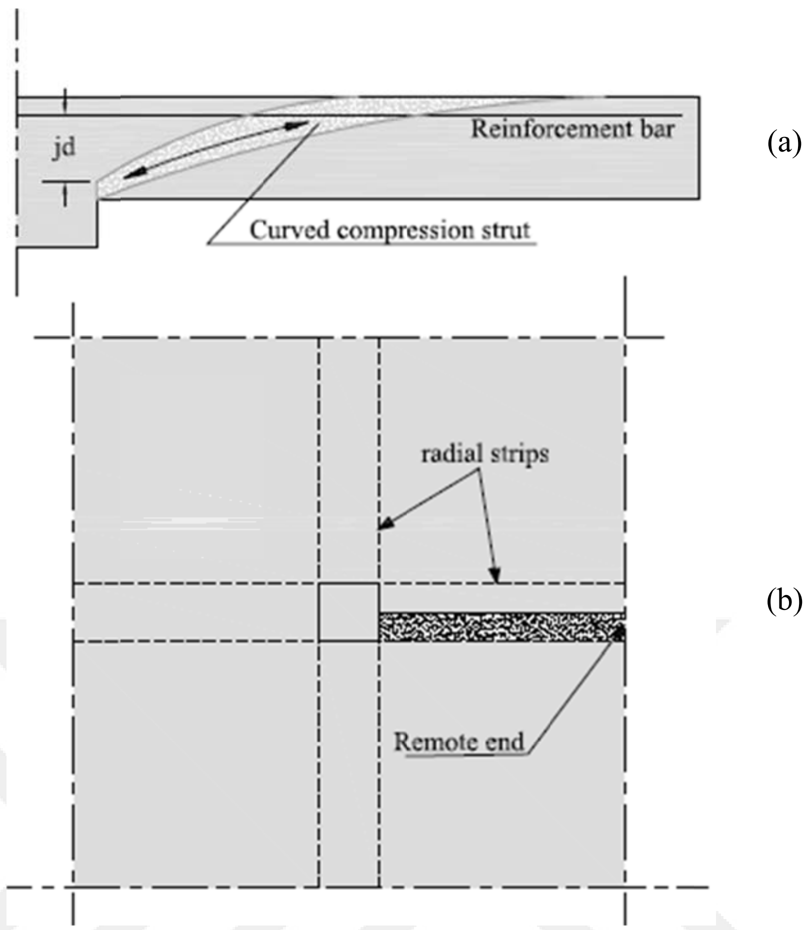

Figure 2.4 Truss analogy model reproduced from Alexander and his fellow researchers [20] (a) compression strut (b) radial strips

2.2.4 Physical behavior approaches

Theodorkapoulos [21] established that the behavior of the slab column system under loading passes through three stages; formation circular crack, formation radial cracks, and initiation inclined shear crack at 50 -70% of the ultimate load. Their failure mechanism is due to the equalization of shear stress to the splitting strength of concrete at the compression zone. In this stage, the applied load will be resisted by both the vertical components of the compression zone above the crack V_c and the dowel action V_d. Because the two previous actions have the same parameters, the following presented model considers them as a whole,

$$V_u = 0.47 \times \frac{0.5X_f}{0.25d + X_f} \times (f'_c)^{2/3} \times b_o \tag{2.6}$$

where b_o is the control parameter = 4c +12d, and ($X_f = \frac{\rho f_s - \rho' f'_s}{k_1 f_{cu}} d$) is the depth of the neutral axis at the flexure critical section. In which, f_s, f'_s, ρ, and ρ' are steel stresses and reinforcement ratio in tension and compression, respectively, where k_1 is a variable in term of concrete strain.

2.2.5 Critical shear crack theory

The Critical Shear Crack Theory (CSCT) is a physical approach that considers the kinematics of the cracked section. The principle of this theory is based on the assumption that the shear strength is dependent on the size and roughness of the shear crack [22,23]. This shear crack passes through the concrete strut, which in turn, transfers a high slab load to the column and, hence, leads to the formation of a diagonal shear crack. As a result, a conical deflected shape is produced outside the crack, as shown in Figure 2.5a, which is linearly displaced with a constant rotation.

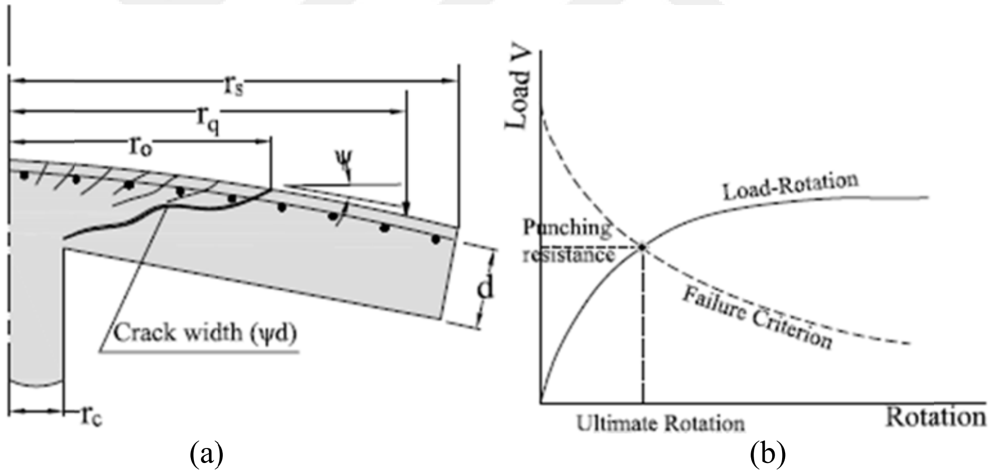

Figure 2.5 Critical shear crack theory (a) Typical slab-column assembly, (b) determination of the punching resistance in the load-rotation domain [22]

The increase of the rotation (ψ) results in an increase in the crack width, which leads to a reduction of the aggregate interlock. The crack width is assumed to be proportional to the product of the rotation and the effective depth (ψd) [24]. In addition, the crack roughness depends on the ratio of the crack width to the maximum aggregate size ($\psi d/(16+d_g)$). In the mentioned bases (CSCT), Muttoni in 2003 [25] modified Muttoni and Schwartz's [24] failure criterion proposed in 1991 to include the effect of the maximum aggregate size as follows:

$$V_R = \frac{0.75\left(u_1 \times d \times \sqrt{f'_c}\right)}{1 + 15 \times \left[\frac{\psi \times d}{16 + d_g}\right]} \tag{2.7}$$

where u_1 is the critical perimeter, d is the effective depth, and d_g is the maximum size of the aggregate. Based on the available experimental results, Muttoni [22] found that the punching shear strength can be obtained from the intersection of the proposed failure-criterion curve with the load-rotation curve, as shown in Figure 2.5b.

To obtain the load-rotation relation to axisymmetric cases, Muttoni [22] proposed a formula to obtain the relationship between the shear force and the slab rotation, assuming the same model behavior that was proposed by Kinnunen and Nylander [4]. In this model, Kinnunen and Nylander assume that the rigid radial sectors of sectorial angle $\Delta\varphi$ outside the tangential shear crack are bounded by two radial cracks. This sector rotates around a line located below the root of the shear crack, as shown in Figure 2.6a. Assuming an equilibrium of forces acting on the outer rigid radial segment, and using a quadrilinear moment-curvature relationship (see Figure 2.6b), Muttoni [22] derived the following formula:

$$V = \frac{2\pi}{r_q - r_c}\begin{pmatrix} -m_r r_0 + m_R \langle r_y - r_0\rangle + EI_1\psi \langle \ln r_1 - \ln r_y\rangle + \\ EI_1\chi_{TS} \langle \ln r_1 - \ln r_y\rangle + m_{cr} \langle r_{cr} - r_1\rangle + EI_0\psi \langle \ln r_s - \ln r_{cr}\rangle \end{pmatrix} \tag{2.8}$$

where r_0, r_s, r_q, and r_c are radii illustrated in Figure 2.5a; r_1, r_{cr}, and r_y are the radii of the stabilized crack, cracked, and yielded zones, respectively; and m_r, m_{cr}, and m_R are the radial, cracked, and nominal moments per unit width, respectively. Finally, EI_o and EI_1 are the flexural stiffnesses after and before cracking, respectively, as illustrated in Figure 2.6b.

r_s is reached by considering the bilinear moment-curvature (dashed line in Figure 2.6b), which is produced by neglecting the effect of the concrete tensile strength and tension stiffening, and assuming flexural strength m_R for r_y = 0.75. Moreover, assuming that the rotation ψ is proportional to $(V_R/P_{flex})^{3/2}$, Equation 2.8 can be reduced to:

$$\psi = 1.5 \times \frac{r_s}{d} \times \frac{f_y}{E_s} \left[\frac{V_R}{P_{flex}}\right]^{3/2} \tag{2.9}$$

where P_{flex} as in Table 2.1

This shows that the percentage of (V_R/P_{flex}) specifies the type of failure. Four percentage ranges have been identified in an isolated concentric slab-column system in ambient conditions:

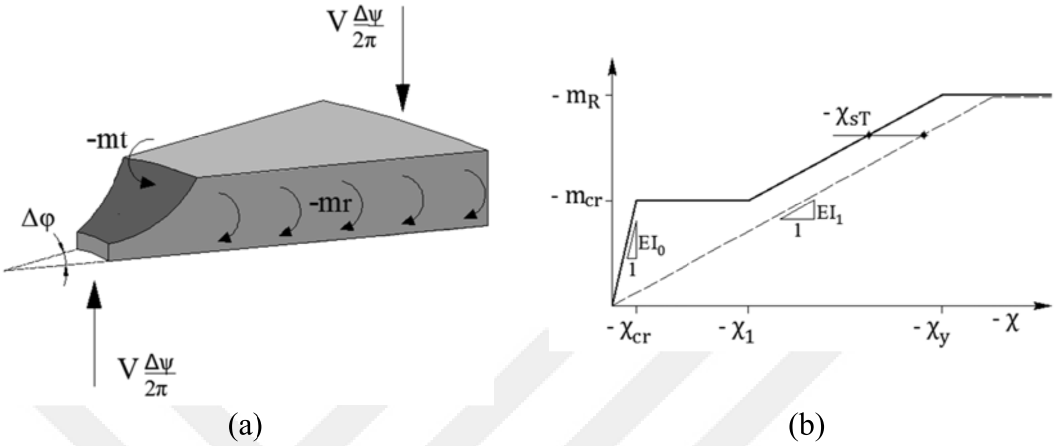

Figure 2.6 CSCT model a) Forces acting on a rigid slab sector; b) Quadrilinear and bilinear moment-curvature relationship [22]

To apply Equations 2.7 and 2.9 to different specimen geometries and test configurations, the column section should be transformed into a circular shape with radius RC, based on the assumption that the shear stress along the column perimeter is the same. However, to transform the square slab to its equivalent circular shape, the maximum flexural capacity P_{flex} should be the same for both the tested and equivalent slabs [26], such that:

$P_{flex,\ square} = P_{flex,\ circular}$.

To equate P_{flex} of the square slab that was tested by Guidotti [26] with that required in Equation 2.9, the radius of the equivalent circular slab r_s and the radius of the load point r_q are as follows:

$$r_s = \frac{4}{\pi} \times \frac{r_q - r_c}{a - c} \times \frac{a^2 - (a \times c) - \frac{c^2}{4}}{[a + b_1 - 2 \times (c + b_2)}$$

$$r_q = \sqrt{\left(\frac{a}{2} - b_2\right)^2 + \frac{b_1^2}{4}}$$

where all parameters are illustrated in Figure 2.1.

2.2.6 Comparison between the mechanical models

Table 2.2 shows a comparison of the model compared to elected test results. The data are collected from the references separately. The missing data were calculated in the current research.

Table 2.2 Comparison of the different models from literature

Ref.	Equilibrium of forces acting models							
	Shehata [17]		Broms [18]		Alexander [27]		Muttoni [22]	
	No.	mean	No.	mean	No.	mean	No.	mean
Elstner [15]	21	0.95	19	1.21	19	1.21	22	0.98
Kinnunen [4]	16	1.04	6	1.06	6	1.06	12	1.05
Moe [13]	7	1.01	9	1.17	9	1.17	9	1.13
Tolf [28]	8	1.10	8	1.05	8	1.05	8	1.06
Hallgren [29]	7	1.02	7	0.96	7	0.96	7	0.98
Σ	59	1.02	58	1.09	58	1.09	58	1.04

2.3 Flat Plate Behavior under Fire Conditions

Fire accidents continue to occur despite developments in the construction industry to avoid such cases. Therefore, studies that clarify structural and structural member's performance under fire conditions are still required. According to the International Association of Fire and Rescue Services [30], 40% of fire accidents around the world during 2013 were defined as structural fires. Moreover, in the USA, 494,000 structural fires were reported during 2014–2015. In England, 154,700 fire incidents were recorded, 28,200 of which were accidental dwelling fires. Therefore, the fire phenomenon should be understood and the performance of buildings under both ambient and fire conditions should be well assessed. This assessment can be conducted experimentally or with analytical and computational tools.

The punching shear problem may aggravate if this part of the structure is without shear reinforcement and is subjected to high temperatures due accidental fire. Therefore, this subject still attracts attention by researchers.

The criterion for determination of the member endurance for a specific period of fire exposure is that it must neither not collapse, nor reaching a specific temperature on the far side of the fire. According to Eurocode 2 [31], shear failure due to fire is generally uncommon. This fact may be true for ordinary structures, but for the flat plates, the case is different. In flat plate under high temperatures, the punching shear problem is considered as a compound of two components. The first is the gradual decay in materials strength (this degradation in strength depends on the temperature gradient through the slab thickness) and Second, is the structural behavior that results from indirect actions. In general, any study on the behavior of flat plate under fire conditions should cover the following three themes:

- Fire scenario, which discusses the real and the standardized fire actions
- Thermal analysis and thermal properties
- Structural behavior of isolated elements and the global structure

The first two themes can be generalized for all structure types exposed to high temperatures; hence, the data can be shared among all structures subjected to fire.
The following sections are reviewed based on the three mentioned themes.

2.3.1 Fire scenario

Fire in real case passes through a series of phases; growth phase, fully developed phase, and decay phase, there is a short transition time from a growth phase to fully development phase known as Flashover [32]. These phases may differ from case to another according to fire density/distribution, fire load behavior for combustion, size, and geometry of the compartment, ventilation, and thermal properties (e.g. fire induced from hydrocarbon fuels cause severe fire effect).

Eurocode 2 [33] classified the severity of fire into two categories. The first is the nominal temperature-time curve that is sub classified into standard, external, and hydrocarbon. The second is the natural fire model that consists of simplified and advanced Computational Fluid Dynamic (CFD) models. Nominal standard temperature-time curve is widely used in the prediction of the fire resistance of the structure or part of which. Examples of this curve are the ISO 834 and ASTM-E119. The former curve is defined by ($T = 20 + 345 \log10 (8 t+ 1)$), while the latter defined by the points on the temperature-time curve, where T is the gas temperature in the fire compartment (°C) and t is the time (min). Matching these two ideal Fire curves is not easy and noticeable variation is expected, hence, a tolerance and correction are also applied to theses codes' method.

An important reservation on these two curves is that they represent a fire independently on ventilation, fuel load, and boundary conditions. Therefore, the thermal conditions associated with these fires seem to be more severe than that ensuing from a real fire [34]. Thus, many equivalent-times calculation methods relating to real fires were proposed. In 1928, Ingberg defend the real fire resistance based on assumption that the 'severity' of a fire is related to the fire resistance requirement. He defined the real fire resistance as a 'time' where two areas under real and standard fire curves (above 300 °C) are equal (so that $A_1 = A_2$ in Figure 2.7a). Blagojevic' [35] deemed that this hypothesis is poor in representing the fire in different heat transfer modes (radiation and convection). Moreover, the unit of areas under the curves has no meaning. Another hypothesis was proposed by the Law [36]. He assumed that the ventilations have a significant effect on determining the equivalent fire severity, which is the temperature on the standard curve that corresponds to the maximum temperature on real fire (see Figure 2.7b), so that the equivalent fire time is,

$$t_e = \frac{K \times L}{\sqrt{A_t \times A_w}} \tag{2.10}$$

Pettersson and his group [37] used the same Law's approach with including the thermal properties of the compartment boundaries. Their proposed equivalent time is,

$$t_e = \frac{0.31 \times C \times L}{\sqrt[4]{H} \times \sqrt{A_t \times A_w}} \tag{2.11}$$

where t_e, L, A_t, and A_w are the fire resistance period, fire load, total internal area of the compartment, and area of ventilation, respectively, while C and K are factors related to the thermal properties of the compartment boundaries.

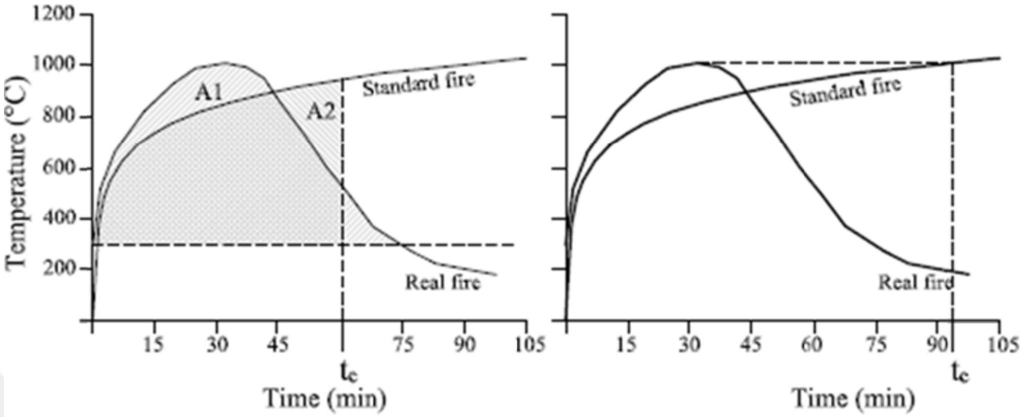

(a) (b)

Figure 2.7 Methods for calculation the equivalent time a) equal area hypothesis: real fire resistance requires 60 min of the exposing to standard fire curve b) maximum temperature hypothesis: real fire resistance requires 80 min of the exposing to the standard fire curve

The most used equivalent time formula is that incorporated in Annex F of EC1 [33], which is based on the dimensions of windows, fuel load, and both the horizontal and vertical openings. The real fire exposing time corresponding to time of standard fire exposure is:

$$t_{e,\ d} = k_b \times q_{f,d} \times W_f \tag{2.12}$$

where W_f is a ventilation factor, k_b is a conversion factor related to the thermal inertia of the boundaries or thermal absorptivity $\sqrt{\rho C_p k_c}$ in the absence of data k_b can be taken as 0.07, and $q_{f,d}$ is the design fire load density.

It is noteworthy that the above formula does not consider the applied load during the fire. Moreover, it is applicable to certain materials (protected steel) and structure size that may not be appropriate for other materials. Drysdale [38] compared the above formulae and rejected out Ingberg's formula for the same reasons of Blagojevic [35]. He also showed that Law's formula is highly conservative and does not consider the compartment boundaries. Thomas [39] found that the Eurocode formula under predicts the fire severity for short exposing time.

Only few real fire scenarios were found in the literature. Bamonte et al. [34] used the simplified two-zone fire model in term of Heat Release Rate (HRR) in order to introduce the fire scenario of flat plates in an underground car parking. The car parking was composed of a slab system with slab-column connections, which was assumed to behave as one compartment. In the first scenario, a single fire was assumed to be caused by the burning of a group of cars. This case was repeated assuming different starting and location points. In the second scenario, six HRR-curves that delayed in time were considered. The results showed that the maximum temperature reached from one single compartment was not the same of that from multi-compartments. Annerel et al. [6], used CFD model to extend Bamonte's study in order to determine the thermal load on the slab, but with some modifications in the ventilation zone. Three scenarios were defined in their study. The first two scenarios considered subsequent ignition of six cars using HRR curve, but with different approaches, to calculate the temperature distribution in the slab. The first scenario was based on the same Bamonte's [9] approach, whereas the second used the average temperature over each slab field. On the other hand, in the third scenario, the temperature distribution was calculated using the CFD model. They found that the zone model is not proper in the prediction of travelling fires over several compartments.

2.3.2 Thermal analysis of reinforced concrete slab

In this section, the behavior and effect of fire on concrete slabs is reviewed through the heat transfer subject and the degradation of materials' thermal and mechanical properties.

2.3.2.1 Heat transfer in slab

Heat transfer through a Reinforced Concrete (RC) slab can be analyzed as a transient (unsteady) one-dimensional problem. This is because of the size of the semi-infinite slabs (long two-plane dimensions of the slab compared to its thickness). This analysis would be easy if the slab is exposed to standard temperature-time curve with uniform distribution of temperature on one side. It is worthy to mention here, that in case of analyzing the heat transfer in a slab that is connected to a column with the fire subjected on the compression face. The heat will flow in two directions. This is because of the differences in temperature and thicknesses between the column and the slab. However, this amount of reduction in heat flow can be ignored because of its low amount.

In most experimental cases, the initial conditions are assumed constant and uniform (initial temperature, thermo-physical properties, and no internal heat generation). However, the temperature distribution across the slab thickness is nonlinear, hence, the thermal strains is also nonlinear, while the total deformation (thermal elongation and thermal curvature) is linear [6]. This nonlinearity is varying significantly between concrete and steel in RC. The concrete elements show obvious nonlinear behavior with temperature, while steel elements seem to have linear behavior rather than nonlinear behavior. This is because of the significant difference in the thermal conductivity between steel and concrete, and therefore the effect of the reinforcing steel bars on the temperature distribution is rather negligible.

The general equation of the three-dimensional heat conduction can be reduced to one-dimensional heat conduction as follows,

$$\frac{\partial T(x,t)}{\partial t} = \alpha \times \frac{\partial^2 T(x,t)}{\partial x^2} \tag{2.13}$$

subjected to $T(x, 0) = T_0$
Where $\alpha = k_c/(\rho c_p)$ is the concrete thermal diffusivity, ρ is the density, c_p is the specific heat, and k_c is the thermal conductivity.

The solution of the heat transfer equation should satisfy the initial and boundary conditions. The boundary conditions usually include the convection and radiation, thermal loads on the exposed surfaces. The solution of the heat transfer differential equation can be achieved using various analytical and numerical approaches. Among these methods are the separation-of-variables, method that developed by Fourier in 1820s [40], the Laplace transformation approach, the finite difference method, and the finite element method.

2.3.2.2 Concrete thermal properties

The most important property that affects the thermal behavior of concrete is the thermal diffusivity. Mathematically, the thermal diffusivity is affected by its three components under fire conditions. Thermal diffusivity decreases with increasing in specific heat and decreasing in thermal conductivity.

Thermal Conductivity: Thermal conductivity can be defined as the concrete's ability to conduct heat. This property is measured by transient or steady-state test methods. Figure 2.8 compares several examples [31,41- 43] of concrete's thermal conductivity at different temperatures. The figure shows that concrete's initial thermal-conductivity value under ambient conditions is in the range of approximately 1.33 to 2.83 W/m.K for carbonate aggregate concrete, while the upper limit is slightly lower for siliceous aggregate concrete. These values decrease significantly under high temperatures. Concrete's thermal conductivity loses approximately 90% of its normal value at 1000 °C. Many methods have been proposed to obtain the thermal conductivity k_c. Further information about these methods is detailed in the literature [31,39,41-44].

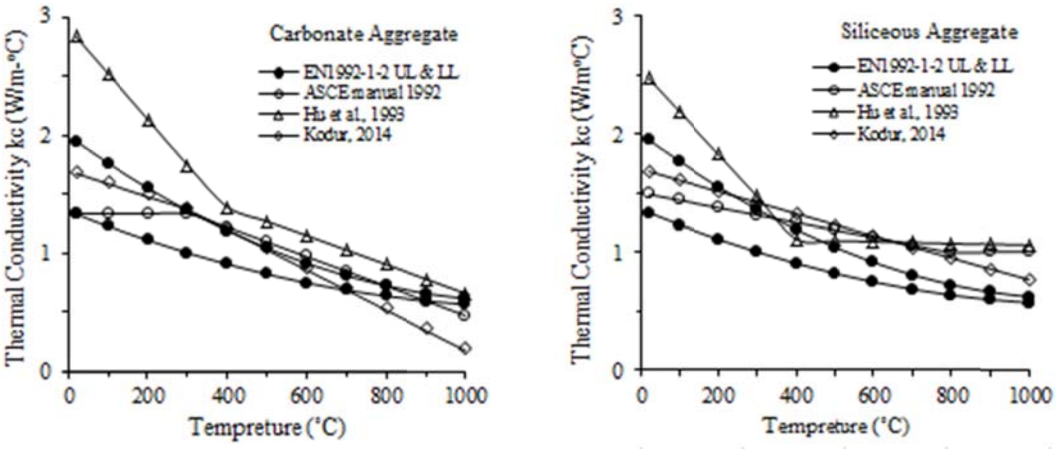

(a) (b)

Figure 2.8 Variation of concrete's thermal conductivity with temperature for (a) carbonate aggregate concrete and (b) siliceous aggregate concrete.

Thermal Capacity: The thermal capacity (ρc_p) is the product of the unit weight and the specific heat (c_p). The thermal capacity is highly influenced by the moisture content, type and amount of aggregate, and, therefore, by density. Figure 2.9 shows the variation of the thermal capacity with temperature from different references [31,41–43]. It is clearly demonstrated that the thermal capacity is almost constant up to 400 ^{o}C. As the temperature increases beyond 400 ^{o}C, an interesting increasing and decreasing variation occurs. However, this variation becomes minimal beyond approximately 800 ^{o}C. The most important note here, as shown by the comparison between Figures 2.9a and 2.9b, is that the type of aggregate controls the variations that occur between 600 and 800 °C.

In conclusion, the aforementioned thermal diffusivity factors are affected by high temperatures. In turn, the thermal diffusivity decreases with a decrease in thermal conductivity and an increase in specific heat.

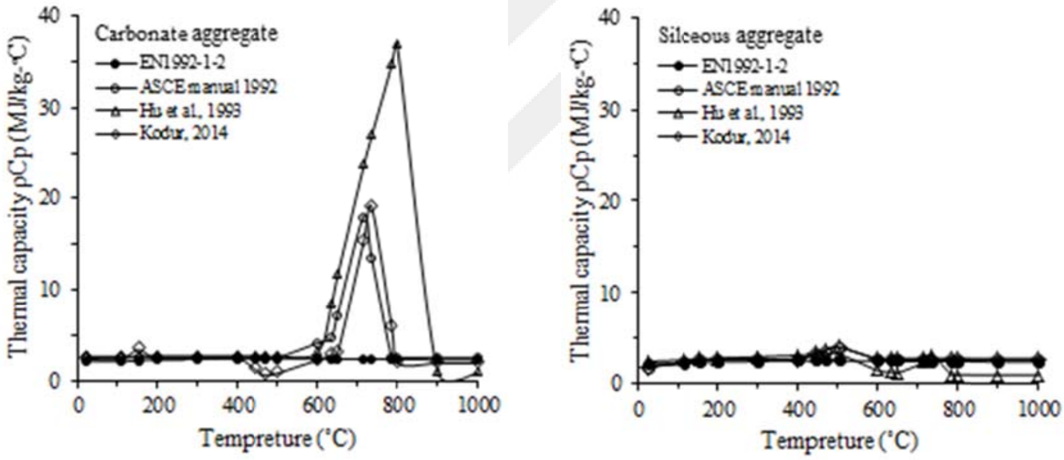

(a) (b)

Figure 2.9 Variation of the thermal capacity of normal-weight concrete with temperature for (a) carbonate aggregate concrete and (b) siliceous aggregate concrete

2.3.2.3 Concrete's mechanical properties

Concrete's mechanical properties play important roles in many of the proposed formulas for predicting the ultimate strength of slabs at elevated temperatures. It is clear from the literature that exposing concrete to fire temperatures leads to a serious deterioration in its mechanical properties.

Compressive Strength: Many factors affect the percentage loss in compressive strength due to heating. Among these factors are the water/cement ratio, aggregate size and type, and test method [45]. However, the concrete's initial strength has a trivial effect on the residual-strength percentage [46]. For unstressed samples, concrete loses approximately 18% to 20% of its initial strength at 400 °C [31,46]. Under the same circumstances, this percentage slightly increases to reach 24%, according to [47]. Moreover, half of the strength is lost between 540 and 590 °C for all curves. Figure 2.10 shows the degradation of the concrete compressive strength under high-temperature conditions based on different proposed relationships [31,41 – 43, 46, 47].

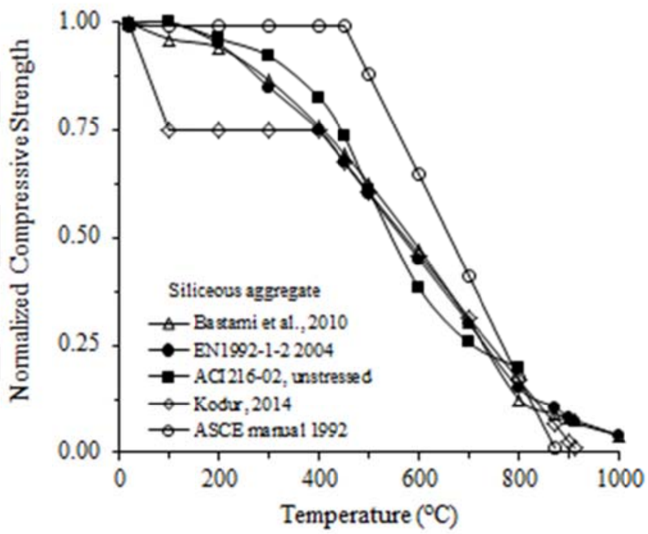

Figure 2.10 Degradation of compressive strength due to high temperature

Tensile strength: In many design cases, the tensile strength is ignored (conservative). Therefore, few tensile strength data can be found in the literature and even these data are significantly deferred from each other depending on the various methods of consideration (direct and indirect). These variances extend in the case of high temperature exposure. Nause [48] found that mostly used test in specifying the effect of high temperatures on the tensile strength is the indirect-tensile strength. Kodur [43] found that 20% of the tensile strength will retained for sample subject to the temperature above 600 °C.

Elasticity Modulus: The main factors affecting the elasticity modulus are approximately the same as those influencing the compressive strength [48]. However, ACI 216 [46] showed that the aggregate type has no significant effect on the elastic-module behavior with temperature. Figure 2.11 shows the deterioration of the elasticity modulus of normal concrete, according to tests carried out by Bastami et al. [47] and Li and Purkiss [49].

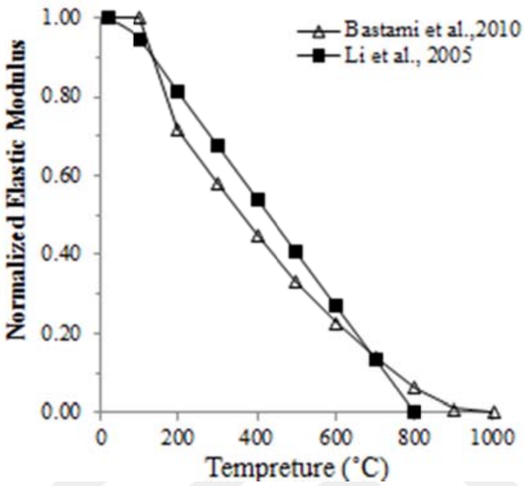

Figure 2.11 Degradation of elasticity modulus of normal concrete under high temperatures

Stress-Strain Relationship: Tests investigating the stress-strain relationship under high temperatures showed that both the strength and stiffness decrease with temperature. However, the ductility increase somewhat between 300 and 800 °C [50]. Table 2.3 includes the latest correlations between the compressive stress and the corresponding strain at elevated temperatures. More stress-strain models can be found in the literature [47,51].

Table 2.3 Stress-strain relations of concrete at elevated temperatures

Ref.	Stress-Strain at Elevated Temperatures
Kodur [43]	$\sigma_{cT} = f'_{cT} \times \left[1 - \left(\frac{30\ (\varepsilon_{cT} - \varepsilon_{max})}{(130 - f'_c)\ \varepsilon_{max}}\right)^2\right],\ \varepsilon_{cT} > \varepsilon_{max}$ $\sigma_{cT} = f'_{cT} \times \left[1 - \left(\frac{(\varepsilon_{max} - \varepsilon_{cT})}{\varepsilon_{max}}\right)^H\right],\ \varepsilon_{cT} \leq \varepsilon_{max}$
Bastami et al. [47]	$\sigma_{cT} = f'_{cT} \times \left[\frac{(a + bt + c) \times (\varepsilon_{cT} / \varepsilon_{max})}{a + bt + c - 1 + (\varepsilon_{cT} / \varepsilon_{max})^{a + bt + c}}\right],\ \varepsilon_{cT} > \varepsilon_{max}$ $\sigma_{cT} = f'_{cT} \times \left[\frac{c \times (\varepsilon_{cT} / \varepsilon_{max})}{c - 1 + (\varepsilon_{cT}/\varepsilon_{max})^c}\right],\ \varepsilon_{cT} \leq \varepsilon_{max}$ where: $a = 2.7(12.4 - 1.66\times10^{-2} f'_{cT})^{-0.46}$ $b = 0.83 \exp(-911/f'_{cT})$ $c = [1.02 - 1.17(E_p/E_c)]^{-0.74}$
EN 1992-1-2† [31]	$\sigma_{cT} = f'_{cT} \times \left[\frac{3\varepsilon_{cT}}{\varepsilon_{max}\left(2 + \frac{\varepsilon_{cT}}{\varepsilon_{max}}\right)^3}\right],\ \varepsilon_{cT} \leq \varepsilon_{cu}$

†For the descending branch, the code permits using linear or nonlinear models and uses the main parameters included in Section 3.2.2 of EN 1992-1-2 [31].

2.3.3 Thermo-mechanical behavior of a flat plate-column connection

An extension of the slab-column assembly's mechanical model in normal conditions, to be adopted for fire conditions, is highly questionable. This is attributed to the complexity of the punching behavior and the nonlinear behavior of both the heat transfer and material properties' decay. However, the attempt is still interesting.

Two major changes have an influence on the total resistance of the slab-column connection behavior. The first, a reduction in materials' properties, is direct, while the second, increasing the applied load, is indirect. When the slab is heated from one side, it undergoes significant thermal curvatures that result in obvious deflections and rotations. The carried load is redistributed away to the adjacent supports with lower temperatures through an extra hogging moment of the slab over the fixed supports. As a result, the load-equilibrium action will increase the axial load on the column until it reaches the plastic capacity, as illustrated in Figure 2.12. This load can reach as high as 40% to 50% of the service load [8,9]. The amount of these loads depends on the slab's bending capacity [10,46].

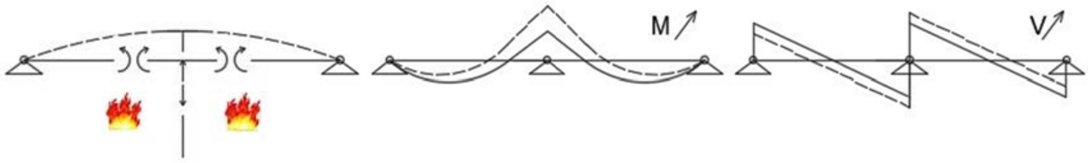

Figure 2.12 Increase of axial load due to thermal deformation restraints [52]

The aforementioned structural behavior is simultaneous with the changes in the material's thermal and mechanical properties. The degradation in these properties will continue until no more concrete contribution can be expected; hence, the concrete resistance is neglected. Therefore, the slab and columns will gradually lose part of their w (T) depth, depending on the temperature development in the concrete. According to Eurocode 2 [31], the norm in determining the fully damaged zone depends on the location of the 500 °C isotherm, where the concrete is considered fully damaged, as illustrated in Figure 2.13a.

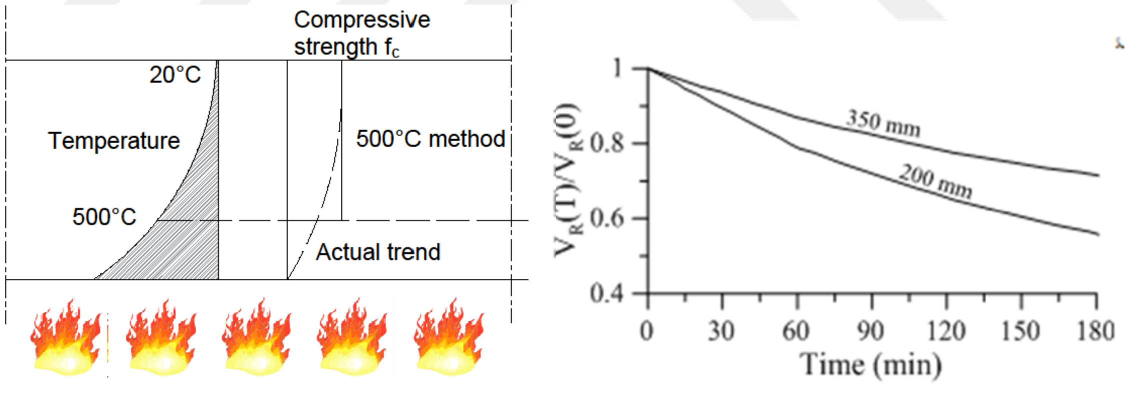

Figure 2.13 (a) Determination of the fully damaged depth (w) using the temperature-strength profile in concrete slabs; (b) decrease in punching resistance over time for 350-mm and 200-mm thick slabs (column size = 300 mm) [34]

Figure 2.14 shows the temperature profiles from different references [8,10,34]. The slabs were 200-mm thick and exposed to a standard temperature-time fire curve (ISO 834) for 120 min. It can be seen that the temperature development in the layers close to the exposed surface (50 mm from the surface) is approximately the same above 350 °C for all curves. However, the temperature profiles near the unexposed surface are slightly different. This is attributed to the different convection-boundary conditions there and the different moisture content that can affect the specific heat.

Few methods were proposed for the previous two direct and indirect influences. The following sections review the proposed methods for predicting the punching behavior under high-temperature conditions.

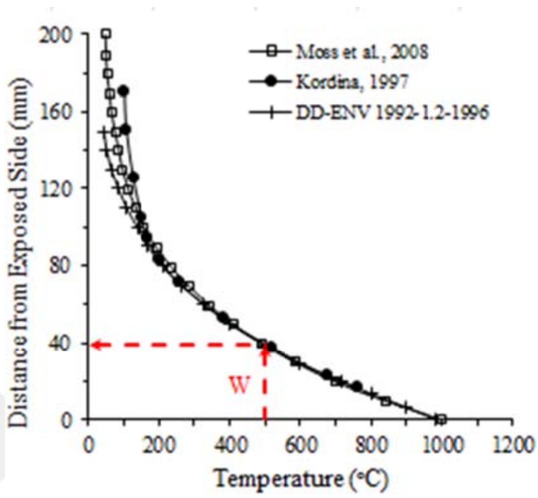

Figure 2.14 Temperature distributions across 200-mm-thick slabs exposed to a standard temperature-time fire curve (ISO 834) for 120 min

2.3.3.1 Effective–section method

Based on the 500 °C isotherm method, Bamonte [34] assumed that punching shear failure occurs under two influences. The first is the above-mentioned load redistribution, while the second is the decay of the material properties, which decreases the size of the slab d(T) so that the critical perimeter (u_1) is implicitly affected, as follows:

$$d(T)= d(0) - w(T) \tag{2.14}$$

and

$$u_1(T) = u_1(0)- \alpha w(T) \tag{2.15}$$

where d(T) and w(T) are the effective depth and the fully damaged depth, respectively (see Figures 2.13a and 2.14), as functions of the fire duration, while u_1 and d are the control perimeter and the effective depth in ambient conditions, respectively. The coefficient α equals 12 and 24 for rectangular sections, depending on the critical perimeter proposed by ACI 318 [19] and EN 1992-1-1 [53], respectively.

Bamonte et al. [34] used the punching shear capacity equations of ACI 318 [19] and EN 1992-1-1 [53] to derive the normalized decay of the section's resistance to punching shear strength, as follows:

$$\frac{V_R(T)}{V_R(20)} = \left[1 - \frac{\alpha w(T)}{u_1}\right] \times \left[1 - \frac{w(T)}{d}\right] \tag{2.16}$$

Bamonte et al. [34] applied Equations 2.14, 2.15, and 2.16 to two 200-mm and 350-mm-thick virtual slabs and showed that thinner slabs were more sensitive to fire than thicker slabs [22]. The reduction in punching resistance was 25% for the 200-mm-thick slab after 75 min of exposure to the ISO 834 standard curve. This percentage was limited to 16% for the 350-mm-thick slab, as shown in Figure 2.13b. This method appears to be as easy as shown in Equation 2.14 because of several adopted assumptions, summarized as follows:

- The remaining nonlinear partially damaged section (d(T) − w(T)) is assumed to maintain its initial compressive strength in ambient conditions.
- The inclination of the damaged cone is as proposed by ACI and/or EN 1992-1-1.
- The damage history is ignored; hence, the section is assumed to be fireproof until reaching 500 °C, without any gradual damage. In this case, this method cannot be applied to specimens exposed to temperatures less than 500 °C.
- A one-dimensional heat transfer is assumed along the slab. This assumption is questionable. According to most mechanical models developed from the Kinnunen/Nylander approach [4], this area (the slab-column contact area across the slab thickness) should be critical, because the failure occurs when the tangential compression strain exceeds a certain value. Thus, the assumption of a one-dimensional heat transfer leads to the elimination of the effect of the fictitious column capital, which is developed during the column damage. In turn, it affects the inclination of the failure cone.

According to both ISO 834 and E119, the furnace temperature should reach 500 °C within the first few minutes (approximately three minutes). However, due to the low concrete conductivity, only few specimens reached 500 °C in the literature.

To compare the effective-section method with the results from experimental specimens, two specimens with the same slab thickness but two different reinforcement ratios were analysed (specimens 1 and 3 tested by Kordina [10]). The experimental and analysis results of the two specimens are listed in Table 2.4. It is shown that specimens with both low and high reinforcement ratios (ρ = 0.56% and 1.54%) reached a similar percentage of residual punching shear strength $V_R(T)/V_R(20)$. The residual punching shear strengths based on the ACI 318 and Eurocode 2 punching equations were approximately 52% and 50%, respectively. This result agrees with Bamonte et al.'s [34] conclusion that the difference in the critical perimeter u_1 between the two codes leads to this similar reduction.

Table 2.4 also shows that both codes result in too-conservative residual strengths. A comparison of the calculated punching shear strength, $V_R(T)_{cal.}$, with the experimental one, $V_R(T)_{test}$, shows that, for the specimen with a low reinforcement ratio (ρ = 0.56%), the strength calculated using the ACI equation is 0.45 of the experimental strength, while this percentage decreases to 0.32 when the Eurocode 2 equation is used. For the specimen with the high reinforcement ratio (ρ =1.54%), the calculated strengths based on the ACI 318 and Eurocode 2 equations are 0.42 and 0.4, respectively. This difference is attributed to the effect of the reinforcement ratio, which is not considered in ACI 318, and to the ACI equation underestimating the strength of the specimen with the low reinforcement ratio in ambient conditions.

Table 2.4 Application on Effective–Section Method

Speci.	d(T) (mm)	ρ (%)	Code	u_1 (mm)	$\frac{V_R(T)}{V_R(20)}$	$V_R(20)$ (kN)	calculated $V_R(T)$ (kN)	tested $V_R(T)$ (kN)	$\frac{cal.V_R(T)}{testV_R(T)}$
1 [(a)]	113.6	0.56	ACI EC2	1612 2923	0.52 0.50	417.77 315	219 158	492	0.45 0.32
3 [(a)]	113.6	1.54	ACI EC2	1612 2923	0.52 0.50	439 440	230 221	550	0.42 0.40

[(a)] Specimens 1 and 3 from Kordina (1997) [10]

2.3.3.2 Extension of the critical shear crack theory

Bamonte and his group [7] extended the CSCT method to adopt the behavior of a column-slab assembly under high temperatures. They separately modified the two curves that underpinned the CSCT (failure criterion and load-rotation curves). This modification considers the deterioration of the material properties, as well as the extra applied load.

The right-hand part of the failure-criterion formula (Equation 2.7) can be modified by simply reducing the effective depth d and then the critical perimeter u_1, as discussed in the effective-section method, which implicitly depends on the compressive-strength decay. This size reduction leads to an increase in the rotation that ensues from the load, and then increases the crack opening and affects the aggregate interlock.

In the next step, the load-rotation curve should be modified with the assumption that the total displacement δ_{tot} of the slab member exposed to high temperature is the result of the displacement due to the applied load (δ_{load}) and the thermal sagging (δ_{th}). The former arises from the stiffness reduction due to a decrease in the section size and the concrete compressive strength. This displacement is assumed to be a linear function. The latter displacement (thermal sagging) is assumed as a second-order parabola, which is induced from the thermal expansion of the slab. This displacement can be defined using the thermal curvature.

Summing the two mentioned displacements (δ_{load} and δ_{th}) is difficult because the thermal strain is nonlinear through the slab thickness. Therefore, Bamonte et al. [7] used another approach, based on the concept that the slab will undergo a thermal curvature even if no load is applied. Figure 2.15 illustrates this fact. The thermal curvature $\chi_{(th)}$ can be defined as the curvature that extends along the x-axis. Thus, the curvature used in the load-rotation curve is related to the zero moment for the temperature under consideration; therefore, the superposition principle can be used.

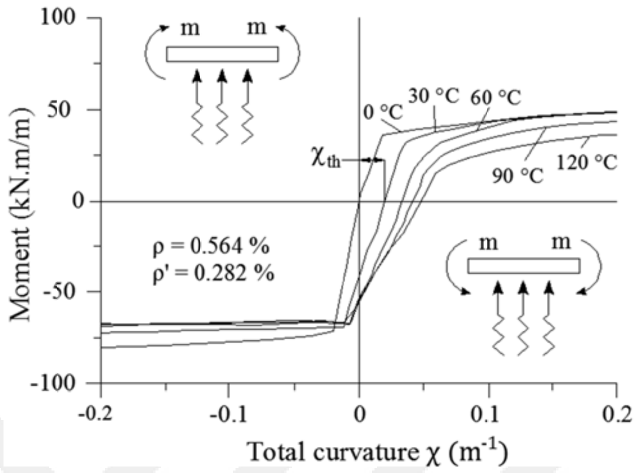

Figure 2.15 Typical moment-total curvature diagrams [7].

Smith et al. [54] utilized the first part of this method. They applied the residual concrete compressive strength (f'_c), reinforcement-bar yield strength f_y, and Young's modulus E_s, which were computed based on Eurocode 2 in both Equation 2.7 and 2.9. Experimentally, the yield strength has no significant effect on the slab shear strength [55] under ambient conditions. It makes no difference if the reinforcement bars yield before or after the punching shear takes place [56]. Moreover, hot rolled bars do not reduce the yield strength in temperatures less than 400 °C [31]. Fletcher et al. [57] found that the nominal strength of the reinforcement bars can be recovered if they are heated to less than 600 °C.

According to Smith et al. [54], the reduction in the reinforcement yield strength is due to the temperature of the reinforcement layer, while the reduction in the concrete compressive strength is due to the maximum temperature received by the entire slab through the exposed face. This means that the concrete along the slab thickness is assumed to be degraded at the same level. This assumption works well with thin slabs, e.g., those used by Smith et al. [54] (see Table 2.5). However, this assumption seems not to apply for thick slabs.

For the thick slabs tested by Annerel et al. [58], the maximum temperature at the exposed surface of the slab was 863 °C. Therefore, according to the previous assumption, the predicted $V_R(T)$ was 191 kN, while the tested $V_R(T)$ was 588 kN. From the previous discussion, it can be concluded that the average temperature should be used instead. This average should be estimated based on the heat-transfer parameters, e.g., heat flux h, exposure time t, and the concrete thermal diffusivity ($\rho\ c_p/k_c$).

Equation 2.9 was applied to ten selected specimens of different sizes and reinforcement ratios. The results are listed in Table 2.5. The development of the specimen rotation and failure criteria of three specimens (HU75-0.8, HU100-0.8, and HU100-1.5 selected from Smith, et al. [54]) is shown in Figure 2.16. The influence of the compressive strength degradation f'_c on the development of the load-rotation curve is obvious from the ten specimens. This is attributed to the implicit effect of f'_c on the cracking moment m_{cr} and the moment capacity of the section m_R, which directly affects the curvature. However, no significant differences are related to the failure criteria between the modelled specimens under ambient and heated conditions, at least for the thicker slabs. The square root of the compressive strength, which is proportional to the punching shear in the failure criterion (see Equation 2.7), has less effect, especially for the thicker slabs, which have a higher effective depth. The results of applying Equation 2.8 are listed in Table 2.5 and compared with a further model in next section. As Equation 2.8 accounts for the tension stiffening and the concrete tensile strength, it gives a more realistic punching shear strength than Equation 2.9, which does not include these parameters.

Table 2.5 Comparison between tested ($V_{R,test}$) and calculated ($V_{R,\ Eq.2.8}$, $V_{R,\ Eq.\ 2.9}$, and $V_{R,\ Eq.2.18}$) punching shear strengths using CSCT and Theodorkapoulos' model.

Specimen code	d [(1)] (mm)	ρ [(1)] (%)	V_R (kN)									
			Ambient Condition			Fire Condition						
			$V_{R,test}$	$V_{R,\ Eq.\ 2.9}$	$\frac{V_{R,\ Eq.\ 2.9}}{V_{R,\ test}}$	$V_{R,test}$	$V_{R,\ Eq.2.8}$	$V_{R,\ Eq.\ 2.9}$	$V_{R,\ Eq.2.18}$	$\frac{V_{R,\ Eq.\ 2.8}}{V_{R,\ test}}$	$\frac{V_{R,\ Eq.\ 2.9}}{V_{R,\ test}}$	$\frac{V_{R,\ Eq.\ 2.18}}{V_{R,\ test}}$
hu100-1.5[(2)] [54]	86	1.5	280	201	0.72	237	226	212	270	0.95	0.89	1.10
hu100-0.8[(2)] [54]	81	0.8	226	163	0.72	175	169	157	188	0.96	0.90	1.07
hu75-0.8[(2)] [54]	58	0.8	101	95	0.94	91	79	75	92	0.87	0.82	1.01
hu50-0.8[(2)] [54]	31	0.8	54	38	0.70	56	27	27	36	0.48	0.48	0.64
A[(3)] [59]	95	1.47	249	273	1.09	235	259	250	236	1.10	1.06	1.00
B[(3)] [59]	95	1.16	225	241	1.07	200	234	229	198	1.17	1.15	0.99
C[(3)] [59]	95	0.63	160	137	0.86	141	136	136	134	0.96	0.96	0.95
S0[(4)] [58]	212	0.51	998	657	0.65	588	263	191	563	0.45	0.32	0.96
1[10]	153	0.5	-	462	-	492	481	436	519	0.98	0.89	1.05
3 [10]	149	1.5	-	697	-	550	575	561	608	1.04	1.02	1.11
A [10]	112	1.5	-	399	-	345	402	375	490	1.17	1.09	1.42

(1) Other properties are shown in Appendix A.
(2) The codes are AU100-1.5, AU100-0.8, AU75-0.8, and AU50-0.8 for those under ambient conditions.
(3) Add T after the listed code for the specimens under fire conditions.
(4) Add "fire" after the listed code for the specimen under fire conditions.

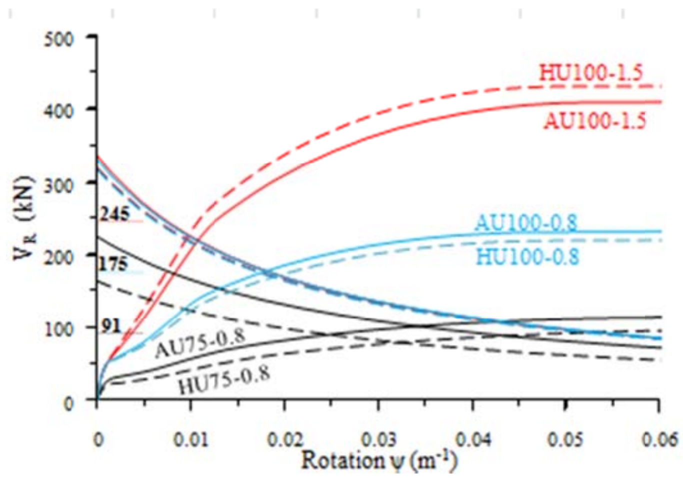

Figure 2.16 Comparison of punching shear strengths under ambient and fire conditions using CSCT, reproduced according to the method proposed by Smith et al. [54]

2.3.3.3 Modification of Theodorkapoulos' model

Ghoreishi et al. [59] adapted the model proposed by Theodorkapoulos et al. [21] to evaluate the shear strength of slab specimens under fire conditions. Originally, the proposed model (see Equation 2.17) assumed that the ultimate strength of the two-way slab was resisted by the compression zone and the dowel action by about 65% to 75% and 25% to 35%, respectively. The shear strength was directly affected by both the moment and shear induced cracks, X_f and X_s, respectively.

$$V_R = u_1 \times X \times \cot\theta \times f_{ct} \tag{2.17}$$

where u_1 is the critical perimeter based on BS 8110 (British Standard for the design and construction of reinforced and prestressed concrete structures), θ is the cracks' angle (assumed 30°), f_{ct} is the tensile strength obtained from the indirect-splitting test, and the neutral axis depth X is based on the harmonic mean of the both depths of compression zone produced from flexural and shear critical section as follows,

$$\frac{1}{X} = \frac{1}{2X_f} + \frac{1}{2X_s} \tag{2.18}$$

where X_f, X_s are the depth of the compression zone of the flexural and shear critical sections, respectively. X_s equals 0.25 of the effective depth d and X_f can be obtained according to the classical steps of flexural derivation equations.

In their modification, Ghoreishi et al. [59] assumed the following:

- The critical perimeter is 1.43 d away from the face of the loaded area (column).
- The reduction in f'_c due to high temperature is estimated based on Eurocode 2 provisions.
- The tensile stress f_s and compressive stress f'_s of the reinforcing bars at X_f are computed using the provisions of the Canadian Concrete Standards CSA A23.1 (2010).
- The tensile strength is related to the compressive strength, as $f_{ct}= 0.323f'^{2/3}_c$

The application of the proposed modification to Equation 2.17 results in:

$$V_R = 2.238 \times (c + 2.86d) \times X \times f'^{2/3}_c \tag{2.19}$$

where c and d are the column size and the effective depth, respectively, and f'_c is the concrete compressive strength of a standard cylinder.

The results of applying Equation 2.19 are shown in Table 2.5. They show that the proposed equation overestimates the shear strength by a maximum of 11%, compared to the experimental specimens. However, for a very thin slab, the estimated strength was lower than that of the tested specimen by 36%. It is worth mentioning here that the materials' resistance factors are ignored (i.e., $\varphi_s = \varphi_c = 1$).

In contrast to the applications of Equations 2.8 and 2.9, using the maximum or the average temperature had no significant effect on the results of Equation 2.19, as shown in specimen S0_fire. This is because of the assumption of a full cracked section and a low concrete temperature in the compression zone.

2.4 Comparison of Available Tests on Punching Shear Strength Exposing to High Temperatures

Only few experimental works were found in the literature on slab-column connections under high temperatures. Table A-1 lists the available experimental data on punching shear behavior under high temperatures, while the following sections review the main studied parameters.

2.4.1 Test setup and specimen configurations

All of the available experimental studies were carried out using a single slab-column connection, but with different configurations. These configurations represent the load-application method and the boundary conditions, which significantly affect the yield line formation, which in turn controls the failure type.

In the literature, three groups of experimental-specimen setup configurations were found. In the first group, the experimental specimens were installed upside down on a specially made furnace so that the weights of the specimen, frame, and devices were held by a bearing support. The load was applied by a tendon, which was passed through the column stub and connected to the free end by a stiff plate [10,58]. For the specimens tested by Kordina in 1997 [10], this load was applied using 16 load points, which were circularly distributed on the top of the slab (tension side) with a central angle of $\pi/8$ (see Figure 2.17a). For the specimens tested by Annerel et al. in 2013 [58], only eight load points were used (see Figure 2.17b). For the two studies, the diameter of the distributed load points was selected according to Eurocode 2 provisions.

In the second group, only the slab-column assembly was supported, leaving the corners free to lift. This setup is considered the oldest test setup and is shown in Figures 2.17c through 2.17e. It was used by Elstner and Hognestad [15] and other studies [54,59-61]. In some of the specimens, e.g., those tested by [59-61], the load was applied directly from the jack to the column stub through a stiff plate. Thus, the self-weight and the applied load were held by the square line support. Instead of directly supporting their specimens with steel sections, Smith et al. [54] used bars with half-circular sections to apply the line supports.

The test setup for the third specimen group is more interesting and more complex than that of the previous two setups. In this setup, the four edges of the slab are clamped. This leads to a restraint of the vertical and axial movements. Thus, additional negative moment is developed. Both the axial resistance and the section negative-moment capacities decrease the positive moment that acts within the high punching-shear stress discontinuity region. This experimental test setup was introduced in two recent studies by Smith et al. [54,62] and is shown in Figure 2.17c.

In their work, Smith and her co-workers [54,62] tested five fully restrained specimens under fire conditions. These specimens were compared with their corresponding unrestrained control specimens, both in ambient and fire conditions. The control-specimen setup was as in the aforementioned second group.

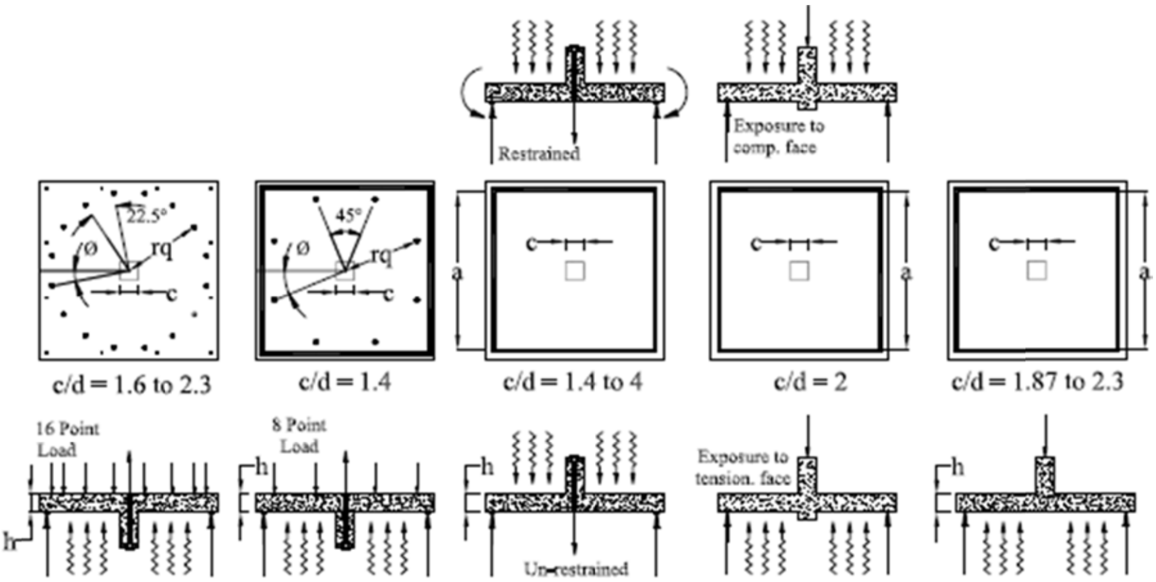

(a) case 1[10] (b) case 2 [58] (c) case 3 [54] (d) case 4[60] (e) case 5 [61]

Figure 2.17 Test setup and configurations for the literature tests listed in Table A -1.

2.4.2 Size and reinforcement ratio

All specimens presented in this study are monolithic square slabs with square columns. The percentage of the column size c to the effective depth d (c/d) ranges from 1.37 to 4, while the percentage of the slab size a to the effective depth d and (a/d) ranges between 10.5 and 45.

Large-scale specimens were tested by Annerel and Taerwe [58], which represent 0.4 of a full-scale slab (6×6 m) according to Eurocode 2, while smaller slab specimens were tested by the other reviewed studies [54,58,59,61]. Dimensions are listed in Table A-1 for the collected experimental specimens.

Regarding slab reinforcement, it is worth recalling that the code provisions related to the effect of flexural reinforcement on punching shear strength are divided into two groups. This effect was included by many European standards, e.g., Eurocode 2, German DIN 1045, and the Model Code 2010. On the other hand, this effect was not considered in many other codes, e.g., the American ACI 318, the Australian AS3600, the Canadian CSA A23.1, the Indian IS 456, the Russian SNiP 2.03.01, and the Turkish TS500.

The effect of flexural reinforcement on punching behavior under high temperatures is investigated by almost all the researchers listed in Table A-1, except reference [58]. In all the slabs, the flexural reinforcement was orthogonally distributed and equally spaced; except the specimens tested by [10], where the reinforcement was concentrated on both sides of the column strips of the tension zone. For all the collected data, the reinforcement ratios ranged between 0.5% and 1.54%, and were applied in two layers (tension and compression reinforcement) except in [54]. To tie the slab and the column stub, Smith et al. [54] added two additional reinforcing bars to the compression face, as recommended by Eurocode 2 [53]. Among the 47 available tested specimens presented in this paper, only six specimens included shear reinforcement in varying quantities and configurations.

2.4.3 Fire exposure scenario

Three different high-temperature exposure scenarios were used in the six studies listed in Table A-1. The ISO 834 [63] standard temperature-time curve was considered by two experimental studies [10-58], while the ASTM E119 [64] curve was used in another study [60]. In the remaining three studies, the slab specimens were exposed to non-standardized constant temperatures, as listed in Table A-1 [54,59,61]. The exposure duration differed among the tested slabs, according to the used standard fire test or the heating method, as listed in Table A-2.

The exposure duration in the ISO 834 [63] provisions is limited to two hours, then the residual strength is determined for those specimens that did not fail during the heating. On the other hand, according to ASTM E119 [64], the fire-endurance test continues for eight hours or until failure occurs. In the non-standardized fire tests, each specimen was heated up to a target temperature to determine the residual strength for a limited exposure to that temperature. Different target temperatures were adopted for the different specimens, as listed in Table A-1. Table A-2 lists the exposure durations and the residual strengths of the specimens listed in Table A-1.

It should be noted that the cooling branches of the standard temperature-time curve is not specified in either ASTM E119 or ISO 834. Therefore, the conducted tests met only the heating branch of the curve. However, Salem et al. [61] considered the cooling effect as one of the study's main parameters, in addition to the exposure duration and the concrete cover.

To represent the service load in real buildings, some specimens were loaded prior to exposure to furnace temperatures. This load was 70% of the punching strength of the slab-column junction, according to Eurocode 2 [10,54,58], and was 54 % of the ultimate specimen resistance of the corresponding specimens in ambient conditions in another study [60]. In most cases, the load was maintained during the heating duration. For four out of 14 specimens tested by Kordina [10], the applied load was increased by 20%, 25%, and 40% within the first 30 minutes, while for three out of 14; the load was applied within the first 15 minutes. Table A-2 shows the details of the applied loads, as well as the resulting punching shear strength, the reduction in the slab element strength due to the temperature effect, and the deflection at mid-span for the experimental tests.

The exposed face of the slab element also differed among the reviewed studies (see Figure 2.17). The specimens of references [10,54,58-60] were exposed to high temperatures on their compression surfaces. On the other hand, the fire was subjected to the tension surface of the remaining four specimens of reference [60], and all the specimens that were tested by reference [61]. The long-term temperature distributions (250 days and 450 days) were compared with the specimens stored for only 88 days. The specimens that were stored for 250 days and 450 days were tested by Liao et al. [60] and Smith et al. [54], respectively. Kordina [10] tested the specimen that was stored for 88 days. The comparison showed that the temperature flow was smoother through the slab layers of the longer-stored specimens.

Figure 2.18 shows a comparison of the temperature history of selected heating times of 35, 65, and 85 minutes (for the missing surface-temperature data, the close thermocouple temperatures were extrapolated to the furnace temperature). It is clear in the figure that the temperature flows smoothly across the slab depth, and the curves are almost parallel for the specimens tested by references [54,60]. This means that the concrete is almost homogeneous and the free water had already evaporated.

However, this case is also valid for the specimen tested by Kordina [10], yet along only half of the slab depth (100–200 mm shown in Figure 2.18) from the exposed surface. For depths of 0–100 mm in Figure 2.18, the curves are distorted. This transferred heat distortion is due to the effect of the energy required to evaporate the free and compound water. This process takes place between 100 and 200 °C [31]. After consuming the water via either evaporation or a chemical reaction, the temperature distribution tends to be more stable along the temperature plateau.

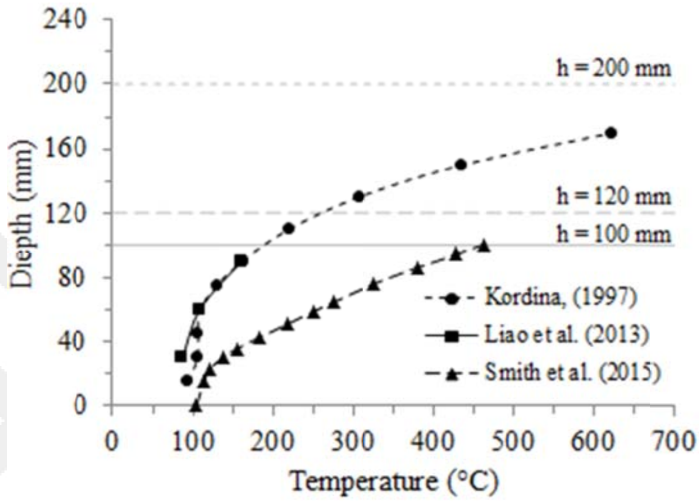

Figure 2.18 Temperature profiles after 85 minutes of exposure to fire for different slab thicknesses

2.5 Summary

Although the flat plate-column connection is a critical region that may cause the collapse of a reinforced-concrete structure under fire conditions, only few experimental studies have investigated the behavior of this region when exposed to high temperatures. From the little available data, it was concluded that:

- High temperatures had two main effects on the exposed structures of concentric flat plate-column joints. The first was due to the direct effect of high temperatures on the material properties; namely, the mechanical and thermal properties decayed dramatically after exposure to fire temperatures. This property degradation might reach 100% at 1000 °C. The second effect was indirect and arose from the unbalanced heating due to the different lengths of the adjacent spans. This effect could add a 50% higher axial load than in ambient conditions.

- The most effective parameters for punching shear behavior under high-temperature exposure were the exposure temperature and time, the fire scenario, support conditions, exposure surface, nominal strength of concrete, amount of reinforcement, and the preloading and stress history.
- The residual strength of specimens with high concrete strength and a high reinforcement ratio that were exposed to fire on their compression surface was more deteriorated by fire than those with a low compressive strength and low reinforcement ratio.
- The effect of shear reinforcement on the residual strength of a slab-column assembly after high temperature exposure was minimal.
- Another conclusion drawn from the reviewed literature was that sudden cooling after exposure to high temperatures led to more strength deterioration than gradual cooling.

CHAPTER 3

ANALYSIS, DESIGN METHODOLOGY AND EXPERIMENTAL WORK

3.1 General

This chapter includes the analysis and design of a prototype of a concrete structural element, which consists of flat plates jointed by slender columns. As a first step, the virtual dimensions of the concrete structure were chosen, the relative size were selected within the relative dimensions found in literature [10,58,60,61]. It was found that the aforementioned references employed the relative size so that, c/d is ranging between 1.39 to 3.87, b/d is ranging between 10.5 to 45, and c/b is ranging between 0.085 to 0.15.

In the second step, the 3D structure was numerically analyzed under static loading. For this purpose, the AUTODESK® ROBOT STRUCTURAL ANALYSIS PROFESSIONAL Program was harnessed. In the third step, the story that includes the slab under consideration was designed. The steel areas required to sustain the applied load were found using the equivalent moments that proposed by Wood and Armer [65].

Finally, the size and the reinforcement ratio of the model were chosen within the lines of contra flexure. Then the selected models were constructed in the structure laboratory of the civil engineering department of Gaziantep University. Many limitations were considered in selecting the size of the slab model used in the experimental work based on well know codes of practice.

3.2 Justification

The experimental program was employed for a slab supported by a column and exposed to fire from two sides. Because there are wide differences in the data obtained from the literature, many different code's provisions and mechanical models were introduced, which make it difficult to tackle. For example, the ACI code provisions require that the design of structural members should be based on an endorsement of eight hours when exposed to standard fire, whereas Eurocode depends the residual strength after two hours of exposing to standard fire. In spite of the two widely used standard fire curves are almost compatible for the first two hours, however, no clear relation between these two curves and a real fire. This is may be due to the differences in the fire conditions. These differences are due to the wide material types that can be the source of the accidental fire.

The extensively testing required by the test and the differentiation in compartments, the expected fire direction, and the expected cooling time and method are other possible variables that make the problem more complex to understand and the obtained data are more scattered. Therefore, the behavior of the slab-column joint is among the wide area of researches that are still in need for more investigations.

In spite of there are lot of available data on punching shear behavior in RC slab, no appropriate attention had been applied to the slabs under fire conditions. Moreover, there are no provisions in the practical design codes related to both punching shear problem under fire conditions and the effect of Steel Fiber (SF) on punching strength at both ambient [45] and high temperature conditions. The concrete strength is also limited in some codes. For example, old versions of ACI (before 2002) considered that the minimum shear reinforcement is not related to concrete strength. In latest shear versions of ACI318 [19], the maximum applicable concrete compressive strength is 68.9 MPa. CSA [66] uses less value (64 MPa). When the limit of concrete strength exceeds these values, minimum shear reinforcement should be applied.

3.3 Design of the Specimens

Most experimental works on the flat plate-column connection had been holding on isolated slab-column joint [21], which does not represent the real structural behavior, where the associated effects of the fire on the structures are ignored, such as the additional load that is developed during the fire action. This load develops from local redistribution. The redistributed loads are significantly differing based on the direction of fire action, especially on the axial loads that are transferred to the column. For example, exposing the temperature from the bottom face of the slab (in real structure) introduces a sagging curvature at the mid-span, with dilation at the support zone [34] as shown in Figure 3.1a. However, when the top face of the slab (in real structure) is exposed to high temperatures, the induced hogging will act positively on the column with an opposite direction of the dilation as shown in Figure 3.1b. This is not easy as it is shown, for instance, the real fire is not uniformly distributed (as it is commonly assumed). In addition, the flammable material gradually loss it's mass during the fire. Mass losing rate has different effects based on its influence direction. The case in Figure 3.1a is the worse, because the service load that acts on the damaged slab will remain as its initial value. However, for the case in Figure 3.1b, the mass of the burning material loss its original values during the fire so that the hogging of the slab causes less damage than the former case.

Almost, all the few tests found in the literature had been devoted to the two aforementioned cases (see Figure 3.1). It is worth to mention here that even there were few scattered data. They all were applied to plain concrete slabs. So that the structural studies on the behavior of punching shear of slabs made from high strength concrete, reinforced by fibers, and exposed to high temperature conditions are still in need.

Recently, researchers have trended to use high strength concrete in order to increase the slab strength. However, the problem was aggravated because of the spalling [67] and brittleness problems that associated with the high strength concrete. Among the best and cheapest processes to improve the flat plate-column joints is by using a FRC. In spite of discontinuity and randomly distribution of fibers that decreases its efficiency in sustaining the tensile stress compared to conventional reinforcing bars [68]. The fibers show good results in controlling the propagation of the local cracks that leads to increasing the ductility and energy absorption [45,69,70]. The contribution of fibers results from increasing the bond between the reinforcement bars and the surrounding concrete matrix and bridging the two sides of crack, which transfer the stresses even in wide crack opening [68,71].

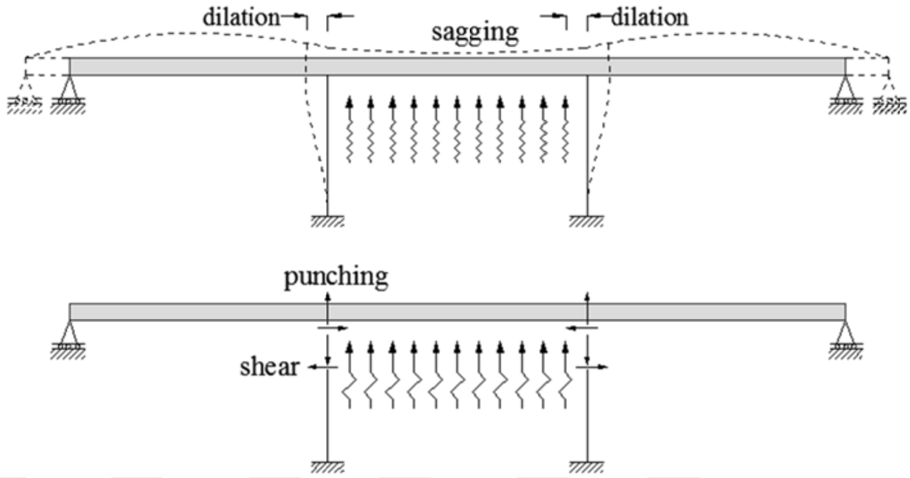

(a)

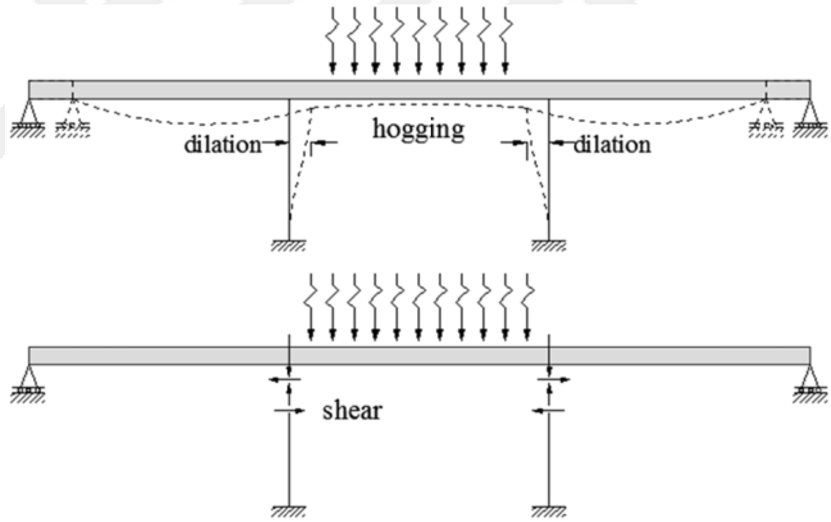

(b)

Figure 3.1 Flat plate-column structural system exposed to fire from (a) the tension face, reproduced from [34] (b) the compression face

3.3.1 Analysis and design of the prototype structure

The typical multistory structure considered in this section is four by four bays of 6 m spans with story height of 3.5 m as shown in Figure 3.2. The flat plates of 240 mm thickness are connected monolithically with square columns of 220×220 mm, there are no column capital or drop panels, so that the span-depth ratio is 25. The relatively small size of columns increases the punching shear stresses at the columns' vicinity that is satisfying the research purposes. The virtual function of the suggested floors is for computer offices use, which applies a sever temperature energy in case of accidental fire, except the ground story that is used as a car parking. The slabs were designed to fail due to weakness in punching shear resistance, so that the flexural capacity are designed to sustain the applied load, i.e the flexural capacity is greater than the one-way and two-way shear capacities of the concrete section ($P_{flex} > V_c$).

A concrete compressive strength(f_c') of 60 MPa was assumed for all members, with modulus of elasticity (E_c) of 38.13 MPa, unit weight (w) of 24 kN/m^3, and thermal expansion coefficient (α) of 0.00001 1/°C. The reinforcement yield strength was assumed to be 400 MPa for the reinforcement used in the current experimental work.

The floors were loaded by gravity uniformly distrusted live load of 4.79 kPa, which is the minimum load calculated for computers office zones that is recommended by ASCE 07-10 [72], and 1 kPa for the roof. In addition to the self-weight, superimposed dead load of 1 kPa was assumed for all slabs. For flexural design under ultimate limit state, the loads were combined according to ACI318 [19] as shown in Equation 3.1a. However, the serviceability limit state was used for deflection calculation as shown in Equation 3.1b, it is worthy to mention here that the fire effect was not considered in this stage.

$$U = 1.2 \text{ D.L} + 1.6 \text{ L.L} \tag{3.1a}$$

$$U = 1.0 \text{ D.L} + 1.0 \text{ L.L} \tag{3.1b}$$

The whole structure analysis aimed to determine the lines of contra-flexure of the portion under consideration. In current work, this portion is considered as that supported by column 3-C (see Figure 3.2 and 3.3). The reason of the selection of column 3-C is to represent the concentric slab-column joint that is not affected by the spans at the edge. At this stage, a static linear elastic analysis of plate with small deflection was applied in order to employ the bending elements of Mindlin plate, which ignores the material nonlinearity. As a result, the assumption of slab small deflection (compared to its thickness) is satisfying the design codes' limitation.

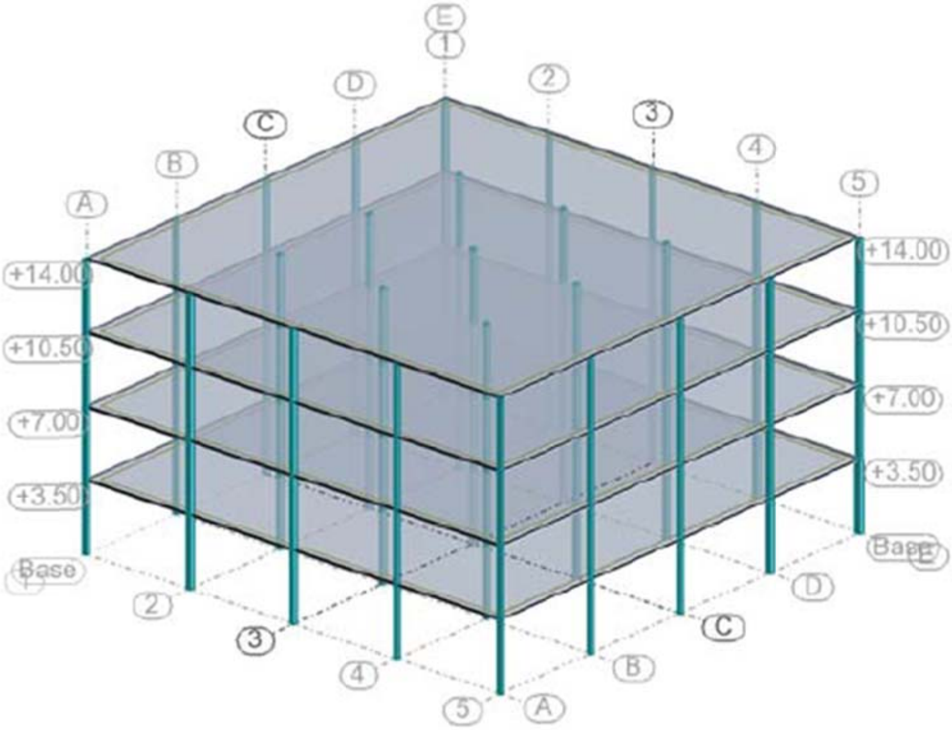

(a)

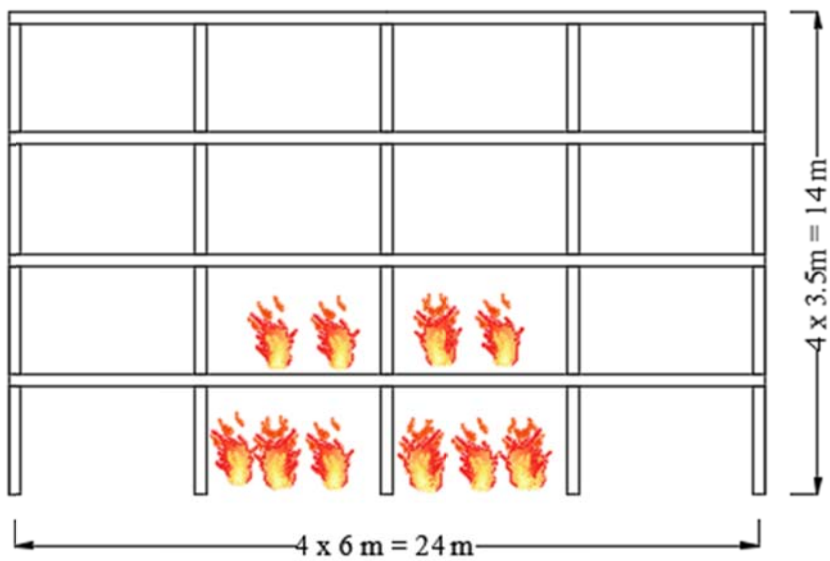

(b)

Figure 3.2 Concrete structure under consideration (a) whole structures (b) section in axis C

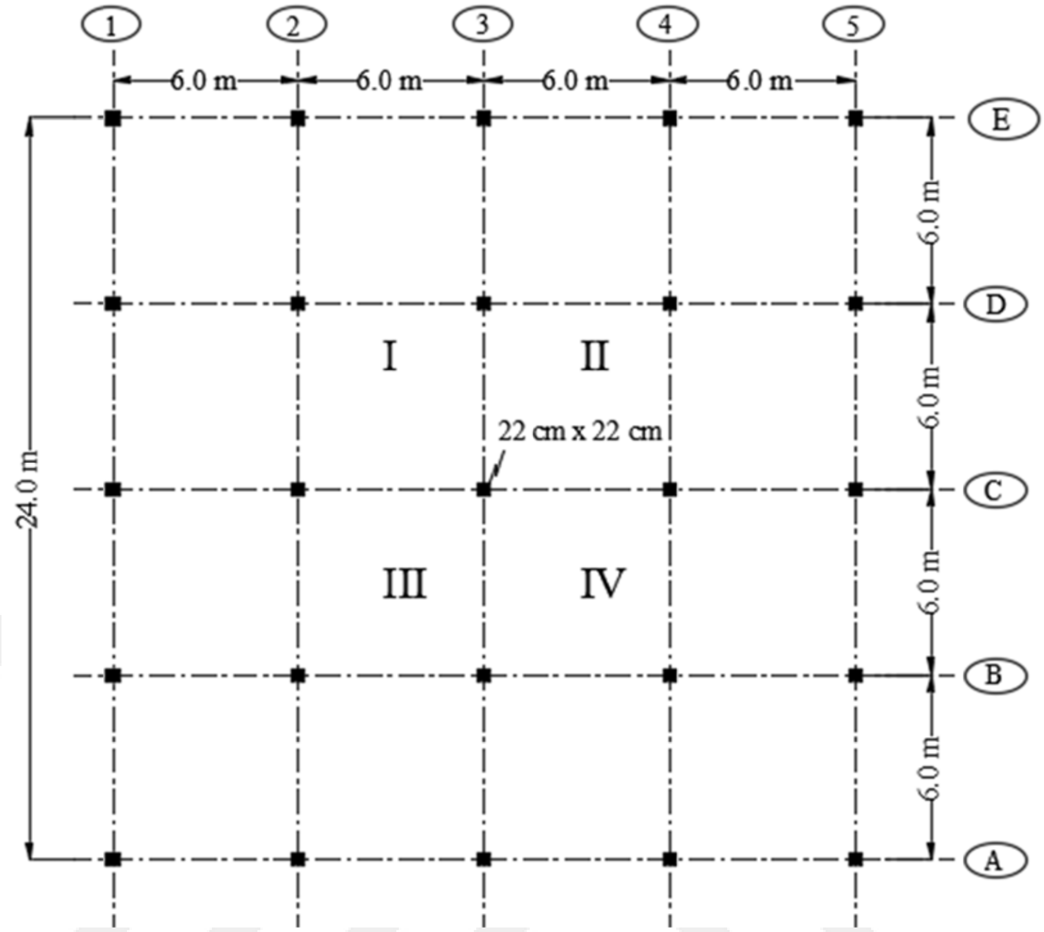

Figure 3.3 Plan of the 1st slab

The slabs were modeled as shell finite elements of a quadratics meshing with 4-node quadratic elements. The interpolation function of the isoperimetric is based on Ahmad et al. [73] methods. In other words, three translations and two rotations at each node were used to interpolate the displacement inside the element. The maximum size of elements is 300 mm. The automatic meshing method was selected with recommended forcing ratio, with allowance to generate nodes at bar intersections. Automatic solver was chosen to solve the equations in order to let the program to choose the appropriate solver. In this case, the program chooses the frontal method based on specific Gauss elimination, which assembles the matrix as an element by element ($K=\sum_{e=1}^{N} K_e$).

The deformations due to the applied load are depicted in Figure 3.4. It shows that under serviceability loading system (see Equation 3.1b), the displacement at mid-span between column C-3 and adjacent columns don't exceed 1 mm, in general, the displacement of the centers of the panels I, II, III, and IV did not exceed 2 mm.

Knowing that the maximum displacements were 6mm that are recorded on the corners' panels.

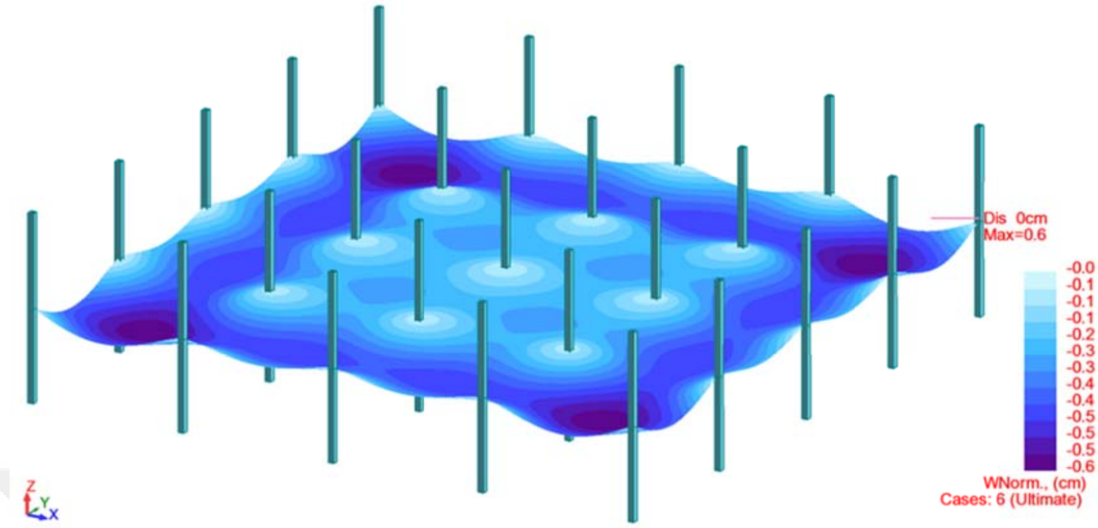

Figure 3.4 Displacements of the first slab under non-factored load

The structure was analyzed under factored ultimate load according to Equation 3.1a. Figure 3.5 shows the moment diagram of the panels under consideration (I, II, III, and IV). Because of symmetry, the maximum moments at the center point of the column C-3 was $M_{XX} = M_{YY} = 217$ kN.m, and the moments were equal in the reverse axes, i.e. M_{XX} in axis C = M_{YY} in axis 3 and vice versa (see Figure 3.5a and b). The torsional moments (M_{XY}) were also equal at the top of column C-3 (see Figure 3.5c).

Flat plat-column connection is often performed using a single test connection that represents the hogging moment zone, which is separated from the real slab behavior by lines of elastic moment contra-flexure. The distance from this line to the column's center can be approximated by 0.22L [4,74].

Based on the premise, the analysis indicates that the line of elastic moment contra-flexure of the column C-3 are located at distance equals to 18 % times the bay's length (L) as shown in Figure 3.5a. It is worthy to mention here, that the results of the finite element analysis often overestimates the negative bending moments at the top of the slab and underestimates the positive bending moments at the mid-span of the slab [75], which would slightly change the contra-flexure.

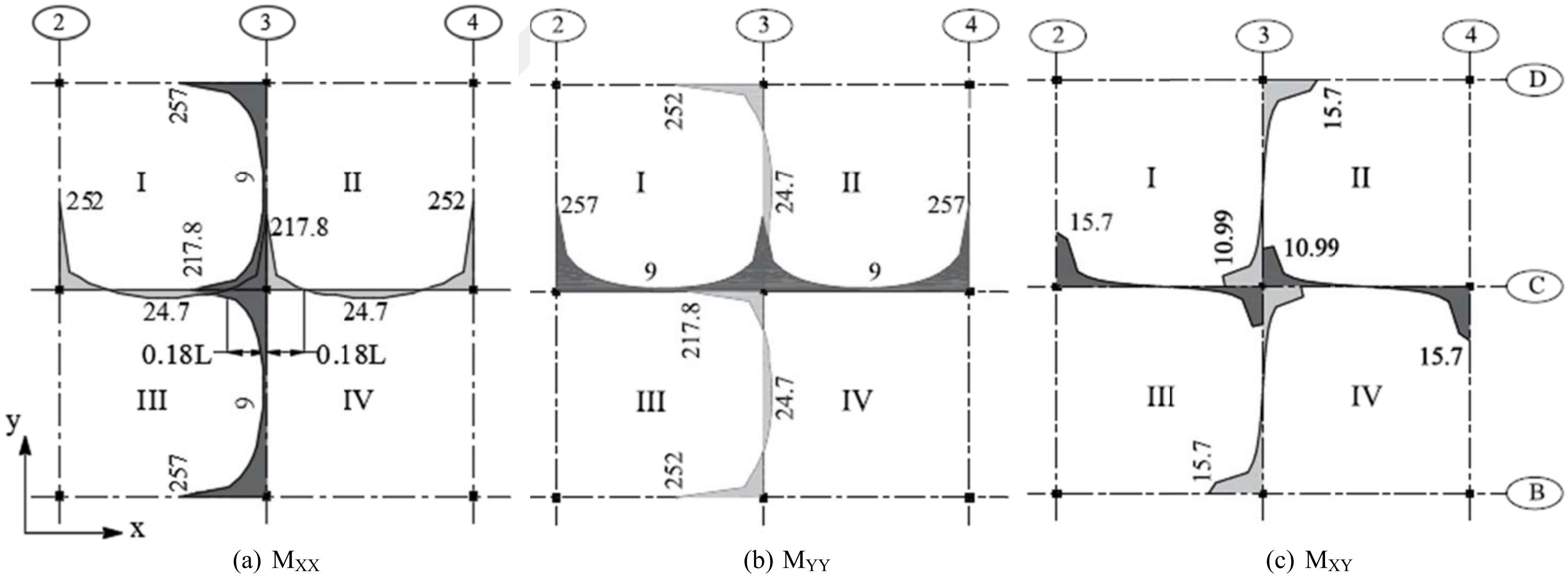

Figure 3.5 Distribution of moment of the slab at level + 3.5 in kN.m under factored live and dead load (a) moment along y-axis (M_{XX}) (b) moment along x-axis (M_{YY}) (c) torsional moment M_{XY}

3.3.2 Reinforcement design of the prototype slab at level +3.5

There are no special design provisions for torsion moments (M_{XY}) in most of codes, however, the moment equilibrium have to consider the torsion effect (see Equation 3.2), which means that the torsion has to be considered in designing the plate.

$$\frac{\partial^2 m_x}{\partial x^2} + 2\frac{\partial^2 m_{xy}}{\partial x \partial y} + \frac{\partial^2 m_y}{\partial y^2} = -q \tag{3. 2}$$

For reinforcement design purposes, the slab was loaded by factored load according to Equation 3.1. Equivalent moments were used as design moments, which were produced from the moments of the principal directions ($M_x$and M_y) while taking the twisting moment (M_{xy}) into account (see Equation 3.2). For this purposes, Wood and Armer method [65] that is adopted by ENV 1992-1-1 Eurocode 2 was used herein. Therefore, for the illustrated direction in Figure 3.5, a design equivalent moments $\widehat{M}_x$ and $\widehat{M}_y$ were used to calculate the reinforcement ratio required to resist the ultimate design moment.

Based on ENV 1992-1-1 Eurocode 2, the equivalent moment $\widehat{M}_y = 0$ because M_y is greater than M_{xy}. Therefore, the upper equivalent moment that causes tension at the top of the slab along the C-axis is $\widehat{M}_x = -M_x + M_{xy}^2 / |M_y|$ and $\widehat{M}_y = 0$, while the equivalent moments along the 3-axis is $\widehat{M}_y = -M_y + M_{xy}^2 / |M_x|$ and $\widehat{M}_x = 0$.

The design process showed that the reinforcement ratio that is required at the tension face (top face) of the first slab above the column C-3 is ρ =1.1%.

3.3.3 Performance of slab (level +3.5) under fire action

The fire was assumed to happen in the panels I, II, III, and IV of the ground and the first floors as shown in Figure 3.3a. Moreover, the ground and first floors were assumed as one compartment. This scenario was investigated by Bamonte et al., [9] where the temperature produced from six cars firing was about 286 ºC. For the first floor fire, the case is different, where the fire is less than at the bottom because the hot gases are directed to the next slab. Moreover, the flooring system has lower conductivity than the plastering, for these reasons the temperature was assumed for the top surface of the first slab as 102 ºC. Figure 3.6 shows the deflections of the first slab, the deflection at the mid-span between column C-3 and adjacent columns (δ_a) is 9 mm and the maximum displacement was recorded at mid-spans of panels (δ_p) that equals to 12 mm.

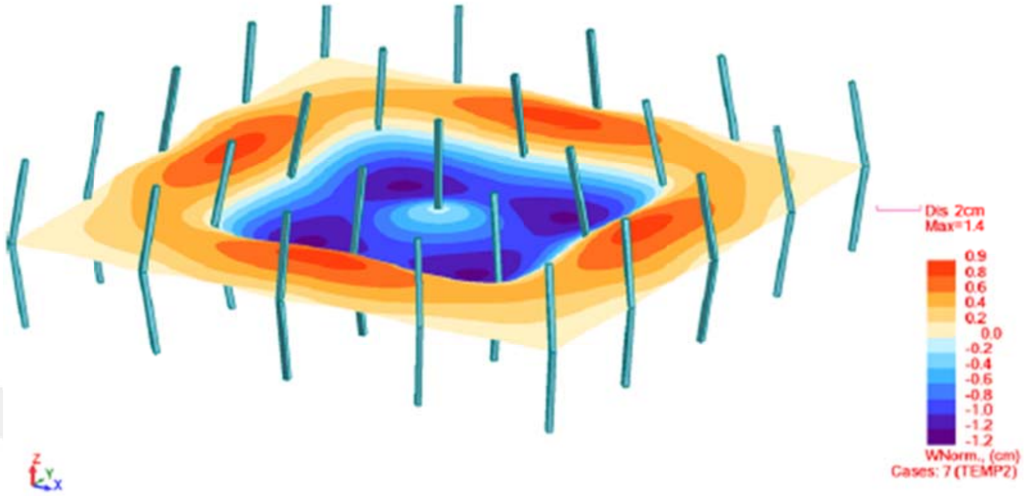

Figure 3.6 Displacement of first floor slab due to fire effect on panels I, II, III, and IV, the temperatures at the top and bottom are 102 and 286 ºC, respectively

3.3.4 Analysis and design of control slab models

For comparison purposes, a model of normal RC flat plate was designed. The enhancement of the fibers in concrete can be found through the construction of a fibrous concrete plate with the same geometry and conventional reinforcement ratio. Therefore, the following subsections concentrate on designing the isolated normal RC flat plate.

In order to investigate the concentric slab-column joint without the complexity expected from the size effect, the boundaries of the models in current work were selected within the lines of contra-flexure of the prototype (0.18L). In other words, the region of the hogging moments was modeled, which have the highest moment at the center of column and zero value of distance a size of 1100 mm from the center. It's worthy to mention here that the analyzing a full panel show a greater strength than the model that selected within the contra-flexure. This is because of the membrane action that acts after the cracking of the slab. Therefore, the test results of the current work conservatively represent the prototype slab.

Two main themes are covered in the current research. Firstly, the ductility of fibrous concrete slabs under ambient conditions, and secondly, the effect of high temperatures on SFRC are investigated.

3.3.5 Slab's geometry

All constructed and tested slabs were of 500×500 mm. It is shown that the thickness has great influencing on the slab behavior, whereas the diameter has "exert a minor influence on performance" [76]. For this reason, the thicknesses were taken fixed as 60 mm. The slabs were loaded with a cubic column stub of 55×55×55 mm (see Figure 3.7). Bases on the aforementioned analysis results of the previous structural analysis, the constructed and tested models represent 0.18 the slab full-scale.

More considerations were taken into account in selecting the dimensions based on the relative size. The relative dimensions in the current work are of c/d = 1.39, b/d = 12.6, and c/b = 0.11. These relative sizes were chosen within the dimensions found in literature [10,54,58-61]. The relative sizes in these references are as follows, c/d is ranging between 1.39 to 3.87, b/d is ranging between 10.5 to 45, and c/b is ranging between 0.085 to 0.15, where b is the width of the slab, c is the column size, and d is the effective depth.

3.4 Research Parameters

The current experimental work is divided in to two separate approaches. The first approach aims to investigate the effect of different fiber types and dosages on the behavior of FRC flat plate-column stub joint. Different dosages, types, and locations of fibers were used. To achieve this purpose, fifteen FRC were used and compared with normal RC flat plate. The second approach aims to investigate the residual strength of SFRC concrete flat plates exposed to high temperatures. For this purpose, sixteen slabs of high strength SFRC slabs were exposed to high temperatures. The high temperatures were applied to all faces of slabs in non-standardized temperature levels. The investigated slabs were reinforced by three SF dosages (0.75%, 1%, and 1.5%). These slabs were exposed to four values of temperature levels of 150, 300, 450, and 550 °C. In order to improve the growth of concrete strength during the fire action, the surface area of the concrete matrix was increased by increasing the fine aggregate compared to the coarse aggregate and high fineness additive materials such as silica fume were used to enhance the behavior of the cementitious material.

Following sections illustrate the details of the parameters and specimens coding.

3.4.1 Fibrous Concrete Specimens at Ambient Conditions

Six groups were used in the investigation the effect of different types and configurations of fibrous reinforced slabs. Table 3.1 illustrates the details of the research parameters and the details of the slab specimens used in the current work.

Table 3.1 Details and the mechanical properties of slabs at ambient condition

Groups	**Specimen code**	**Fiber type**	**fiber** (%)	**h (mm)**	**ρ** (%)	**f'_c** **Plain**	**fiber**	**f_{ct}** (MPa)
I	P50	Plain concrete	0	50	1.2	43.2	-	3.85
	P60-11		0	60	1.2	43.2	-	43.2
	P80		0	80	1.2	43.2	-	3.85
	P60-10B		0	60	1.1	40.83	-	5.28
	P60-10S		0	60	1.1	55.0	-	5.63
	P60-8		0	60	0.9	32.12	-	6.14
II	SF0.5	SF	0.5	60	1.1	62.04	68.92	4.40
	SF1		1			67.79	78.56	4.48
	SF1.5		1.5			59.55	80.88	5.88
III	NM0.5R	NM	0.5	60	1.1	-	37.94	5.68
	NM1R		1			-	37.35	4.93
	NM2R		2			-	41.50	5.43
IV	PV6	PVA	2	60	1.2	-	43.2	6.6
	PV12	PVA	2		1.2	-	39.18	7.80
	PP12	PP	2		1.2	-	31.51	6.61
V	NM0.5	NM	0.5	60	0	-	37.94	5.68
	NM1		1			-	37.35	4.93
	NM2		2			-	36.06	7.32
VI	NM0.5P	NM	0.5	60	1.1	51.98	37.29	4.66
	NM1P		1			51.98	43.46	5.43
	NM2P		2			63.42	41.50	5.67

SF; Steel fiber, **NM**; Nylon monofilament, **PVA**; polyvinyl Alcohol, **PP**; polypropylene

3.4.1.1 Group I (Effect of reinforcement ratio and thickness on normal concrete RC slabs)

This group consists of six reinforced normal concrete slabs used to investigate the effect of the reinforcement ratio and slab thickness on flexural and punching shear behaviors of flat plat-column stub connection. Three slabs (P50, P60-11, and P80) of different thickness (50, 60, and 80 mm), and three slabs of the 60 mm thickness (P60-8, P60-10B, and P60-11) with different reinforcement ratios (0.9, 1.1, and 1.2%) were constructed. The numbers directly following the letter (50, 60, and 80) that used in coding the specimens in this group refer to the thickness of the slab, whereas the number after the dash refers to the numbers of reinforcement bars used in one direction. Two slabs (P60-10B and P60-10S) of 60 mm thickness and 1.1% reinforcement ratio were used to investigate the effect of bar ends' configuration, where the ends of the bars in slab P60-10B were hooked with 90-deg bends as shown in Section 3.6, whereas the bars in slab P60-10S did not consider the development length.

3.4.1.2 Group II (Effect of steel fiber dosages on FRC slabs)

In this group, the effect of SF volume fraction V_f on the ductility and the ultimate resistance of slab-column stub assembly was investigated. Three specimens (SF0.5, SF1, and SF1.5) of 0.5, 1, and 1.5% SF fiber contents were cast and tested in this group.

3.4.1.3 Group III (Effect of nylon monofilament dosages on FRC slabs)

This group has the same target of the Group II with different type of fiber. The specimens are NM0.5R, NM1R, and NM2R that include of 0.5, 1, and 2% of monofilament fiber of virgin nylon.

3.4.1.4 Group IV (Effect of fiber types)

In addition to specimen NM2R mentioned above, other types of fibers were used in specimens PVA6, PVA12, and PP12, where two different ECC of polyvinyl - alcohol (PVA) were used. The first ECC contains 6 mm length PVA fiber, whereas the second contains 12 mm length PVA fiber. Moreover, ECC of 12 mm polypropylene fiber length was also constructed.

3.4.1.5 Group V (Effect of fiber dosages on unreinforced fibrous concrete slabs)

In order to find the contribution of fibers isolated from the effect of conventional reinforcement bars, three unreinforced ECC slabs made from nylon monofilament coded as NM0.5, NM1, and NM2 were fabricated. The differences in the ultimate resistance and ductility factor between the unreinforced and reinforced slabs are attributed to the fibers, for the mentioned reason, same fiber dosages of the previous groups were used.

3.4.1.6 Group VI (Effect of fiber congestion in D-zone)

For optimization purposes, two types of concrete mixtures were used in specimens NM0.5P, NM1P, and NM2P. The mixture of engineered cementitious composites (ECC) that contains nylon monofilament fiber was congested within a circular critical area (D-zone) in the slab zone above the column, while the rest of the slab was constructed using normal concrete. The circular critical area was chosen so that the outer periphery distances 2d from the face of column stub. This critical distance was chosen according to Eurocode 2 [53].

3.4.2 Fibrous concrete specimens under high temperature condition

Five groups are used for comparison purposes, the groups are coded based on the maximum exposure temperature. Four slabs are used for each group named as the same group letter with the subscript refers to the SF volume fraction.

Four levels of temperature were used in this test (150 °C, 300 °C, 450 °C, 550 °C), each group consists of four slabs ({A0, A0.75, A1, and A1.25}, {B0, B0.75, B1, and B1.25},{C0, C0.75, C1, and C1.25}, and{D0, D0.75, D1, and D1.25}) with different SF dosages (see Table 3.2). In addition, all mentioned groups are compared to a control group {P0. P0.75, P1, and P1.25} that is constructed and tested under ambient conditions (20 °C).

Table 3.2 Details and mechanical properties of slabs exposed to high temperatures

Spec. No.	Max.Temp. (°C)	Steel fiber V_f (%)	Age at day of test (Day)	f'_c (MPa)	f_{ct} (MPa)	Moisture content (%)	E_c (GPa)
P0	Ambient condition	0	34	53	7.1	_	38.13
P0.75		0.75	37	51	6.8	_	37.27
P1		1	34	60	11.5	_	37.32
P1.25		1.25	37	59	7.0	_	37.41
A0	150	0	46	63	6.2	0.777	33.21
A0.75		0.75	45	60	9.2	1.353	31.22
A1		1	48	71	8.6	0.915	34.57
A1.25		1.25	44	65	8.0	1.472	38.37
B0	300	0	46	51	5.3	1.476	23.82
B0.75		0.75	43	55	6.6	1.688	20.93
B1		1	47	64	8.8	0.745	21.50
B1.25		1.25	44	61	8.3	1.037	23.78
C0	450	0	32	34	4.0	0.929	10.73
C0.75		0.75	33	46	6.9	1.039	9.64
C1		1	32	47	6.5	1.104	9.98
C1.25		1.25	33	49	8.0	1.008	10.53
D0	550	0	48	24	2.9	0.738	5.39
D0.75		0.75	45	39	5.0	0.743	5.86
D1		1	47	32	5.5	0.949	4.32
D1.25		1.25	43	30	4.5	1.246	4.07

3.5 Boundary Conditions

It is noted that using continuous supports along the four sides of the slab are increasing the shear resistance [15]. Therefore, a steel support was constructed so that the slab is simply supported on eight steel half-balls that are located on eight pivots symmetrically arranged around its circumference as shown in Figure 3.7. The steel half-balls are uniformly distributed with a central angle equals π/4 and the radius r_q equals 200 mm. The curvature of the pivot half-balls were manufactured so as not to penetrate the concrete slab due to the singularity of the stress in the contact area. On the other hand, the ball's height is configured so that the specimen does not come into contact with any portion of the support. Moreover, the circulation of the balls is necessary to allow for free rotation of the slab in two directions without a significant resistance. Most resistances are due to the friction induced from radial forces in horizontal axes. Although this force has slightly effect on punching shear failure that can be neglected. However, for bending failure (such as the designed specimens of the current work) and toughness, the friction force is considerably effective. It is shown from the literature [77] that the 35% of the energy absorbed in panels that were fully supported was because of friction, while the remaining 65% was due to fiber action in the concrete panels. In the same manner, the maximum loads are reduced by 15 % when the friction is eliminated.

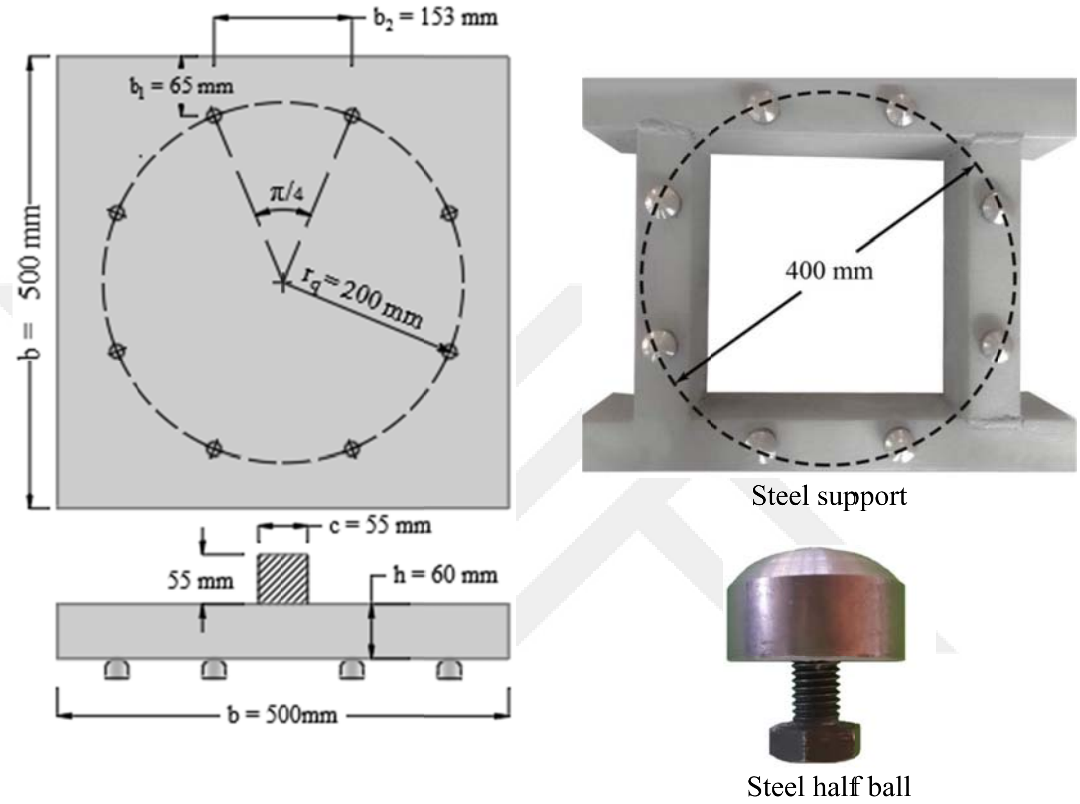

(a) **(b)**

Figure 3.7 (a) Radius of the load applied at the circumference (b) rigid support of eight half-balls

Important concept has to be concerned about, which is appearing in case of direct supporting. This concept is well known as "shear arm ratio a/d" (see Figure 3.8), where the distance from the column to the support has significant influence on the punching resistance. It is noted that a/d less than 1.5 showed the highest punching shear strength [78], while minimum strength can be obtained at a/d = 2.5 [79].

Another limitation is controlling the contra-flexural, which is the extension of the reinforcement to 3 times the slab effective depth from the column face [80].

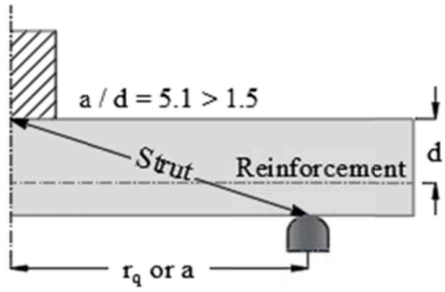

Figure 3.8 Effect of shear distance concept, reproduced from CEB-fib bull-12

3.6 Reinforcement Ratio

All slabs were reinforced on tension side only, the deformed rebars were tied orthogonally. Generally, one reinforcement ratio was used for all slabs in each group except Group 1 and Group 3, where three reinforced ratios (0.9%, 1.1%, and 1.2%) were considered in Group 1, and no reinforcement was considered in Group 3. The reinforcement ratio in all slabs of Group 4 and slabs that are exposed to high temperatures are 1.1%, while 1.2% in all slabs of Group 5. Eight ϕ 5.3 mm diameter reinforcement bars were used for slab with 0.9% reinforcement ratio, 10 ϕ 5.3 or equivalent numbers (7 ϕ 6.3) for slabs with 1.1% reinforcement ratio, whereas 11 ϕ 5.3 for 1.2% reinforcement ratio. All bars in all tested slab were equally spaced so that the center-to-center spacing between the bars is $S_x = S_y = 66$, 52, and 47 mm as shown in Figure 3.9 and Figure 3.10. There were no shear and compression reinforcements. The average reinforcement ultimate strength was found to be equal to 477 MPa and 706 MPa for bars of ϕ 5.3 and ϕ 6.3, respectively, with yield strengths of 400 MPa and 558 MPa, respectively. The bars used in the second group were hooked with 90-deg bends as shown in Figure 3.9. Moreover, additional one horizontal bar in each edge was fixed to the free hooks' ends. The concrete covers was 15 mm for all slabs, which leads to an average effective depth of d = 39.7 mm.

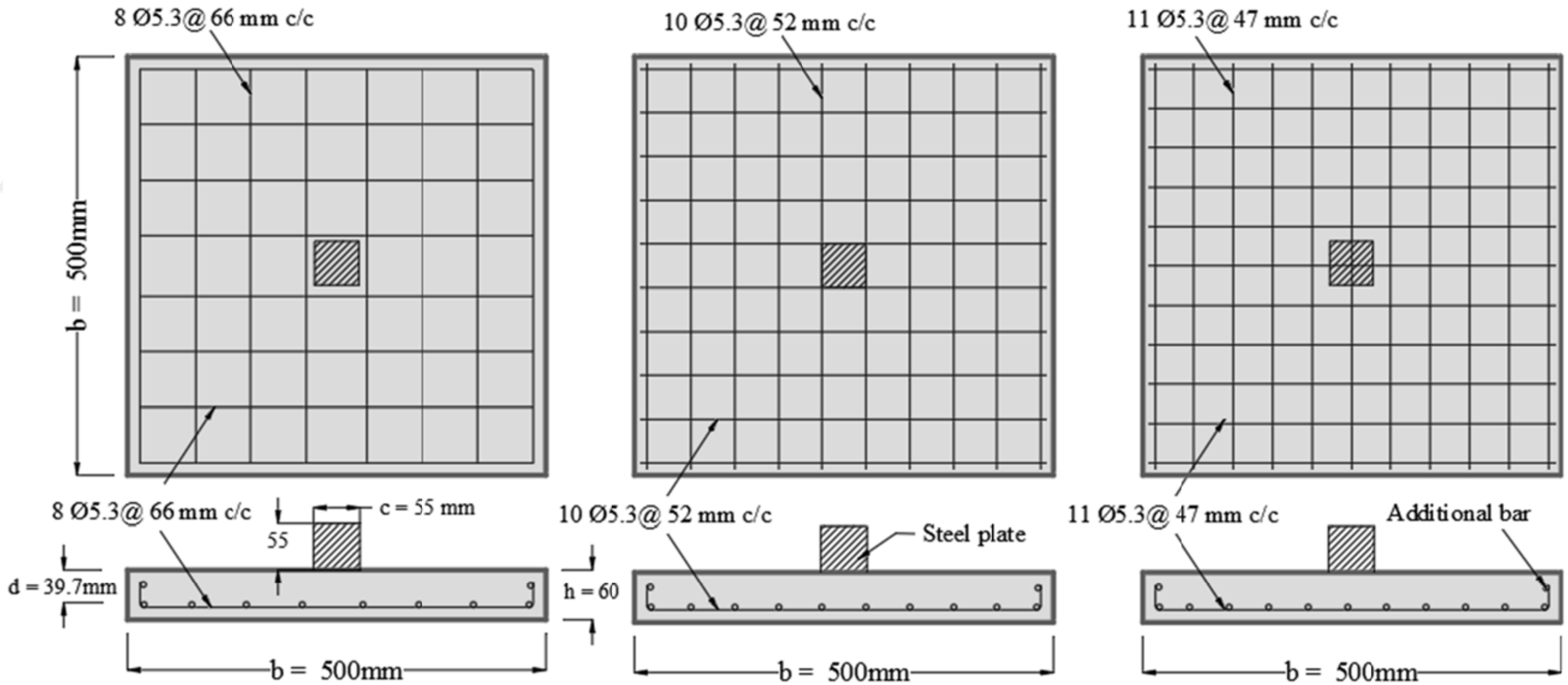

(a) Slab P8

(b) Slab P10B and all slabs in Group III and V

(c) Slab P11 and all slabs in Group IV

Figure 3.9 Typical geometry and reinforcement details for slabs of Group 1, 2, and 3

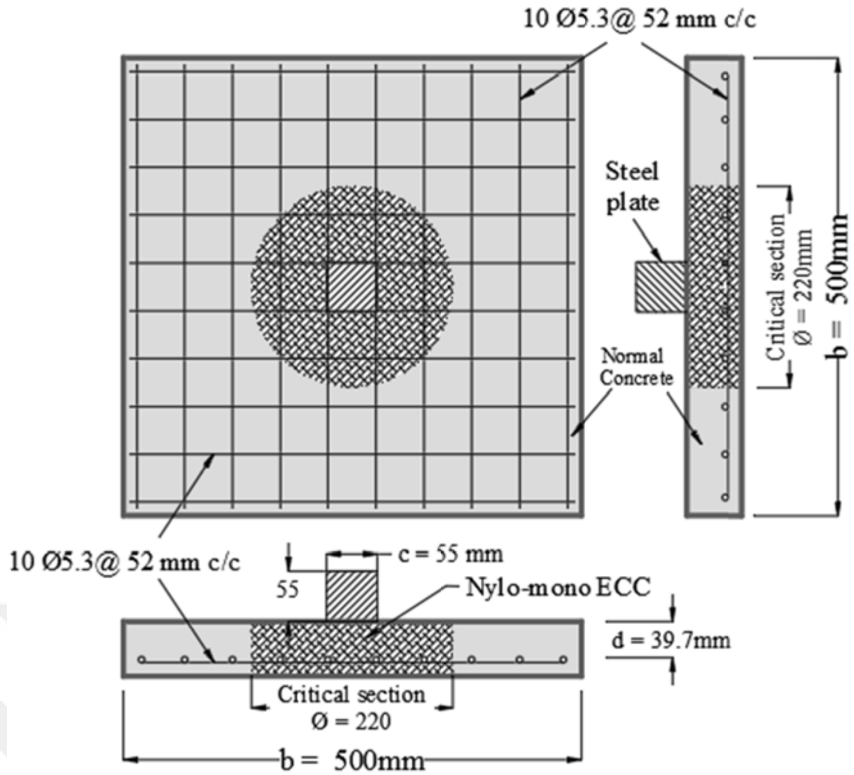

Figure 3.10 Typical slab geometry and reinforcement details for slabs of Groups II and VI

3.7 Strength Prediction of the Designed Specimens

Slabs are designed to sustain the bending moment induced from the imposed live and dead loads in addition to self-weight. Therefore, the punching shear resistance is checked in different ways. The specimens under ambient conditions that are reinforced by conventional deformed steel bars were designed to fail in punching shear ($P_{flex} > V_c$) in order to recognize the effect of the interaction of the fibers with reinforcement bars. For this purpose, a nominal shear strength for plain concrete was calculated based on the provisions of ACI318 [19], EN1992-1-1 [53], and TS500 [81]. Whereas, the SFRC was checked based on the proposed equations by Shaaban and Gesund [70], Harajli et al. [82], and De Hanai and Holanda [45]. The results were compared with the failure mode that is proposed by Gesund and Kaushik [12]. Finally, the flexural capacity of the slab was determined based on the yield line analysis that is proposed by Guandalini et al. [83].

The details of the mentioned codes provisions are introduced in Chapter 4, while the results of the calculations are shown in Table 3.3. The flexural capacity of the RC slab, punching shear capacity of SFRC, and failure mode (Q) are introduced in the following sub-sections.

Table 3.3 Designed slab parameters and predicted punching shear strength based on different codes of practice.

Specimen	d (mm)	f'_c (MPa)	f_y (MPa)	ρ (%)	V_c [1] (kN) ACI318	EC2	TS500 [2]
Designed slab	39.7	60	400	1.1	39	41	50

(1) Concrete punching shear capacity.
(2) Assumed concrete characteristic tensile strength f_{ctk} = 5 MPa

3.8 SFRC Punching Shear Strength According to Proposed Models

As mention before, there are no code provisions on the resistance of SFRC slabs to punching. However, many equations have been proposed [45,82,84] to predict the punching shear stress derived from the ACI318 provisions with the inclusion of the SF.

Shaaban and Gesund [70] proposed Equation 3.3 based on the relationship between concrete tensile and compressive strengths of the tested specimens for compressive strength ranging between 25 and 47 MPa. Moreover, their tested slabs were loaded uniformly through an air bag so that the load is well represented as follow.

$$\nu_c = \left(\frac{196.25 \times V_f}{w_c} + 0.567\right)\sqrt{f'_c} \qquad (3.3)$$

Harajli et al. [82] used small simply supported slabs 600×600 mm with two different thickness (55 and 75 mm). They predicted the increasing in the ultimate stress of SFRC slab related to its plain concrete punching shear stress based on the following equation,

$$\nu_{c,\,SF} = \nu_{c,\,ACI} + (0.096 \times V_f) \times \sqrt{f'_c} \qquad (3.4)$$

where $\nu_{c,\,ACI}$ is the shear stress optioned according to ACI318 [19].

De Hanai and Holanda [45] used the same Shaabans' approaches in their work, they proposed following equation,

$$\nu_c = (0.15 \times V_f + 0.51)\sqrt{f'_c} \tag{3.5}$$

Equations 3.3 to 3.5 were used to predict the punching shear stress of SFRC slabs in the current work. Figure 3.11 shows the predicted punching shear resistance of the designed slab models based on Equations 3.3 to 3.5. In spite that three models were employed with ACI318 provisions, Equation 3.4 is conservative by approximately 50% than the other two equations. This is because the used specimens were not similar in geometry, test conditions, and the boundary conditions (supports).

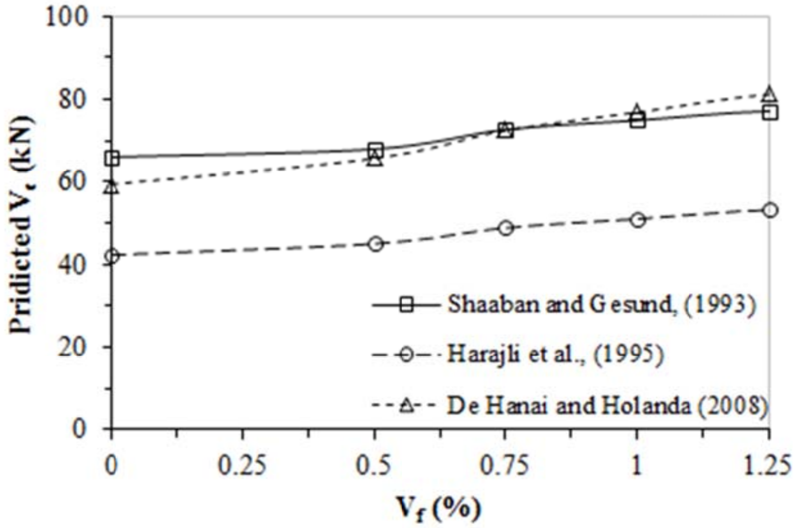

Figure 3.11 Prediction of designed SFRC slab according to different proposed models found in literature

3.9 Failure Mode Criterion

The designed sections were checked by another approach, which is the failure mode criterion that was proposed by [12], which was addressed in Chapter 2 (see Equation 2.1).

The designed slab had a Q of 2.66, therefore either failure is expected. Knowing that this criterion is conservative in shear, flexural may not be conservative [84].

3.10 Flexural Capacity (Yield Line)

Based on the kinematic theorem (upper bond solution), the capacity of the plastic moment can be determined using the virtual work concept, so that the external work is equated to the slab moment resistance that is constant when an inelastic rotation takes place. These rotations occur around the axis of yield lines. As mentioned in Chapter 2, there were many test configurations to represent the real applied load, where the boundary conditions affect the failure modes and subsequently influencing the section flexural capacity. In the current work, three yield line patterns were expected for the designed reinforced and unreinforced square slabs that are supported by eight points.

Because of the upper bond nature of this theory, it is shown that the calculated P_{flex} is higher than the real value. Pure flexural failure can take place if the membrane forces are absent, which can be reached if isolated slabs are tested. However, the internal membrane forces cannot be excluded because of the shear distance concept that is shown in Figure 3.8. Kuang and Morley [5] characterized the pure flexural failure when the $V_{u,\,test}$ is greater than P_{flex} by 15% (see Section 1.2).

3.10.1 Reinforced slabs

For reinforced slabs, there are two expected yield crack patterns. The first pattern is eight fans like cracks that are extended from the column edges and ring negative moment cracks located at the column vicinity as shown in Figure 3.12a. The flexural capacity (P_{flex}) are obtained from Equations 3.7 [83]. The second expected pattern is a single line extended from one column edge to the slab edge as shown in Figure 3.12b, where P_{flex} can be obtained from Equations 3.8 that is produced by Guidotti (2010) [26]. It is shown that P_{flex} produced from Equation 3.8 is almost equal to that produced from Equation 3.7 (65.34 kN and 65.19 kN, respectively).

$$P_{flex} = \frac{4\ m_R}{r_q(\cos(\pi/8) + \sin(\pi/8)) - c} \times \frac{b^2 - (b \times c) - (c^2/4)}{b - c} \tag{3.6}$$

$$P_{flex} = 8\ m_R \times \frac{b}{b + b_2 - 2 \times (c + b_1)} \tag{3.7}$$

where, m_R is the section moment capacity for reinforced slabs that equal to,

$$m_R = f_y \times \rho \times d^2 \times \left(1 - 0.5\rho \times \frac{f_y}{f'_c}\right)$$

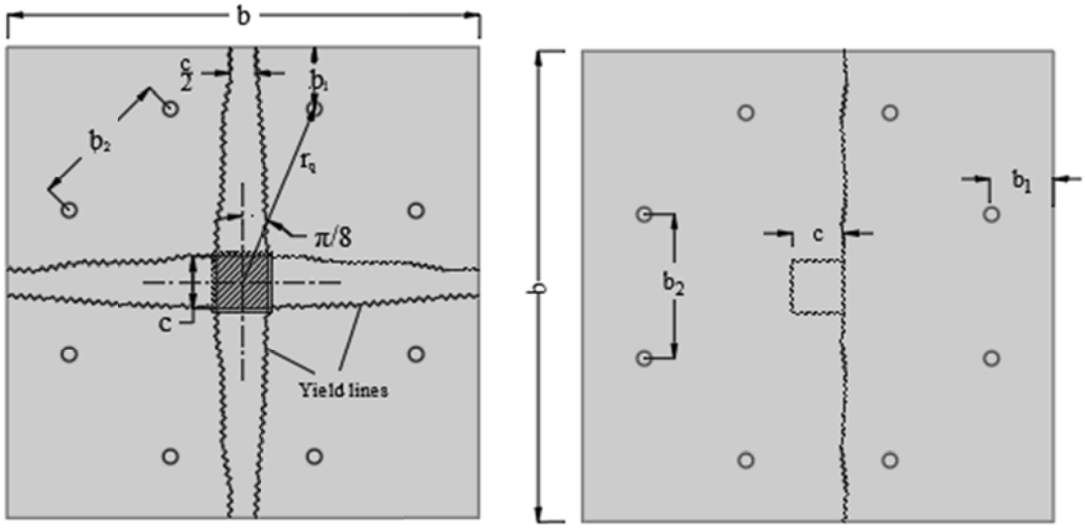

$P_{flex} = 9.65\ m_R$ $P_{flex} = 9.69\ m_R$

(a) **(b)**

Figure 3.12 Expected yield line patterns for reinforced slab (a) fan like yield lines reproduced from [83] (b) single yield line reproduced from [26]

3.10.2 Unreinforced slabs

For unreinforced (plain concrete) slabs, two expected crack patterns are illustrated in Figure 3.13 and 3.14, which are fan and cross like cracks. The cracks shown in Figure 3.13 start from the corners of the column and propagate toward the slab edges at distance x from the corners, which divide the slab into eight yielding regions, while the second crack patterns assumes that there are four perpendicular cracks form as shown in Figure 3.14. These cracks start from the slab center at tension face and propagate to the center of each slab edge, which divide the plate into four symmetric yielding regions.

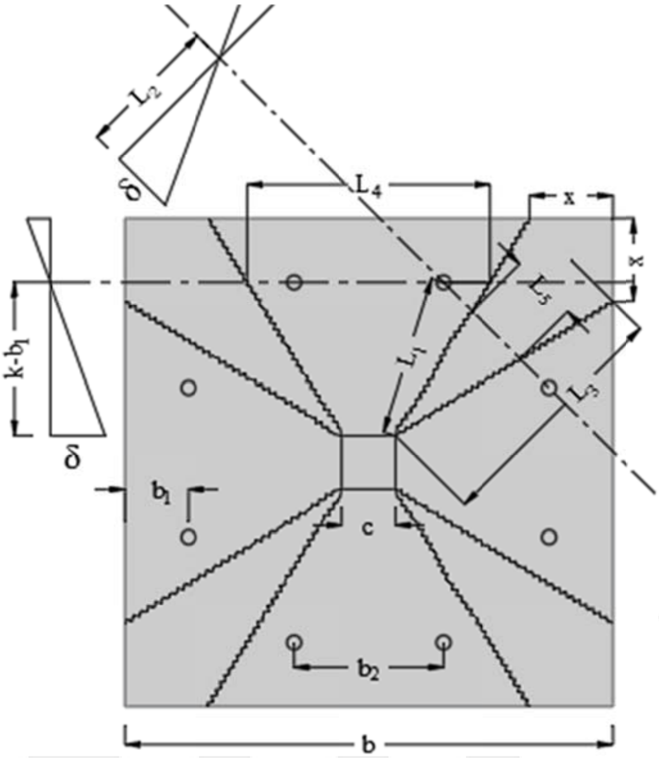

P_{flex} = 8.03 m_R

Figure 3.13 Expected fan-like yield line patterns for unreinforced slab

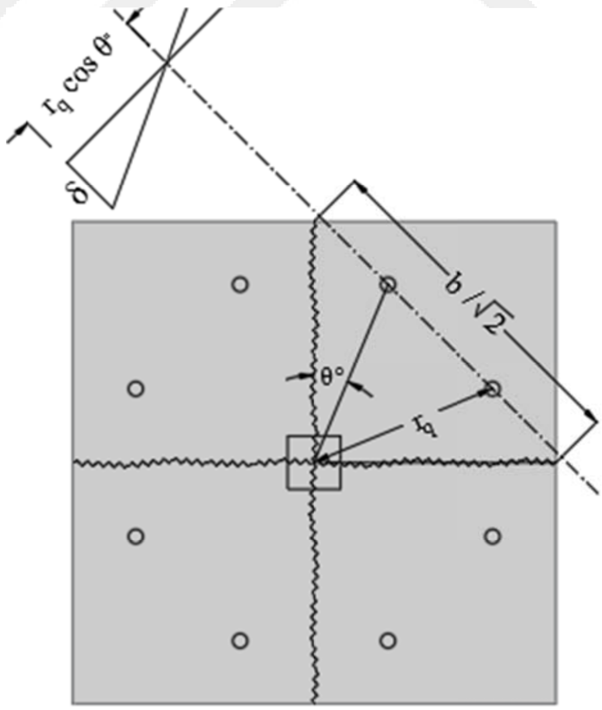

P_{flex} = 6.32 m_R

Figure 3.14 Expected cross-like yield line patterns for unreinforced slab

The external work induced from the applied load is according to Equation 3. 9, while the internal response work induced from the movement of the yielding regions can be calculated from Equation 3.10.

$$w_{ext.} = P \times \delta \qquad (3.8)$$

$$w_{int..} = - \sum m_R \times L \times \theta \qquad (3.9)$$

where

m_R is the plastic moment capacity (isotropic).

L is the yield line projection on the axis of rotation.

θ is the rotation.

Applying the virtual work concept to the slab in Figure 3.13 leads to following derivation, where the internal work done is the sum of eight regions of two different shapes,

$$w_{int..} = - [w_1 + w_2] \qquad (3.10)$$

$$w_1 = 4\ m_R \times L_1 \times \frac{\delta}{k - b_1} \qquad (3.11)$$

$$w_2 = 4\ m_R \times L_3 \times \frac{\delta}{L_2} \qquad (3.\ 12)$$

where,

m_R is the cracking moment of unreinforced slab, which can be determined using the elastic theory,

$$m_R = \frac{\sigma_t \times h^2}{6}$$

where,

σ_t is the concrete tensile stress, and h is the slab thickness.

and,

$$k = \frac{b - c}{2}$$

$$L_1 = \frac{2\,(k - x)\,(k - b_1)}{k} + c$$

$$L_2 = \sqrt{L_5^{\,2} - \left(\frac{b_2}{2}\right)^2}$$

$$L_3 = \sqrt{2} \times \frac{x\,L_2}{L_4}$$

$$L_4 = (\sqrt{2} \times k) - \frac{x}{\sqrt{2}}$$

$$L_5 = \sqrt{(k - b_1)^2 + \left(\frac{b_2 - c}{2}\right)^2}$$

Substituting Equations 3.12 and 3.13 into Equation 3.11 produces the following,

$$w_{int..} = 4\ m_R \times \left[L_1 \times \frac{\delta}{k - b_1} + L_3 \times \frac{\delta}{L_2}\right] \tag{3.13}$$

Assuming one unit virtual moving of the entire yield sector ($\delta = 1$) and substituting L_1, L_2, and L_3 and equating Equations 3.9 and 3.14 yields,

$$P = 4\ m_R \times \left[\frac{2(k - x)}{k} + \frac{c}{k - b_1} + \frac{\sqrt{2}x}{\sqrt{2}\ \ k - \frac{x}{\sqrt{2}}}\right] \tag{3.14}$$

A yield-line pattern can be related to a value of x that gives a minimum value of P in Equation 3.16,

$$\frac{dP}{dx} = 0 \text{ gives } x = (2 \mp \sqrt{2})\ k$$

Substituting x value in Equation 3.16 leads to the following minimum load strength,

$$P_{flex} = m_R \times \left[16\,(\sqrt{2} - 1) + \frac{8c}{b - c - 2\,b_1}\right] \tag{3.15}$$

Applying the same previous procedure to the slab in Figure 3.14 leads to the following virtual work equilibrium,

$$P = 4\ m_R \times \frac{b}{\sqrt{2}} \times \frac{\delta}{r_q \cos\theta} \tag{3.16}$$

Assuming one unit virtual moving of the entire yield sector ($\delta = 1$) and substituting $\theta = \pi/8$, Equation 3.17 can be introduced as follows,

$$P_{flex} = 4\ \sqrt{\frac{2}{5}} \times m_R \times \frac{b}{r_q} \tag{3.17}$$

It is shown that the minimum load strength required to create a cracks such as in Figure 3.13 is 8.03 times the section moment capacity (m_R), while lower load is required to create cracks such as in Figure 3.14 (6.32 m_R). For general purposes, the load strength is used for comparison. However, for analysis purposes, the values are calibrated according to the patterns shown in the tested specimens.

3.11 Experimental Program

3.11.1 Materials properties and concrete mixture

Concrete mixes are designed to achieve a 28-day cylinder compressive strength f'_c of 60 MPa for normal concrete and 35 MPa for ECC.

For the normal concrete mixes, high percentages of fine aggregate were used. In all specimens, two types of aggregate were used, crashed stone as coarse aggregate and sand as fine aggregate. The judgment on the specifying of the nominal maximum size of aggregate is based on the largest sieve that retains 10% of the amount of aggregate used in test, which was 9.5 mm as shown in Figure 3.15. Mixes details are listed in Table 3.4. From the table, it can be concluded that the percentage of the fine aggregate is 63% of the total amount of aggregate, while the percentage of coarse aggregate is 37%. Moreover, there is a gap between the particles smaller than 9.5 mm and greater than 4.75 mm. The reasons of using the high percentage of fine aggregate are to increase the particle surface area that leads to faster concrete strength gaining, enhancing the stresses transforming through the specimen section, and to improve the bond between the matrix and the small fiber size.

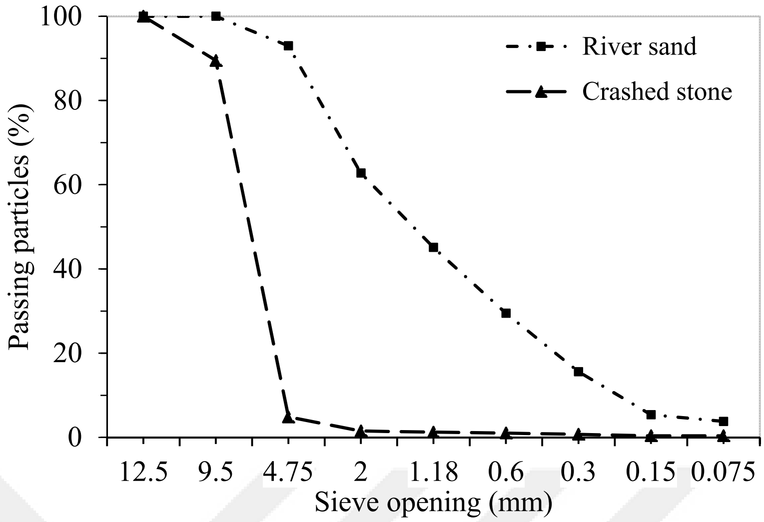

Figure 3.15 Sieve analysis of the river sand and the crushed stone

Table 3.4 Concrete mixture amount per cubic meter

mix code	Fiber type	V_f (%)	C kg	G kg	S kg	SS kg	S.fm kg	FA kg	HWR kg	W Lt
P	_	-	465	680	1170	-	35	-	6.6	216
SF0.5 SF1 SF1.5	Steel fiber	0.50 1 1.50	465	680	1170	-	35	-	6.6	216
NM0.5 NM1 NM2	Nylon-mono	0.50 1 2	566	-	-	452.8	-	679	6.792	323
PVA6 PVA12 PP	Poly-vinyl-alcohol Poly-propylene	2 2 2	566	-	-	452.8	-	679	6.792	323

C; Cement, **G**; Gravel, **S**; Sand, **SS**; silica sand, **S.fm**; Silica fume, **HWR**; High water reducer, **W**; Water

Portland cement of type CEM II/ A-LL 42.5 R conforms to EN 197-1 provisions were used. In addition to increase the fine particles, silica fume of 7% of the total weight of the binder (Cement + Silica fume) was added to increase the surface area by 40 to 100 times the equivalent cement amount. It is expected that increasing finer materials in the presence of SF and with approximately moderate water / (Cement + Silica fume) produces a mixture with low slump. In order to get sufficient slump, fixed content of high range water reducing “Glenium 51” was used in all mixtures. The recorded slump of the produced mixtures is shown in Table 3.4.

At the first stage of mixing, the fine and the coarse aggregate were mixed together for 10 minutes before adding the cementitious materials and then all the materials were mixed for 5 minutes. Water was then gradually added and the slump was checked in this stage. The water reducer was added prior to adding the fibers. Three percentages of cold drawn glued SF of 0.75, 1, and 1.25% by weight of concrete were used. The characteristics of the SF with hooked-ends that employed in this study are shown in Figure 3.16 and listed in Table 3.5. The SF was added manually with mixer rotating at high speed. After the completion of the specified amount of SF, the mixer was slowed down and the mixture was rotated to 45 revolutions. All the SFRC in the standard molds and the slabs were externally vibrated in order to avoid balling of the SF, whereas the plain concrete (without SF) in slab molds was internally vibrated. However, the cylinders were consolidated by rodding according to ASTM C31 provisions. All cast works were kept under laboratory condition for 24 hours. The slabs and the associated cylinders were removed from their molds and were cured in a water pool for a 28 days, so that both slab and cylinders are exposed to the same curing conditions. In order to overcome any errors, the average of three standard cylinders with the same properties and conditions were employed in structural analysis.

ECC mixtures incorporate fine silica sand with sand to binder ratio (S/B) of 0.36 to maintain adequate stiffness and volume stability. ECC has water to binder (w/b) ratio of 0.26 to attain a good balance of fresh and hardened properties. The binder system is defined as the total amount of cementitious material, i.e. cement and fly ash (Type F). The same mentioned mixing procedure was used for ECC. However, it was found that the period required to get consistence mixture is 30 min.

Steel fiber 30/55

Steel fiber 30/40

Nylon monofilament 19/380

Polypropylene 12/400

Polyvinyl Alcohol 6/400

Polyvinyl Alcohol 12/800

Figure 3.16 Fibers types, the numbers refer to length/aspect ratio

Table 3.5 Properties of fibers

Type	Density	l_f †	D_f †	l_f/D_f	Tensile strength	Elastic modulus
	kg/m^3	mm	mm	mm/mm	MPa	(GPa)
Hooked-ends Steel fibers (SF)	7850	30	0.55	55	1500	200
	7850	30	0.75	40	1225	200
Nylon fibrous monofilament (NM)	1140	19	0.05	380	966	25
Polypropylene (PP)	910	12	0.03	400	350	1.4
Polyvinyl alcohol (PVA)	1260	6	0.015	400	1600	34
	1260	12	0.015	800	1600	34

† l_f and D_f are the length and diameter of the fiber, respectively

The experimental program includes four test series. In the first, standard cylinders of 100×200 mm subjected to uniaxial compression load were used to evaluate the concrete compressive strength f'_c according to ASTM C39. Secondly, similar cylindrical specimens were subjected to indirect tensile load (cylinder splitting) to evaluate the concrete tensile strength f_{ct} according to ASTM C 496. Thirdly, the specimens were subjected to compression load to evaluate the Young's modulus according to ASTM C469. Finally, the casted two-way slabs with concentric column were tested under monotonic increasing load.

3.11.2 Instrumentation

During the test, several visual and mechanical observations were made. In this section, detailed descriptions of thermocouples, strain gages, LVDTs are given and their instrumentation is explained.

3.11.2.1 Dial gages and Linear Variable Differential Transformers (LVDT)

The displacement at the slab center was measured using an LVDT located at the bottom of slabs along the direction of the load application, which is termed LVDT1. Moreover, the displacement of the top center was measured directly from the jack displacement that is termed as LVDT2. Two dial gages were fixed at the top of the slab, one at the corner (DG1) and another at the center of the slab edge (DG2) as shown in Figure 3.17a. These two LVDTs were used to measure the edge lifting at the free edges and the slab rotation. In order to synchronize between the dial gages and the jack loading, a photo was captured each 30 sec, and then both load and the dial gage reading were recorded manually.

3.11.2.2 Strain gages

Measuring the strain of the reinforcement and predicting the first initial cracks is one of the main goals of the experimental work. Strains in reinforcement were measured for each specimen using two strain gauges located on the critical area around the connection perimeter. Bar strain gauge (SG1) was located at 22.5 mm from the center of the specimens directly underneath the column, while SG2 was located at the same axis of SG1, but at a distance of 2d from the face of the column where d is the effective depth. The strain gages are shown in Figure 3.17b.

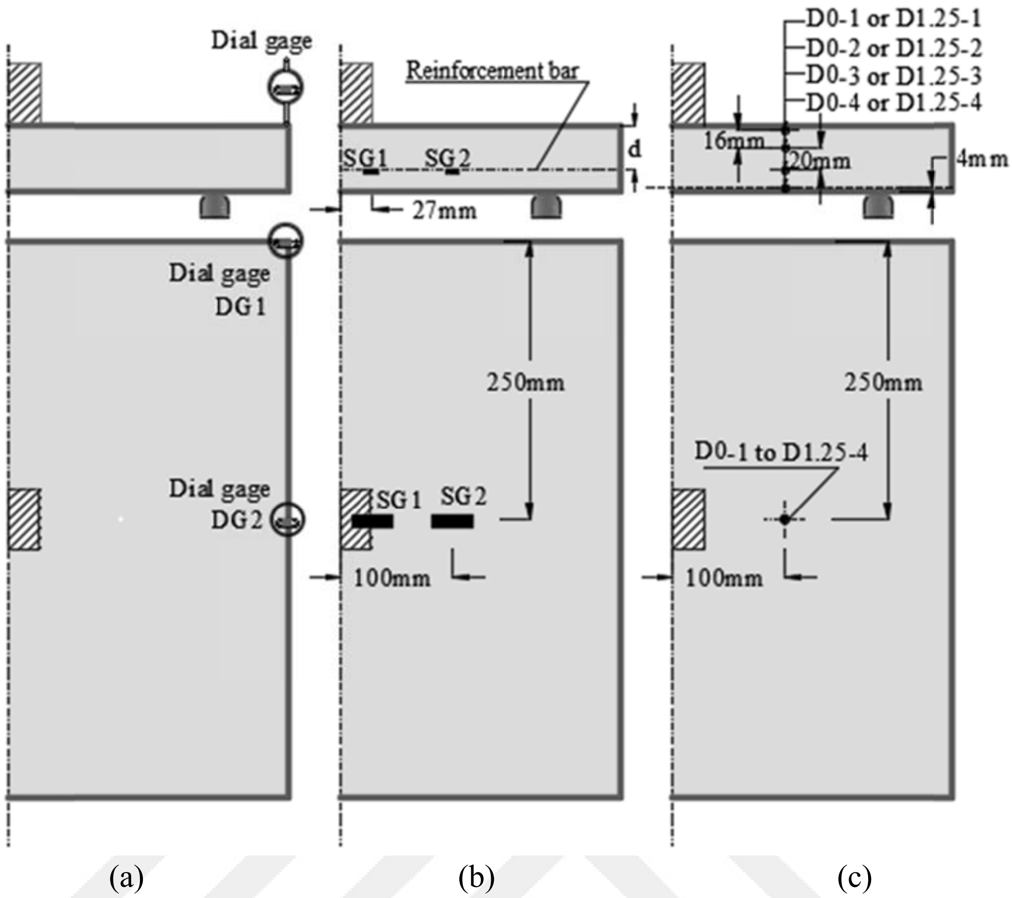

Figure 3.17 Location of (a) Dial gages (b) Strain gages (c) Thermocouples

3.11.2.3 Thermocouples

Four high temperature (up to 1200 °C) thermocouples were installed in the slab concrete. Type K Chromel (Nickel-Chromium Alloy) is the most general-purpose thermocouple with a sensitivity of approximately 41µV/°C. This type of thermocouples was distributed along z-axis of the slabs in specimen D0 and D1.25 in distances shown in Figure 3.17c. The temperature inside the furnace was measured using a thermocouple attached to the furnace's wall (according to manufacturer design). The interior two thermocouples (D0-2, D0-3, D1.25-2, and D1.25-3) were fixed before casting the concrete, while the two exterior thermocouple were interred in a hole drilled after the hardened of the concrete and fixed by gypsum, this is was not the proper fixing because the gypsum has low thermal conductivity compared to the concrete. The problem has not affected the result after long soak time.

3.12 Heating Process

All the produced specimens in Group 6 were cured in a water pool and after 28 days all the slabs and the standard cylinders were removed from curing water for the next process. Except Group P (specimens exposed to ambient condition), the surfaces of the other groups were dried and then heated for 24 hours at 105 °C before the specified temperatures are applied in order to remove the free water in the concrete pores. This process minimized the sudden increasing in excessive pressure induced from water vapor emission, this process is important to reduce the effect of the cylinder shape compared to the plane shape of slabs, in other words, the surface area of the cylinder to its volume is less than that for slab, which have the high water evaporation capacity. It is important to know, that the higher fine particle content leads to less porosity, this may increase the pore water pressure due to the less expelling of the free water. In the conventional concrete mix, seven days of drying in 105 °C can remove 60 to 64 % [58].

Each group of the four specimens and their associated standard cylinders were step inside a furnace of clear dimensions of 1360×1300×620 mm and of 1200 °C capacities (see Figure 3.18). Except the furnace floor and ceiling, the four other sides are applying the temperature. This is to ensure that the heat is applied homogeneously for all specimens.

In the next step of the heating process, each group was heated under three continues stage, known as heating, soaking, and cooling. The temperature rates of these stages are depicted in Figure 3.19. The furnace was programed to apply a temperature rate of 10 °C/min. It is worthy to mention here that the temperature rate does not affect the results. For the specimens exposed to temperatures less than 300 ºC [86], Zhang et al., [86] studied the residual strength under three different heating rates (1, 3, and 10 °C/min). They found that the 10 °C/min is the worst case. Increasing the heating rate from 3 to 10 °C/min leads in a strength difference of 36 % and 60 %, respectively. This results from test up to 450 °C. Various heating rates can be adopted depending on the research parameters, where Purkiss [87] used 2 °C/min, Chen et al., [88] and Poon et al., [89] used 2.5 °C/min, Lawson et al., [90] used 5 °C/min. All the mentioned rates are lower than the rate of temperature-time standard curve proposed by ISO834. However, the standard rate is more severe than the effect of real fire [6].

Based on the previous drying and heating rates, four Groups A, B, C, and D were exposed to 150 °C, 300 °C, 450 °C, and 550 °C, respectively (see Figure 3.16b). The maximum temperatures were chosen within the temperature employed by many researchers [85, 88- 90]. Moreover, the highest temperature level is the same of that produced by analysis of Bamonte and Felicetti [9] on fire scenario for six cars firing in sequential ignition. The compartment assumes as close car parking that includes lot of flat concrete plates. Incidents of burning six cars in the closed car parking are within the 97.9 % of the incident found in Paris [91].

The test furnace is programmed to apply a constant rate for three hours before cooling. As it is known that, the temperature distributes in high nonlinearity [88]. Therefore, the soaking time is important to allow the temperature distribution to take place. Moreover, it is important to reduce the shape effect as it is illustrated previously.

As a final stage, the specimens were cooled down gradually by turning off the furnace and opening the ventilation cover located at the furnace roof (see Figure 3.18). This smooth cooling is important to reduce the effect of thermal strains induced from sudden cooling.

3.13 Test Setup

Both slabs and the standard cylinders of the same age and mixture properties were tested at the same time. All tests were conducted using monotonically increasing load until failure. For the slabs, the test was conducted using INSTRON device of 250 kN capacity (see Figure 3.20) loaded at displacement rate. ASTM C1550 accepts that the small changes in the displacement rates within the range of 0.5 to 10 mm/min have only a minor influence on the energy absorption. In the current work, a displacement rate of 0.4 mm/min was used with closed-loop loading rate system. Crack initiation was characterized from the load-deflection curve, while the crack propagation was monitored by using a mini camera, which was fixed at the base of the testing device and connected to a computer. The monotonic load was applied from the hydraulic jack through the load cell to a steel cubic shift of 55 mm size that represents the column stub. In such case of loading, the slab has some freedom to control its internal forces to distribute to the boundary points [92].

Figure 3.18 Furnace of 1360×1300×620 mm

(a)

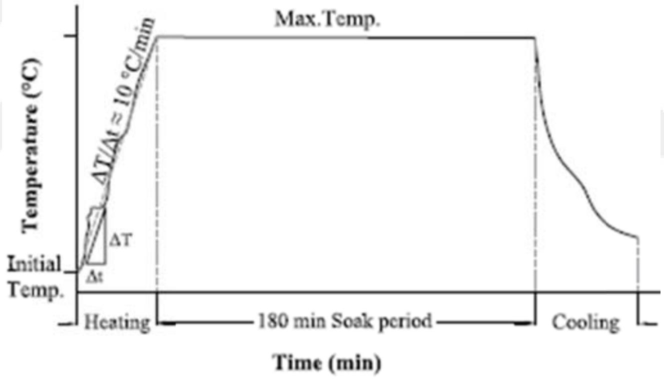

(b)

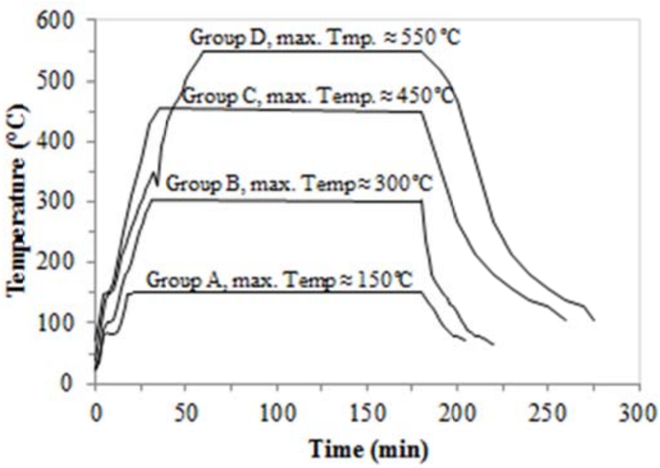

Figure 3.19 Heating process (a) typical stages in heating process (b) actual temperature-time curves

Figure 3.20 Test configuration of slab specimens

CHAPTER 4

EXPERIMENTAL RESULTS AND DISCUSSION OF FIBROUS REINFORCED FLAT PLATE-COLUMN CONNECTION UNDER AMBIENT CONDITIONS

4.1 General

Preferable structural failure should show ductile failure mode when subjected to collapse loading so that the large deformation and multi-cracking would be a precede caution of the structure breakdown. Most of the codes of practice consider this concept for many structural members and connections. For flat plate-column connections, there is a great risk of brittle collapse due to the punching shear failure. Many types of shear reinforcement are applied to enhance the load capacity. Based on the provision of many codes, it is shown that the ductility of the flat plate is not achieved by a proper punching and flexural strength design. Moreover, if the flexural and punching strengths are considered independently as in ACI318, AS3600, and CSA A23, then the design should allow the yielding of all reinforcement before punching takes place. This can be achieved by increasing the punching capacity compared to the flexural capacity. Many researches had been conducted on using different configurations of shear reinforcement in order to increase the punching shear capacity, and in turn increase the post-failure rotational capacity and the ductility. On the other hand, there are new trends aim to increase the concrete strength so that the punching strength increases, but the brittleness problem is would be aggravated. For this reason, there are wide trends to use fibers to control the cracks in flat plate-column connections. The inclusion of fibers aims to increase the toughness of the concrete member and hence prevents or at least decreases the cracking due to temperature change. The inclusion of fibers with the concrete materials increases the ultimate resisting load capacity, but the main purpose of the fiber is to enhance the behavior of the members during the post-peak loading.

This chapter concentrates on the enhancing of the ductility of the slabs without shear reinforcement where the ultimate strength, ultimate deflection, and the post-failure rotational capacity of the concrete are the main parameters. This is achieved by investigation the effect of fibers with different dosages and types on the ductility of the slabs. Different fibrous materials are used (Steel fibrous concrete, nylon-monofilament (NM-ECC), Polyvinyl-alcohol (PVA-ECC), polypropylene (PP-ECC), and a composite between normal concrete and the NM-ECC, where the NM-ECC is placed in the critical region D-zone). Table 4.1 shows the groups details and the concrete properties used in discussion.

4.2 Codes' Provision on the Flat Plate-Column Connection

Different codes of practice introduce the nominal punching shear stress (v_n) as a shear force per critical area ($V_n/u_1.d$). This stress should be resisted by concrete strength or/and using special shear reinforcement. It is easy to observe that the codes equations are in the general form of,

$$V_n = V_c + V_s \tag{4. 1}$$

where V_c is the characteristic concrete shear strength, which equals,

$$V_c = \tau_c \,.\xi\,(d)\,.\,f\,(\rho).\,u_1\,.d \tag{4. 2}$$

(τ_c) is a function in terms of compressive strength, (ξ) is the size factor in terms of effective depth (d), and f (ρ) is a function of tension reinforcement ratio.

For slabs without shear reinforcement, the nominal punching shear strength is then equal to the concrete punching capacity V_c. Table 4.2 summarized the different code provisions for (V_c). Critical punching shear perimeter for square and circular column, other column’s shape are shown in Figure 4.1. It is easy to conclude, that the presented codes are almost differ in all terms in Equation 4.2. Three groups of codes' equation are observed. The first group are Eurocode 2 [53] and DIN1045 [93] that considered the size and reinforcement ratio effect, while the second group includes ACI318 [19], CSA A23.3 [66], AS-3600 [94] and IS456 [95] where the mentioned effect is not considered and the nominal punching shear strength is based on the concrete strength only. TS500 [81] and SNiP 2.03.01-84 [96] can be considered within this group, yet the concrete strength is represented in terms of concrete tensile strength. Different considerations were adopted in the provision of MC2010 [97].

The model the code, adopts the failure criterion and the load deflection curve of the critical shear crack theory proposed by Muttoni [22].

Table 4.1 Details of the specimens' properties and their groups

Group No.	Group details	Spec.	Fiber V_f (%)	density (kg/m^3)	b (mm)	h (mm)	d (mm)	ρ (%)	f_{sp} (MPa)	f'c normal (MPa)	f'c fiber (MPa)
I	Plain RC. with Varying ρ and d	P50	0	2330	500	53.905	29.7	1.2	3.85	43.20	_
		P60-11		2287		62.72	39.7	1.2	3.85	43.20	_
		P80		2387		82.13	59.7	1.2	3.85	43.20	_
		P60-10B		2298		62.59	39.7	1.1	5.28	40.83	_
		P60-10S		2292		60.00	38.7	1.1	5.63	55.00	_
		P60-8		2227		62.60	39.7	0.9	6.14	32.12	_
II	Varying SFRC	SF0.5	0.5	2307	500	60.00	38.7	1.1	4.40	62.04	68.92
		SF1	1	2316		60.00	38.7		4.48	67.79	78.56
		SF1.5	1.5	2327		60.00	38.7		5.88	59.55	80.88
III	Reinforced NM-ECC	NM0.5R	0.5	1941	500	63.09	39.7	1.1	5.68	_	37.94
		NM1R	1	1961		60.54	39.7		6.73	_	37.35
		NM2R	2	1966		60.00	39.7		7.32	_	41.50
IV	PVA6-ECC	PV6	2	1996	500	62.05	39.7	1.2	0.00	_	0.00
	PVA12-ECC	PV12		1779		63.63	39.7		7.80	_	39.18
	PP12-ECC	PP12		1827		64.46	39.7		6.61	_	31.51
V	unreinforced NM-ECC	NM0.5	0.5	2054	500	62.30	0.00	0	5.68	_	37.94
		NM1	1	2062		61.14	0.00		6.73	_	37.35
		NM2	2	1991		61.95	0.00		7.32	_	36.06
VI	Plain RC + NM-ECC	NM0.5P	0.5	2067	500	60.00	38.7	1.1	5.53	51.98	37.29
		NM1P	1	2076		60.00	38.7		6.60	51.98	43.46
		NM2P	2	2079		60.00	38.7		6.90	63.42	41.5

Table 4.2 Code's provisions for punching shear of flat plate without shear reinforcement supported by concentric interior columns

Codes	Critical perimeter l_{cri} (1)	Critical perimeter u_1. (2)	Punching shear resistance $V_c = \phi.\tau_c.\xi.f(\rho).u_1.d$ — ϕ	(τc)	(ξ)	$f(\rho)$	Limitation — Size factor	Reinf. ratio	other
Eurocode 2 [98]	2d	Square col., $= 4(\pi d + c)$ Circular col., $= \pi(4d + c_1)$	0.67	$0.18\sqrt[3]{f_{cl}}$	$1 + \sqrt{\frac{200}{d}}$	$\sqrt[3]{100\rho}$	$\xi \leq 2$	$\rho \leq 0.02$	-
DIN1045-1 [93]	1.5d	Square col., $= 3\pi d + 4c$ Circular col., $= \pi(3d + c_1)$	0.67	$0.21\sqrt[3]{f_{cl}}$	$1 + \sqrt{\frac{200}{d}}$	$\sqrt[3]{100\rho}$	$\xi \leq 2$	$\rho \leq 0.5\ f_{cd}/f_{yd}$ $\rho \leq 0.02$	$4c \leq 11d$ $b/w \leq 2$
MC 2010 [97]	0.5d	Square col., $= \pi d + 4c$ Circular col., $= \pi(d + c_1)$	0.67	$\sqrt{f_{ck}}$	$k_\psi = \frac{1}{1.5 + 0.9k_{dg}\psi d}$	1	$k_\psi \leq 0.6$	-	$\psi = 1.5\frac{r_s}{d}\frac{f_y}{E_s}$ $k_{dg} = \frac{32}{16+d_g} \geq 0.75$
ACI318 [19]	0.5d	Square col (3) $= \pi d + 4c$ Circular col.(4) $= \pi d4 + c_1\sqrt{\pi}$	0.75	$0.33\sqrt{f'_c}$	1	1	-	-	$\sqrt{f'_c} \leq 8.3$ Mpa
AS-3600 [94]	0.5d	Square col., $= 4(d + c)$ Circular col., $= \pi(d + c_1)$	0.70	$0.34\sqrt{f'_c}$	1	1	-	-	-

Table 4.2 ………Continued from previous page.

Codes	Critical perimeter l_{cri} (1)	Critical perimeter u_1. (2)	Punching shear resistance $V_c = \varphi.\tau_c.\xi.f(\rho).u_1.d$ φ	(τc)	(ξ)	Limitation f(ρ)	Size factor	Reinf. ratio	Other
CSA A23.3 [66]	0.5d	Square col., = 4(d + c)	0.65	$0.38\sqrt{f'_c}$	ξ = 1, d ≤ 300 $\xi = \frac{1300}{1000+d}$, d>300	1	-	-	$\sqrt{f'_c} \leq 8.0$ Mpa
IS456 [95]	0.5d	Square col., = 4(d + c) Circular col., $= 4(d + c_1)$	0.67	$0.25\sqrt{f_{cu}}$	ξ = 1, d ≤ 300 $\xi = \frac{1300}{1000+d}$, d>300	1	-	-	$f_{cu} < 55$
SNiP 2.03.01-84 [96]	0.5d	Square col., = 4(d + c) Circular col., $= \pi(d + c_1)$	0.67	f_{ct}	-	-	-	-	-
TS500 [81]	0.5d	Square col., = 4(d + c) Circular col., $= \pi(d + c_1)$	0.67	f_{ct}	-	-	-	-	-

(1) Distance from column face

(2) Critical punching shear perimeter for square and circular column, other column's shape are shown in Figure 4.1.

(3) ACI318-14 permits to use straight sides, hence the perimeter can be $u_1 = 4(c + d)$ for square column and $u_1 = 4(r\sqrt{\pi} + d)$ for circular column.

(4) For circular column section, assuming a square column of equivalent area (see Figure 4.1)

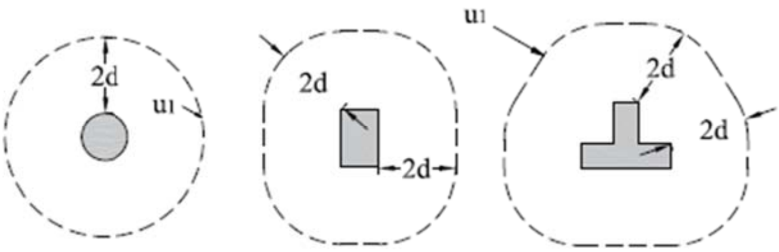

(a) According to Eurocode 2 [53]

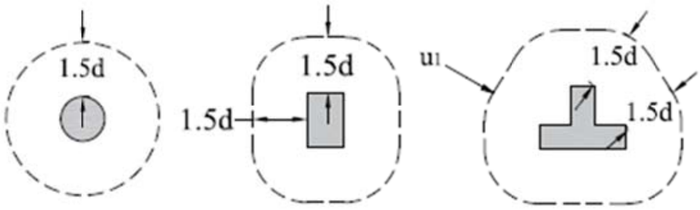

(b) According to DIN1045-1-2008 [93]

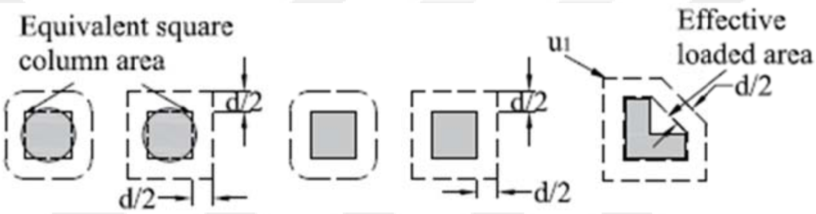

(c) According to ACI318-14 [19], CSA A23.3-2004 [66] and MC2010 [97]

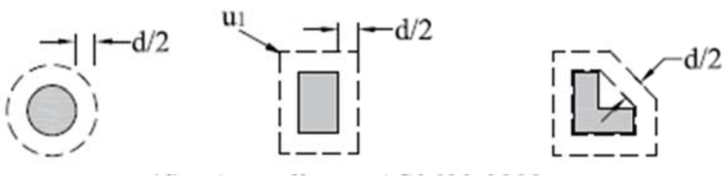

(d) According to AS3600-2009 [94] and TS500 [81]

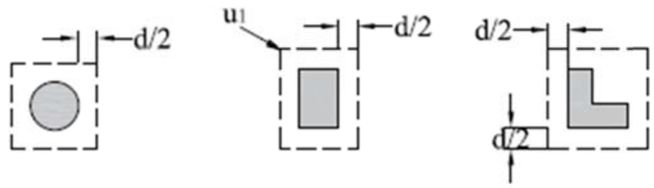

(e) According to IS456-2000 [95]

Figure 4.1 Critical shear crack perimeter according to different codes of practice

4.3 Comparisons among the Codes of Practice

Most codes of practice are based on semi-empirical models and don't provide a proper failure mechanism. These codes assume that the distribution of shear force around the critical perimeter is uniform. However, the true is that the distribution of shear varies markedly around the perimeter and is accompanies by torsional moments. These disagreements lead to many confusing differences among them, which leads to different levels of predictions of the punching shear strength. The critical distance (l_{cri}), which is always represented in term of the effective depth, is varying according to different codes from d/2 to 2d, Figure 4.1 shows different provisions of l_{cri}. The Eurocode 2 [53] adopts 2d as the distance of the critical section, whereas the critical distance is 1.5d in DIN1045 [93]. Table 4.2 lists the critical distance for all of the included codes. The variation of the critical distance between the different codes affects the critical punching shear perimeter (u_1). In addition, the shape of the critical punching crack also differs according to the codes' considerations and the column shape. Eurocode 2 [53] and DIN1045 [93] permit to use a circular shape for connection of circular column, while the rectangular shape with curved corners are adopted for rectangular column. This results in the same distance from any point of the column even if high stresses are induced from the column corners. Almost the same provision is adopted in AS-3600 [94] but with angular shape for rectangular columns. Both IS456 [95] and ACI318-14 [19] consider a square shape for circular columns, yet, the latter advices to use the equivalent square area of the circular column, while straight lines of the rectangular shape is permitted for the calculation the critical perimeter in the former code.

Effect of flexural reinforcement ratio (ρ) and size factor ξ (d) in terms of the effective depth (d) are also different among the mentioned codes, which leads to more confusion. Some codes do not considered these effects such as ACI318 [19], AS3600 [94], CSA A23.3 [66], and IS456 [95]. The missing factors may have small effect in the case of analyzing thick slabs with moderate reinforcement ratio. However, these effects are significantly active in thin slabs. For example,. ACI318 equation overestimates the shear stress in case of $\rho < 1\%$ and $d > 200$mm, [83,99]. In contrast, the advocates of this code deems that the proposed equation is never used as shear prediction, but intended to be interact with proper flexural design aimed to fail in flexural shear $P_{flex} < V$, so that full moment redistribution is allowed [100].

Another difference in codes' provision is the inclination of the punching shear crack. Both ACI318 and SNiP 2.03.01-84 assume that the angle of inclination is 45° with the horizontal axis. This angle is less in Eurocode 2 and DIN1045, where the crack is inclined by only 26.6°, and 33.7°, respectively. Formally, the angle of inclination was 45° in BS8110-85, while it was later changed to be 33° in BS8110-97.

Gardener [101] showed that the Eurocode 2-2003, and DIN 1045-1 use non conservative prediction methods to calculate the punching shear capacity of concentrically assemblies loaded by 26.6%, and 23.5%, respectively. These codes have significantly smaller coefficients of variation than ACI318-05.

4.3.1 Influences of the nominal punching shear strength parameters

The parameters discussed in the previous section have different levels of affection. The following sub-sections show the influence of the main parameters (fc, ρ and d) in the codes equations of the nominal punching shear strength. 174 test results from 25 references (collected directly or through other sources) had been conducted for comparisons purposes between ACI318 and Eurocode 2 provisions. The data used in Figures 4.2 to 4.4 are un-factored for safety. It is shown that the codes' equation do not capture the tested slab strengths. The two codes used in comparisons show wide scattered results where only 20 and 22% of the election results lay within the safe area $\left(0.75 \leq \frac{P_{u,\,test}}{P_{u,\,code}} \leq 1\right)$ according to ACI318 and Eurocode 2, respectively. Moreover, 18% of the tested slabs are overestimated by ACI318, while Eurocode 2 overestimates only 1%. The remaining 62 and 77 % are underestimated by ACI318 and Eurocode 2, respectively. The Mean, standard deviation and the coefficient of variance of the tested specimens according to ACI318 are 1.15, 0.5 and 0.44 respectively, while the same statistical tools for Eurocode 2 are 1.29, 0.46 and 0.35 respectively.

The mentioned tested slab properties used in these comparisons are listed in Appendix B.

4.3.1.1 Influence of concrete strength

There is no disagreement among the codes’ equation about the influence of concrete strength on the punching resistance. The differences are that how would the compressive strength be represented in these provisions. Different representations of the concrete compressive strength are used by the different codes where theACI318 uses the square root of the compressive strength based on Moe’s proposal [13], while the cubic root is incorporated in Eurocode2. Figure 4.2 shows the effect of concrete compressive strength of the prediction of the punching shear strength according to both ACI318 and Eurocode 2.

Control compressive strength is varying in the two mentioned codes. The ACI318 specifies the standard cylinder compressive strength (f'_c) where 9% of standard cylinder results could fall below the mean strength, while the percentage is 5% in Eurocode2. The relation between these two strengths used herein is,

$f_{ck} = f'_c - 1.6$

It is observed that using $fc^{1/2}$ tends to be overestimated in the case of using high strength concrete [2]. Consequently, the codes limited the validity of its equation by 69, 64, and 55 MPa for ACI318, CSA A23.3, and IS456, respectively. Moreover, Sacramento et. al. [2] showed that, using $fc^{1/3}$ provides a good representation of the punching resistance.

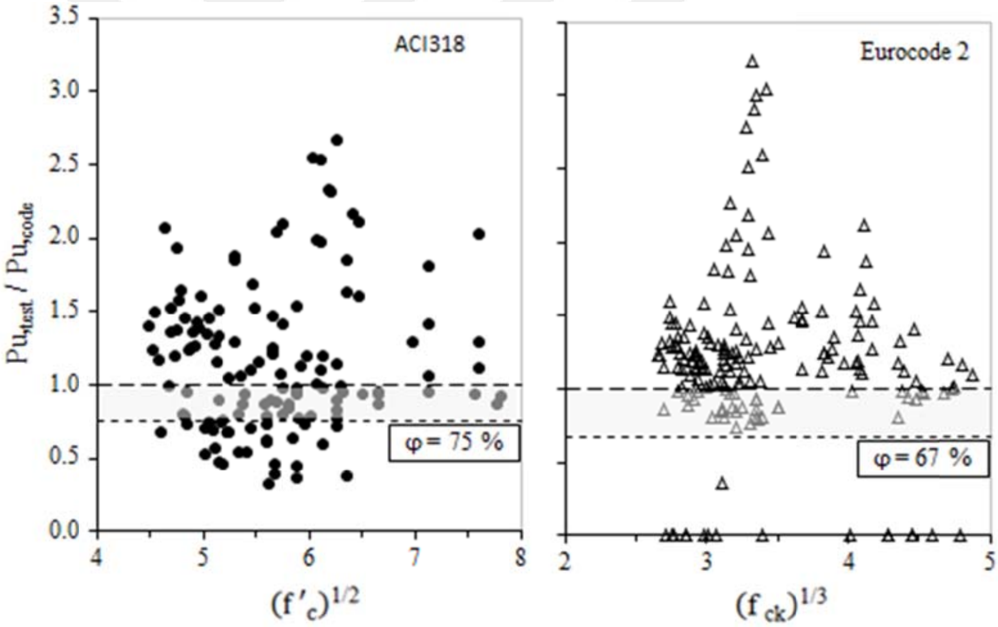

Figure 4.2 Effect of compressive strength on punching resistance according to Eurocode 2 and to ACI318 (the points on the x-axis refer to test results where one or more of code conditions are not satisfied)

4.3.1.2 Influence of reinforcement ratio

For the codes that not include the effect of reinforcement ratio (ρ) (such as ACI318 [19]), various design methods are allowed, and the strength of these slabs are not clearly specified in the codes. Generally, ρ = 0.3% is the minimum reinforcement requirement [83]). Hence, the punching shear effect is governing the slab behavior.

The reinforcement ratio may affect the punching strength by shifting the neutral axis that leads to a reduction in the compression zone, which is active in supporting the shear [100]. Moreover, increasing the ρ leads to increasing the membrane action that leads to enhanced the restraint the concrete at the reinforcement plane, which increases the punching strength. However, yielding of the flexural reinforcement bars decreases this restraint, in turn decreases the transferring shear as the bars are extending [99].

Increasing the flexural reinforcement ratio (ρ) would contribute to the punching shear strength by increasing the depth of the compression zone of the uncracked concrete as well as increasing the dowel action. Nevertheless, the effect of (ρ) on the punching shear capacity has had conflicting opinions. This mismatch in views is clearly shown in the codes provisions that are listed in Table 4.2, Eurocode 2, and DIN1045 consider the effect of the cube root of reinforcement ratio on punching resistance. However, this effect is missing in CSA A23.3, IS456, AS3600, and ACI318. Muttoni [22] has disadvantages to the deformation capacity, but affected the punching capacity, on the contrary, Elstner and Hognestad [15] showed that the increasing of ρ near columns have disadvantageous on the punching strength. Moe [13], agreed the Elstner and Hognestad [15] showed that the decrease of strength by approximately 6% by increasing the steel ratio may be due to the use of big size bars compared to the slab thickness. In other words, the concentration of tension bars leads to bond failure [14,27].

Broms, 2005 [18], found that the punching capacity depends on the flexural capacity. He identified three zones depending on the quantity of tension reinforcement. For high reinforcement ratio, the slab resistance will be higher and the punching failure occurs without any yielding of reinforcement bars. In this zone, both concrete and reinforcement behave elastically and the punching resistance can be derived from the yield line theory. In the second zone (low reinforcement ratio), all the reinforcement would yield, and the elastic theory cannot be applied, instead a flexural hinge is assumed to form at the column edges and the rigid slab sectors are rotating around this hinge. The third zone is complex to identify, where the reinforcement ratio is in between the above two zones. Shehata [17] assumes that in case of using ρ <1.75%, all the reinforcement bars within the punching radius will be yielded.

Previous paragraphs summarized the effect of the flexural reinforcement ratio because most researches deal with the tension reinforcement, nevertheless, in most designs, the slabs includes two layers of reinforcement (in tension and compression zones). A few set results showed that the increasing of the reinforcement in compression zone would increase the punching resistance not more than 12% [102].

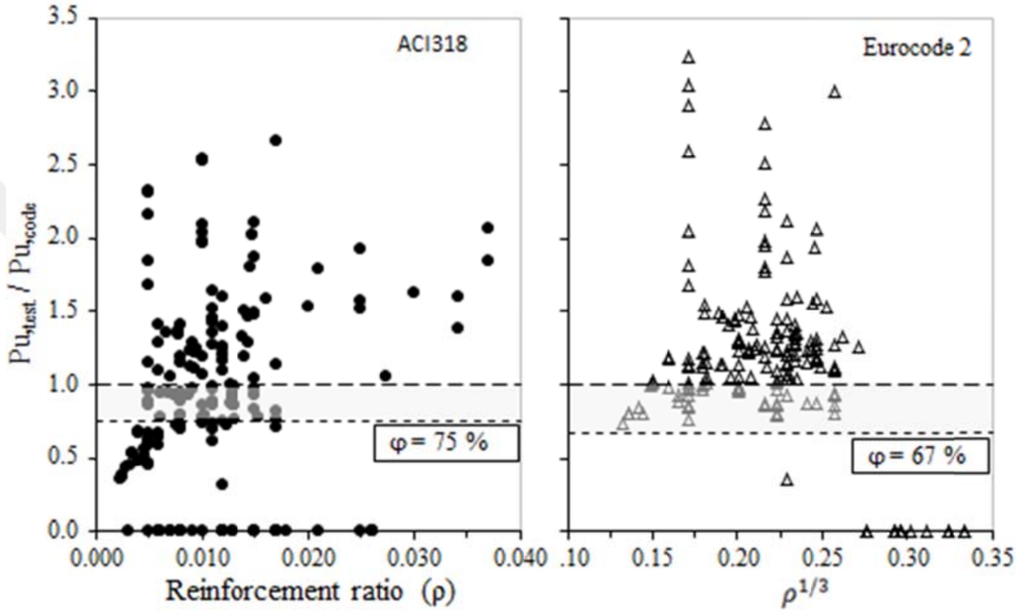

Figure 4.3 Effect of reinforcement ratio and effective depth on punching resistance according to Eurocode 2 and to ACI318 (the points on the x-axis refer to test results where one or more of code conditions are not satisfied).

4.3.1.3 Size effect

It is observed that the increasing of slab thickness will rapidly decrease the shear stress resistance [24,103,104]. Therefore, this reduction in nominal shear strength is taken into account in some codes [93,98] by using the coefficient (ξ) as a function of the effective depth (d). However, other codes do not consider this effect such as ACI318, CSA A23.3, and IS456. It is observed that using ACI318 equation, only 89% of nominal shear resistance was reached for the a slab of 300 mm thickness [103], and only 64% for a slab with 500 mm thickness [83]. Broms [18] deemed that this decay in strength is due to the initiation of cracks in the compression zone due to thermal effects during the hydration of concrete in early stage. He introduced his size effect factor as $(0.15/x_{pu})^{1/3}$ where x_{pu} is the compression zone depth. This means that this factor is implicitly proportional to the reinforcement ratio. Regan [102], introduced a correlation obtained between $V_u/A_c\sqrt[3]{f_{cu}.100A_s/bd}$ and the fourth root of thickness $(1/d)^{1/4}$, while Shehata [17] proposed the size effect as $(500/d)^{1/3}$. Moreover, Bazant and his group [104] proposed the size effect on the nominal shear stress as $v_n = C(1+ d/\lambda_o d_a)^{-0.5}$, in which $C = k_1 f'_{ct}(1+ k_2 d/b)$, λ_o is an empirical parameter based on fracture energy and shape, d_a is the maximum size of aggregate, and $k_1$and k_2 are constants.

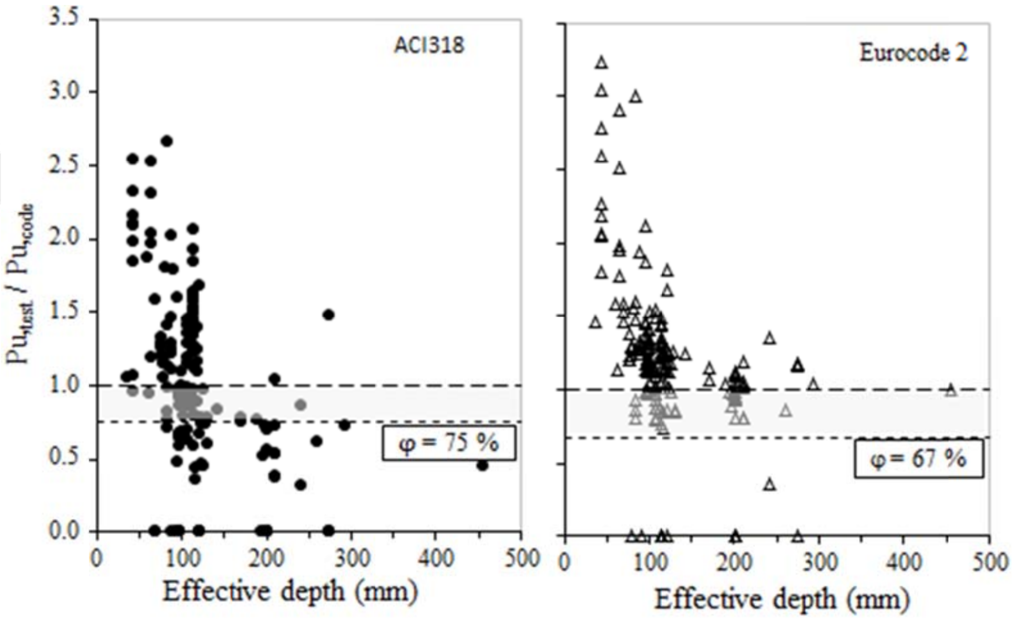

Figure 4.4 Effect of effective depth on punching resistance according, to Eurocode 2 and to ACI318 (the points on the x-axis refer to test results where one or more of code conditions are not satisfied).

4.4 Punching Shear Capacity of Fibrous and Normal RC Slab

As mentioned previously, the inclusion of fibers significantly enhance the load resistance capacity by increasing the tensile strength and slightly the compressive strength. This depends on the fiber dosage and type. From Figure 4.5 and Table 4.3 it is shown that the slabs reinforced with SF showed the higher improvement in load capacity, where 0.5% of SF increased the load capacity by 33%. Moreover, 76% of load capacity increase was recorded when 1% of SF is included, whereas increasing the fiber volume fraction to 1.5% did not provide a significant change to the load resistance upon the 1% SF, yet it highly increased the ductility as it will be discussed later.

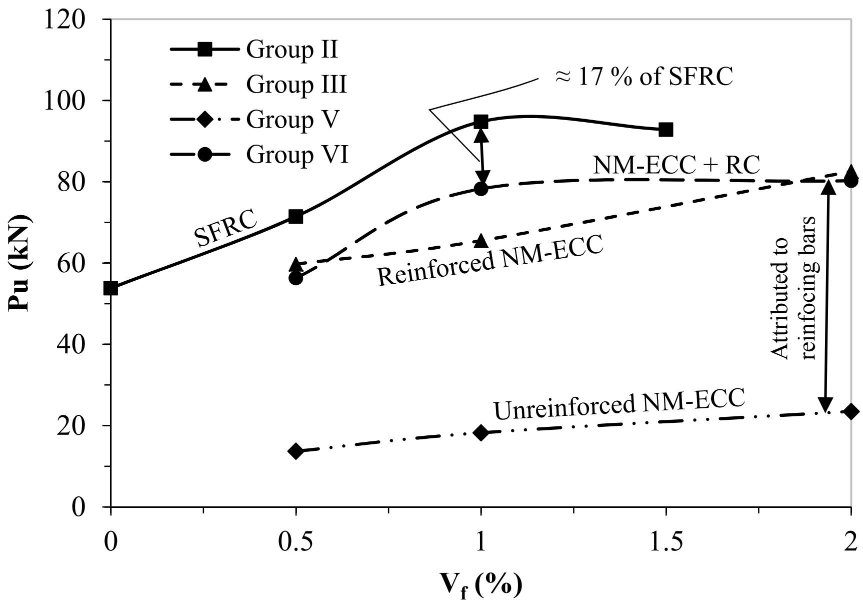

Figure 4.5 Effect of fiber volume fraction on load resistance capacity

Using nylon-monofilament (NM) to produce ECC matrix in the whole slabs size (Group III) shows that increasing the fibers from 0.5 % to 1% has increased the ultimate load by 9.6%. This percentage increased dramatically to be 38% when 2% of NM was used, which led to high ductility as it will be shown later in this chapter. There are no differences in the case of using NM-ECC in the whole slab or only in the critical area (with diameter of 220 mm, i.e. distance 2d from the column face) while normal concrete are used in the remaining slab area (see Figure 4.1). As shown in Figure 4.5, the enhancements of ultimate load in Group VI (NM-ECC slabs) are almost the same as for Group II (SFRC slabs) but are about 17% less than SFRC strength.

In order to obtain the participation of reinforcement bars to the ultimate resisting load of NM-ECC unreinforced slabs (in Group V), three slabs with 0.5, 1, and 2 % of NM were used for comparison. Figure 4.5 shows that increasing the NM volume fraction from 0.5 to 2% increases the ultimate load by 42 % (compared with 38% in Group III and V). In other words, the effect of NM fibers has almost the same behavior for the reinforced and unreinforced slabs. Therefore, the differences between the resistance load of Group V and Group VI can be attributed to the reinforcing bars. It is shown that the participation of reinforcement bars is approximately 72% of the ultimate load whereas the matrix hold 28% of the ultimate load. This means that the matrix continues to hold the stress through the fibers in spite of that the cracks already took place. The process continues until the fibers are sliding due to weak bond or broken when the stress exceeds their yielding point. After this stage, the slab survives due to membrane action. The interaction among the f'_c , yield strength of the fibers, and the bond between the fibers and the matrix, have a major role in controlling the response of the structure (slab and column). Including the effect of $\sqrt{f'_c}$ shows that the participation of the matrix is higher in SFRC slabs. This is clearly shown in Figure 4.6, where the elimination of the square root of compressive strength shifts the $P_u / \sqrt{f'_c}$ of Group II. The results are almost within those of Group VI, in other words, the tolerance of 17 % that appears in Figure 4.5 does not exist in Figure 4.6.

Table 4.3 Strength and deformation characteristics of tested slabs

Specimens	$\mathbf{P_{cr}}$ (kN)	$\boldsymbol{\delta_{cr}}$ (mm)	$\boldsymbol{\psi_{cr}}$ (mrad)	$\mathbf{P_u}$ (kN)	$\boldsymbol{\delta_u}$ (mm)	$\boldsymbol{\psi_u}$ (mrad)	$\mathbf{P_{flex}}$ (kN)	$Pu_i/Pu_{(plain\ conc.)}$	$\mathbf{P_{u,test}/P_{flex}}$	$\mathbf{P_{cr}/P_{u,test}}$ (%)
P50	9.89	0.36	0.05	51.31	4.7	0.38	38.29	0.81	1.34	0.19
P60-11	16.94	0.41	0.05	74.89	3.02	0.2	70.25	1.18	1.07	0.23
P80	14.95	0.18	0.03	120.71	1.81	0.16	153.96	1.90	0.78	0.12
P60-10B	14.04	0.37	0.06	63.41	2.85	0.25	64.01	1.00	0.99	0.22
P60-10S	9.53	1.23	-	53.83	4.83	-	85.84	1.00	0.63	0.16
P60-8	14.10	0.55	0.07	58.87	3.02	0.29	51.16	0.93	1.15	0.24
SF0.5	14.05	0.80	-	71.44	5.74	-	86.89	1.33	0.82	0.05
SF1	17.38	0.82	-	94.78	4.76	-	87.40	1.76	1.08	0.18
SF1.5	31.40	1.35	-	92.83	5.74	-	87.51	1.72	1.06	0.34
NM0.5R	9.60	0.40	0.05	59.75	2.46	0.19	63.73	0.94	0.94	0.16
NM1R	6.06	0.47	0.03	65.52	4.40	0.23	63.67	1.03	1.03	0.09
NM2R	5.49	0.50	-	82.55	8.83	-	84.15	1.30	0.98	0.07
PV6	11.68	0.45	0.07	92.42	4.24	0.41	70.26	1.46	1.32	0.12
PV12	10.00	0.32	0.01	69.27	2.98	0.19	69.82	1.09	0.99	0.14
PP12	7.94	0.40	0.07	59.23	3.95	0.36	68.69	0.93	0.86	0.13
NM0.5	5.73	0.81	0.05	13.70	3.54	0.26	23.22	0.22	0.59	0.42
NM1	7.05	0.78	0.00	18.23	4.02	0.20	19.41	0.29	0.94	0.39
NM2	8.28	0.65	0.06	23.50	5.67	0.50	30.71	0.37	0.79	0.35
NM0.5P	9.53	0.55	-	56.33	4.18	-	83.37	0.89	0.68	0.17
NM1P	18.93	1.25	-	78.26	6.93	-	84.46	1.23	0.93	0.24
NM2P	18.80	1.16	-	80.27	6.54	-	84.15	1.27	0.95	0.23

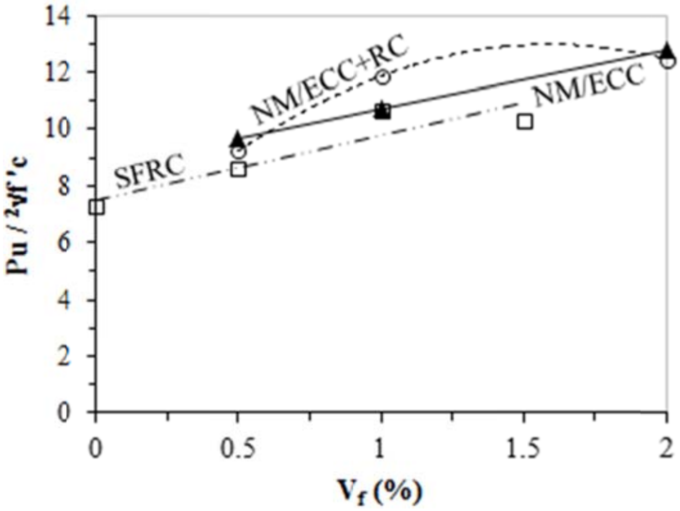

Figure 4.6 The effect of fiber volume fraction on the load resistance capacity by eliminating the effect of compressive strength in terms of square root

As mentioned in Section 4.2, the square root of compressive strength is adopted by many codes in a simple manner to ease calculations. ACI318 [19], CSA A23.3 [66], and AS3600 [94], in their shear provisions, the $\sqrt{f'_c}$ is correlated to the shear strength as corresponding to the tensile strength. Many researchers have employed the ACI318 equations to simulate the FRC slab column connections [45,70]. Linear regression formula from the experimental results of the current study, including the effect of NM-ECC on the ultimate punching strength, can be introduced as follows,

$$P_{\mathbf{u}} = (2\ V_f + 8.8)\ \sqrt[2]{f'_c} \qquad (4.\ 3)$$

Although Equation 4.3 is limited to the NM-ECC in the present work, it also can be used for SFRC as it is shown in Figure 4.6, where the SFRC's linear relation has almost the same slope of NM-ECC but with a 30% tolerance. Further details of SFRC slabs are discussed in Chapter 6.

In addition to its effect, fiber has different values of first crack load, where for the normal concrete slab, the first crack load P_{cr} was approximately 22 to 24% of the ultimate load. In the SFRC slab test, it is shown that the first crack in the slab with high SF content (V_f = 1 to 1.5%) was increased to be 34% of the ultimate load, whereas the slabs of NM-ECC has cracked at 16% of the ultimate load. Although the slabs in Group VI include NM-ECC in addition to normal concrete, it shows that the cracks developed firstly at normal concrete zone in 17 to 24% of the ultimate load, which is the first crack load at normal concrete slabs (Group I).

4.5 Comparing the Results with Different Codes Equations' Provisions

Bases on the code equations in Table 4.2, the tested slab are compared with the predicted punching shear strengths of slabs having the same properties. Figure 4.7 and Table 4.4 summarize these comparisons. Generally the predicted strengths were underestimated when compared to test results. All codes were conservative in predicting the strength of PV6. For example, Indian standards [95] recorded the lowest predicted value, and the highest predicted value for PV6 was 41% of the measured value and was calculated by Eurocode 2. The highest predicted values were calculated for specimen P60-10S, where the shear strength predicted using the Canadian code [66] was 76% of the measured value, while for the same specimens, the predicted value was 50% when IS456 was considered.

As aforementioned in Section 4.2, not all the code provisions account for the effect of reinforcement ratio (ρ). Two opposite opinions can be recognized according this point. The first assumes that the punching strength is a function of reinforcement ratio and size [53,93], while the second shows that there are no benefit from the increasing of ρ and d on the punching strength [19,66,81,94,95]. There are many considerations on the effectiveness of the effective depth and reinforcement ratio, each one have to be discussed separately.

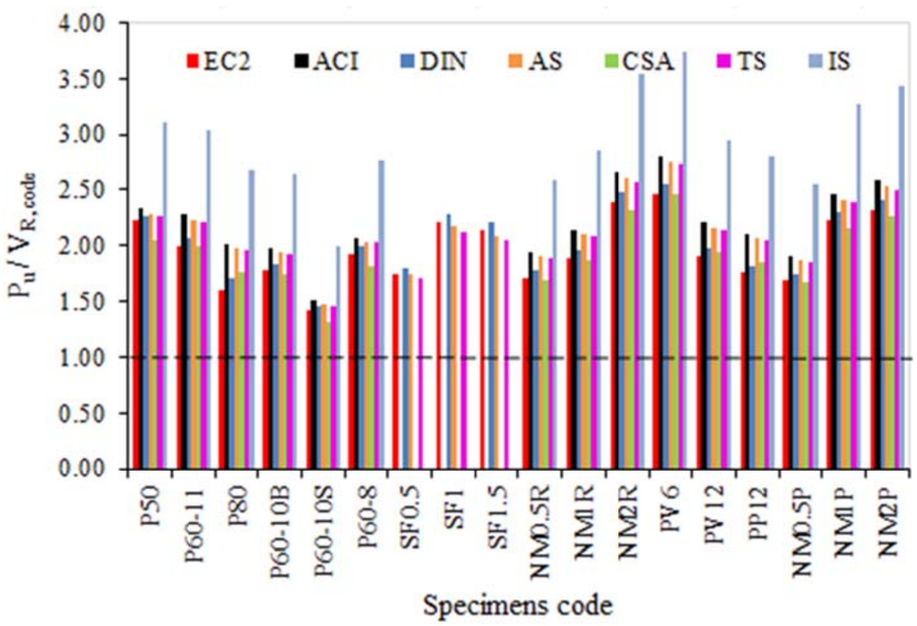

Figure 4.7 Experimental ultimate slab strength compared to different codes' predictions

Table 4.4 Nominal punching shear strength of tested slabs according to different codes' equations

Specimen	†$V_{R, Codes}$ (kN)							P_u / $V_{R\ code}$						
	EC2	**ACI**	**DIN**	**AS**	**CSA**	**IS**	**TS**	**EC2**	**ACI**	**DIN**	**AS**	**CSA**	**IS**	TS
P50	23	22.02	22.59	22.49	25.13	16.54	22.72	2.23	2.33	2.27	2.28	2.04	3.10	2.26
P60-11	38	32.92	36.23	33.61	37.56	24.71	33.95	1.99	2.28	2.07	2.23	1.99	3.03	2.21
P80	75	59.95	70.98	61.21	68.41	45.01	61.84	1.60	2.01	1.70	1.97	1.76	2.68	1.95
P10B	36	32.00	34.43	32.67	36.52	24.02	52.94	1.78	1.98	1.84	1.94	1.74	2.64	1.92
P10S	38	35.82	36.75	36.57	40.88	26.89	54.44	1.41	1.50	1.46	1.47	1.32	2.00	1.45
P60-8	31	28.38	29.45	28.98	32.39	21.31	61.58	1.93	2.07	2.00	2.03	1.82	2.76	2.02
SF0.5	41	_‡	39.67	40.94	_‡	_‡	42.55	1.74	_‡	1.80	1.74	_‡	_‡	1.72
SF1	43	_‡	41.46	43.71	_‡	_‡	43.35	2.21	_‡	2.29	2.17	_‡	_‡	2.13
SF1.5	43	_‡	41.87	44.35	_‡	_‡	56.86	2.14	_‡	2.22	2.09	_‡	_‡	2.05
NM0.5R	35	30.85	33.57	31.49	35.20	23.16	56.95	1.72	1.94	1.78	1.90	1.70	2.58	1.88
NM1R	35	30.60	33.39	31.25	34.92	22.98	49.43	1.89	2.14	1.96	2.10	1.88	2.85	2.08
NM2R	35	31.12	33.38	31.77	35.51	23.36	52.48	2.39	2.65	2.47	2.60	2.32	3.53	2.57
PV6	38	32.91	36.22	33.60	37.55	24.70	33.94	2.46	2.81	2.55	2.75	2.46	3.74	2.72
PV12	36	31.34	35.03	32.00	35.77	23.53	78.20	1.91	2.21	1.98	2.16	1.94	2.94	2.15
PP12	34	28.11	32.49	28.70	32.08	21.10	66.27	1.76	2.11	1.82	2.06	1.85	2.81	2.06
NM0.5P	33	29.49	32.17	30.11	33.66	22.14	45.05	1.69	1.91	1.75	1.87	1.67	2.54	1.86
NM1P	35	31.84	33.91	32.51	36.34	23.91	52.48	2.23	2.46	2.31	2.41	2.15	3.27	2.38
NM2P	35	31.12	33.38	31.77	35.51	23.36	54.83	2.32	2.58	2.40	2.53	2.26	3.44	2.50

†**EC2**; Eurocode 2[53], **ACI**; ACI318-14 [19], **DIN**; DIN1045-1[93], **AS;** AS3600 [94],
CSA; CSA A23.3 [66], **IS;** IS456 [95], **TS;** TS500 [81],

‡ Compressive strength exceeds the code limitation so the values are not given in table

4.5.1 Size effect

As mentioned previously, the slab thickness affects the ultimate load resistance of flat slab column joints. There is no unified formula for the size effect can be found in the codes. Many codes do not consider the size effect such as ACI318 [19], CSA A23.3 [66], AS3600 [94], TS500 [81], and IS456 [95], which indicates probable unsafe designs of these codes [103]. However, there are many interesting formulas (related to size effect) proposed by researchers can be found in literature. This disagreement on resolving this issue is due to several complex interacted parameters. Among these parameters is the type of the used concrete. As it is mentioned previously, high percentage of fine size aggregate was used in the present work, which is expected to change the brittleness behavior of the slabs under consideration, through decreasing the expected flaws in the matrix structure. The size effect in this quasi-brittle material is quite apparent. For this reason, three slabs of different thicknesses were tested and compared with slabs found in literature [103].

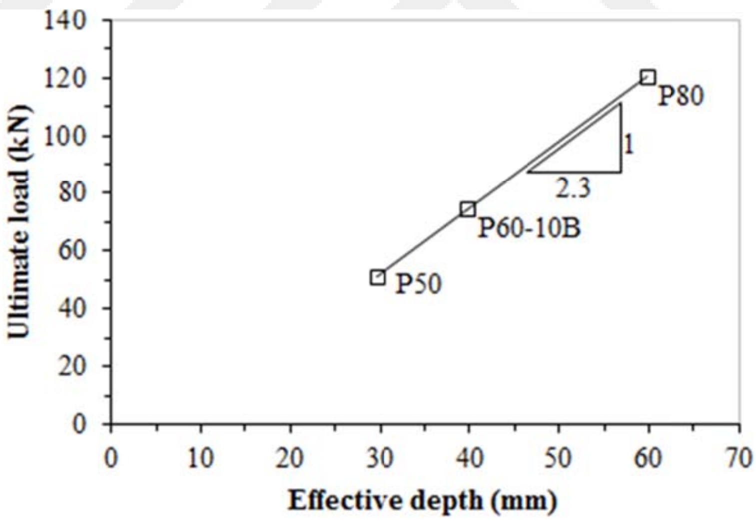

Figure 4.8 Effect of slab effective depth on the ultimate resistance of the tested slabs

Figure 4.8 shows the effect of the variation of slab thickness on the ultimate resistance, where increasing the effective depth by 20% increases the slab strength by 46 %, whereas increasing the slab thickness to 60 mm increases the slab strength by 135%. This means that the slab strength is related to the slab thickness by ($\Delta P_u/\Delta d$ = 1/2.3). It is worth to mention here that the compressive strength and reinforcement ratio are constant for all slabs (Table 4.1), therefore no need for eliminating the effect of compressive strength.

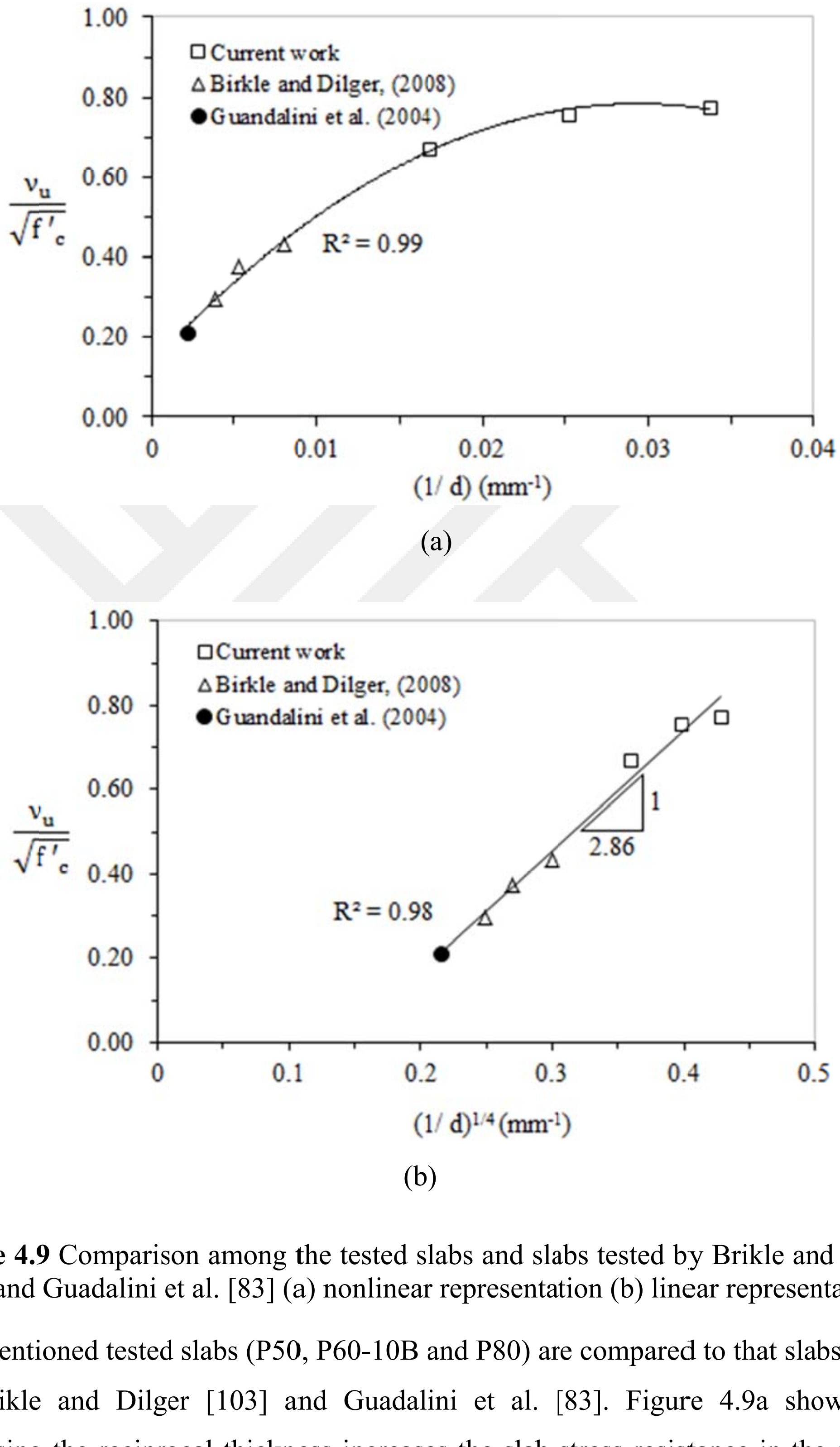

Figure 4.9 Comparison among the tested slabs and slabs tested by Brikle and Dilger [103] and Guadalini et al. [83] (a) nonlinear representation (b) linear representation

The mentioned tested slabs (P50, P60-10B and P80) are compared to that slabs tested by Brikle and Dilger [103] and Guadalini et al. [83]. Figure 4.9a shows that increasing the reciprocal thickness increases the slab stress resistance in the second order regression. In order to linearize the relationship, fourth root of the reciprocal effective depths $\left({}^{1}/_{d}\right)^{1/4}$ was used (see Figure 4.9b), which agrees with Regan's proposed relation [102]. It is shown that the ultimate slab stresses are related to the reduced reciprocal d by (1/2.86). The details of the specimens used in the comparison are listed in Table 4.5. Because of the differences in material properties, the ultimate stress was used and the square root of the f'_c was eliminated. Moreover, the critical shear perimeter (b_o) is based on ACI318 [19] provisions, which is distance d/2 from column face.

Table 4.5 Summary of specimens used in comparison from Brikle and Dilger 103] and Guadalini et al. [83]

Specimen	**c**	**h**	**d**	**b_o**(3)	**f 'c**	**ρ**	**v_u**
	mm	mm	mm	mm	MPa	%	MPa
S1(1)	250	160	124	1496	36.2	1.54	2.6
S7(1)	300	230	190	1960	35	1.3	2.22
S10(1)	350	300	260	2440	31.4	1.1	1.65
PG-3(2)	520	500	456	3936	32.4	0.32	1.18

(1) Data from Brikle and Dilger [103]
(2) Data from Guadalini et al. [83]
(3) Critical punching shear perimeter according to ACI318 [19]

4.5.2 Effect of reinforcement ratio

Three reinforcement ratios are investigated herein (0.9, 1.1, and 1.2%), the 0.9% is chosen in order to govern the low limitation of the ACI318 [19], while the 1.1% is chosen to govern the flexural design requirement (see Section 3.3.2).

The tested slabs showed that increasing ρ by 22% leads to increasing the punching shear strength by 8%, while increasing ρ by 33% increases the punching shear strength by 27%. Figure 4.10 shows an application of the different codes' equations using the properties of the experimental slabs in the current work, which are also compared with the results obtained from the tests. It is shown that most codes have almost similar predictions for the nominal punching shear strength of the mentioned slabs. These predictions increase smoothly with increasing ρ in approximately linear manner. However, the tested slabs showed that increasing ρ increases the strength of the slabs in a second order manner. Generally, all codes used to predict the punching capacity for the tested slabs underestimate the punching strength by percentages shown in Table 4.4.

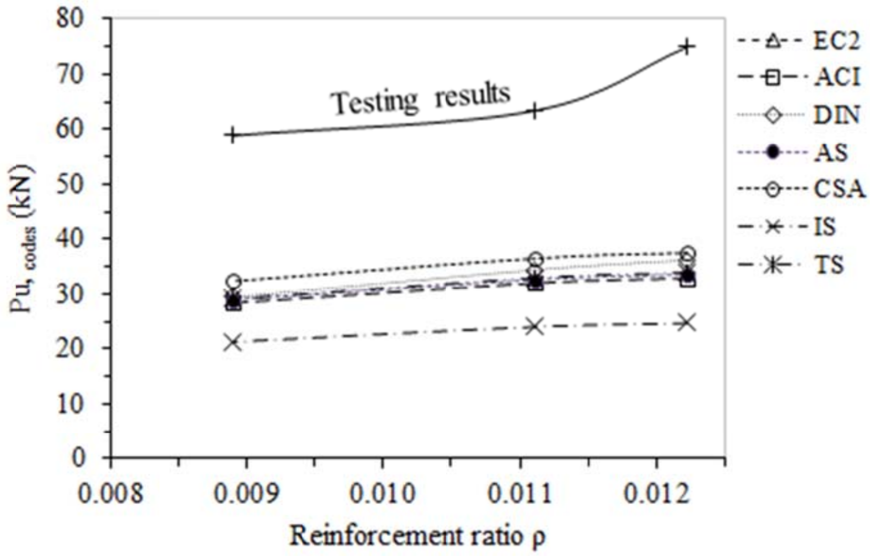

Figure 4.10 Predications of the punching resistance of the tested slabs according to different codes

4.6 Load-Deflection Behavior

As mentioned in Section 3.11.2, the load-deflection of the slabs is measured using both the cross head of the testing machine (δ_1) and the deflection of the tension face (δ_2) of the slab. In order to monitor the membrane action, all slabs were loaded beyond the maximum load up to failure, except for three slabs (NM1R, PV12, and PP12 where tests were stopped before collapse because the LVDT1 reached its end-stroke. Moreover, some of the load-deflection curves that were recorded from the load jack showed extraneous displacements that appear as offsets from the origin as shown in Figure 4.11. Therefore, the recorded load-deflection curves are adjusted according to ASTM C1550. The adjustment was done by extrapolating the linear portion of the load-deflection curve to the horizontal axis so that the extraneous displacements that associated to δ_1 are eliminated. It is worth to mention here that the development of δ_2 is not changed because there is no crushing shown in the slabs due to the penetration of the half balls.

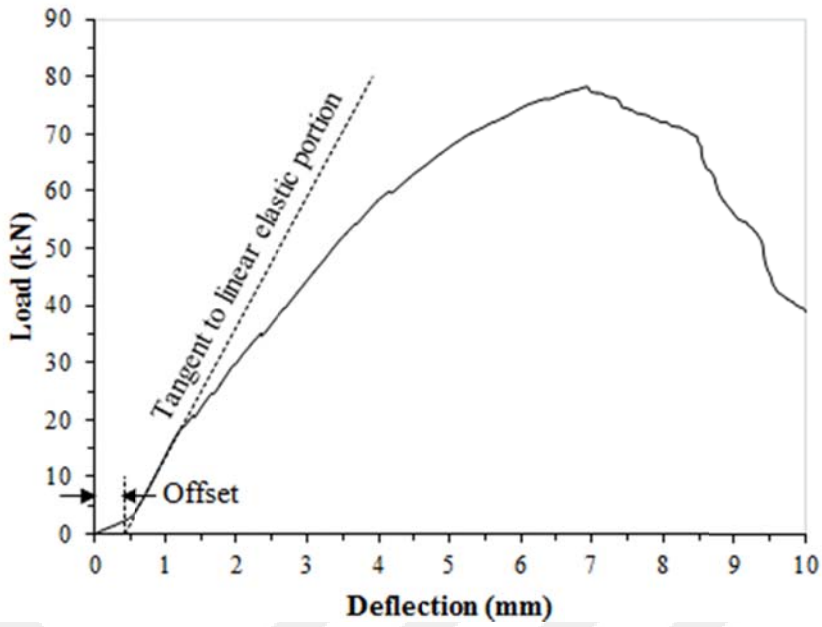

Figure 4.11 Typical Adjustment of the true load-deflection curve

The large amount of output data makes it possible to evaluate the different slab responses very carefully. The summary of the deflection at mid-slab corresponding to first crack and maximum loads are shown in Table 4.3. Generally, the load-deflection curves are characterized by four different stages as shown in Figure 4.12. These stages are introduced by many researchers [15,27,69.105]. The limitations of each stage are differing from slab to another based on concrete type used in construction. However, the transition between the first three stages is smooth and gradual because of the gradual cracking up to yielding stage. Stage I is limited by the origin and the first crack load ($\mathbf{P}_{cr}$). As mentioned previously, the first crack limit is characterized by the descending load values. In Stage I, the load increases linearly with respect to the deflection. Once the slab is cracked, the compression zone decreases and slab stiffness also decreases, which initiates Stage II. As the load increase, more cracks appear in the tension side. These cracks propagate from the slab center toward the slab edges so that the curve order is changing from its initial linear elastic sate to the flexural cracking up to P_y. For normal concrete, a short displacement plateau was observed. This happens along the stabilization of the crack formation before the load is raised again. Stressing the reinforcement bars continues up to the first bar yielding (Stage III). This stress spreads along the bar [105] and further decreasing in the slab stiffness is observed. The slab shows significant increasing in deflection rate; it is worthy to mention here that this stage was not reached in most specimens with low fiber contents. Moreover, the cracks start to appear in the compression face, while two cases of cracking development are observed in the tension face depending on the type of concrete and its fiber percentage. In the first case, the flexural cracks propagate beyond the punching shear cracks and reach the slab edges, while in the second case; the cracks propagate after the initiation of shear cracks. In this case, most flexural cracks do not reach the slab edges and are interrupted by shear cracks. For slabs with high fibrous content (2%), a deflection plateau of 5 mm was observed. At the Stage IV, the width of the circumference crack increases and the load resistance drops sharply for the slabs with normal and low fiber contents, whereas the resistance decreases gradually for the slabs with high fiber content (2%).

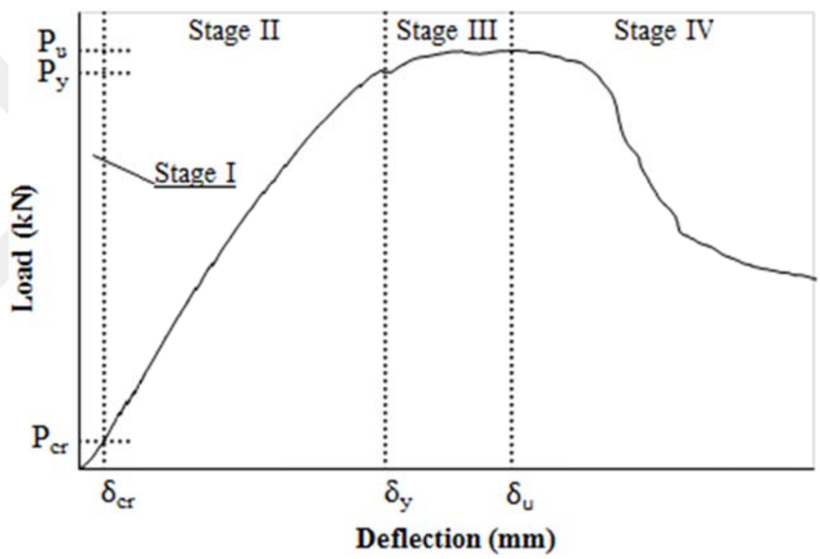

Figure 4.12 Typical flexural load-deflection diagram

The histories of deflection at the tension face (recorded from LVDT1) are illustrated in the following subsections. The first crack load and its corresponding deflection are characterized from the recorded data as the first descending in load values and visually observed with a magnifying glass, while the maximum resisting loads is directly obtained from the recorded data.

Following subsections discuss the effect of the parameters of each group based on the load-deflection relations obtained from the test.

4.6.1 Group I, Effect of reinforcement ratio and effective depth

Figures 4.13 and 4.14 show the typical load-deflection curves of the slabs in Group I (slabs made with normal concrete), where the effective depth (d) and the reinforcement ratio (ρ) are the main variables. The brittle behavior is clearly shown in specimens P60-11 and P80 where they show somewhat steeply load increments (compared to P50) before reaching the maximum load, and then the curve goes sharply. In P50, the curve increases smoothly (low load rate) up to maximum load and then show slightly softening up to failure. The high load rate in thick slabs lead to substantial reduction in deflection, where increasing the slab thickness by 20% and 60% leads to decreasing the deflection at maximum load by 36% and 61%, respectively.

Increasing ρ significantly affects the maximum load resistance and slightly affects the load rate ($\Delta P/\Delta\delta$) beyond P_{cr} and up to the maximum resistance load P_u, where specimen P80 (ρ = 0.9 %) showed a higher load rate than the other two slabs. This is not surprising, because the slabs with higher ρ introduce higher resistance due to their high reinforcement area and high bond with the surrounding matrix that prevents the reinforcement bars from sliding.

The effect of sliding of reinforcement bars is clear, where P60-10S shows less resistance to the applied load up to the maximum resistance load due to the sliding in reinforcement bars. However, beyond the failure load, both slabs show the same descending rate. It is worth to mention here, that the development length required for bars was calculated according to ACI 318 [19], where l_d equal to,

$$l_d = \left(\frac{0.24 f_y \psi_t \psi_e}{1.4 \lambda \sqrt{f'_c}} \right) d_b \tag{4.4}$$

where ψ_t, ψ_e, and $\boldsymbol{\lambda}$ are factors depend on the reinforcement location, reinforcement coating and concrete weight, respectively. In the present work and based on ACI318 requirements, all factors were taken as 1.

The l_d required for P10S is 81 mm. Four bars out of seven are with l_d less than 81 mm. It is shown that the reduction of l_d by 37% in the present work causes led to 17% reduction in the resistance load. Moreover, the term ($\Delta P/\Delta\delta$) equals 16 kN/mm for P60-10B, whereas ($\Delta P/\Delta\delta$) equals 11 kN/mm for P10S. The area between the two curves can be considered as a fictitious energy absorption that is discussed in Section 4.8.

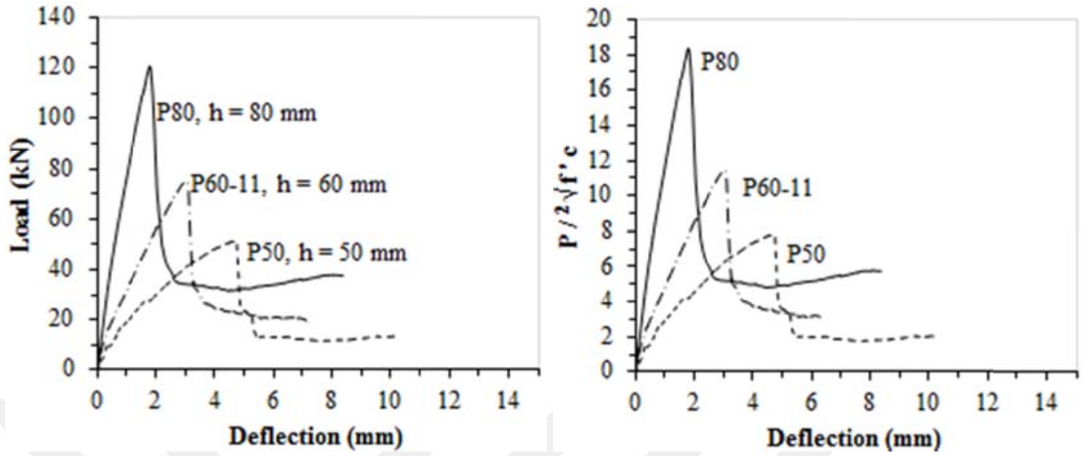

(a) (b)

Figure 4.13 Load-deflection curves of Group I (varying depth) (a) f'_c is not considered (b) effect of f'_c is included

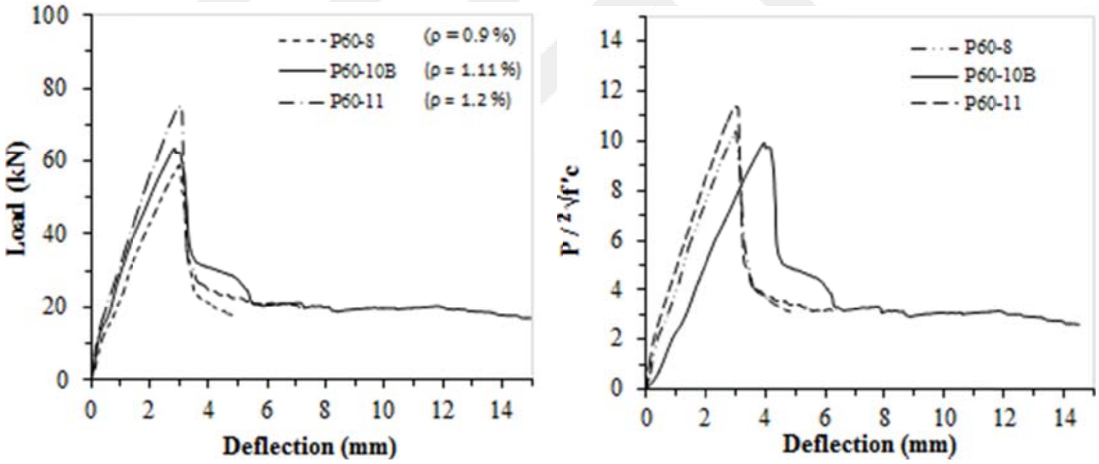

(a) (b)

Figure 4.14 Load-deflection curves of Group I (varying reinforcement ratio) (a) f'_c is not considered (b) effect of f'_c is included

4.6.2 Group II, Effect of steel fiber volume content

Table 4.3 and Figure 4.15 show that the inclusion of the SF increases the load rate ($\Delta P/\Delta\delta$) up to the maximum load compared to the control slab P60-10S. Slab SF1.5 shows a small plateau after the first yield, and the load rate was larger than in the other specimens. The slab response due to applied load decreases with decreasing the SF percentage compared to the steep descent of the control slab (P60-10s). These responses are related to the high ductility of the SFRC that incorporate high fiber contents (to be discussed in Section 4.5).

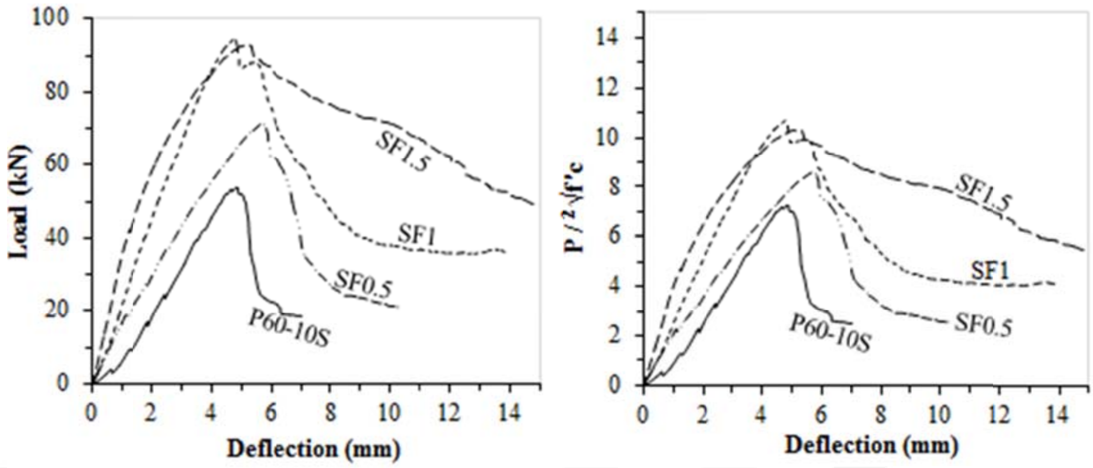

Figure 4.15 Load-deflection characteristics for Group II

4.6.3 Group III, Effect of nylon-monofilament fiber content

From Figure 4.16, it is shown that the use of nylon-monofilament fiber with ECC (NM-ECC) has significantly enhanced the load-deflection behavior of slab specimens. The slabs with 0.5 and 1.0% of NM showed the same increasing rate compared to plain concrete up to the maximum load, while short displacement plateau beyond the maximum load was shown in slab with 1% NM. However, the effect of ECC of 2% of NM is clear on the maximum load and the post-peak load stage. In this stage, the slab deflected about 83% of the deflection at the maximum load, which occurred before the membrane action took place.

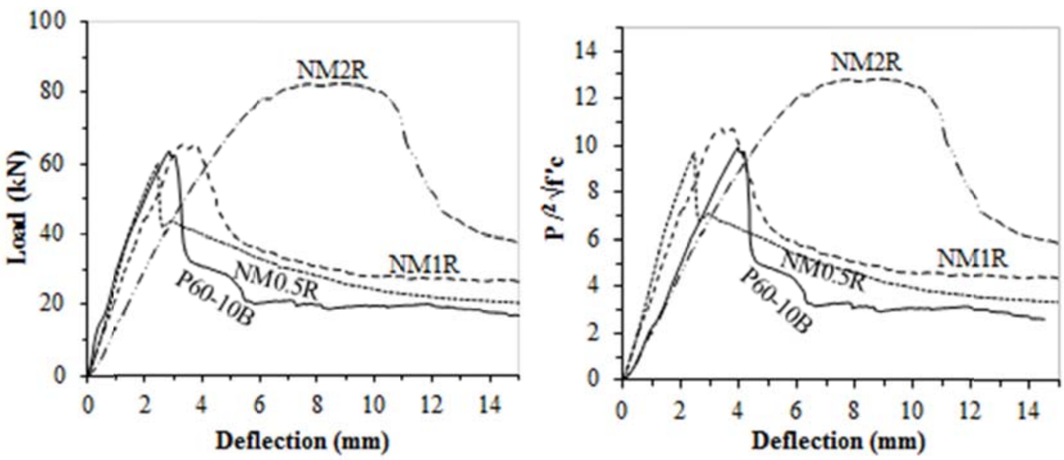

Figure 4.16 Load-deflection curves of Group III

4.6.4 Group IV, Effect of fiber type

In Group IV, five types of fibers are compared. All the fiber volume fractions were 2% except the specimen SF1.5 where 1.5% SF was used. This is because many researchers showed that the 1 to 1.5% of SF content shows the threshold of SFRC. The load-deflection behavious of the three slabs of different fibers (SF, NM, and PV6) were enhanced due to fiber effect and all types of fibers showed high continuity after maximum resistance. Figure 4.17 shows the comparison results among the four mixtures. Both SF1.5 and PV6 showed significant strength enhancement. However, NM2R was the best slab related to post-peaking load. The judgments of the ductility and toughness are shown in Section 4.5.

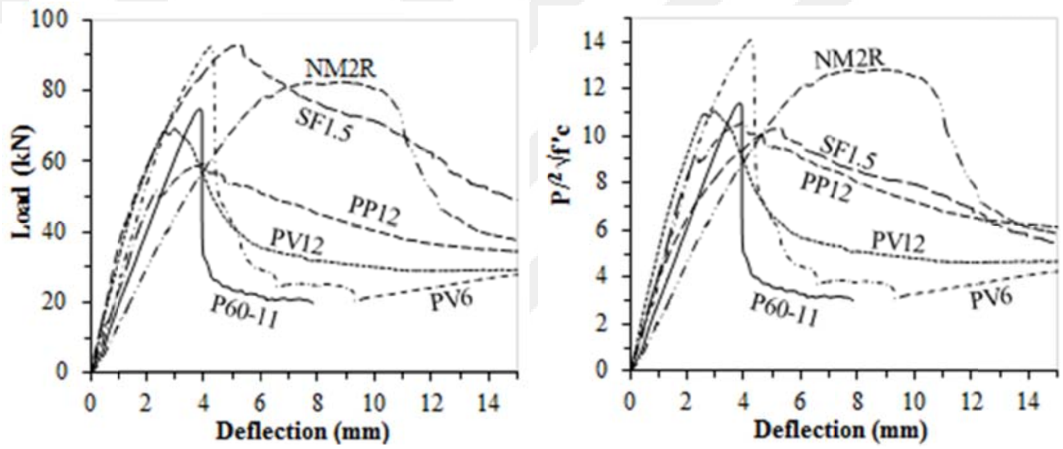

Figure 4.17 Load-deflection curves of Group IV

4.6.5 Group V, Effect of nylon-monofilament fiber on unreinforced slabs

As mentioned in Section 4.2, these slabs are used to determine the participation of the conventional reinforcement bars in NM-ECC slabs. Figure 4.18 shows the load-deflection curves of the three percentages of the used fiber. The unreinforced fibrous slabs showed high continuity and high displacement hardening due to multi-cracks development. The maximum resistance load was gained by the NM2, which was 37% of that of the normal RC slab (P60-10B).

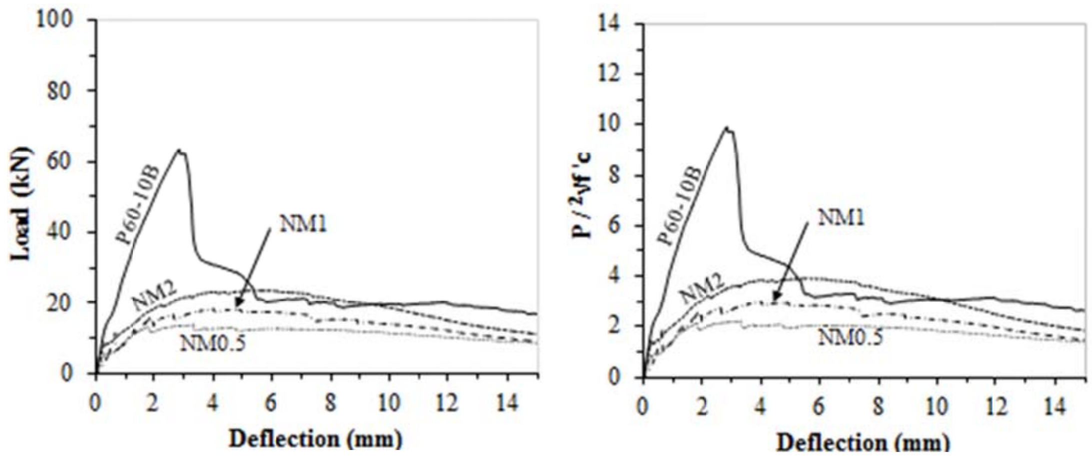

Figure 4.18 Load-deflection curves of Group V

4.6.6 Group VI, Effect of fiber congestion in the D-zone

Figure 4.19 shows that providing NM-ECC near the column head within the D-zone (for a distance of two times the slab effective depth) was as effective on maximum load capacity as providing NM-ECC in the whole slab size. Moreover, the deflection of the slab with 1% NM-ECC was significantly improved at post-peak load. This is because the energy is absorbed by the NM-ECC before extending the stress to the normal concrete.

The red lines in Figure 4.19 refer to the loads divided by the square root of the normal concrete compressive strength, which result in curves with low ultimate load but with the same ductility behavior as in the black lines curves.

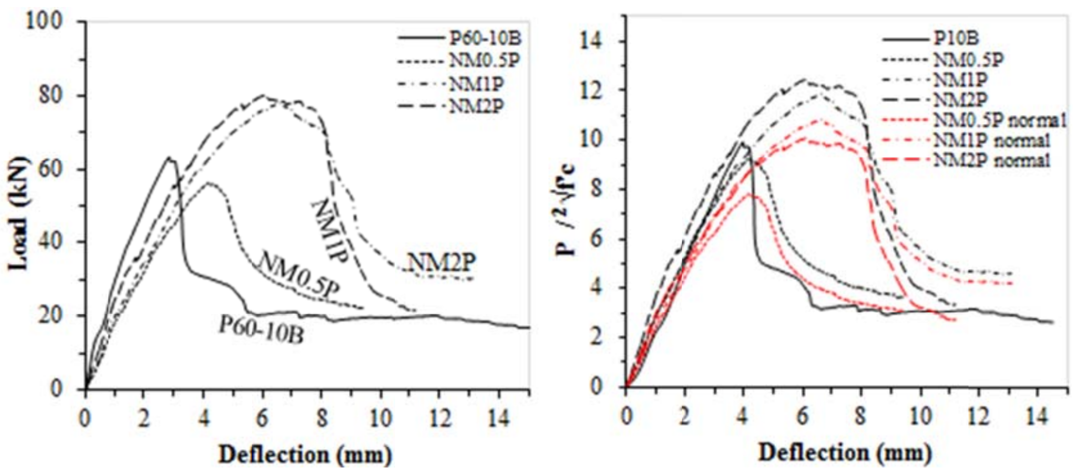

Figure 4.19 Load-deflection curves of Group VI

4.7 Ductility and Energy Absorption Capacity

In spite of that the strength is a simple tool to describe the load bearing capacity of brittle materials, while the quasi-brittle materials such as concrete resist the reduced load down to a considerable strain; this response is termed as strain softening. The strength is not enough to describe the response of the structure, therefore, there is other important structural characteristics are in need, such as ductility and energy absorption. The ductility of the members can be defined according to ACI Terminology [1] as "The ability of a material to undergo large permanent deformation without rupture". Similarly, toughness is defined as "The ability of a material to absorb energy without rupturing", or toughness can be defined as the amount of energy per unit volume of material required to rupture the material. There are interesting arbitrary procedures reported in the literature. Criswell [106] idealized the load-deflection curve by an elasto-plastic relation. Pan and Moehle [107] used this procedure when they worked on slabs exposed to lateral load from the end of the column. The elastic portion of the idealized relation is a secant start from the origin and intersects with the load-deflection curve at ($2/3\ P_u$), whereas the idealization of the plastic portion is a horizontal line passes through the maximum load and intersects with the secant line at a point named as the effective yield displacement (D_y). They defined the displacement ductility (μ) as the ratio of the displacement that corresponds to the maximum load (D_u) to the effective yield displacement (D_y). ($\mu = D_u / D_y$). Polak [108] measured the ductility of a flat plat-column joint as the ratio of the deflection corresponding to the first yield of reinforcement to that at ultimate resistance load. According to later definition, the yield displacement is often hard to capture because of many reasons such as the nonlinearity of the materials (like that used in the present work) or because many moment stages are required for bars to create a plastic hinges (such as in slabs). A different procedure was applied by Swamy and Ali [69]. They continued the applying load until the resistance reached 25% of the maximum load, then the ductility is calculated as the ratio of deflection at 25% (at descending zone) to the deflection at the first crack (δ_{cr}). This percentage was chosen so that the effect of membrane action of their work is included.

Determination of the ductility and energy absorption in the present research is similar to that used by Swamy [69]. However, the deflection and the area under the curve are taken so that the load at the descending zone equals to 50% of the maximum resistance load. This percentage is based on the effect of membrane action and the displacement hardening observed in the present work (as it is shows in Section 4.6). Figure 4.20 illustrates the concept of the two mentioned procedures. Moreover, Figure 4.21 illustrates the mentioned area under the load-deflection curve up to 50% of the maximum load.

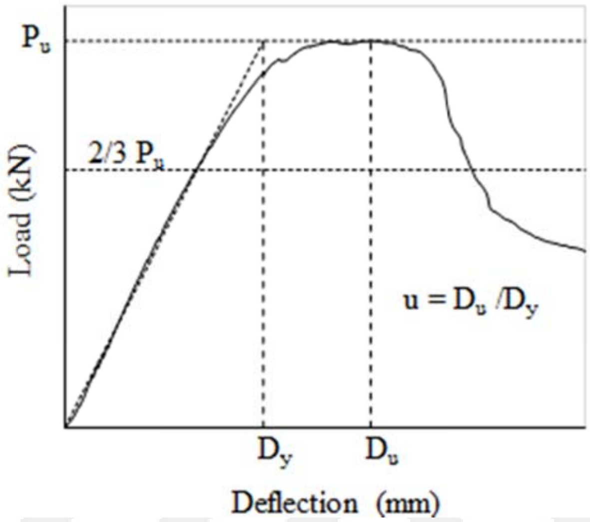

Figure 4.20 The displacement ductility according to Pan and Moehle [107]

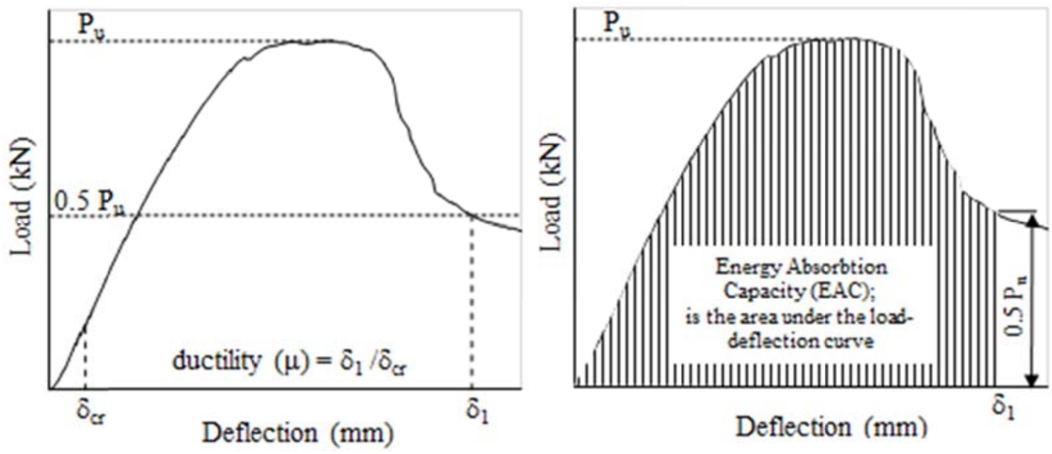

Figure 4.21 Determination of the ductility and energy absorption from the load-deflection curve up to 50 % of the maximum load

Table 4.6 summarizes the calculated ductility. For comparison purposes, each slab ductility (μ_i) in the group is normalized by its corresponding control slab of normal concrete.

Although increasing the slab thickness increases the load resistance, however, the deflection corresponding to the maximum load is decreased (see Figure 4.9). In other words, the ductility is decreasing with the increase of the slab thickness. The determined ductility of the slabs in Group 1 shows that the decreasing of the slab thickness from 80 to 50 mm (about 38%) leads to the increasing of the ductility by about 12 %. Whereas, decreasing ρ from 1.2 to 1.1% increases the ductility by 26%. Further increasing can be obtained by un-bent the reinforcement bars as in slab P60-10S, where the ductility is increased by 183%. The later increase can be due to bar sliding that weakens the stress transformation from the concrete to the bars.

Fiber in concrete and ECC significantly increase the ductility, where using PVA or PP fiber (both of 12 mm length) in ECC matrix increases the ductility by 580 and 508% (compared to the P60-10B), respectively. However, Shorter PVA (6 mm) increased the ductility by only 13%. In the same manner, NM-ECC also showed a significant improvement in the ductility of ECC by 78, 162 and 166% for the three percentages of 0.5, 1.0, and 2.0%, respectively. Inclusion the NM-ECC in critical zone improved the ductility by 21%. The low improvement in ductility in this group compared to Group III is because of the presence of the normal concrete out of the critical zone. Therefore, the NM-ECC in the critical zone is governing the initiation of the first crack and its corresponding deflection; while the normal concrete is govern the failure deflection. The mechanical behavior is discussed in Chapter 7.

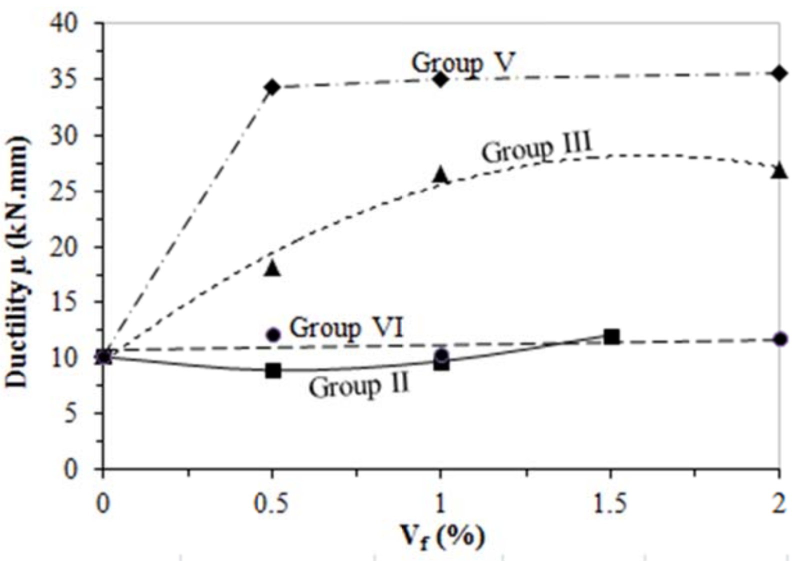

Figure 4.22 Development of the ductility with increasing fiber volume fraction

Figure 4.22 shows the development of slabs ductility by increasing the fiber volume fraction. The lowest improvement in ductility is shown in SFRC slabs, where the slab includes 1.5% of SF, which increased by only about 19% compared to the slab P60-10B. This is because of the high elastic modulus of the SF (200 GPa) compared to other fibers that does not exceed 34 GPa. Moreover, the bond of the SF, is high because of the hooked ends, which leads to less elongation compared to other fibers that are partially slide and elongate.

For all tested fibrous concrete slabs, the fiber shows significant improvement in the energy absorption compared to the normal concrete. Table 4.6 summarizes the EAC for test specimens. For all tested slabs and EAC as unity for the normal concrete, the slab P60-10B is used as a reference specimen for comparison. It is shown that the SFRC with 1.5% SF dramatically increases the EAC by 825%. If this percentage is compared with the test results obtained by Swamy [69], which was 110 % improvement and obtained for slabs that are reinforced by both SF and shear reinforcement, one may conclude that this high improvement is implicitly due to the inclusion of high fine particles content in concrete, which is apply a bond interaction with the fibers and enhancing the stresses flow through the particles.

Other fibers (PVA, PP, and NM) also show significant enhancements, for instance, PVA increased the EAC by 122 and 156% for 6 and 12 mm fiber length, respectively, while PP of 12 mm length increased the EAC by 470%. The best improvement among the used synthetic fibers was 580 %, which was found for NM reinforced slab that contains 2% fiber. This percentage improvement is greater than those obtained from slabs of NM only in the critical zone, where the EAC was improved by 344% in the slab NM2P.

Figure 4.23 shows the development of energy absorption capacity (as unity for plain concrete slab) with increasing the fiber volume fraction.

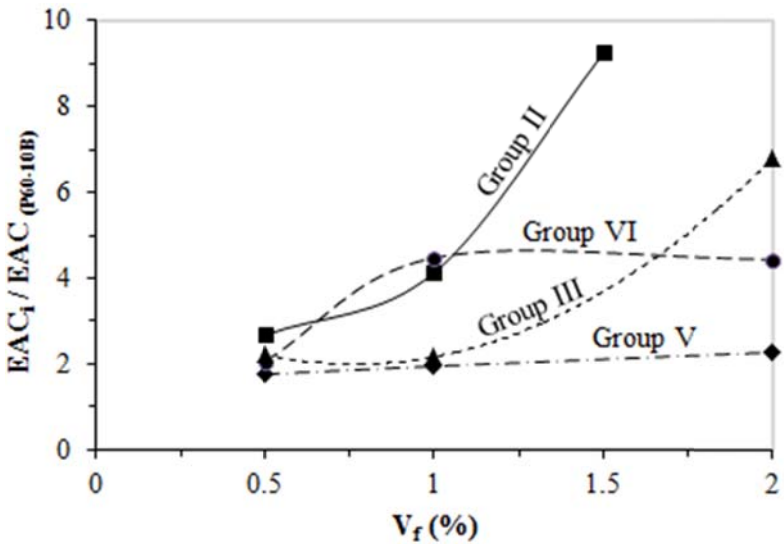

Figure 4.23 Development of energy absorption capacity with increasing fiber volume fraction

4.8 Membrane Action

As mentioned in Section 4.4, the test was continued beyond the maximum load. In this case, the transverse flexural reinforcing bars are restraining the concrete at the reinforcement plane, so that the slabs can survive after the punching takes place. This action is known as membrane action due to the bars' dowel forces.

Table 4.6 and Figures 4.24 to 4.30 shows that the inclusion of any type of fibers is enhances the maximum slab resistance load due to the increased ductility of the FRC slabs. All slabs of plain concrete behaved in a brittle manner where the resistance load dropped suddenly. The resistance load in the slab P8 (with ρ = 0.9 %) and the slab P10S (with ρ = 1.1 %, un-bent reinforcement) dropped to about 40 and 47% of their maximum load resistance, respectively. The slab P10B (with ρ = 1.1%, bent reinforcement) was survived after punching took place. The membrane action was 50% of its maximum load. These values are higher than those reported by Swamy [69] and Criswell [106]. This is may be due to the high percentages of fine aggregate used in the mix.

Fibrous concrete in slab-column connection shows significant increasing in membrane action, that affected the slab strength. For the SFRC slabs, the membrane action was about 88 to 92%. Similar values are reported for the slabs NM1P and NM2P (slabs include NM-ECC in critical zone). However, for full NM-ECC slabs

(NM0.5R, NM1R, and NM2R), the values ranged between 72 to 77% of the maximum load. Moreover, these values decreased for slabs containing polypropylene (PP) and polyvinyl alcohol (PVA) by 37 and 49%, respectively.

Table 4.6 Strength and deformation characteristics of tested slabs

Specimens	**V_f** (%)	**P_u** kN	**$\delta_{(at\ P=0.5Pu)}$** mm	**μ^***	**$\mu_i/\mu_{(P60-10B)}^{\ddagger}$**	**Energy Absorption (EAC_i)** kN.mm	**$\left(\frac{EAC_i}{EAC_{(P60-10B)}}\right)^{\dagger}$**
P50	0	51.31	4.89	13.64	1.35	158.67	1.10
P60-11	0	74.89	3.26	8.00	0.79	144.02	1.00
P80	0	120.71	2.14	11.98	1.18	151.62	1.05
P60-10B	0	63.41	3.72	10.13	1.00	114.54	1.00
P60-10S	0	53.83	5.54	22.66	2.24	140.77	1.23
P60-8	0	58.87	3.42	6.18	0.61	153.29	1.34
SF0.5	0.5	71.44	7.11	8.93	0.88	306.60	2.68
SF1	1	94.78	8.03	9.74	0.96	473.63	4.13
SF1.5	1.5	92.83	16.39	12.10	1.19	1060.07	9.25
NM0.5R	0.5	59.75	7.18	18.06	1.78	254.03	2.22
NM1R	1	65.52	7.07	26.53	2.62	247.73	2.16
NM2R	2	82.55	13.42	26.98	2.66	779.15	6.80
PV6	2	92.42	5.19	11.46	1.13	253.84	2.22
PV12	2	69.27	21.91	68.88	6.80	293.26	2.56
PP12	2	59.23	24.66	61.57	6.08	653.19	5.70
NM0.5	0.5	13.70	19.49	34.33	3.39	199.82	1.74
NM1	1	18.23	16.06	35.04	3.46	225.35	1.97
NM2	2	23.50	14.33	35.63	3.52	261.56	2.28
NM0.5P	0.5	56.33	6.76	12.21	1.21	236.27	2.06
NM1P	1	78.26	9.68	10.33	1.02	513.50	4.48
NM2P	2	80.27	8.95	11.75	1.16	508.80	4.44

* Ultimate ductility deflection at 50 % of peak load
‡ $\mu_i / \mu_{(P60-10B)}$ as unity for normal concrete slab P60-10B
† $EA_i / EA_{(P60-10B)}$ is the energy absorption as a unity for normal concrete slab P60-10B

4.9 Cracks Pattern and Failure Mode

Almost all slabs are reinforced by the same reinforcement ratio of the control slab, which is designed to fail due to low shear resistance as it is discussed in Chapter 3. Moreover, no cracks were observed in the compression face of all slabs. The punching shape, size, and angle of failure are varying considerably. Table 4.7 and

Figures 4.24 to 4.30 show the details of these mentioned parameters. The control slabs with ρ = 1.1 and 1.2% failed suddenly in punching shear. The punched part showed multi radial cracks passed uncompleted circular surfaces, whereas slab P60-8 (ρ = 0.9) and slab P60-10S (with un-bended bars' ends) failed gradually in flexural punching with multi radial cracks and nearly square punching surface. The varying thickness has not affected the angle of failure, where the slabs P50, P60-11 and P80 showed angles ranging between 16 to 20 degree, with slightly less angle than that found by Swamy [69] (24 degree), while the angles of failure of slabs P60-10S, and P60-8 were 36 and 29 degrees, respectively. The multi-cracks are showing in this group may be due to the inclusion of high percentage of fine aggregate, which enhances the stress distribution along the slab thickness. Moreover, the increasing of the failure angle of the slabs with 0.9% reinforcement ratio and the slab with un-bent bar's ends may be due to the low transferred stresses to the reinforcement compared to the previous slabs. Only slab P60-10B showed spalling where the spalled area was 7% of the total slab area. Approximately half of the spalled area was within the punching area, whereas the remaining spalling area was out of the punching area extending up to one slab edge.

The using of ECC matrix in slabs not only enhanced the ultimate resistance load, but also changed the failure shape and reduced the punching surface as in NM2R and PP12 where the angles of failure were 54 and 35 degrees, respectively.

The number of cracks in fibrous slabs is greater and the crack opening is less. Interesting crack pattern can be shown in slab PP12, where the radial cracks extend from the edge of the punching surface to the edges of the slab. Moreover, there was a white color circular area surrounding the punching surface of slab PP12, which distances 116 mm from the column face. This circular area refers to the high strain resistance in this area, which may develop another punching surface. This means that the fibers are actively transferring the stresses even after the slab is extensively cracked. This case is also shown in the slab NM2R where two failure surfaces were shown.

Pure flexural failure with fully development yield line is shown in slabs of Group V. For the slab NM-ECC with 0.5% of fiber content, the crack pattern was same as expected in Figure 3.13. Increasing the fiber content to 2%, significantly increased the yield lines and the two expected patterns in Figures 3.13 and 3.14 are appearing.

Table 4.7 Failure mode, shape, and radius of punching failure

Specimen	**V_f** (%)	**failure mode**	**failure shape**	**$r_{0, test}$** (mm)	**Distance from column face in term of d**	**Punching angle of failure** (deg)
P50	0	FP	circular	173	4.9d	20
P60-11	0	FP	circular	197	4.3d	18
P80	0	P	circular	190	2.7d	16
P60-10B	0	P	circular	199	4.3d	17
P60-10S	0	F	square	112	2.2d	36
P60-8	0	F	square	114	2.2d	29
SF0.5	0.5	FP	square	109	2.1d	29
SF1	1	FP	circular	189	4.2d	18
SF1.5	1.5	FP	circular	200	4.5d	17
NM0.5R	0.5	F	square	90	1.6d	35
NM1R	1	FP	circular	164	3.4d	21
NM2R	2	F	square	45	0.5d	54
PV6	2	P	circular	166	3.5d	20
PV12	2	P	circular	192	4.1d	17
PP12	2	FP	square	90	0.7d	47
NM0.5	0.5	F	_	_	_	_
NM1	1	F	_	_	_	_
NM2	2	F	_	_	_	_
NM0.5P	0.5	FP	circular	198	4.4d	17
NM1P	1	FP	circular	177	3.9d	20
NM2P	2	FP	circular	189	4.2d	18

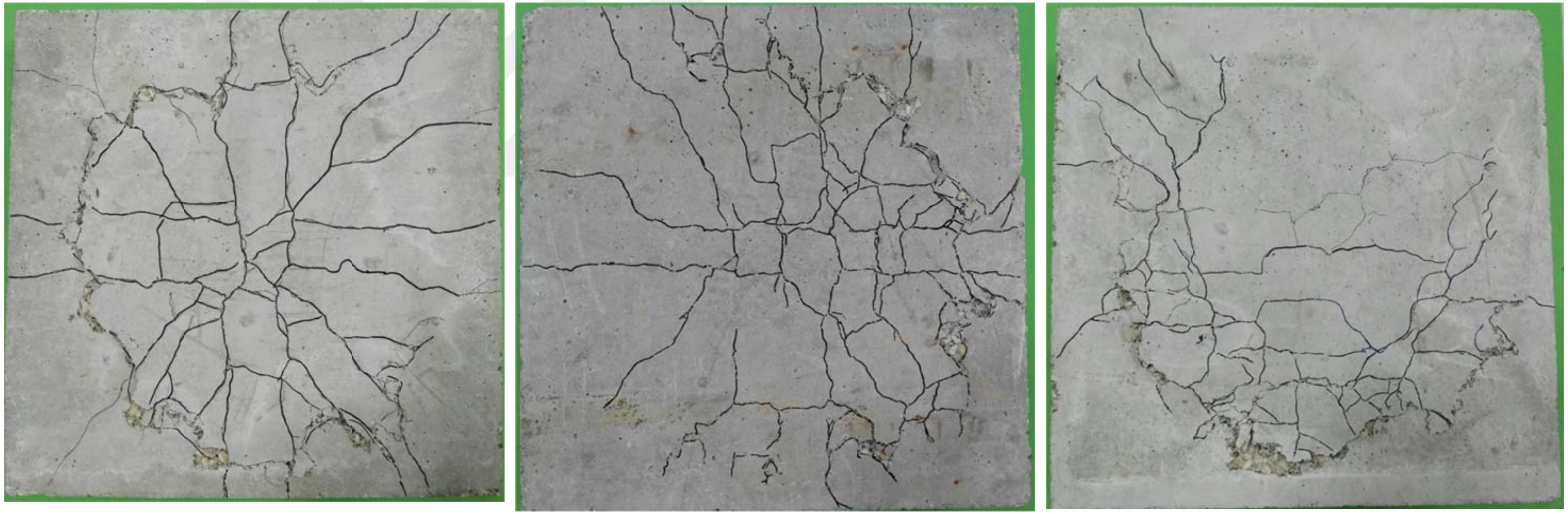

Specimen code; P50
P_u = 51.31 kN
f'_c = 43.20 MPa
h = 50 mm
Normal concrete

Specimen code; P60-11
P_u = 74.89 kN
f'_c = 43.20 MPa
h = 60 mm
Normal concrete

Specimen code; P80
P_u = 120.71 kN
f'_c = 43.20 MPa
h = 80 mm
Normal concrete

Figure 4.24 Crack patterns of tested flat slabs in Group I (Effect of thickness on the behavior of normal concrete RC flat plate-column connection)

Specimen code; P60-10B
P_u = 63.41 kN
f'_c = 40.83 MPa
ρ = 1.1 %
Normal concrete

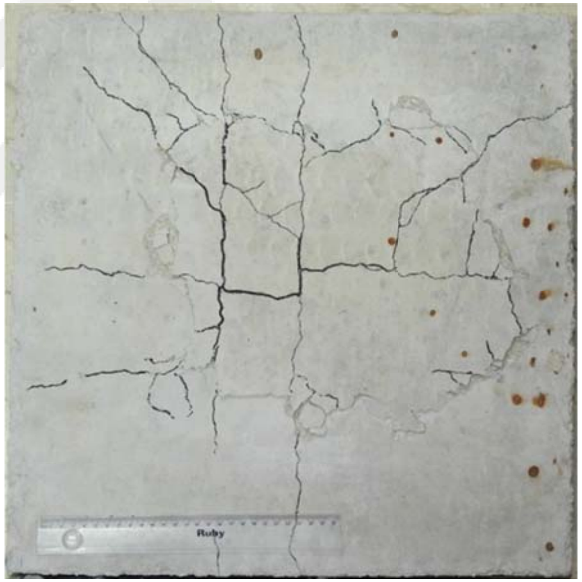

Specimen code; P60-10S
P_u = 53.83 kN
f'_c = 55 MPa
ρ = 1.1 %
Normal concrete

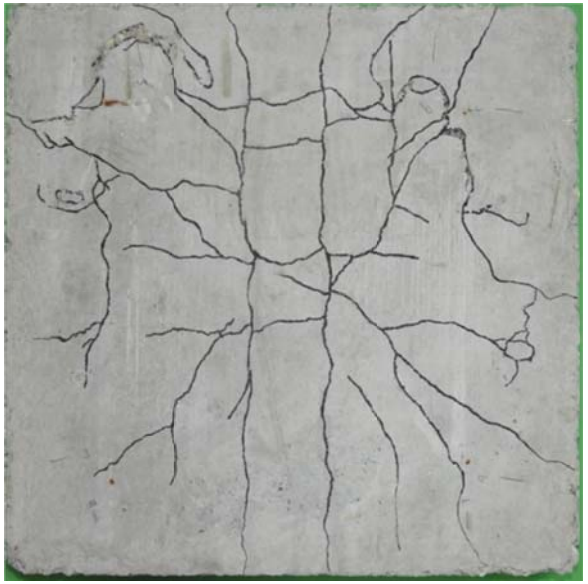

Specimen code; P60-8
P_u = 58.87 kN
f'_c = 32.12 MPa
ρ = 0.9 %
Normal concrete

Figure 4.25 Crack patterns of tested flat slabs in Group I (Effect of reinforcement ratio on normal concrete RC slabs)

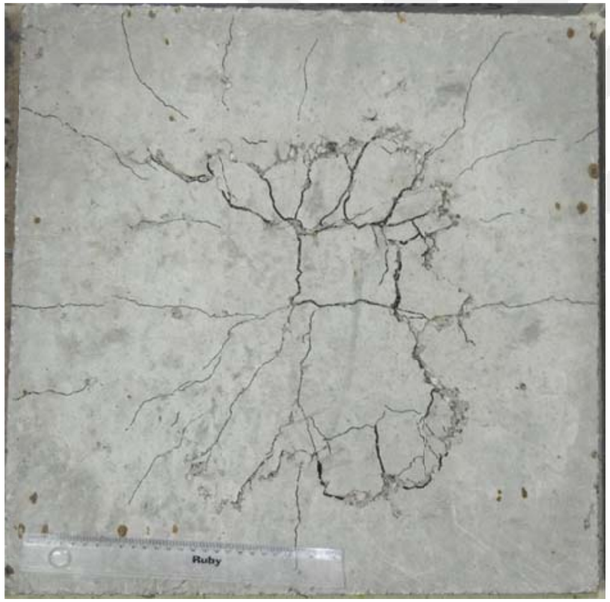

Specimen code; SF0.5
P_u = 71.44 kN
f'_c = 68.92 MPa
ρ = 1.1 %
V_f = 0.5 % of SFRC

Specimen code; SF1
P_u = 94.78 kN
f'_c = 78.56 MPa
ρ = 1.1 %
V_f = 1 % of SFRC

Specimen code; SF1.5
P_u = 92.83 kN
f'_c = 80.88 MPa
ρ = 1.1 %
V_f = 1.5 % of SFRC

Figure 4.26 Crack patterns of tested flat slabs in Group II (Effect of fiber dosages on SFRC slabs)

Specimen code; NM0.5R
P_u = 59.75 kN
f'_c = 37.94 MPa
ρ = 1.1 %
V_f = 0.5 % of NMECC

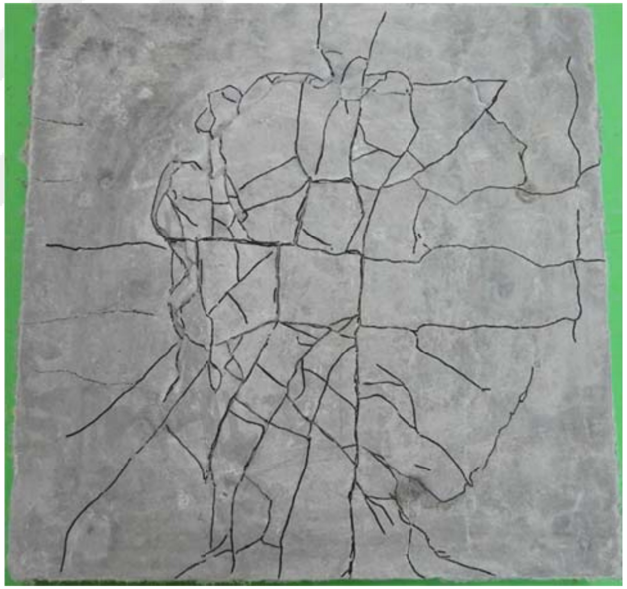

Specimen code; NM1R
P_u = 65.52 kN
f'_c = 37.35 MPa
ρ = 1.1 %
V_f = 1 % of NMECC

Specimen code; NM2R
P_u = 82.55 kN
f'_c = 41.5 MPa
ρ = 1.1 %
V_f = 2 % of NMECC

Figure 4.27 Crack patterns of tested flat slabs in Group III (Effect of fiber dosages on NMECC - slabs)

Specimen code; PV6
P_u = 92.42 kN
f'_c = 43.18 MPa
ρ = 1.2 %
V_f = 2 % of PVA6 mm-ECC (RC slab)

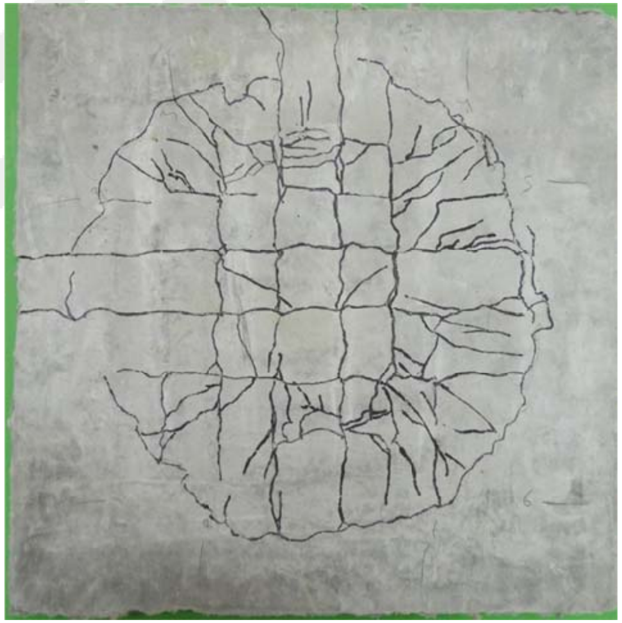

Specimen code; PV12
P_u = 69.27 kN
f'_c = 39.18 MPa
ρ = 1.2 %
V_f = 2 % of PVA12 mm-ECC (RC slab)

Specimen code; PP12
P_u = 59.23 kN
f'_c = 31.51 MPa
ρ = 1.2 %
V_f = 2 % of PP12 mm-ECC (RC slab)

Figure 4.28 Crack patterns of tested flat slabs in Group IV (Effect of fiber types)

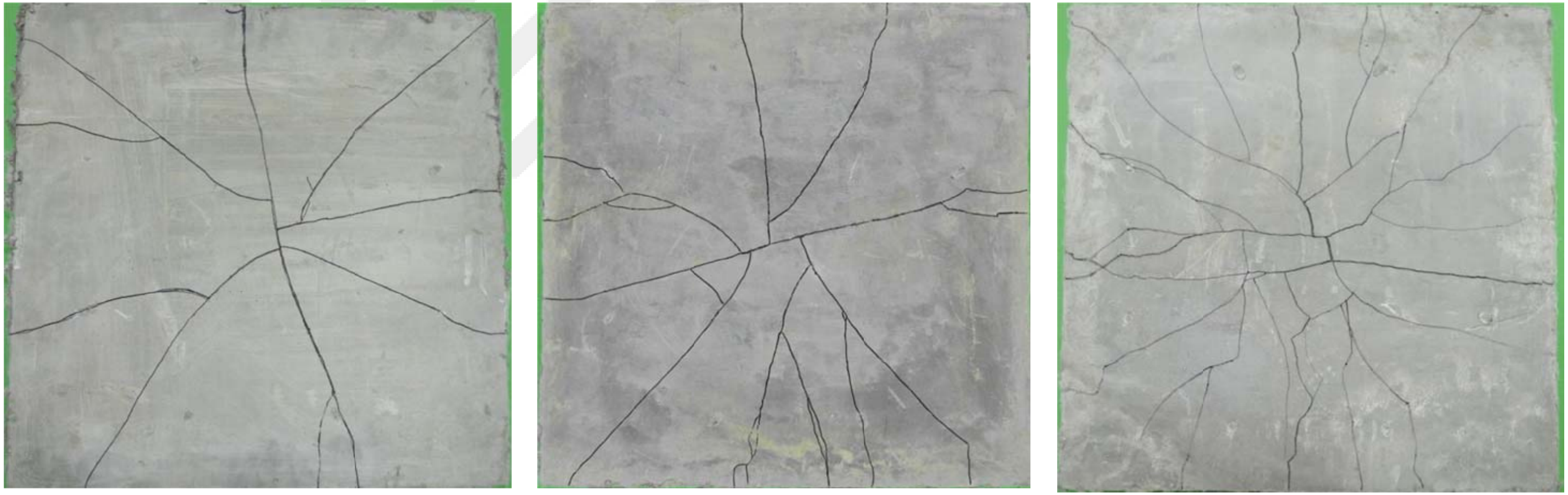

Specimen code; NM0.5
P_u = 13.7 kN
f'_c = 37.94 MPa
ρ = 0.0 %
V_f = 0.5 % of NMECC

Specimen code; NM1
P_u = 18.2 kN
f'_c = 37.35 MPa
ρ = 0.0 %
V_f = 1 % of NMECC

Specimen code; NM2
P_u = 23.5 kN
f'_c = 36.06 MPa
ρ = 0.0 %
V_f = 2 % of NMECC

Figure 4.29 Crack patterns of tested flat slabs in Group V (Effect of fiber dosages on unreinforced NM-ECC concrete slabs)

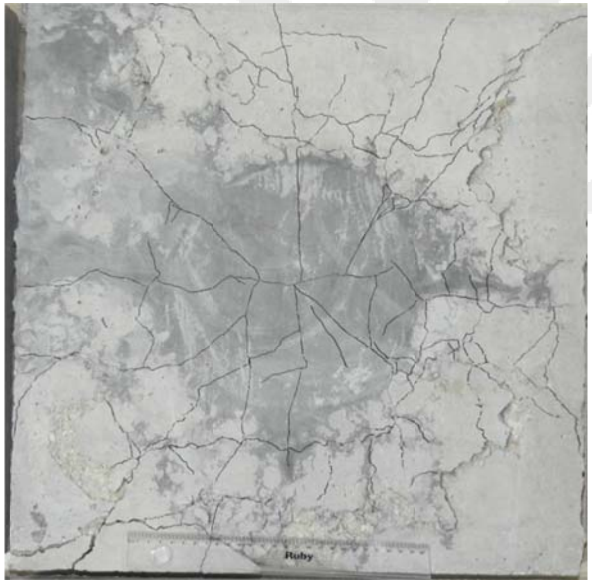

Specimen code; NM0.5P
P_u = 56.33 kN
$f'_{c\ (fiber)}$ = 37.3 MPa, $f'_{c\ (Normal)}$ = 51.98 MPa
ρ = 1.1 %
V_f = 0.5 % of NMECC +Normal concrete

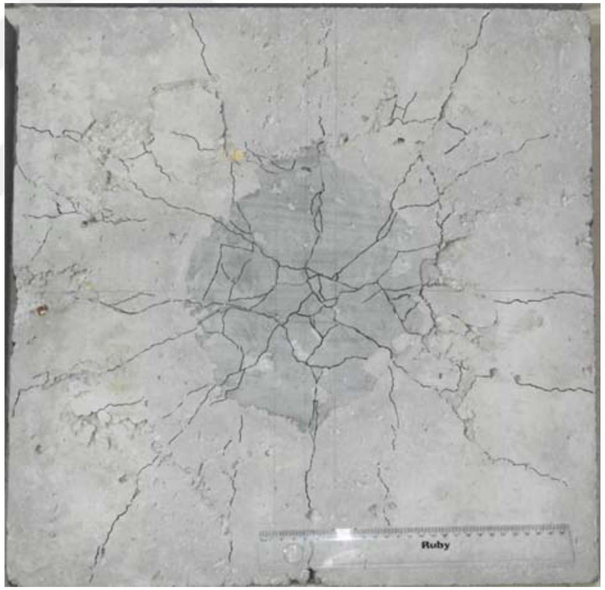

Specimen code; NM1P
P_u = 78.26 kN
$f'_{c\ (fiber)}$ = 43.5 MPa, $f'_{c\ (Normal)}$ = 51.98 MPa
ρ = 1.1 %
V_f = 1 % of NMECC +Normal concrete

Specimen code; NM2P
P_u = 80.27 kN
$f'_{c\ (fiber)}$ = 41.5 MPa, $f'_{c\ (Normal)}$ = 63.4 MPa
ρ = 1.1 %
V_f = 2 % of NMECC +Normal concrete
NM2P

Figure 4.30 Crack patterns of tested flat slabs in Group VI (Effect of fiber congestion in NM-ECC slab

CHAPTER 5

ANALYSIS OF TRANSIENT HEAT TRANSFER IN SLABS

5.1 Behavior of Slab under High Temperature

The important reasons for the modeling of the heat transfer in the present work are to determine the decay of the concrete strength that is used in the subsequent stress analysis as a predefined field of temperature.

In most tested specimens found in literature (Table A-1), the heat is flowing from one side (compression or tension face), and the temperature that passes through the body is varying with time and distance. Thus, it is required to solve one-dimensional transient heat transfer, so that the temperature is a function of time and distance along one principal axis, $T = T(y, t)$. However, in a small area around the top vicinity of the column there is different behavior of heat flow, where the rate of temperature in that connect area is always smaller than the remainder area. This means that the temperature in this area is flowing in three directions, $T = T(x, y, z, t)$. This is because of the differences in thickness between slab and column, where the heat is transferred through to the closest cold area. This dissipated temperature is affected by the temperature gradient between the slab and the column. For such problem, two cases are found in the literature. Firstly, the column is exposed to the same slab temperature, while in the second case, the column is insulated during the test.

In the first case, the differences in temperature between the slab and column are small and have minimal influence because the column is also exposed to fire from all sides. In order to clarify this idea, the 500 °C isotherm (see Section 2.3.3.1) is applied to specimen 1 that was tested by Kordina [10] as shown in Figure 5.1a, which is simulated as the test configuration shown in Figure 2.17a. It shows that the structural system behave as a flat slab (slab with fictitious drop panels) but with a reduction in column size. Where both slab and column are losing approximately 6.4 mm from the compression side (numerical simulation details of the slab are discussed in the following sections).

In the second case, the column is insulated so that the column is exposed to less temperature than the slab. This difference is decreasing until the temperature in the column and slab is neutralized. This may happen before the failure is taken place, or the slab may fails before the temperature neutralization. The same structural behavior of the previous case is expected (flat slab with fictitious drop panel), but with less damage in the column vicinity (see Figure 5.1b).

(a)

(b)

(c)

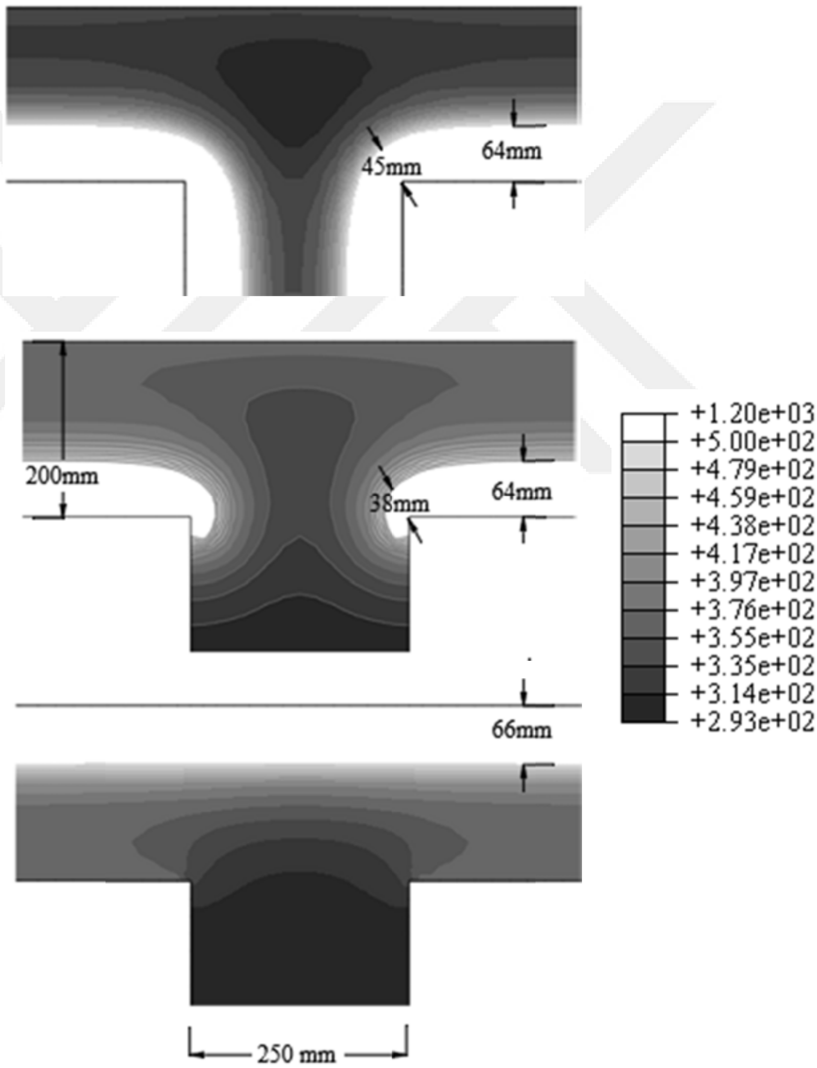

Figure 5.1 Typical temperature distribution in critical zone for column after eliminating the element exposed to temperature higher than 500 °C (a) insulated (b) exposed to the same fire of the slab (c) fire exposed to the tension face

In the two aforementioned cases (see Figures 5.1a and 5.1b), the strengths of the concrete at the tension face and the reinforcement are not significantly affected by the temperature, whereas both materials in the compression zone are deteriorated. This leads to the decreasing of the effective depth (d) and the compression stress block (a). The residual moment strength can be obtained as follows,

$$m_T = \rho f_s d_T^2 \left(1 - \frac{a_T}{3d_T}\right) \tag{5.1}$$

where, A_s and f_s are the reinforcement area and stress, respectively, while d_T and a_T are the reduced effective depth and the reduced depth of the compression stress block.

There is also another case found in literature, where the slab is exposed to fire from tension as shown in Figure 5.1c. For this testing system, the tensile strengths of the concrete and the reinforcement at the top of the specimen are decreased with temperature rising. Thus, the residual moment strength is also decreased, and Equation 5.1 can be re-write as follows:

$$m_T = A_s f_{yT} \left(d - \frac{a_T}{2}\right) \tag{5.2}$$

It is shown that d is not affected, but the stress for both concrete and reinforcement are decreasing with temperature.

Different scenario is assumed in the current work, where the fire is exposed to the two faces of the slab. The fire is assumed to be subjected to the ground and first floors of the structure illustrated in Figure 3.2. The fire is limited by four bays of one compartment (I, II, III, and IV) in the same time and period, but with different intensity as explaind in Section 3.3.3. In order to represent this case experimentally, the tested specimens were placed on the furnace floor (without any support) where the compression face is up and the tension face is down. So that the compression face is exposed to less temperature than the tension face.

Four thermocouples were installed in each tested slab. The exposed temperature and thermocouple locations and distributions are introduced in Figure 3.17c. In order to compare the deterioration of concrete strength in standard cylinders with that in slabs, two thermocouples were fixed at the center and on the face of the standard cylinder.

In the following sections, the temperature histories recorded by the thermocouples through the slabs D0 and D1.25 (plain concrete and SFRC slab reinforced by 1.25 steel fiber) are introduced, discussed, and numerically simulated.

5.2 Test Result

5.2.1 Recorded temperature profiles

Figure 5.2 shows the recorded temperature profiles for slab D0 of normal concrete (see Figure 5.2a), the slab D1.25 with 1.25% steel fiber (see Figure 5.2b), and for the standard cylinder (see Figure 5.2c) of 100 mm diameter and 200 mm height. All specimens were exposed to the same heating conditions (550 °C (823.15 °K)), but it was not possible to control the uniformity of the heating bar and thus the temperature. Yet, it is shown that the specimens were exposed to different temperature values based on the distance of those specimens from the heat source. All specimens surfaces were reached the maximum temperature approximately after 263 minutes, but with different values as mentioned. This is because of the resistance of concrete to the temperature transfers (weak thermal conductivity). The thermocouple installed on the face of the standard cylinder recorded higher temperature than that of the furnace. This might be due to a technical issue, where the temperature reached 680.17 °C (953.32 °K). Therefore, the recorded temperature of this thermocouple was ignored.

The peak temperatures recorded at the top surfaces of the slabs D0 and D1.25 are 430.79 °C (703.94 °K) and 575.99 °C (849.18 °K), respectively. The temperature was maintained at its initial values for approximately 40 minutes after the ignition for D0, 30 minutes for D1.25, and 25 minutes for the cylinder. After which, the curves were separated according to the material thermal conductivity and the specific heat that is affected by the water content. The form of the curves separation is different, where the temperature profile in the slab D0 (of normal concrete), the differences were less than those in D1.25 (SFRC slab). After the temperature reached its value at a specified time, the furnace was turned off and the door was opened and all specimens were exposed to convection cooling. The upper thermocouples curves were decayed in higher rate than those of the other thermocouples. However, the thermocouples at the bottom face (tension face) showed low decay rates. This is not surprising, because the wider free surface area speeds up the convection cooling, whereas the bottom face of the slabs are remained in contact with the hot furnace floor, and thus it is constrained by the cooling of that floor.

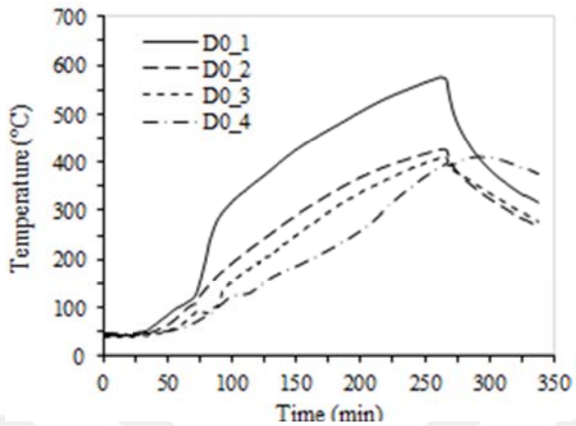

(a) Slab D0

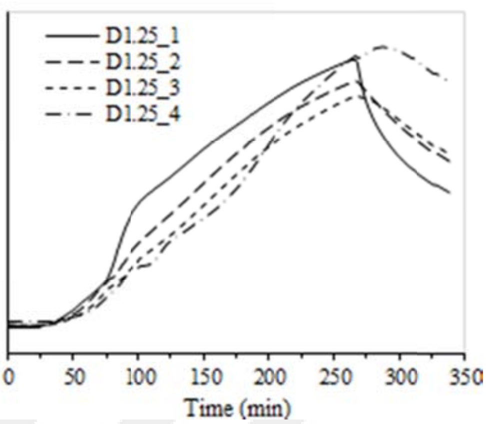

(b) Slab D1.25

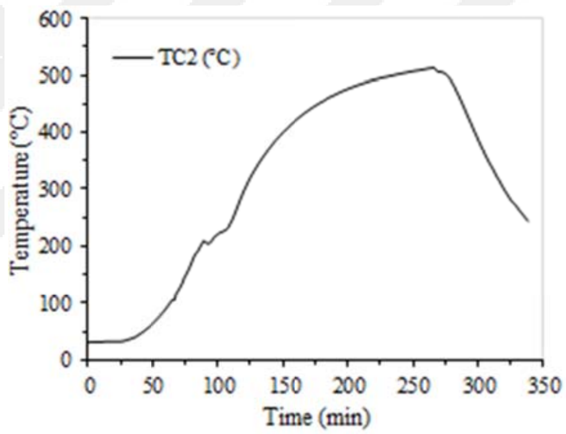

(c) Standard cylinder

Figure 5.2 Recorded temperature histories for specimens exposed to 550 °C (a) normal RC slab D0 (b) SFRC slab D1.25 (c) plain concrete in standard cylinder

5.2.2 Temperature gradient

The temperature is always represented through temperature gradient, which effects the heat transfer equations. For the aforementioned reason, the temperature gradient profiles were investigated. In order to simplify the understanding and following-up of the explanation, the temperature gradient (ΔT) between two numbered thermocouples is represented as the numbers between parenthesis followed the symbol ΔT These numbers refer to the number of thermocouples under consideration. For example, the temperature between thermocouple D0_1 and D0_2 is represented as ΔT(1,2) as shown in Figure 5.3.

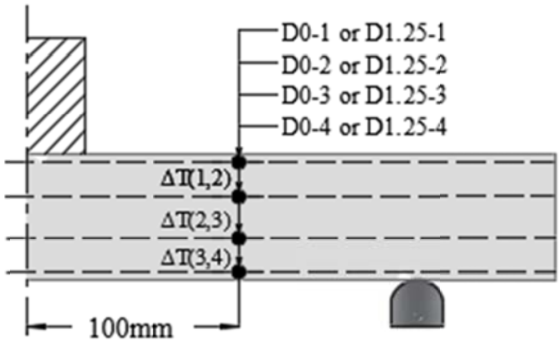

Figure 5.3 Location of thermocouples and the isotherms

Figure 5.4 shows the temperature gradients recorded by the thermocouples at isotherms. The negative value means that the temperature at the lower thermocouples is higher than that in the upper ones. This can occur at the first minutes (based on the initial temperature), or at the cooling branches (based on the cooling convection).

The important conclusion from the analysis of the curves in Figure 5.4 is that the temperature gradients ΔT(2,3) in slab D1.25 (SFRC slab) are less than those in D0 (slab of normal concrete). This is because that the thermal conductivity (k_c) and the specific heat of the SFRC are more than of the normal concrete, as explained in Section 5.4.2.

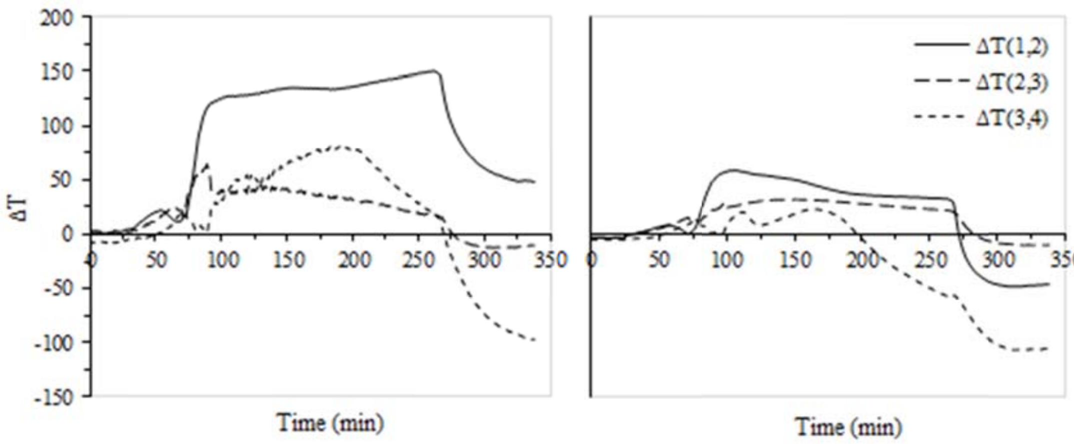

(a) D0 slab (b) D1.25 slab

Figure 5.4 Development of temperature gradients between the surface and interior thermocouples

5.3 Simulation Heat Transfer

One of the strategies of simulating the behavior of slab-column joint is coupling the heat transfer module with the mechanical module into a thermo-mechanical one using the weak form. For this reason, the basics of heat transfer should be recalled. Three modes of heat transfer can be recognized. Namely, conduction depends on the medium. However convection and radiation are independent of the medium. In other words, the three modes of heat transfer are based on the same sources, but behave in different forms depending on the relation of each mode with the medium that is passing through. The conductivity is active and dominates in approximately low temperature, while the radiation is influenced when more pores are present.

Conduction is the bone process of heat transfer, while convection is a surface thermal load. On the other hand, radiation itself can be categorized in different branches, as it once be a surface thermal load and once again it is a type of reversed cooling process that depends also on the surface properties of the material (longwave radiation). In the following sub-sections, the governed equation of the three heat transfer modes are introduced.

5.3.1 Conduction heat transfer

In order to represent the temperature magnitude and its direction, the temperature scalar T should represent through temperature gradient vector ΔT. For the slab portion close to the column, the temperature gradient is then,

$$\Delta T == \frac{\partial T}{\partial x}\vec{i} + \frac{\partial T}{\partial y}\vec{j} + \frac{\partial T}{\partial z}\vec{k} \tag{5.3}$$

For the two-direction conduction heat transfer, the vector k is then terminated so that only the flow in x and y direction is considered, and thus Equation 5.3 becomes,

$$\Delta T = \frac{\partial T}{\partial x}\vec{i} + \frac{\partial T}{\partial y}\vec{j} \tag{5.4}$$

The heat flux vector $\vec{q}$ can be written in proportion to the temperature gradient ΔT as follows;

$$\vec{q} \propto \Delta T \tag{5.5}$$

This proportionality is based on the concrete thermal conductivity k in W/m.K, which leads to the well-known Fourier's law,

$$\vec{q} = - k \, \Delta T \tag{5.6}$$

The minus sign in Equation 5.6 means that the heat flux and temperature gradient are effected in the opposite direction. Applying Equation 5.3 to Equation 5.6 leads to,

$$q_x = - k_x \frac{\partial T}{\partial x}, \; q_y = - k_y \frac{\partial T}{\partial y}, \tag{5.7}$$

Concrete is assumed as a homogeneous isotropic material, so that the thermal conductivity is the same in the three principal directions, $k_x = k_y = k_c$. Moreover, thermal conductivity k_c can be taken constant for low temperatures. But for high temperatures, k_c is varying according to temperature variation. Temperature depends on the direction and the exposed time, in turn, the thermal conductivity is a function of direction, temperature, and time, i.e., $k_c = k \, [\, \vec{r}, T(\vec{r}, t)]$, where $\vec{r}$ is a vector of the two directions x and y.

The temperature is dissipated into the surrounding ambient air through the slab surface elements dS. This surface can be identified by two vectors, unit normal $|\vec{n}|$ and heat flux as introduced in Equation 5.6. Therefore, the heat absorbed within the body Q is,

$$Q = -\int_{s} \vec{q} \, dS \tag{5. 8}$$

According to the first law of thermodynamics, the internal material energy that varies with the time is equal to,

$$\frac{dU}{dt} = \int_{V^e} \rho \, \frac{\partial T}{\partial t} \, dV^e \tag{5. 9}$$

where ρ is the concrete density, it is worthy to mention here that the temperature is applied in partial form because of its dependence on the direction and the time.

Based on the basic energy balance [109], Equation 5.8 is equated with Equation 5.9 to produce the following,

$$\int_{s} q\, dS = \int_{V} \rho \frac{\partial T}{\partial t} dV \tag{5. 10}$$

The constitutive relationship between the internal energy U and the temperature T can be specified in either latent heat or directly in terms of the specific heat c_p. However, if the latent heat is applied, it is supposed to be in addition to the specific heat c_p, where c_p is,

$$c_p = \frac{dU}{dT} \tag{5. 11}$$

5.3.2 Convection heat transfer

The boundary conditions are applied as prescribed temperature in term of initial condition, $T(y, t = 0) = T(y = L, t = 0) = T_0$, where T_0 = 293.15 °K, and L is the slab thickness and for other times $T(y, t > 0) = T(y = L, t > 0) = T_F$. Moreover, for slabs that are exposed to fire from the bottom or top face, the transient heat is dissipated to the contact ambient air by means of convection boundary condition. The equation that expresses the overall effect of convection cooling, is that well-known as Newton's law of cooling,

$$q = h_c\, S\, (T_a - T_s) \tag{5. 12}$$

where $h_c = h(x, t)$ is the film coefficient, S is the area, and the subscripts a and s refer to air and surface, respectively. The temperature gradient at the contact surface depends on the rate at which the air can carry the heat away. Heat transferred into a surface by conduction is equal to heat transferred into a surface by convection The representation of the equilibrium of heating and cooling takes a form of,

$$h_c\, A\, (T_a - T_s) = -\, k_c\, A \left.\frac{\partial T}{\partial y}\right]_{y = L} \tag{5.13}$$

According to Eurocode 1 [33], the heat transfer by both convection q_c and radiation q_r should be considered in order to find the net heat flux q_{net} on the exposed surface, so that,

$$q_{net} = q_c + q_r \tag{5. 14}$$

$$q_c = h_c \times S \times (T_a - T_s) \tag{5. 15}$$

$$q_r = \varepsilon_m \times \sigma \times [(T_a+273)^4 - (T_s+273)^4] \tag{5.16}$$

where, S is the convicted surface area, h_c, is the coefficient of heat transfer by convection equal to 25 W/m^2.K for exposed surfaces in specimen tested under temperature – time standard curve condition (see Section2.3.1), whereas for the unexposed surface h_c = 4 W/m^2.K for heat transfer by convection, The subscripts a, and s, that are associated with the temperature symbol T refer to gas and specimen surface, respectively. ε_m is the emissivity of the member surface, which is equal to 0.8, and σ is constant of Stephen Boltzmann that is equal to 5.67× 10^{-8} W/m^2.K^4.

5.3.3 Heat diffusion equation

Applying Gauss theorem to Equation 5.10 in order to produce it as a volumetric integral,

$$\Delta^2 T = \frac{\rho c_p}{k_c} \times \frac{\partial T}{\partial t} \tag{5. 17}$$

Equation 5.13 is known as a three-direction heat diffusion equation with no convection,

where Δ^2T is equal to,

$$\Delta^2 T = \frac{\partial^2 T}{\partial x^2} + \frac{\partial^2 T}{\partial y^2} + \frac{\partial^2 T}{\partial z^2} \tag{5. 18}$$

Because the temperature is distributed in a uniformly form through the z-direction, Equation 5.13 can be abbreviated to the two-dimensional problem as follows,

$$\frac{\partial^2 T}{\partial x^2} + \frac{\partial^2 T}{\partial y^2} = \frac{\rho c_p}{k_c} \times \frac{\partial T}{\partial t} \tag{5. 19}$$

In order to solve the differential in Equation 5.14 to be suitable for finite element formulation, there are many methods can be used. The most common method is the weighted residual method, and particularly Galerkin method that equates the weighting function to the shape function. The most important advantage of Galerkin method is that the produced matrices become symmetrical if the both differential equation and the specified boundary conditions are "self-adjoint".

5.4 Numerical Simulation of Heat Transfer

The modeling of any structural system exposed to high temperature, such that analyzed in current research, is based on the formulation of finite element theory. The major parts of the analysis consist of three themes: (i) simulation of the fire scenario and the compartment details, (ii) simulation of the slab-column geometry and the compartment (furnace in the current case) and choosing proper meshing (element discretization) and element type based on the degree of freedoms selection. (iii) The modeling of the mechanical and thermal properties and their decay under high temperature effect, (iii) the modeling of the external structural effects and internal structural response such as small or large displacements. As limited to the current chapter, the second and third themes (ii, and iii themes) are covered herein. The general purposes finite element software ABAQUS 6.14-1 was utilized to simulate the heat transfer in the following sections, and then the load deformation characteristics of the slab column assembly are introduced in Chapter 7.

Twenty slabs exposed to four levels of temperatures (150, 300, 450, and 550 ºC) were modeled. The modeled specimens were calibrated based on the experimental temperature recorded from thermocouples attached to two slabs (D0 and D1.25) and one standard cylinder (as introduced in previous sections).

5.4.1 Geometry, meshing, and element selection

The geometry and meshing are proposed so that the modeling system has to cover both separated thermal and mechanical studies, i.e. the loading and supporting system, the element size, and mesh topology are supposed to be the same. However, in fire engineering, the compartment is simulated and the surrounding air is also simulated and the air elements acquire node numbers that are not considered in the mechanical model. This creates many interpolation errors when transferred from the thermal to mechanical step that obtained from dissimilarity between the mesh topology. Therefore, the compartment was not modeled, and the heat transfer due to convection was considered instead. In the same manner, the steel plate column and the half balls support were not heated, but had to be included in the mechanical step. Therefore they were simulated in this step without ties to the slab, so that the temperature in the slab is not dissipated to the column and the supporting balls.

As it is shown, heat transfer is highly non-linear (fourth order) temperature field that can be solved by a series of linear finite elements; hence the size and the number of elements highly affect the accuracy. High number and small elements size lead to increase the computational efforts and required storage. In the current step, the structural behavior was omitted, where the element type used herein cannot be used for subsequent mechanical analysis. Three-dimensional solid 8-node linear brick element (DC3D8) was used for heat transfer model (another type of element was used for the mechanical study). Linear hexahedral elements were used for both studies, with the maximum size of 20 mm. The geometry, mesh topology, and boundary conditions are shown in Chapter 7.

ABAQUS uses a Gaussian quadrature method for most of the elements. There is no reduced integration element available for heat transfer, so that full integration with high order was applied for the finite element analysis, which leads to less dependency on the geometry of the element, order of interpolation, in turn the accuracy.

5.4.2 Material's thermal properties at elevated temperatures

Based on Eurocode 2, the influence of the reinforcement bars can be ignored in the temperature field. However, the degradation of the yield stress is considered for the mechanical step. It became known that the concrete properties are varying due to increasing temperature, especially in terms of stiffness and strength degradation because of the materials' physical and chemical altering at high temperatures [110]. The details of the effect of high temperatures on the concrete properties were depicted in Section 2.3.2.

As mentioned in Section 2.3.2.2, the thermal conductivity (k_c), the specific heat C_p, the density (ρ), and the thermal expansion coefficient (α_c) are the four main material thermal properties that affect the amount of heat transfer through the body. These properties are assumed temperature-dependent.

5.4.2.1 Thermal conductivity

There are many decay models proposed for k_c in the literature (it can be found in Figure 2.8). Moreover, there are slight differences between SFRC and normal concrete thermal conductivities. These differences in k_c may be imputed to the high conductivity of the steel compared to the concrete (30 times higher). The thermal conductivity of the SFRC with 1.5% steel fiber that was tested by Lie and Kodur [111] was 3.08 W/m.°C. However, ACI 544.5-10 adopts a SFRC thermal conductivity based on the fiber volume fraction, where k_c is 3.03, 2.74, and 2.84 W/m.°C for 0.5, 1.0, and 1.5% hooked steel fiber content, respectively (see Figure 5.5a).

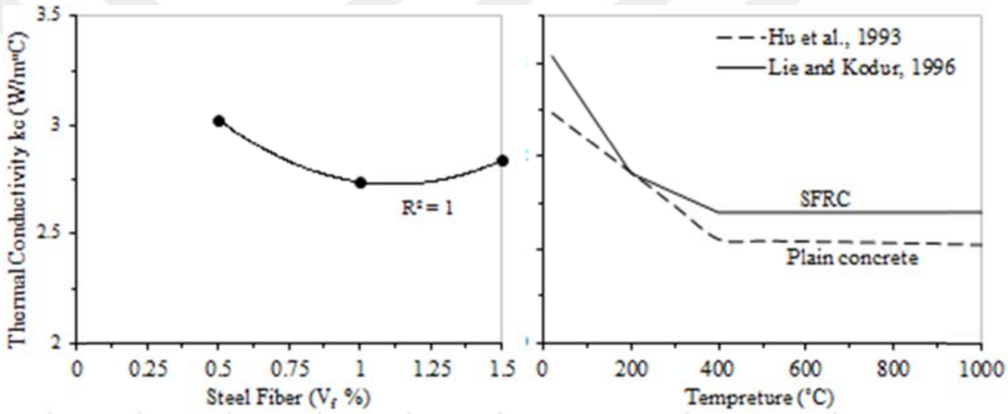

(a) (b)

Figure 5.5 The adopted thermal conductivity and its decay for concrete (a) k_c for SFRC (b) decay of k_c due to exposing to high temperature for plain concrete and SFRC

The thermal conductivity of SFRC can be represented by the following second order equation with 100% coefficient of determination,

$$k_c = 0.78\,(V_f)^2 - 1.75(V_f) + 3.71 \tag{5.20}$$

Therefore, the missing k_c for other steel volume fractions (0.75 and 1.25%) was obtained from Equation 5.20. These values were calibrated according to test results.

Two decay models used in simulation of the heat transfer for SFRC and plain concrete were adopted in current work (see Figure 5.5b). For plain concrete, the proposed model by Hu et al., [42] was considered, while, the model proposed by Lie and Kodur [111] was considered for all SFRC slabs. The SFRC shows sharp decay in

k_c up to 200 °C and less deterioration between 200 and 400 °C, and no decay can be shown after 400 °C. Almost the same thermal conductivity was proposed for both SFRC and plain concrete at 200 °C. Similarly, constant thermal conductivity was considered for plain concrete above 400 °C. It is expected that the sharper decay in the k_c of the SFRC may cause difficulties in convergency.

5.4.2.2. Thermal capacity

It is found from the literature that the concrete Thermal Capacity (ρC_p) is highly affected by the aggregate type and moisture content (as discussed in Section 2.3.2.2). Moreover, Eurocode 2 considers the effect of the moisture content on ρC_p. It shown that the energy consumption due to vaporizing of the compound water leads to peak in the ρC_p between 600 and 800 °C (see Figure 2.9). Therefore, it is assumed that the temperature plateu can be neglected because the exposed temperature in the current work is less than 600 °C and the slabs were dried for 24 hours before the heating process took place. It is worthy to mention here, that the enthalpy can be used instead of C_p [112] or fully coupled hygro-thermal model can be analyzed. In the current work, C_p with 900 (J/Kg ºK) showed most accurate results. The variation of C_p and the mass (ρ) are assumed to be within the provisions of Eurocode 2.

5.4.3 Interactions

No variation of the film coefficient (h_c) due to high temperature could be found in the literature. Therefore, the constant h_c was considered for all slabs but with different values for fully and partially exposed surfaces. As mentioned previously, Eurocode 2 adopts two values for exposed and unexposed surfaces, while no values are available for partially exposed surfaces such as in current work. Therefore, for exposed surfaces, the heat transferred by convection per unit area per degree temperature difference between the surface and the air was used as proposed by Eurocode 2 (25 W/m^2.K), while h_c for partially exposed surface (tension face) was assumed to be 16 W/m^2.K for plain concrete and 12 W/m^2.K for concrete with 1.25 % SF. For other steel percentages, the values of h_c were considered differing in the same percentages of the variation of thermal conductivity obtained from Equation 5.20.

5.4.4 Verification of heat transfer

Basid on the aforementioned premises, uncoupled transient heat transfer in slabs and standard cylinder was modeled. Two tested slabs (D0 and D1.25) and one cylinder of normal concrete (100 mm diameter and 200 mm height) were simulated as presented in the next two sections.

5.4.4.1 Heat transfer in the slabs

Figure 5.6 shows the simulation results for the slabs D0 and D1.25. The aim of this simulation is to reach the maximum temperature at the nodes, so that the temperature profile is not that important in the mechanical model. It is shown that the previous assumptions for the mesh and the material properties produced accepted results for all data recorded from thermocouples, except the profile of D0-1 and D1.25-1, yet, the maximum temperature is still close the recorded values. This is because the exterior thermocouples were fixed by gypsum after the concrete is hardened. This was not the proper way, because the gypsum has low thermal conductivity compared to the concrete. However, after long soak time, the predicted temperatures were more accurate to well meet the experimentally measured ones.

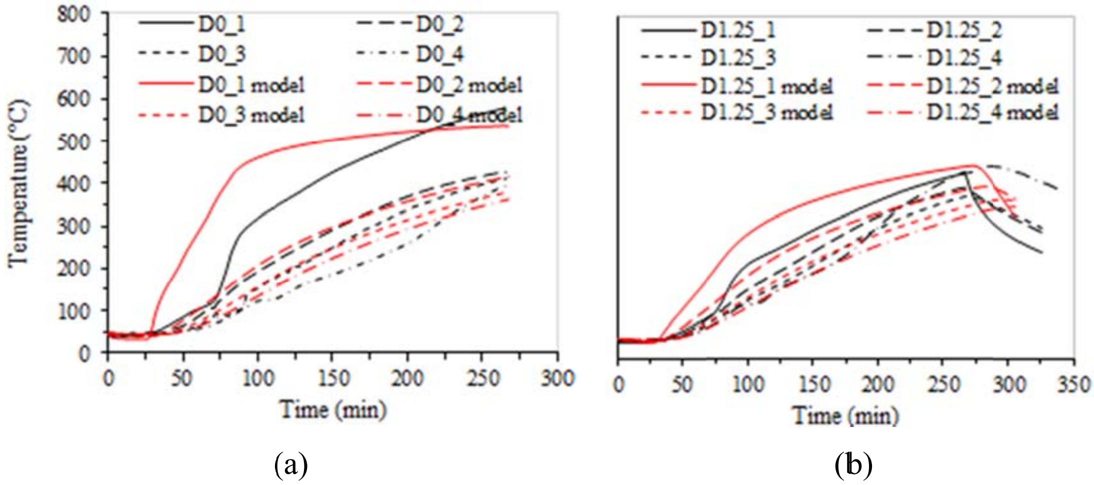

Figure 5.6 Comparison between measured and modeled temperature profiles for (a) slab D0 (b) slab D1.25

The isoplane of the slabs at the maximum temperature are depicted in Figure 5.7. The figure shows that the temperature distribution is contoured with smooth rounded corners near the slab edge. This contour didn't much affect the resistance of the slab, because it lies outside the supports. However, the differences in temperature levels are shown in the critical area. This means that the soak time was not enough to make all nodes with the same temperature.

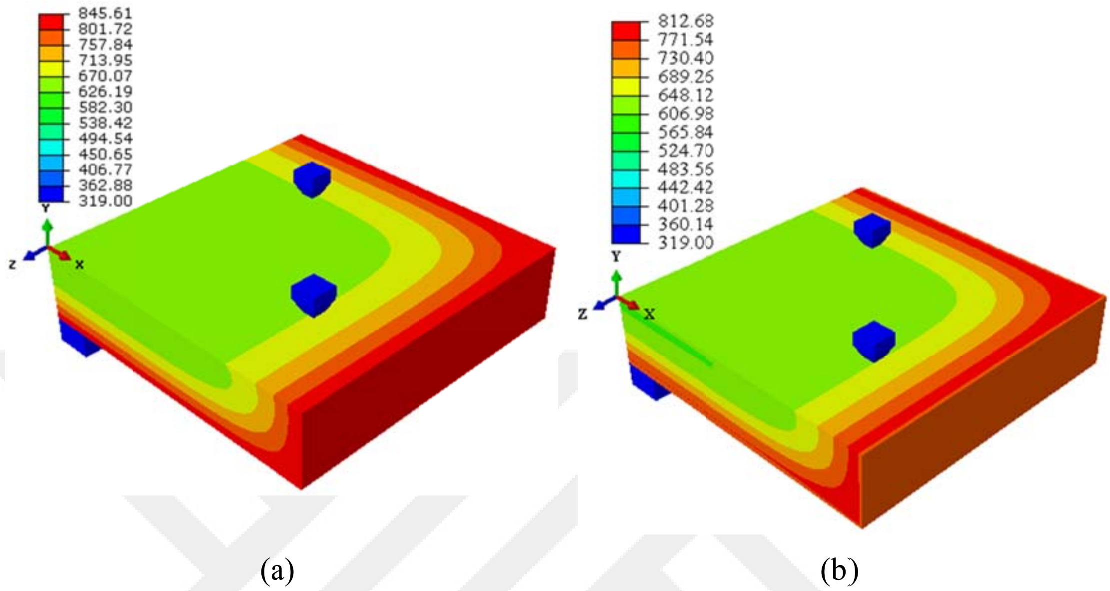

Figure 5.7 Temperature distribution isoplane (in ºK) for slabs exposied to a temperature up to 550 ºC (a) slab D0 after 267 min (b) slab D1.25 after 272 min

Using the same setting and consideration of the previous model, the simulation was extended to cover the remain temperature levels. Figures 5.8 to 5.11 summarize the temperature profile for all remained tested slabs. For all slabs, it is shown that the differences between the temperature of the thermocouples mounted near the top surface (compression face) is increasing with increasing the exposed temperature, which means that the soak time depends on the specified temperature. In turn, the obtained compressive strength of the standard cylinder exposed to the same temperature may not represent the real compressive strength. This conclusion is discussed in the next section. Figures 5.12 to 5.15 depicted the isoplanes of the mentioned slab specimens exposed to 150, 300, and 450 ºC.

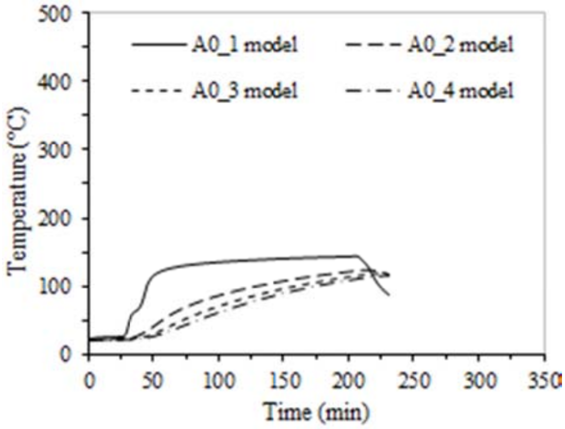

Slab A0 (150 ºC)

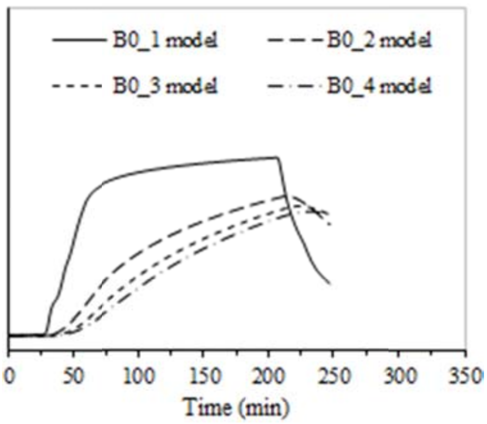

Slab B0 (300 ºC)

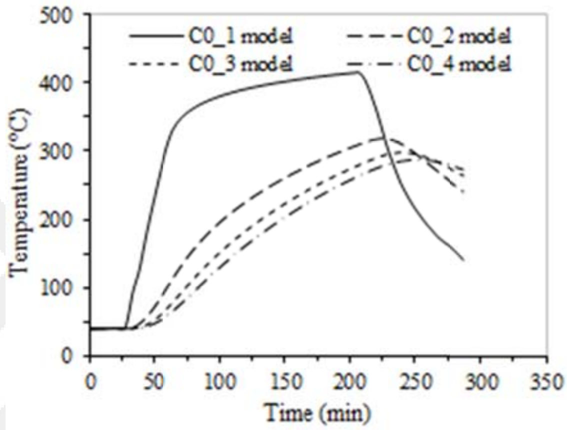

Slab C0 (450 ºC)

Figure 5.8 Temperature profile for slabs of normal concrete exposed to three levels of temperature 150, 300, 450 ºC

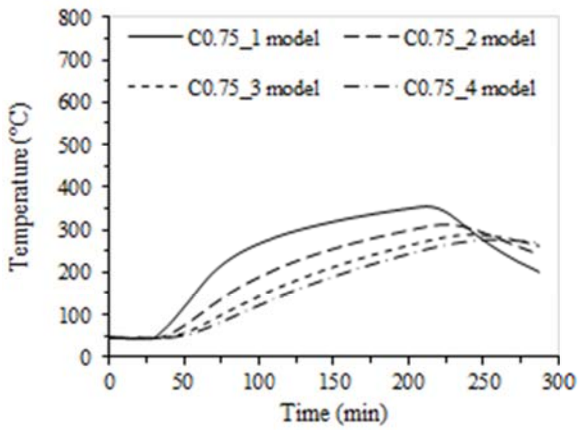

Slab C0.75

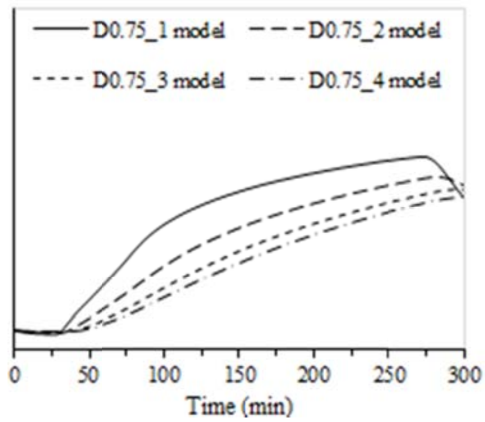

Slab D0.75

Figure 5.9 Temperature profile for SFRC slabs of 0.75% steel fiber content exposed to three levels of temperature 150, 300, 450 ºC

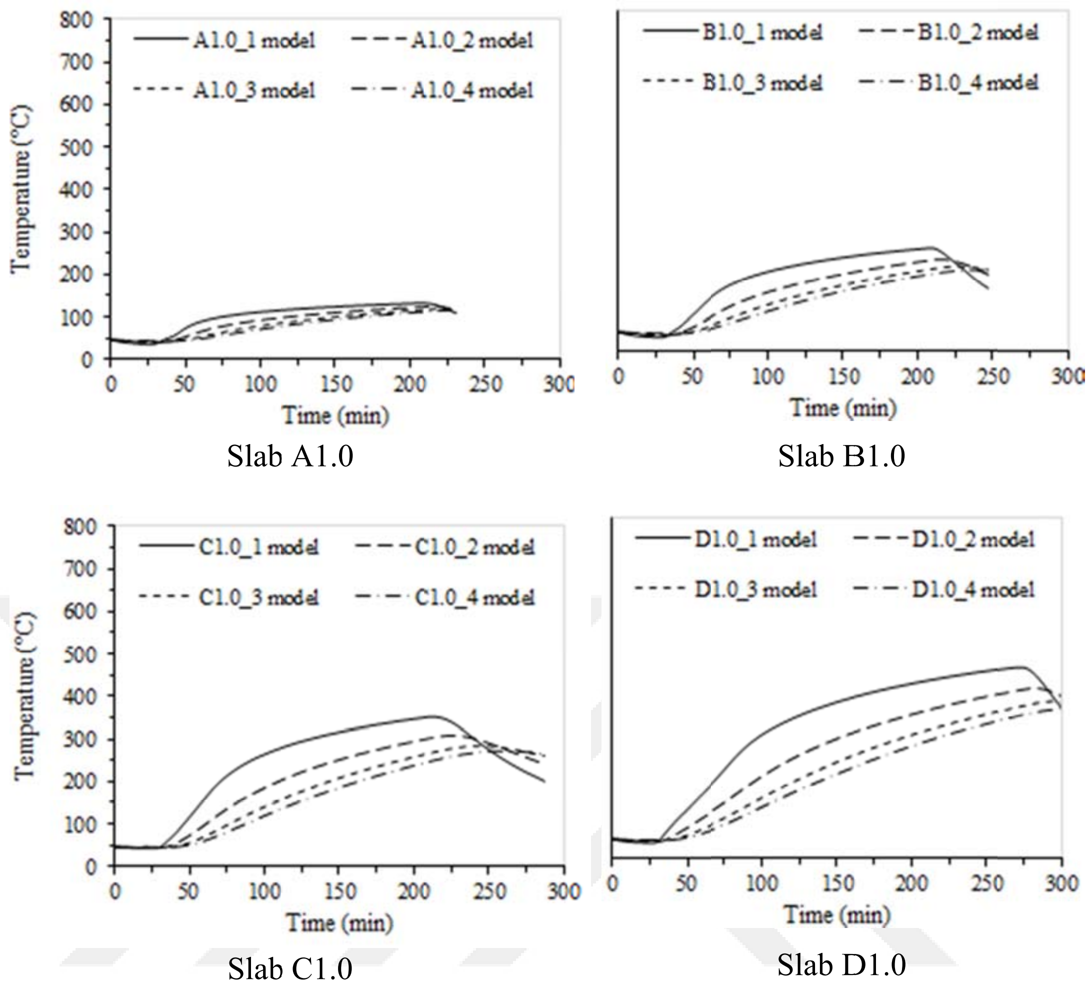

Figure 5.10 Temperature profile for SFRC slabs of 1.0% steel fiber content exposed to three levels of temperature 150, 300, 450 ºC

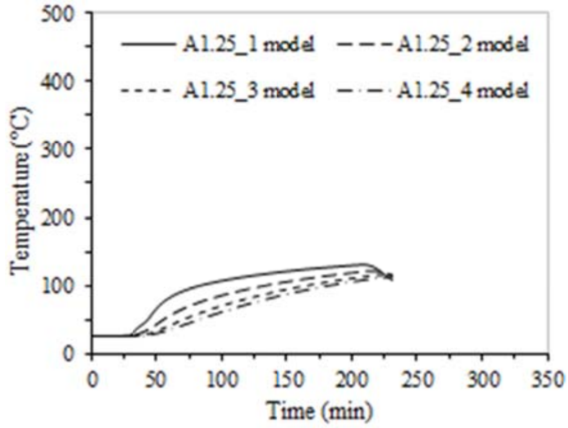

Slab A1.25

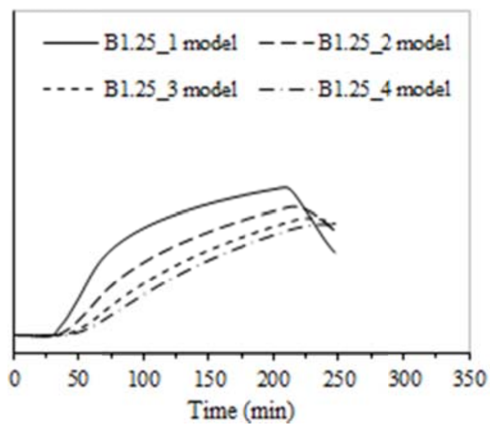

Slab B1.25

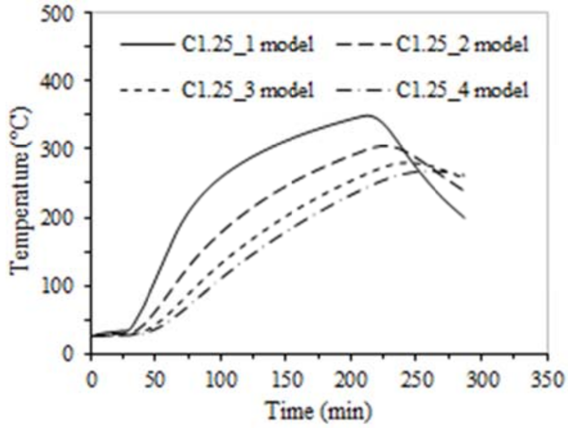

Slab C1.25

Figure 5.11 Temperature profile for SFRC slabs of 1.25% steel fiber content exposed to three levels of temperature 150, 300, 450 ºC

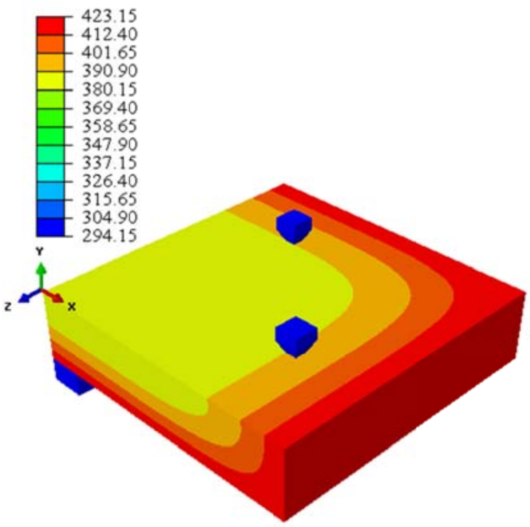

Slab A0

at 206 min

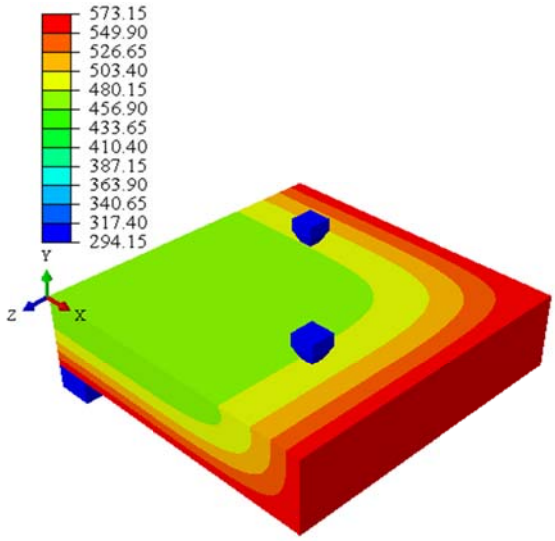

Slab B0

at 206 min

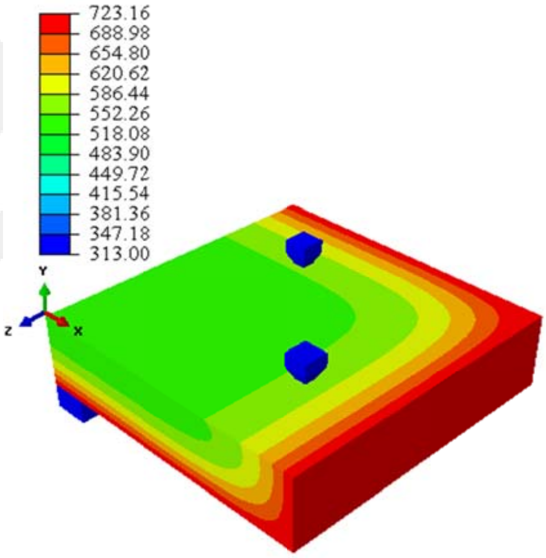

Slab C0

at 215 min

Figure 5.12 Temperature distribution isoplane (in ºK) for slabs of normal concrete at the mentioned time

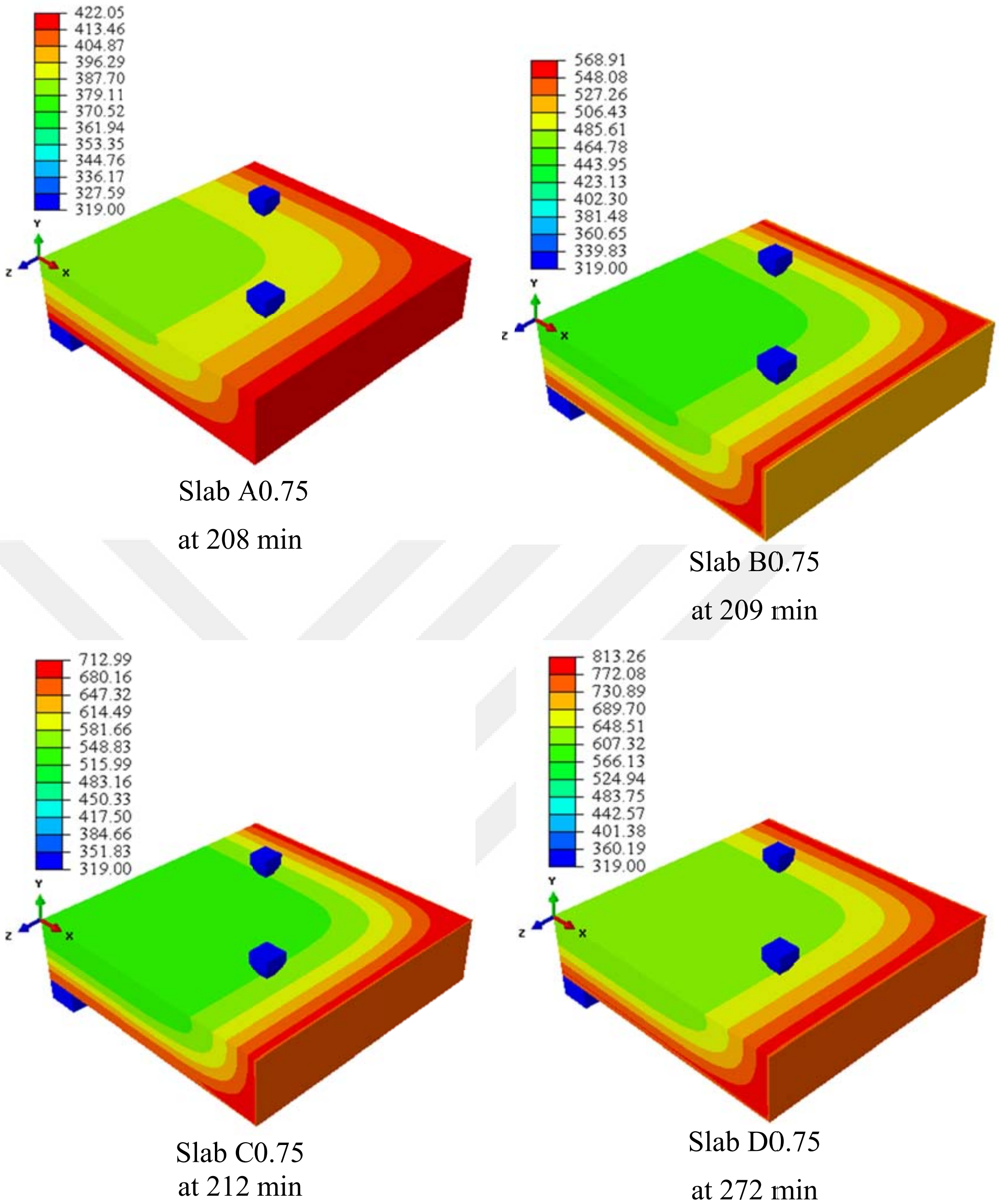

Figure 5.13 Temperature distribution isoplane (in ºK) for slabs of 0.75% steel fiber at the mentioned time

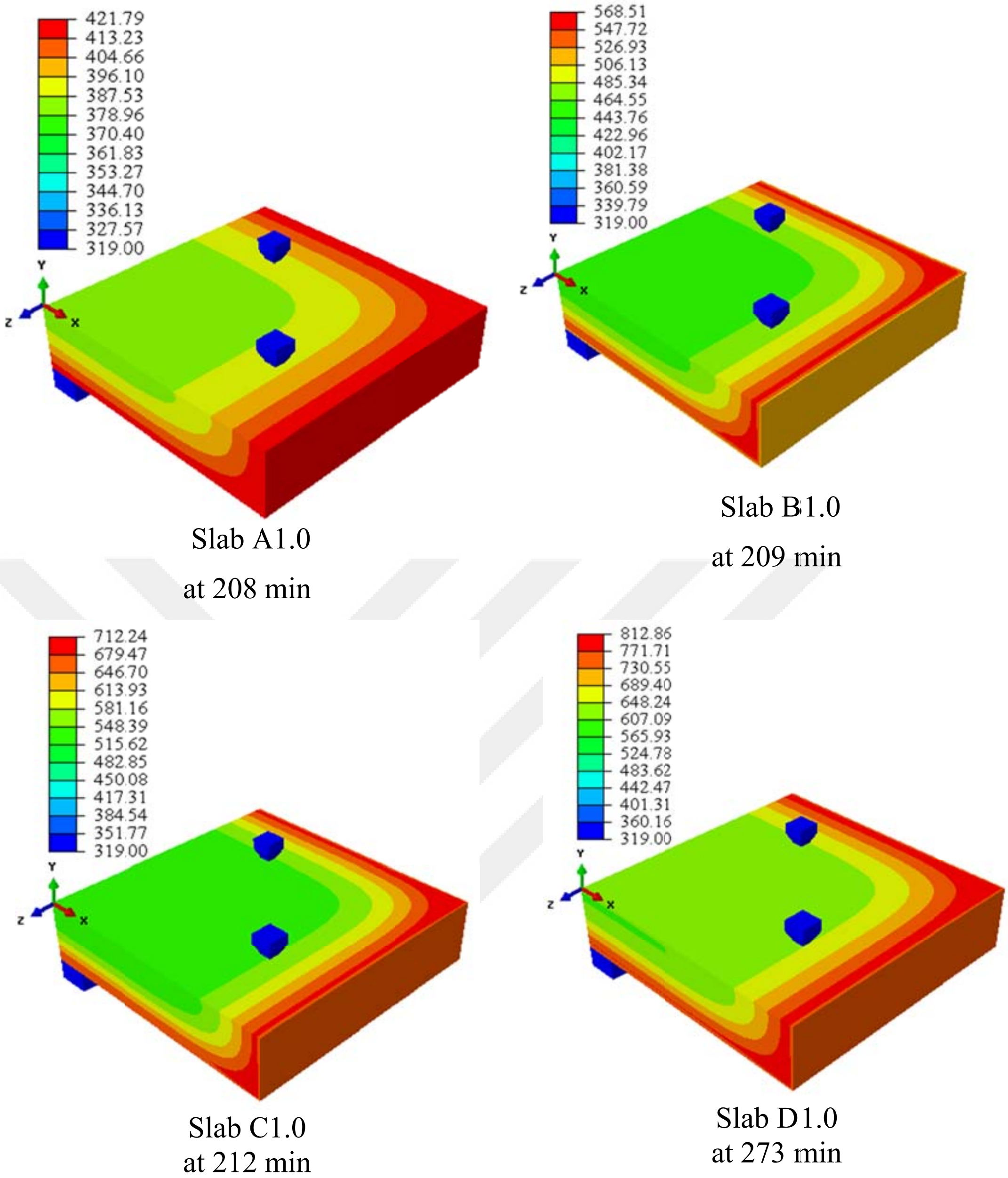

Figure 5.14 Temperature distribution isoplane (in ºK) for slabs of 1.0% steel fiber at the mentioned time

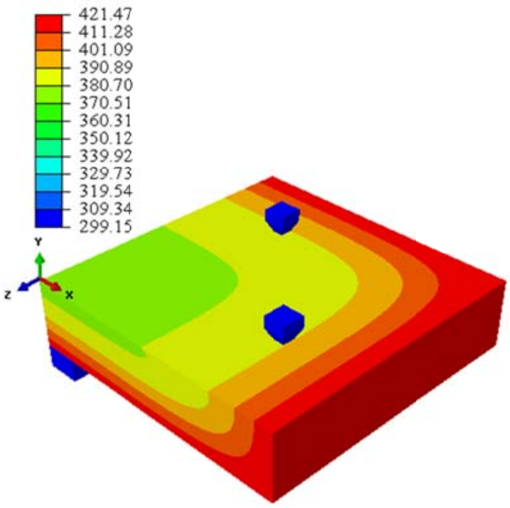

Slab A1.25

at 209 min

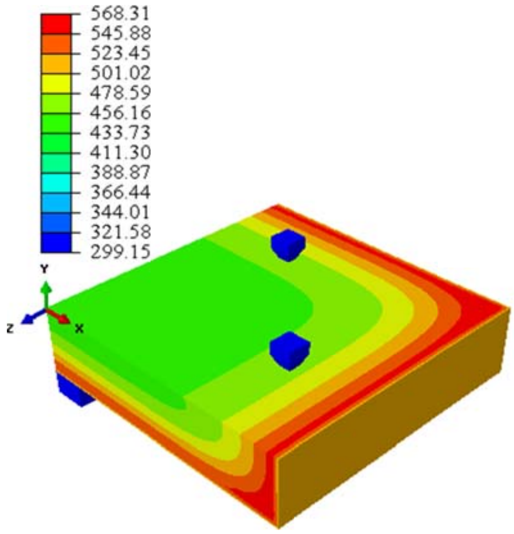

Slab B1.25

at 209 min

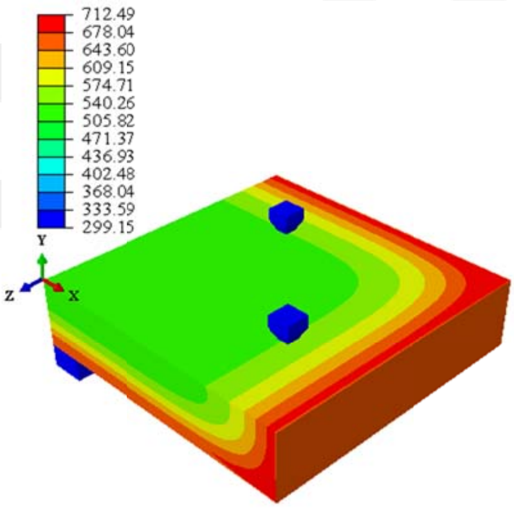

Slab C1.25

at 212 min

Figure 5.15 Temperature distribution isoplane (in ºK) for slabs of 1.25% steel fiber at the mentioned time

5.4.4.2 Heat transfer in the standard cylinder

Following the same procedure in Section 5.4.1 and the decay of the material's thermal properties according to Eurocode 2 [31] that mentioned in Figures 2.8 and 2.9, the heat transfer of the standard cylinder made from normal concrete exposed to 550ºC was simulated. The top and the side of the cylinder supposed to be exposed to the recorded temperature of the furnace thermocouple, while the bottom of the cylinder was exposed to less temperature. This is the thermocouple located near the cylinder base.

Figure 5.16a illustrates the temperature profile in the cylinder. The temperatures were recorded for nodes located in the center and face of the cylinder, at 29 mm, and at 39 mm from the center. The mentioned distances were chosen so that the nodes temperatures are obtained instead of the integration points of the elements, in order to simulate the point temperature of thermocouples. Temperature history of the thermocouple at the center of the cylinder (see Figure 5.16a), shows that the modeled temperature is highly agree with that recorded at the maximum temperature, which matches to the scope of the model.

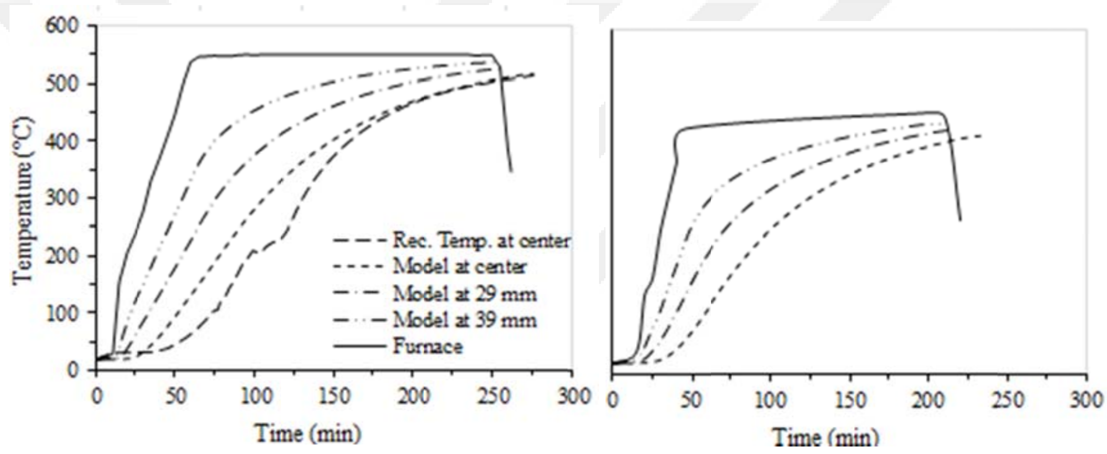

(a) (b)

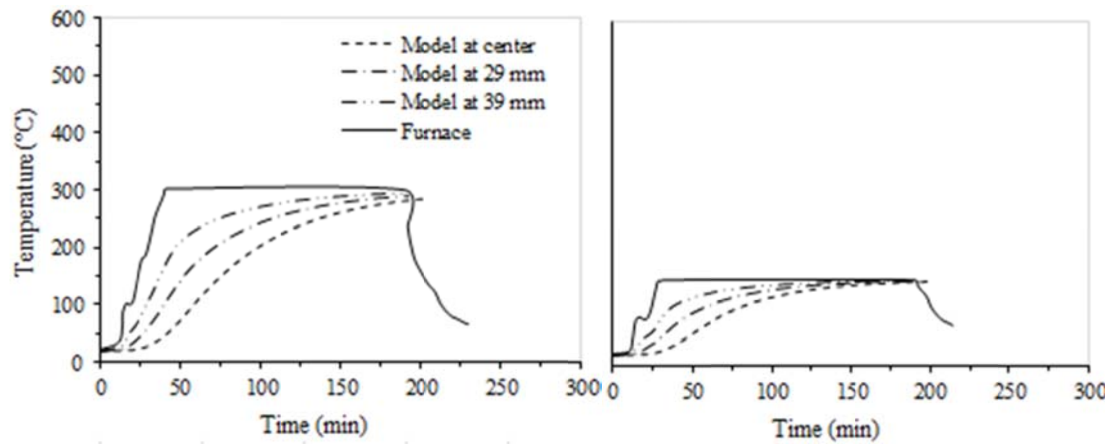

(c) (d)

Figure 5.16 Modeled temperature profiles at different spaced nodes, for standard cylinder (200 ×100 mm) exposed to (a) 550 ºC, (b) 450 ºC, (c) 300 ºC and (d) 150 ºC

However, for the low temperatures, there is some mismatching between the actual and model temperatures. This is because the effect of the specific heat as it is discussed in Section 5.4.2.2. In order to decrease the time and effort the same setting and material properties were extended for cylinders exposed to 450ºC, 300ºC, and 150ºC. Figure 5.16 b, c and d depict the temperature histories of the three mentioned temperature levels.

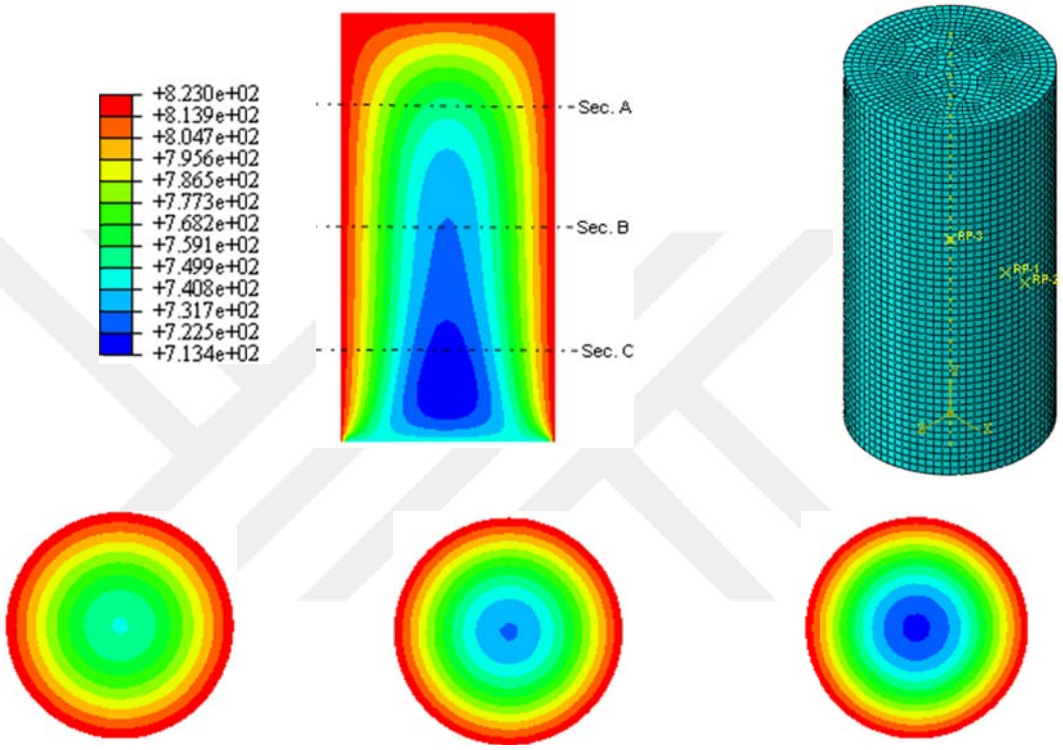

Sec. A, 50 mm from the bottom

Sec. B, 100 mm from the bottom

Sec. C, 150 mm from the bottom

Figure 5.17 Modeled temperature distributions in standard cylinder (200×100 mm) exposed to 550 ºC at the end of soaking time.

It is shown that up to the end of heat soak process (constant temperature process) there was still low temperature gradient between these isotherms. The temperature gradient decreases with the decrease of the exposed maximum temperature as shown in Table 5.1b. This means that the soaking times were properly chosen. The heat soak time do not last long in the most real fire cases as was discussed in Section 2.3.1, which does not allow the heat to be equalized through the members. The produced different layers of different strength make the cylinder under compression behave as a composite structure. This leads to the important question, does the standard cylinder represent the compressive strength of the slab exposed to the same fire conditions as it is in ambient conditions? The answer of this question depends on many variables, mainly on the level of temperature and the exposing time. Table 5.1a shows the modeled temperatures at the isotherms at the end of the heating processes.

Table 5.1. Maximum modeled temperatures reached in standard cylinders exposed to four temperature levels

(a) At the end of the **heating processes**

Nominal Temp. (ºC)	**Time** (min)	**Isotherms Maximum Temperature (ºC)**				**T3 – T0**
		T0 at center	**T1** at 29 mm	**T2** at 39 mm	**T3** at face	
550	98	273	370	450	550	277
450	46	63	142	237	428	365
300	41	48	105	173	302	253
150	31	27	53	87	150	122
(b) At the end of the **soaking processes**						
550	251	506	525	537	545	38
450	209	405	425	438	450	45
300	189	281	289	295	300	19
150	189	146	148	149	150	4

[a] distances are measured from the cylinders' center

The temperature gradient in this stage plays an important role. Figure 5.18 represents the variation of the compressive strength (f'_c) through the cylinder's cross-section at the mid height. Varied f'_c is due to the exposing to high temperatures directly at the end of the heating process. The percentage of variation depends on the test result of the cylinders exposed to heat and soaking process, i.e., the temperature gradients are as low as possible. It is shown that the compressive strength is varying based on the maximum temperature employed, where for the cylinder exposed to 150 ºC, almost all the elemental strengths were increased by 8%. Thus, the cylinder can behave same as the cylinder under ambient conditions (see Figure 5.18a), while the strength of the outer elements of the cylinder exposed to 300 ºC decreased by 3% compared to the corresponding cylinders at ambient conditions (see Figure 5.18b). For these two exposure temperatures, the tested cylinders can represent the compressive strength as normal. Different behavior was observed in the cylinders exposed to 450 ºC and 550 ºC, where the temperature gradient was significantly increased. In turn, the strength varied by about 35% between the core and the outer elements of the cylinder. In these two cases, the cylinder test cannot represent the strength of the slabs as normal, because the different size slabs receive different heat quantities with no change of the cylinder size. Moreover, different maximum temperature levels cause varied strength. Therefore, the compressive strength should be obtained from cubic tests, so that the temperature gradient is almost equal on all sides.

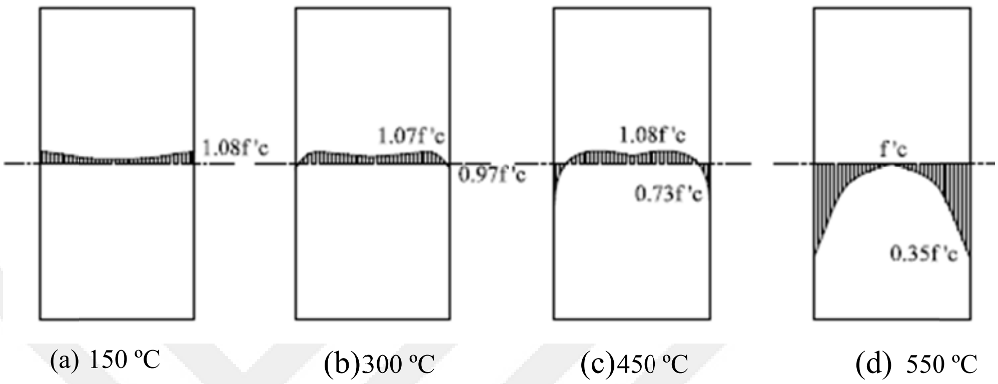

Figure 5.18 The decay of the compressive strength along the cross-section of cylinders exposed to high temperature

The compression failure mechanism for cubic specimens can be understood through the fracture energy approach that introduced by Bazant [113]. In spite of the complexity of the axial splitting due to compression [114], the difficulties are decreasing due to non-uniform macroscopic strain field (produced from non-homogeneous elements' strength, such as cylinder shown in Figure 5.18c and d).

The compressive strength for cube can be obtained as stocky column [113] as follows:

$$f'_c = 2.76 \times \left[\frac{E(T)^3 (G_F(T))^2}{(2k \times a + h)^2}\right]^{1/5} \tag{5.21}$$

where

$$a = \frac{h}{2k} \times \frac{(\tilde{\sigma} - \sigma_{cr} + \sigma_N)(\tilde{\sigma} + \sigma_{cr} - \sigma_N)}{(\sigma_N - \sigma_{cr})^2}$$

and

$$\tilde{\sigma} = \sqrt{2E \times G_F \times h/s},$$

$$\sigma_{cr} = -\frac{\pi^2 \times E \times s^2}{3h^2}$$

$$\sigma_N = \frac{P}{A}$$ is the compressive strength at ambient condition

$$s_i = 0.41 \times \left[\frac{G_F}{E \times (2k \times a + h)}\right]^{1/5}$$

All parameters have to be temperature dependent, where E and G_F are modulus of elasticity and fracture energy, respectively. The parameter h is the width of the crack band as shown in Figure 5.19, k is the slope of the crack band. For concrete at ambient condition k is constant, however, for concrete exposed to high temperatures, k is varying according to cylinder size and the maximum temperature reached. The parameter s_i (the crack space) at high temperature has different from than under ambient conditions because the spacing is increasing in logarithm matter. This area is open for a future research.

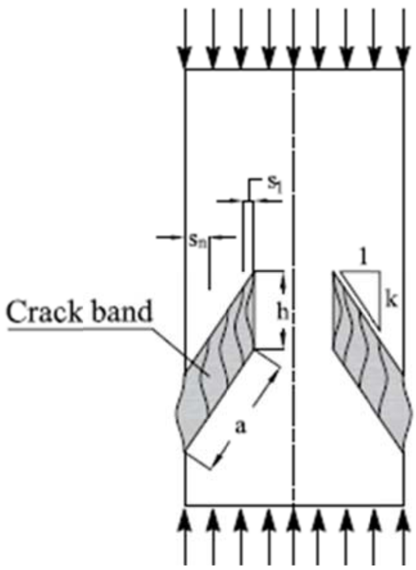

Figure 5.19 Splitting crack band producing macro-slabs,

5.5 Fictitious Composite Behavior

In order to simulate the residual strength of the slab that exposed to high temperatures, the decay of the mechanical properties should be considered. It is shown that the slab exposed to high temperatures from both sides can be introduced as a fictitious multi-layers composite member, each layer can be selected based on ΔT between the isotherms, Then the temperature at the center of the fictitious layer is considered as the temperature of that layer. Based on this assumption, the decay of the mechanical properties is considered according to the peak temperature reached in this layer. As introduced in Figure 5.3, the slab can be divided into three fictitious layers, with a temperature equal to the average temperature recorded by two thermocouples.

Figure 5.20 shows the temperature profiles through the slab thickness at 30 minute intervals. The solid black curve represents the temperature profile at the end of the heating process, while the dashed black curves represent the cooling process. This figure clarifies the previous findings, where the ΔT(2,3) in D0 are higher than those in D1.25 for all temperature intervals, and remain at the same rate after cooling,

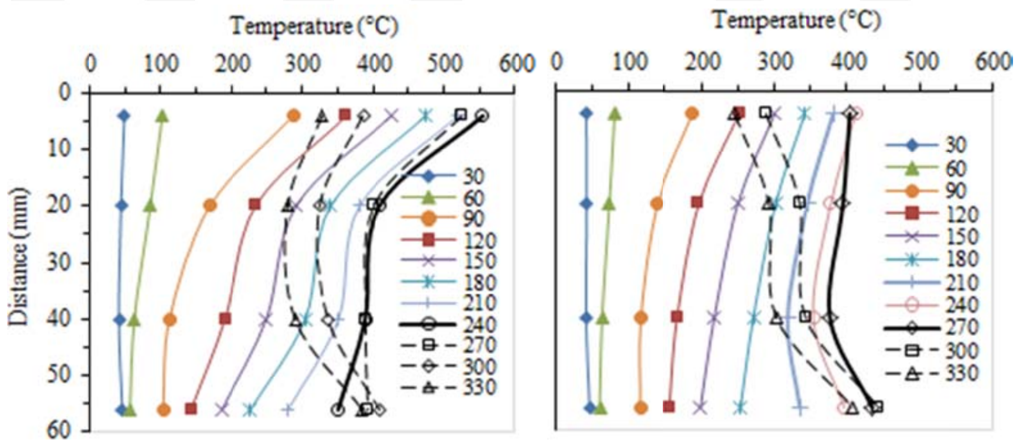

(a) (b)

Figure 5.20 Temperature profiles at 30-minute intervals for (a) D0 slab (b) D1.25 slab

CHAPTER 6

TEST RESULTS AND DISCUSSION OF RESIDUAL STRENGTH OF FLAT PLATE-COLUMN JUNCTION EXPOSED TO HIGH TEMPERATURES

6.1 General

The data obtained from Chapter 4 showed that the SF have significantly increased the slab resistance load (P_u) and the EAC. Compared to its corresponding normal RC slab, the inclusion of 1.0% of SF increased P_u and EAC of SFRC slabs by 76% and 413%, respectively, while the inclusion of 1.5% of SF increased the ductility by 19%. The mentioned improvements in the structural response of the slab are due to the interaction between the SF effect and the structure of the used matrix, which includes a high percentage of fine particles (fine aggregate and binder). The inclusion of high content of fine particles is involved in improving the gaining of strength by increasing the surface area, the bond between matrix particles, and more importantly the stress distribution.

For the aforementioned reasons, the SFRC flat plate-column joint was elected to investigate the residual strength due to exposing to high temperature. The heating method was selected to simulate the fire scenario as mentioned in Chapter 5. From heat transfer analysis, it is shown that the exposed slabs are formed of three layers of different properties with high nonlinearity. In this chapter, the test results of standard cylinders and the flat plate-column assembly specimens are analyzed empirically to derive the relations between the SF volume fraction and the exposed temperatures that simulate the semi-empirical methods found in some codes of practice and in literature.

6.2 Mechanical Properties of Fresh and Hardened Concrete

6.2.1 Slump test

The main problem in fibrous concrete is the tendency to produce balling of fibers in the fresh mix, which is affected by many factors such as maximum size of aggregate, and its overall gradation and the fiber's three main parameters (aspect ratio, volume fraction, and shape). It is found that, the larger the maximum size of aggregate with high aspect ratio, the less the volume fraction of fibers should be used (ACI 544 1). Hence, the maximum size of aggregate in the present work is considered as small. However, the used quantity of fine aggregate in the mix is high, which decreases the slump of the fresh concrete, where this problem is aggravated when high SF contents are used. Figure 6.1 shows the experimental results of the SFRC fresh mixture. It can be clearly seen that the slump decreases when the SF is used. Adding 0.75% of SF decreased the slump by 33%, while duplicating this percentage of SF decreased the slump by only more 7%. The results are compared with tests found in literature [115,116]. In general, in the mixtures of the mentioned literature, the sand-total aggregate ratio was between 0.31 and 0.4, while it is 0.63 in the present work. Furthermore, the SF used are of different aspect ratio (l /D). It is shown that the slump values in the present work were less than those found in the literature. Moreover, increasing the SF did not decrease the slump significantly. This is because that the reversed effect of the used high quantity of fine aggregate was more than the effect of SF.

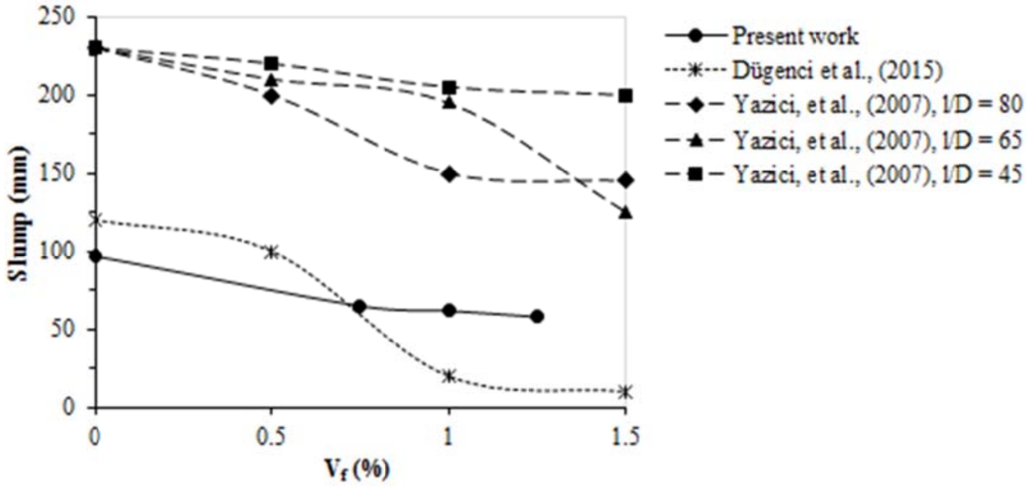

Figure 6.1 Effect of variation of SF dosage and aspect ratio on slump

6.2.2 Concrete compressive strength

After completion of heating and cooling processes, the diameter of the cylinder was checked to ensure that there are no differences in diameters more than 2% according to ASTM C39. The top contact surface with compression machine was capped using melting sulfur mortars.

From Figure 6.2a and Table 3.2 (Chapter 3), it is shown that (f'_c) of the standard cylinders exposed to 150 °C was increased by 10% to 19% compared to its strength at ambient conditions. The aforementioned improvements decreased to about 5% to 8% for the cylinders exposed to 300 °C. This improvement in f'_c after exposing to temperature up to 300 °C is in agreement with findings of Yermak et al. [67,87]. However, increasing the temperature to 450 °C and 550 °C decreased f'_c compared to its strength at ambient condition. The decreasing rate defers based on the used dosages of SF, where the cylinders with 0.75% SF showed less decay (about 9% at 450 °C and 23% at 550 °C) compared to the mixture with 1.0% SF, which was decreased by 23% and 46% at 450 °C and 550 °C, respectively. The mentioned decays are close to those values of the cylinders with 1.25% (17% and 49% at 450 and 550 °C, respectively). This is because the effect of SF bridging was significantly lost due to the formation of macro cracking that induced from excessive pore moisture pressure, which led to the fragile bond between SF and the matrix.

On the other hand, the growth or low rate decay in compressive strength obtained is due to the increasing of the contact surface area of cementitious materials, which leads to the increasing of the rate of reaction process of the components. The activity of the reaction rate is then decreasing after reaching the optimum strength of concrete. The chemical reaction is beyond the research purposes.

Nonlinear regressions of the second order (see Figure 6.2b) were obtained to the effect of high temperatures on the normalized f'_c, which are represented by following equations.

$$f'_c(T)_0 = f'_c\left[\left(-4\times10^{-6}\,T^2\right)+(0.0011T)+1\right] \tag{6.1a}$$

$$f'_c(T)_{0.75} = f'_c\left[\left(-3\times10^{-5}\,T^2\right)+(0.0013T)+1\right] \tag{6.1b}$$

$$f'_c(T)_{1.0} = f'_c\left[\left(-5\times10^{-5}\,T^2\right)+(0.0017T)+1\right] \tag{6.1c}$$

$$f'_c(T)_{1.25} = f'_c\left[\left(-4\times10^{-6}\,T^2\right)+(0.0016T)+1\right] \tag{6.1d}$$

where $f'_c(T)$ is the compressive strength of plain concrete and SFRC that exposed to temperature T, the subscript 0, 0.75, 1.0, 1.25 represent the SF volume fractions.

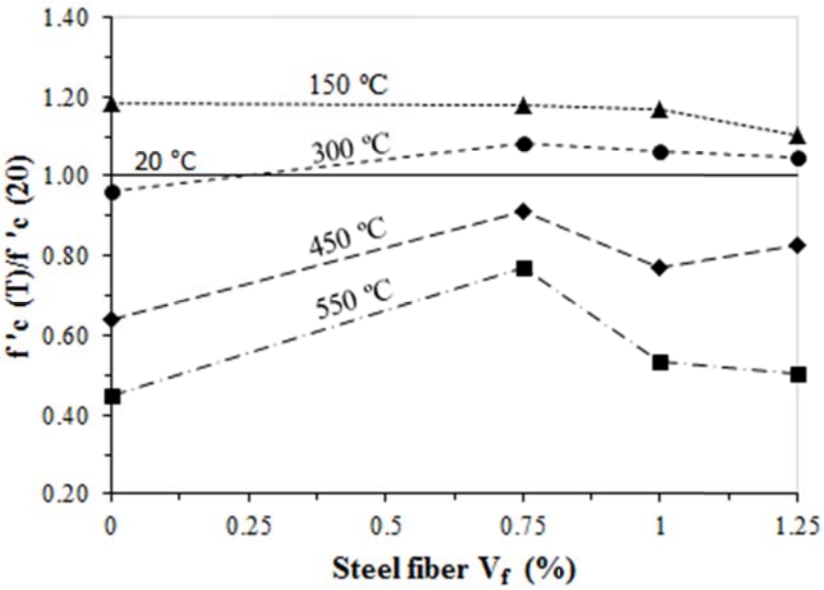

(a)

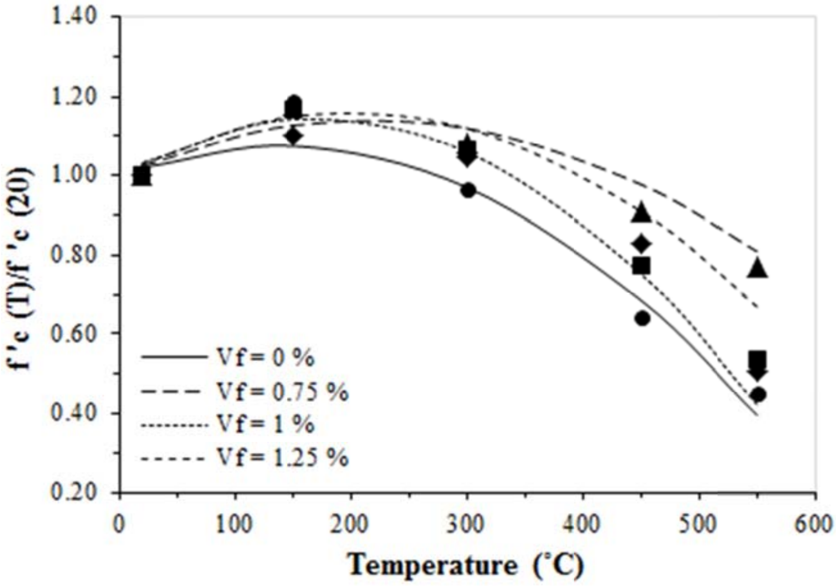

(b)

Figure 6.2 Normalized compressive strength versus (a) SF volume fraction V_f% (b) Exposed temperature

Equation 6.1a of plain concrete that exposed to high temperatures was compared with other references [33,46,47,88] as shown in Figure 6.3. For the standard cylinders exposed to temperatures between 300 °C and 550 °C, the results show that the rates of decay in f'_c are within the formulae in the mentioned references. For the standard cylinders exposed to temperatures less than 150 °C, there was a substantial increase in compressive strength for plain concrete of about 19% of its corresponding strength at ambient conditions. Less improvement (10%) was recorded for specimens with 1.25% SF. This decay in improvement decreases with increasing the temperature, reaching 5% of specimens exposed to 300 °C with 1.25% of SF.

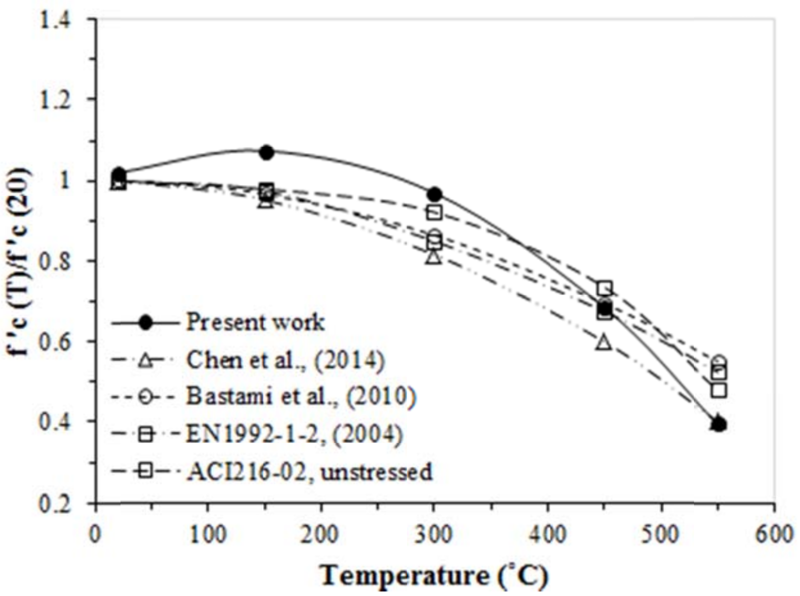

Figure 6.3 Comparison of decay in tested compressive strength of plain concrete due to exposing to high temperatures with different references

6.2.3 Concrete tensile strength

A cylinder splitting test was conducted to represent the tensile strength. Table 3.2 (Chapter 3) shows the test results. Although, the presence of fiber does not always enhance the tensile strength, Di Prisco and Felicetti [117] assume that the Brazilian test cannot well represent the tensile behavior of SF concrete. The tested specimens in the current work showed significant improvement in concrete tensile strength due to bridging activity of SF. Generally, the best improvement in tensile strength was obtained from the inclusion of 1.25% of SF. From Figure 6.4 and Table 3.2, it is shown that the tensile strength of SFRC of 1.25% SF was improved by 13%, 17 %, and 14 % of specimens exposed to 150 °C, 300 °C, and 450 °C, respectively, compared to the plain concrete under the same conditions.

Comparing the decay of tensile strength of plain concrete with that adopted by Eurocode 2 [31] and other reference [118], it is shown that the three decay curves have the same response up to 200 °C. However, the decay rate of tensile strength in the current work is low compared to Eurocode 2 and high compared to that obtained by Faiyadh and Al-Ausi [118]. That means that the splitting tensile strength of high strength concrete is less affected by exposure to high temperatures than that of normal strength concrete. The residual tensile strength, in the current work, of cylinders exposed to 450 °C was 56% compared to 30% adopted by Eurocode 2.

Similar results were obtained for cylinders exposed to 550 °C, where the residual tensile strength was 40% in the present work compared to 10% according to Eurocode 2.

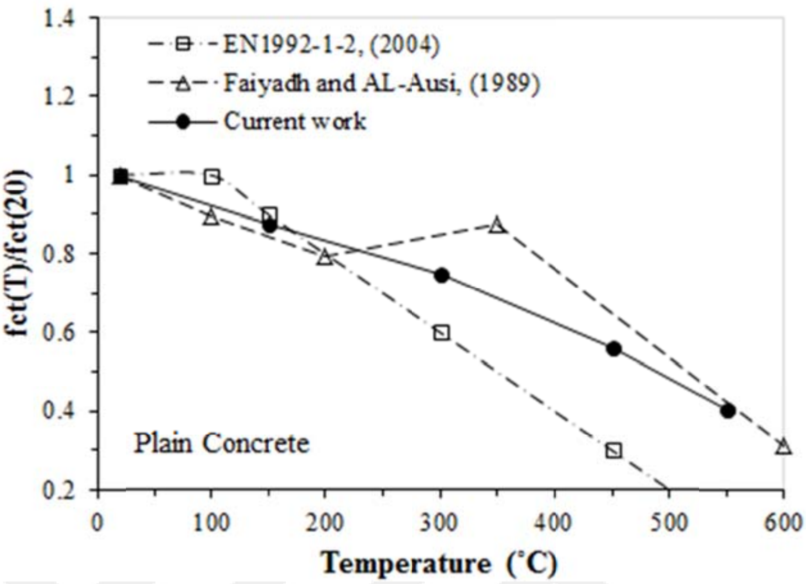

Figure 6.4 Comparison of decay of plain concrete tensile strength obtained in the current work due to exposing to high temperatures with those proposed by EN1992-1-2-2004 and found by Faiyadh and Al-Ausi [118].

6.2.4 Compressive-related tensile strength

As a first step to evaluate the ultimate slab strength similar to that adopted by codes of practice, and in order to justify the large variation of the two strengths ratio (f_{sp}/f_c), it is required to proportion the test results by limit analysis [117]. It is known from Chapter 4 that the codes of practice have different forms of nominal punching shear. The differences are clearly related to the effect of f'_c, where references [19,66,94,95] adopt square root of compressive strength $\sqrt{f'_c}$. In the same context, references [53,93] impose the use of the cubic root $\sqrt[3]{f_c}$. However, Russian code [96] and Turkish code [81] both employ (f_{ct}). In the same manner, Gardner [80] has preferred to use the cubic root as a relation between shear strength and compressive strength.

In general, a correlation between tensile and compressive strength of plain concrete can take the following form,

$$k = \frac{f_{sp}}{(f_c)^n} \tag{6.2}$$

where f_{sp}, and f_c are is the splitting tensile and compressive strengths, k and n are constants determined based on the experimental results. There are many proposed correlations between f_{sp} and f_c. Table 6.1 summarizes the most known codes' proposed correlations.

Table 6.1 Splitting and compressive correlation parameter values according to different codes

Code	k	*n*
EN.1992.1.1-2004	0.3	0.67
ACI318-2014	0.56	0.5
AS3600-2009	0.22	0.5
BS8007-1987	0.12	0.7
TS500-2003	0.525	0.5

Inclusion a SF in the concrete mix affects the relation between the compressive and tensile strength based on the SF percentage. Narayanan and Darwish [119] assume that the splitting tensile strength is related to the compressive strength of standard cubic specimens based on the SF volume fraction and aspect ratio as follows,

$$f_{sp} = \frac{f_{cu}}{20} + 0.7 + \left(V_f\, b_f\, \frac{l_f}{D_f}\right)^{1/2} \tag{6.3}$$

where f_{sp} is the splitting tensile strength, f_{cu} is the compressive strength obtained from standard cubic test, l_f and D_f are the length and diameter of SF, V_f is the SF volume fraction, and b_f is the fiber bond factor based on the fiber type, which equals 0.75 for the hooked-ends SF.

Two more interesting relations are found in literature for SF concrete specimens tested and treated at room temperature. Shaaban and Gesund [70] introduced their correlation by weight of SF (Equation 6.4) based on group of standard cylinders that were consolidated in two different methods (rodding and vibrating).

$$k_1 = \frac{196.25 \times V_f}{w_c} + 0.567 \quad (6.4)$$

De Hanai and Holanda [45] proposed Equation 6.5 based on many mix proportions where the percentage of sand to the total aggregate did not exceed 49%.

$$k_1 = (0.15 \times V_f + 0.51) \quad (6.5)$$

where k_1 is related to $\sqrt{f_c}$, and w_c is the plain concrete unit weight. Equation 6.4 and Equation 6.5 were applied to the current standard specimens of SF that cured and tested under ambient condition as shown in Figure 6.6. It is shown that the obtained experimental results are higher than the resulted values from Equation 6.4. Therefore, it can be modified by increasing the constant value in a linear equation by 67%. This leads to the good representation of the k_1 for the specimens under ambient conditions of the present work. Based on the present experimental results, Equation 6.4 can be modified to the following,

$$k_1 = \frac{196.25 \times V_f}{w_c} + 0.95 \quad (6.6)$$

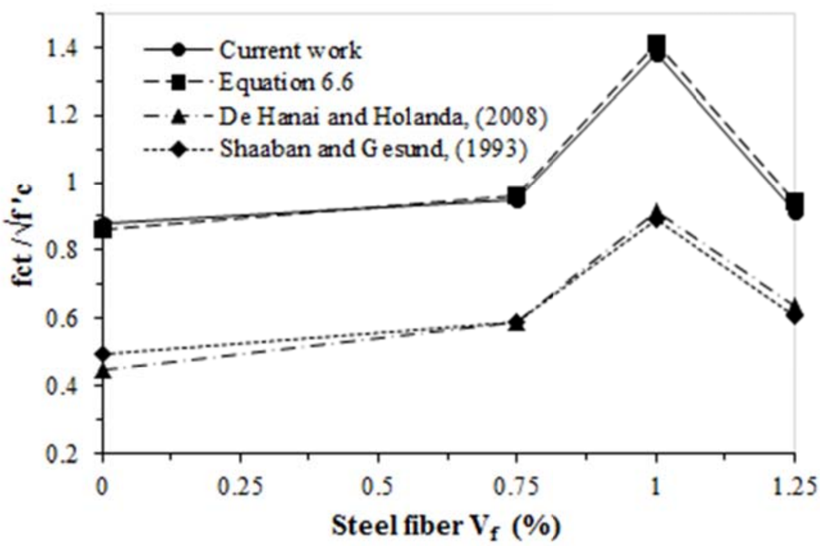

Figure 6.5 Prediction of SFRC strength according to different proposed equations found in the literature

In the same manner, it is shown that the splitting tensile strength of SFRC exposed to high temperatures well represented by the cubic root of the compressive strength $\sqrt[3]{f_c}$ as shown in Equation 6.7. Moreover, the test results showed that the constant k is affected by high temperatures depending on the SF dosage.

$$k_2=\frac{f_{ct}}{\sqrt[3]{f_c}} \tag{6.7}$$

Figure 6.7 shows the relationship between k_2 and the exposed temperature for different SF contents (V_f %). The experimental data were represented by polynomial curves with R^2 = 0.99. In order to produce a consistent relationship, cylinders with 0.75% SF dosage were modified (dashed line in Figure 6.7). This modification is conservatively considered. It is clearly shown that k decreases consistently with increasing the temperature. All curves approach each other gradually until having approximately the same value at 550 °C. It is found that the variation of k can be expressed in terms of SF with the growth of temperature according to the following,

$$k_{2\,(0.75\%)}=\left(-\,17\times10^{-5}\,T^2\right)+(0.061T)+50.814 \tag{6.8a}$$

$$k_{2\,(1.0\%)}=\left(-\,19\times10^{-5}\,T^2\right)+(0.0409T)+67.607 \tag{6.8b}$$

$$k_{2\,(1.25\%)}=\left(-\,22\times10^{-5}\,T^2\right)+(0.0693T)+59.241 \tag{6.8c}$$

where the subscript 0.75%, 1.0%, and 1.25% refer to the SF volume fraction.

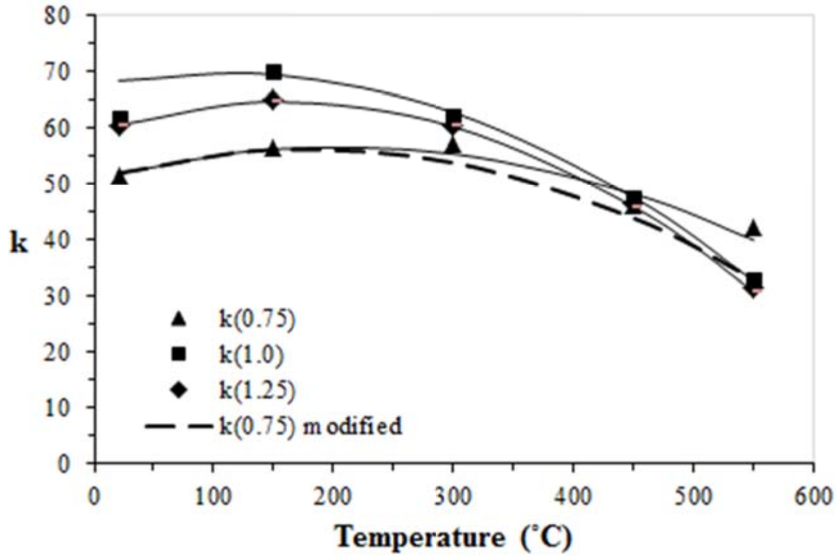

Figure 6.6 Variation of k_2 in Equation 6.7 due to exposing to high temperatures

6.2.5 Concrete modulus of elasticity

Concrete modulus of elasticity (E_c) was measured based on ASTM C469, where f'_c of 100×200 mm standard cylinders that obtained from Section 6.2.2 were considered herein. The specimens were placed in the compressometer that includes two linear variable differential transformers LVDT, which are located in two opposite diametrically lines parallel to the axis and centered at mid height of the tested specimens.

The deteriorations of the modulus of elasticity due to exposing to high temperatures $E_c(T)$ are shown in Table 3.2 and illustrated in Figure 6.8. The comparisons between the $E_c(T)$ of the current work with that proposed decay in $E_c(T)$ by the works found in literature [47,49] are drawn in Figure 6.9.

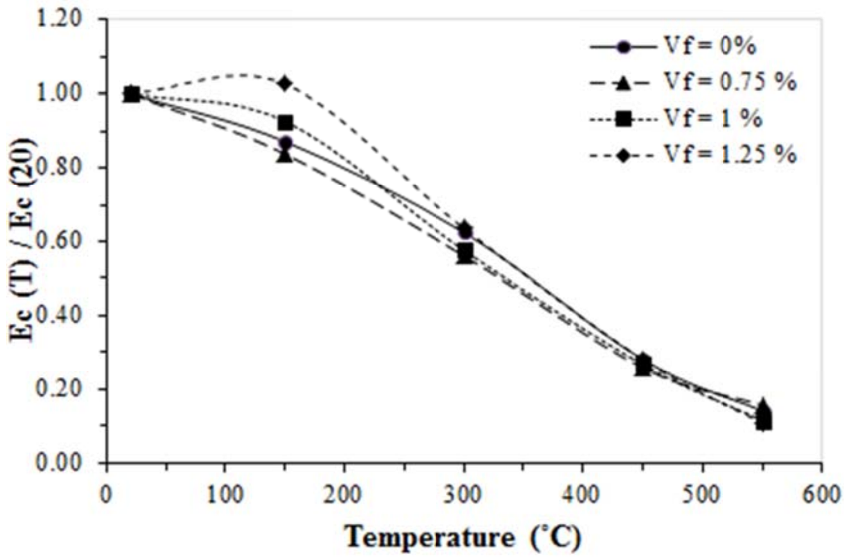

Figure 6.7 Decay of SFRC modulus of elasticity due to exposing to high temperatures

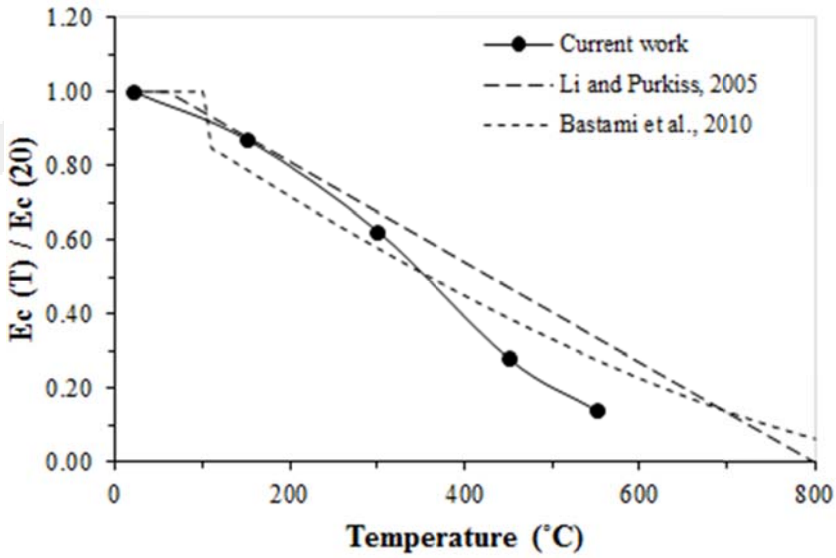

Figure 6.8 Comparison between experimental results with proposed decay curves in modulus of elasticity found in the literature

It is worthy to mention here, that the decay of the mechanical properties of the concrete occurs based on the physico-chemical effects, where some parts of aggregate shows crystalline transformations under high temperatures, moreover the structure of the concrete is broken down. From the chemical effects, the high temperatures change the chemical composition, which leads to change in the microstructure of the particles of the produced concrete. The variations in the composition and the structure occur gradually with continuous variation in the phases at temperatures up to 1000 ºC. Naus [51] found that at ambient conditions, 2 to 10% of concrete includes free water that is evaporable. At low heating rates and low temperatures (up to 105 °C), the free water is driven off. The velocity of vapor bases on the concrete density and the composition phase. Approximately 60 to 64% of the free water can be lost after seven days exposing to constant temperature of 105 °C [85]. Increasing the temperature beyond 400 ºC would significantly affect the rate of losing the hydration water. In this temperature, the calcium hydroxide is still not dehydrated [51], beyond 535 °C the dehydration rate increases up to 850 °C where the dehydration can be completed.

6.3 Ultimate Slab Strength

Twenty slabs of 500×500 mm dimensions and with 60 mm thickness were exposed to different target temperatures. All specimens were tested under monotonically increasing concentric loading until failure. The load was applied through a steel plate of 55 mm size. Table 6.2 shows the test results of the flat plate-column concentric connection. Figure 6.10 shows the normalized strength load vs the SF volume fraction.

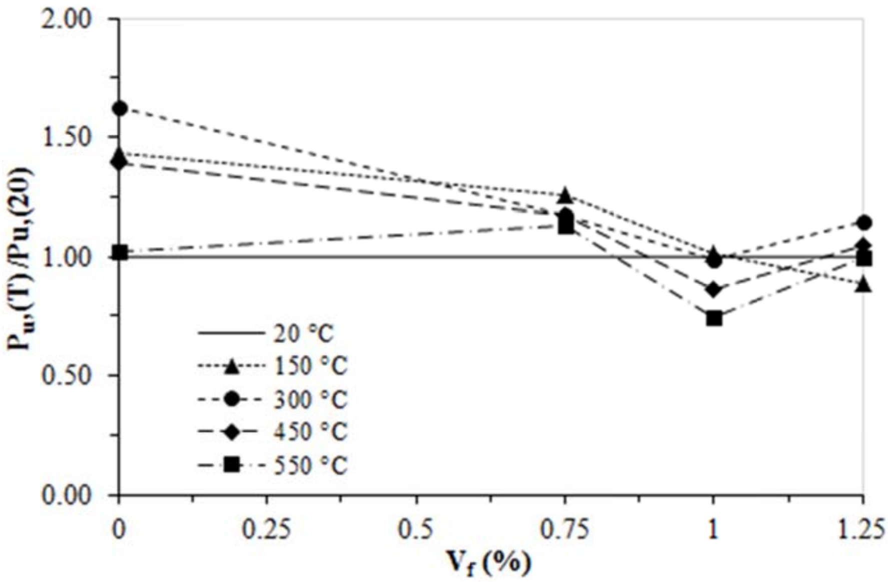

Figure 6.9 Residual strength of SFRC exposed to high temperature

The strength of the normal concrete slabs was increased due to exposing to high temperatures, where the slab exposed to 300 ºC the ultimate resisting load is increased 63 % compared to slab resistance load at exposed to ambient conditions. The inclusion of SF (for most percentages) decreased the rate of load resistance up to 550 ºC. However, the strength of almost all slabs with 0.75 and 1.25 % of SF increased due to exposing to all temperature levels. The highest increment percentage was 26%. However, two slabs with 1.25% of SF showed reduction in their ultimate strengths at 300 and 450 ºC compared to control slab (at ambient condition). Different behavior is recognized in slabs with 1.0% of SF, where the strength of the slabs at all temperature levels was reduced compared to the corresponding slabs at ambient conditions. This confirms the results of the compressive strength of the standard cylinders (see Figure 6.2), the decadent strength reached 25% for slabs exposed to 550 ºC.

Table 6.2 Experimental characteristics of SFRC flat plates

Spec.	P_u (kN)	δ_1 [(1)] (mm)	$\frac{P_u}{P_{flex}}$ [(2)]	$\frac{P_u(T)}{P_u(20)}$	Failure[(3)] type	Punching shape	$r_{0,\,test}$ [(4)] (mm)	Angle of failure (deg.)
P0	63.4	4.0	0.99	1.00	P	Circle	162	24
P0.75	78.8	3.7	1.22	1.00	P	Circle	160	18
P1	94.8	4.8	1.08	1.00	P	Circle	189	20
P1.25	93.3	4.0	1.43	1.00	P	Circle	179	18
A0	91.1	4.0	1.39	1.14	P	Ellipse	218	17-18
A0.75	99.0	3.8	1.52	1.26	P	Circle	170	20-27
A1	95.8	3.5	1.46	1.34	P	Circle	180	21
A1.25	82.9	2.8	1.27	0.89	P	Circle	195	19
B0	103.2	3.8	1.59	1.30	F	-	-	-
B0.75	92.4	4.0	1.42	1.17	F	Ellipse	170	-
B1	93.7	4.3	1.43	1.31	P + F	-	185	-
B1.25	106.9	4.4	1.64	1.15	F	-	-	-
C0	88.5	5.8	1.40	1.11	P	Ellipse	200	19-22
C0.75	92.5	5.9	1.44	1.17	P	Circle	160	27-29
C1	82.1	4.9	1.27	1.15	P	Circle	180	21
C1.25	98.1	5.7	1.52	1.05	P	Ellipse	200	19-21
D0	65.0	4.7	1.06	0.82	P	Circle	180	22
D0.75	89.2	6.2	1.40	1.13	P	Square	180	27
D1	70.6	3.2	1.12	0.99	P	Circle	190	20
D1.25	93.1	4.8	1.49	1.00	P + F	Circle	200	19

(1) δ_1 are the displacement at the center that corresponding to ultimate loads $P_{u,\,test}$

(2) P_{flex} calculated according to Equation 3.7

(3) Prefer to punching shear failure and, F refers to flexural failure

(4) Radius of the critical punching crack taken as the longest size in ellipse and square

In order to assess the SF effectiveness, the SFRC slabs' residual strength P_u,(T) was compared with the residual strength of plain concrete slabs ($P_{u,\ control}$). The comparison results are illustrated in Figure 6.11 and Table 6.2. It is shown that the inclusion of 0.75 and 1.25% of SF slightly increased or at least maintained the same strength of the normal concrete, whereas the inclusion of 1.0% of SF played a negative role, particularly at the highest temperature. The variation of SF effectiveness may be attributed to the phase behavior of the matrix with higher cement and fine aggregate contents (the concrete mix used in the current work). The chemical behavior of the cement and the other binders is beyond the research scope.

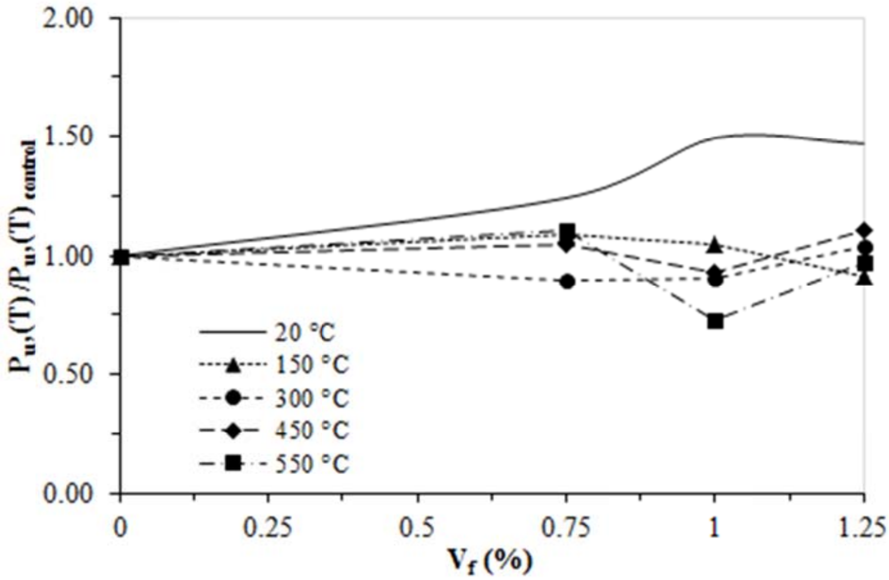

Figure 6.10 SF effectiveness in slabs exposed to high temperatures

6.3.1 Comparisons of test results with different codes' equations

The comparison results are shown in Figure 6.12. All codes underestimate the ultimate strength with high safety factors, where the maximum and minimum predictions reach to 234% and 61%, respectively, whereas the safety factor introduced in all codes ranges from 65% to 75%. There are some missing bars in Figure 6.12 because the compressive strength values exceeded the actual compressive strength required in the associated code. For example, $\sqrt{f'_c}$ of specimen A1 is more than 8.3 MPa, so that it does not satisfy the conditions of both [19,66].

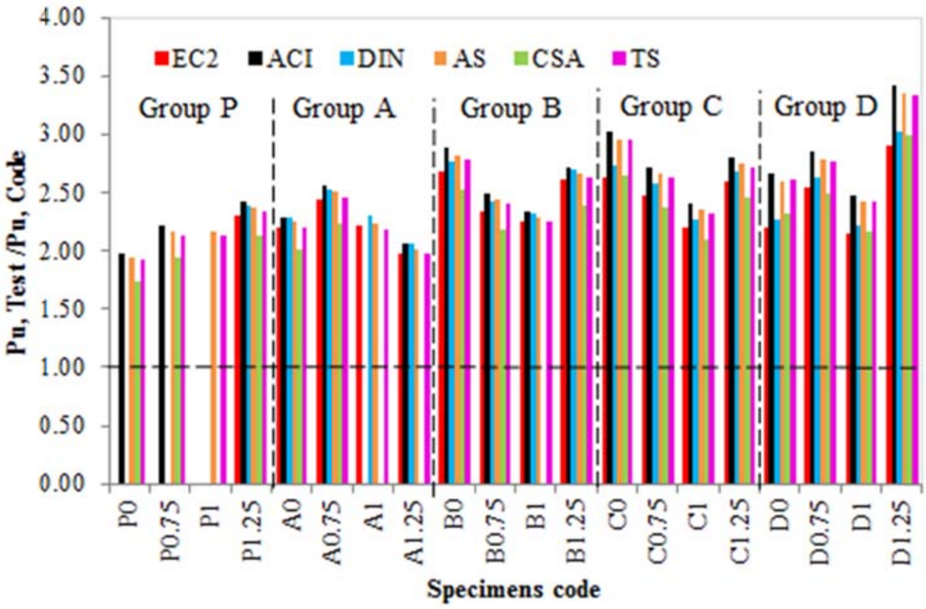

Figure 6.11 Experimental ultimate slab strength compared to different codes proposed equations

6.3.2 Comparison of tested results with proposed equations found in literature

In addition to Equations 3.3, 3.4, and 3.5, which are derived based on ACI318, there is an interesting equation proposed by Narayanan and Darwish [119]. This equation includes the slab size, reinforcement ratio, SF volume fraction, and aspect ratio, and is as follows,

$$P_u = \xi_s u_b d \left(0.24\, f_{sp} + 16\rho + 0.41\tau_{uf}\, V_f\, d_f\, \frac{L}{D}\right) \quad (6.9)$$

where ξ_s is the slab size effect that is equal to:

$$\xi_s = 1.6 - 0.002h$$

u_b is the critical punching perimeter that is also affected by the inclusion of SF so that,

$$u_b = \left(1 - 0.55 V_f\, d_f\, \frac{L}{D}\right)(\pi c + 3\pi h)$$

τ_{uf} is the bond stress of the fiber-matrix interfacial that is assumed equal to 4.15 MPa, and f_{sp} is the splitting tensile strength obtained from Equation 6.3. The conversion of the standard cylinder compressive strength to the standard cube strength is according to Eurocode 2 provisions.

The current tested results are used to assess the available predictions of Equations 3.3, 3.5, 6.9, and 3.4 that are proposed by Shaaban and Gesund [70], De Hanai and Holanda [45], Narayanan and Darwish [119], and Harajli et al. [82], respectively. The comparison results are summarized in Table 6.3 and illustrated in Figure 6.13. The bars in this figure are arranged in an ascending order according to their conservatively, where Equation 3.3 is the less and Equation 3.4 is the highest conservative. Generally, all the mentioned methods underestimate the ultimate strength of the tested slabs, where the safety factors range between 8 and 100% using Equation 3.3. However, the safety factor ranges between 68 and 212% using Equation 3.4.

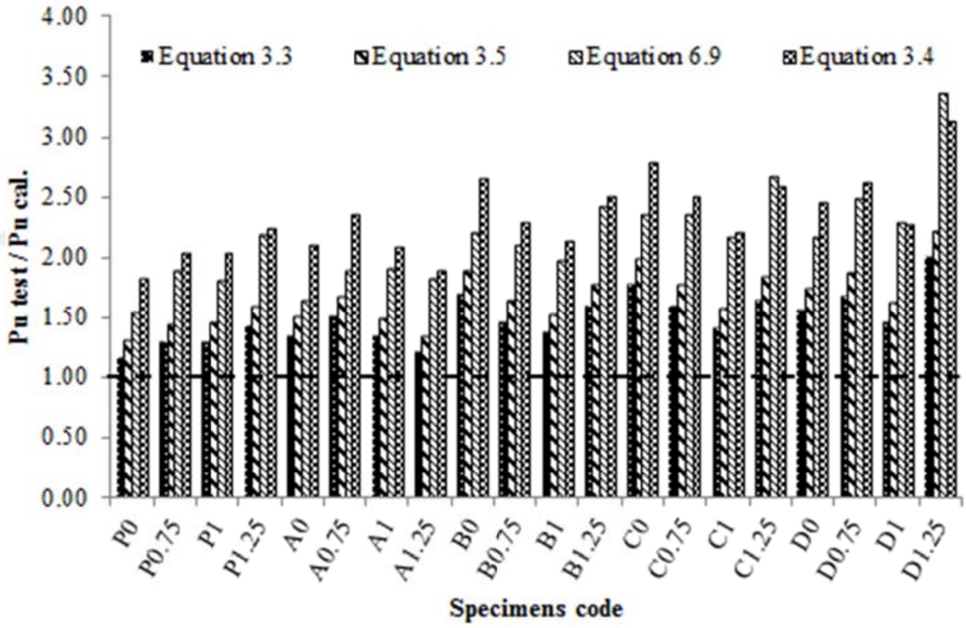

Figure 6.12 Comparison of the test results with calculated predictions based on available equations

Table 6.3 Comparison of the test results with calculated predictions based on available equations

Speci.	SF V_f %	Temp. °C	$P_{u,\ test}$ kN	$\frac{P_{u,\ Test}}{P_{u,\ (Eq.\ 3.3)}}$	$\frac{P_{u,\ Test}}{P_{u,\ (Eq.\ 3.4)}}$	$\frac{P_{u,\ Test}}{P_{u,\ (Eq.\ 3.5}}$	$\frac{P_{u,\ Test}}{P_{u,\ (Eq.\ 6.9)}}$
P0	0	20 °C	63.41	1.16	1.82	1.29	1.53
P0.75	0.75		78.80	1.30	2.02	1.44	1.88
P1	1		94.78	1.3	2.03	1.44	1.79
P1.25	1.25		93.28	1.43	2.22	1.58	2.18
A0	0	150 °C	91.10	1.35	2.10	1.50	1.64
A0.75	0.75		98.95	1.50	2.34	1.67	2.07
A1	1		95.81	1.34	2.08	1.48	1.90
A1.25	1.25		82.86	1.21	1.88	1.34	1.82
B0	0	300 °C	103.23	1.69	2.64	1.88	2.19
B0.75	0.75		92.45	1.46	2.28	1.62	2.09
B1	1		93.66	1.37	2.13	1.52	1.96
B1.25	1.25		106.88	1.60	2.49	1.77	2.42
C0	0	450 °C	88.50	1.78	2.78	1.98	2.35
C0.75	0.75		92.48	1.59	2.49	1.77	2.35
C1	1		82.08	1.41	2.20	1.56	2.17
C1.25	1.25		98.06	1.65	2.57	1.83	2.66
D0	0	550 °C	64.99	1.56	2.44	1.74	2.17
D0.75	0.75		89.23	1.67	2.61	1.86	2.47
D1	1		70.65	1.45	2.27	1.61	2.29
D1.25	1.25		93.10	2.00	3.12	2.22	3.36

6.3.3 Analytical investigation

As mentioned previously, there are some differences regarding the parameters that are considered in each code. Since the specimens in the present work are of the same dimensions and reinforcement ratio, then the ultimate punching shear capacity can be characterized by a function of compressive strength (τc). Equation 6.10 shows the typical form of the relation between the ultimate strength of the flat slab-column connections and the SF dosage,

$$\frac{P_u}{\sqrt{f'_c}b_o d} = (a \times V_f) + c \tag{6.10}$$

Firstly, the parameters of Equation 6.10 are found from the tested results of slabs at ambient conditions (Group P). Moreover, results and data found in the literature [45,69,82,119,120] are also employed. The normalized ultimate strength is then drawn in terms of the SF volume fraction (V_f) as shown in Figure 6.14.

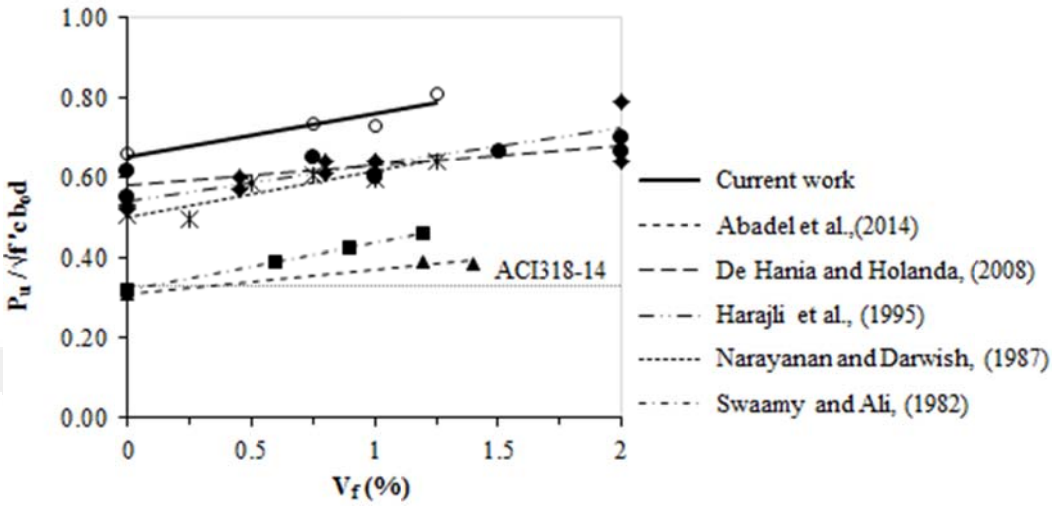

Figure 6.13 Comparison of the normalized ultimate strength with data collected from the literature (a) with reinforcement ratio effect (b) without the effect of reinforcement ratio

The comparison showed that inclusion of SF generally increases the maximum strength. The normalized ultimate slab strength enhanced by increasing the SF dosage at the same rate. This can be represented by a linear regression, analog to Equation 6.10, where a is the rate (trend lines slope) of normalized strength, which can be averaged to 0.1, which is also found by [45,69,119], and c is a constant that is depends on the normal concrete compressive strength and many variables, such as test setup, column size, and the relative size. The comparison between the results obtained in the current work and the mentioned references in Figure 6.14 shows that the mentioned results have approximately the same slope based on the type and the aspect ratio of the SF. However, as mentioned before, the c value differs in a lower manner by 10% of that obtained from the results of the current work, which equals 0.65. It is worthy to mention here that the 10% variation is attributed to the type of support, which is clearly shown in specimens obtained from Abadel et al. [120]. These specimens are restrained by two edges of the slab. The distributions of the stresses also play important roles herein, where the results of tested slabs in the current work are more regular because of the greater amount of fine aggregate. The data collected from the mentioned references are listed in Appendix C

It shows from Section 5.4.2, that the compressive strength obtained from standard cylinder is based on the heating level and soak time. The variation of the standard cylinder size due to exposing to three dimensions of heating is highly effected the slab strength. In other word, the relation between the nominal shear strength equation and the compressive strength under ambient condition is not similar to those under high temperature conditions. Applying the square root of compressive strength to heated slabs provides meaningless relations. Moreover, Eurocode 2 has adopted the cubic root of compressive strength $\sqrt[3]{f_c}$, in shear equation (Table 4.2). Therefore, the variation ultimate resisting strength P_u (V_f, T) (due to SF dosage and temperature) of the tested slabs are drawn in terms of cubic root of the compressive strength as shown in Figure 6.15a. A second polynomial regression of the tested specimens leads to following relationships,

$$P_u(0\%, T) = (f'_c)^{1/3}\left[\left(-13\times10^{-5}\,T^2\right) + (0.075T) + 16.689\right] \quad (6.11a)$$

$$P_u(0.75\%, T) = (f'_c)^{1/3}\left[\left(-4.7\times10^{-5}\,T^2\right) + (0.0293T) + 21.513\right] \quad (6.121b)$$

$$P_u(1.0\%, T) = (f'_c)^{1/3}\left[\left(-5.8\times10^{-5}\,T^2\right) + (0.0242T) + 21.8\right] \quad (6.131c)$$

$$P_u(1.25\%, T) = (f'_c)^{1/3}\left[\left(-7\times10^{-5}\,T^2\right) + (0.0395T) + 21.5\right] \quad (6.141d)$$

From Figure 6.15a, it is clear that the exposing to 300 °C increased the ultimate slab resistance for normal concrete slab. As mentioned previously, the slabs that include SF behave in a stable manner, where the slab resistance increased in low rate up to 300 °C and then decreased at the same low rate. Slabs of 0.75% and 1.25% of SF showed high residual strength compared to that of plain concrete and that with 1.0% SF. This is confirmed by the cylinder test results that are illustrated in Figure 6.2 and 6.4. However, Figure 6.15b shows that the rate of variation in the ultimate strength due to exposing to temperature ($\frac{\Delta Pu}{\Delta T}$) for the specimens of plain concrete are higher than of SFRC. The equations govern the residual strength of the punching shear of the slabs exposed to high temperature is as follows,

$$P_u(0\%, T) = P_u(0\%, 20)\times\left[\left(-9\times10^{-6}\,T^2\right) + (0.0052T) + 0.88\right] \quad (6.15a)$$

$$P_u(0.75\%, T) = P_u(0.75\%, 20)\times\left[\left(-1.9\times10^{-6}\,T^2\right) + (0.0013T) + 1\right] \quad (6.12b)$$

$$P_u(1.0\%, T) = P_u(1.0\%, 20)\times\left[\left(-2\times10^{-6}\,T^2\right) + (0.0006T) + 1\right] \quad (6.12c)$$

$$P_u(1.25\%, T) = P_u(1.25\%, 20)\times\left[\left(-2\times10^{-6}\,T^2\right) + (0.0011T) + 0.98\right] \quad (6.12d)$$

where the $P_u(0\%, 20)$ is the ultimate punching strength, which can be any of the codes' equation for specimen of plain concrete, while Equation 6.10 can be used for SFRC under ambient conditions.

(a)

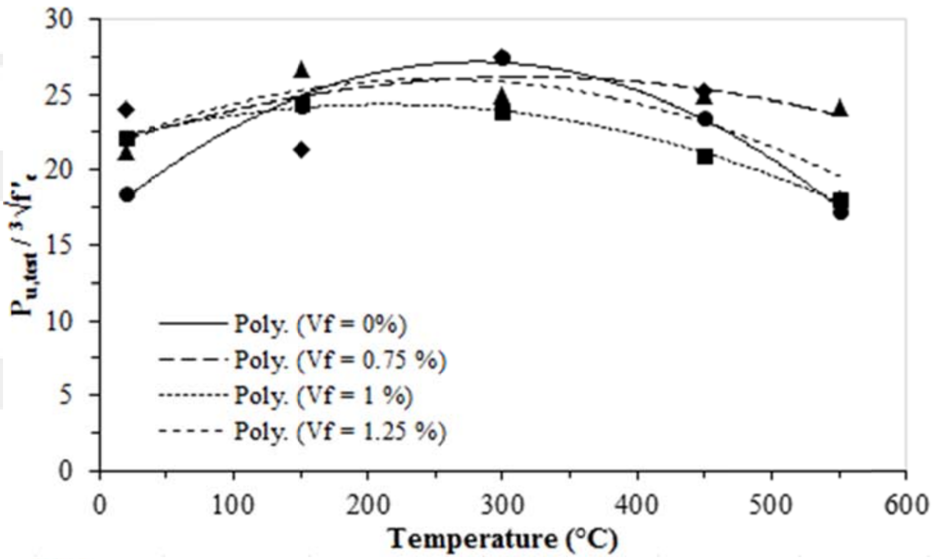

(b)

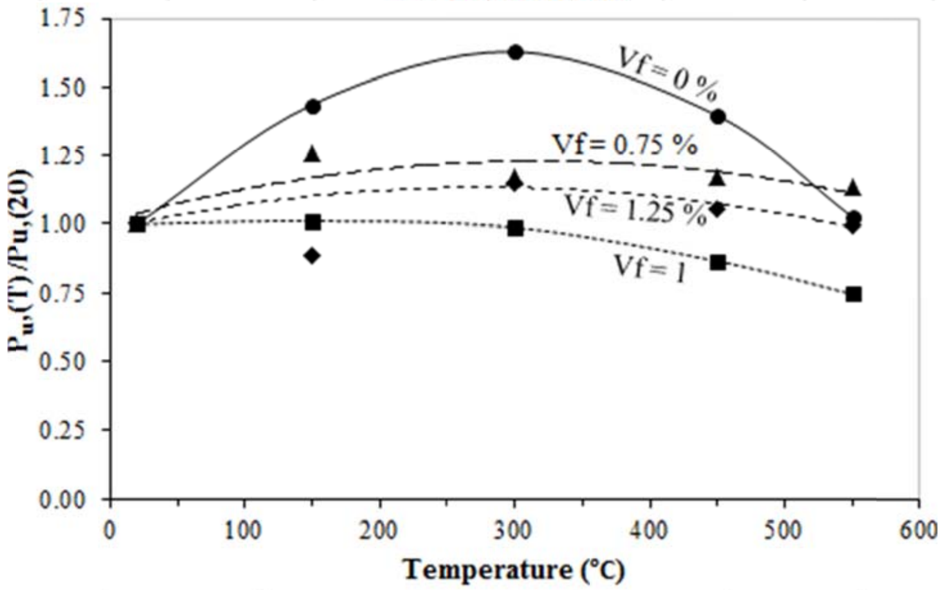

Figure 6.14 The effect of high temperatures on the ultimate loads of tested SFRC flat plates

6.4 Load-Deflection Behaviors

Two LVDTs were attached to each specimen. The first LVDT was positioned at the mid-span of the slab directly beneath the column, whereas the second LVDT was located at 110 mm from the center of the slab (2d from the column face). The deflections obtained from the LVDTs are symbolized by δ_1 and δ_2. The highest values were obtained from δ_1 for all tested slabs. Figure 6.16 depicts for the effect of SF volume fraction on the deflections along the slab half span. Moreover, Figure 6.17 summarizes the load-δ_1 curve (LVDT at the center of the slab) of all groups according to their maximum exposed temperature.

Except Group B (slabs exposed to 150 ºC), the curves obtained from load displacement relations exhibited sharp increments to the failure load and then followed by gradual softening. This means that the mentioned slabs failed due to brittle cracking of concrete, whereas the specimens of Group B failed by the plasticity of steel or concrete. It is shown that the SF has significantly reduced the specimen deformation. This agrees with [69] finding. Again, except Group B (see Figure 6.17c), the specimens with 1.25% showed the highest $(\frac{\Delta Pu}{\Delta\delta})$, i.e. lower deformations at all loading stages. This means that the enhancing of the ductility by SF contributed to the high temperature ductility effect, where specimens with 1.25% SF can sustain the highest deformations in addition to enhancing the failure load. Whereas specimens with 0.75% and 1.0% showed almost the same behaviors for specimens exposed to temperatures higher than 300 °C. It is worthy to mention here that B0 (specimen without SF) at 300 °C shows unexpected behavior after 50% of the failure load. This may be due to the laying on the excessively spalled part, knowing that the specimens in Group B showed flexural failure.

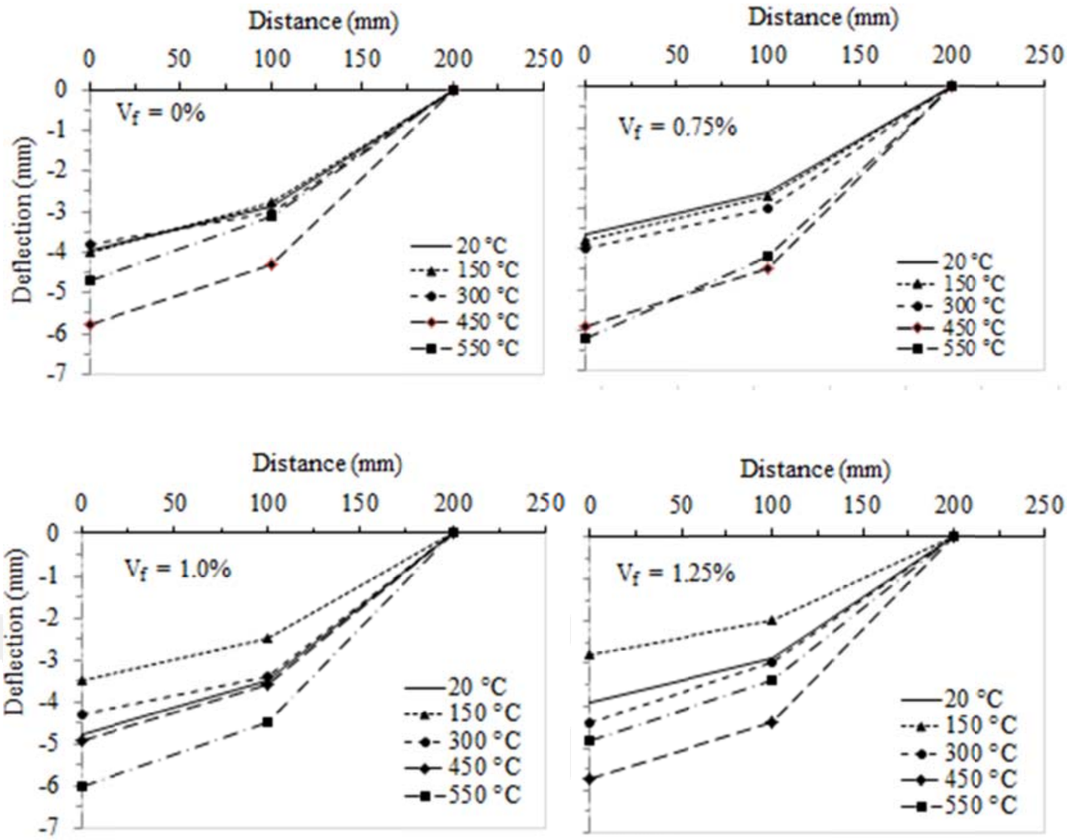

Figure 6.15 Deflections along the slab width

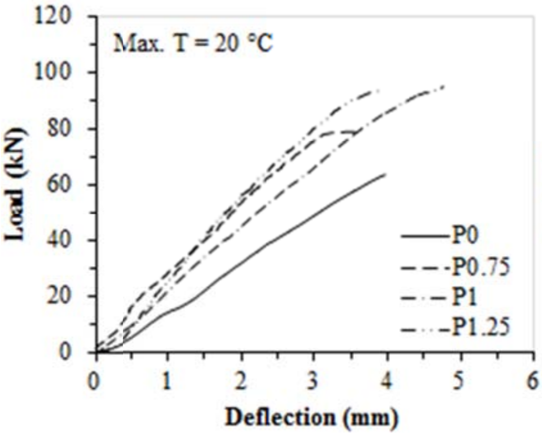

(a) Group P (ambient conditions)

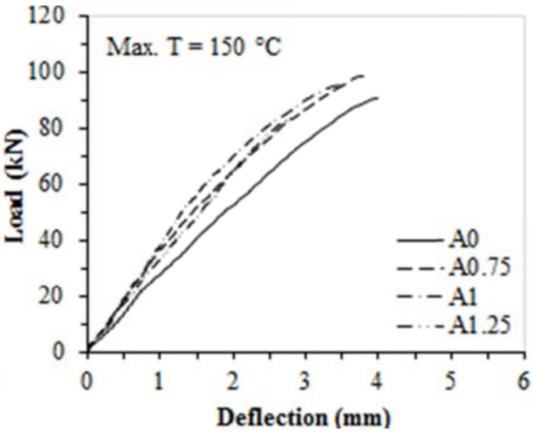

(b) Group A (exposed to 150 ºC)

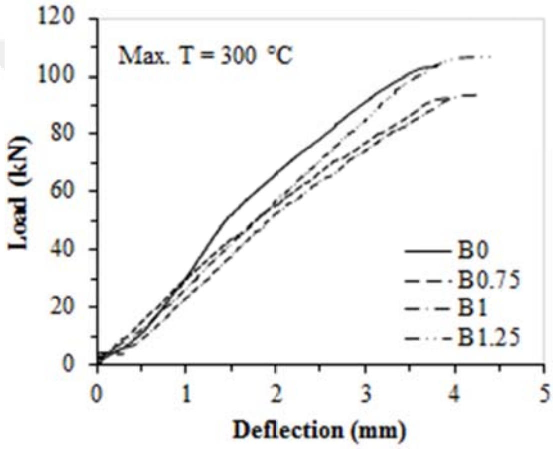

(c) Group B (exposed to 300 ºC)

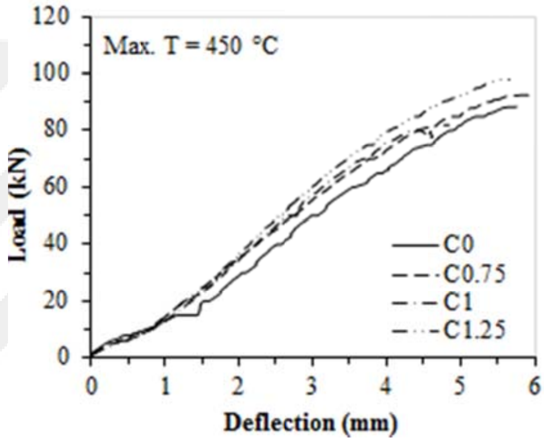

(d) Group C (exposed to 450 ºC)

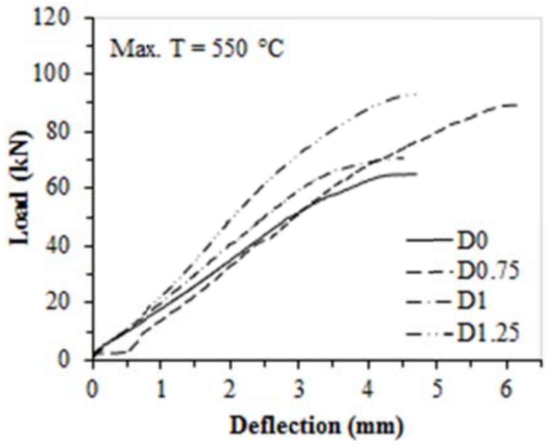

(e) Group D (exposed to 550 ºC)

Figure 6.16 Load-deflection curves for slabs exposed to (a) 20 ºC (b) 150 ºC (c) 300 ºC (d) 450 ºC (e) 550 ºC

6.5 Failure Mode

At the end of the test, the failed specimens were removed from the test machine, the type of failures was checked, the actual critical radius were measured, and type of failures were classified visually as listed in Table 6.2. The hair cracks in some specimens were indicated by red marker for a better visibility as shown in Figures 6.18 to 6.22. In spite that the slabs are designed to fail in punching, at the tension face of the slabs, many types of failures can be recognized based on the effect of the SF used and the level of temperatures that were applied. At the compression face, there were no cracks. This may be due to the confining of the compression stresses. For the Group P (under ambient conditions), all of the four slab specimens of plain concrete (in different temperature levels) were failed in punching with uncompleted circular failure surfaces and showed extensive spalling, where wide parts have fallen. This is because of the intersection between the flexural and punching cracks that confirmed the design purposes. The angle of shear cracks ranged between 17° and 22°. These angles slightly increased with increasing the temperature level. The same behavior was shown in specimens P0.75 and P1.25 (0.75% and 1.25% SF) but with incomplete punching behavior that allowed the propagation of flexural cracks to reach the edges of the slab.

Pure punching failure was shown in the specimens of Groups A and C that were exposed to 150 °C and 450 °C, respectively. However, with significant differences in hair cracks density, where the higher temperature in Group C increased the hair cracks and the spalling thickness with falling down in some parts of concrete in specimens of plain concrete (A0 and C0).

Significantly different behavior was shown in Group B that exposed to 300 °C (see Figure 6.20), where a pure flexural failure was recognized in some tested slabs such as in specimens B0 of plain concrete and B1.25 of 1.25% SF. Moreover, incomplete punching cracks and small spalling thickness that is associated with the flexural cracks were shown in specimens B0.75 and B1 that include 0.75% and 1.0% of SF, respectively.

In Group D, where the specimens exposed to 550 °C, excessive spalling was shown in the specimen D0 of plain concrete. The color of concrete in the exterior peels changed to light brown for more than 20 mm thickness and wide parts along the thickness can be easily removed by hand. The inclusion of different dosages of SF (D0.75, D1, and D1.25) prevented these parts from falling down despite of the thermal and load stresses that lead to increase the hair cracks.

It can be concluded that the inclusion of SF did not significantly affect the failure shape, which agrees with the conclusion of reference [84]. The inclination of cracks with the horizontal axis for the tested specimens under ambient conditions (Group E) were 17-22 degree, which agrees with references [80,84]. However, the crack inclinations of the SFRC specimens with 0.75% SF that exposed to high temperatures reached up to 37 degree.

P0, Normal Concrete

P0.75, SFRC, V_f = 0.75%

P1, SFRC, V_f = 1.0%

P1.25, SFRC, V_f = 1.25%

Figure 6.17 The failure pattern of slabs in Group P (exposed to ambient conditions)

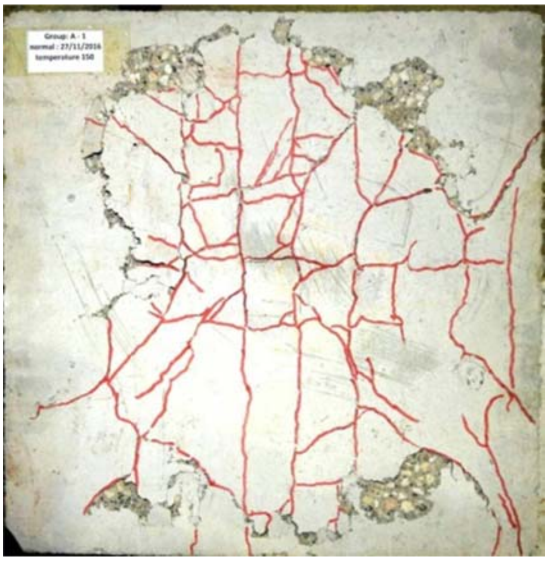

A0, Normal Concrete

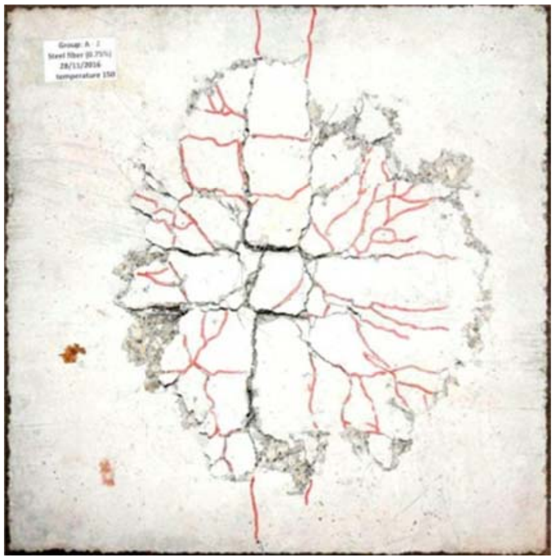

A0.75, SFRC, V_f = 0.75%

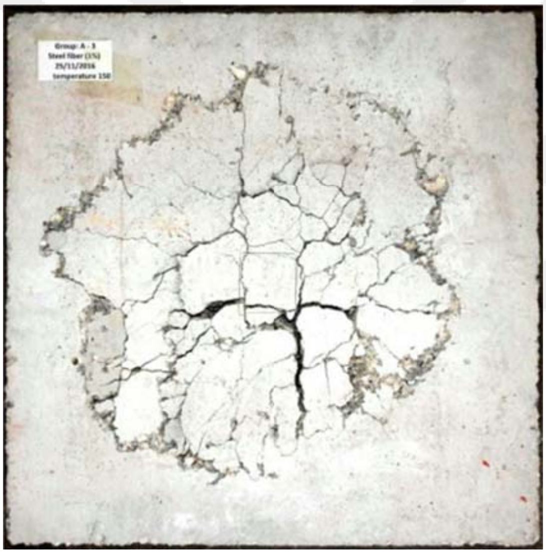

A1, SFRC, V_f = 1.0%

A1.25, SFRC, V_f = 1.25%

Figure 6.18 The failure pattern of slabs in Group A (exposed to 150 ºC)

B0, Normal Concrete

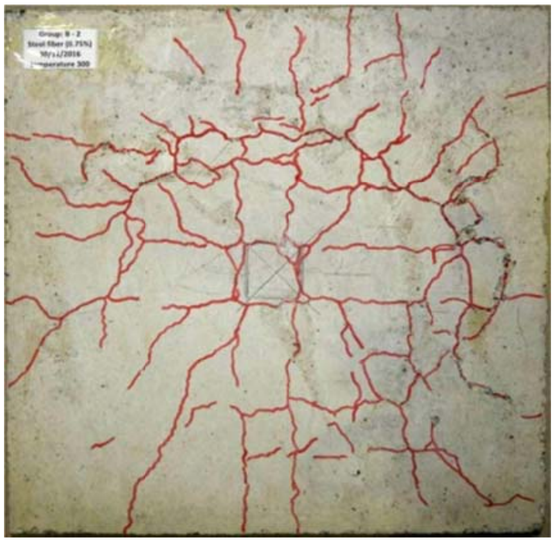

B0.75, SFRC, V_f = 0.75%

B1, SFRC, V_f = 1.0%

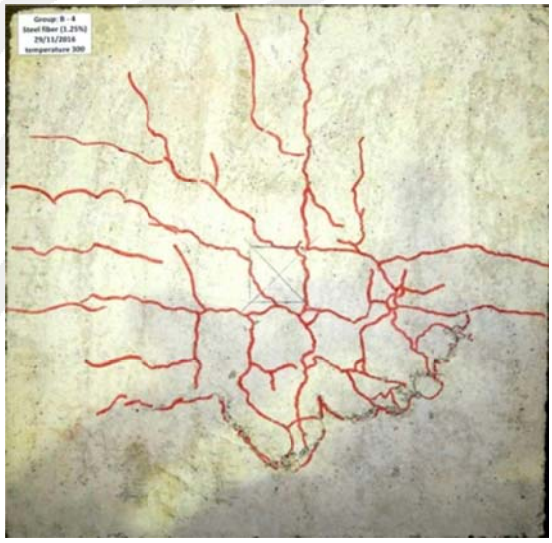

B1.25, SFRC, V_f = 1.25%

Figure 6.19 The failure pattern of slabs in Group B (exposed to 300 ºC)

C0, Normal Concrete

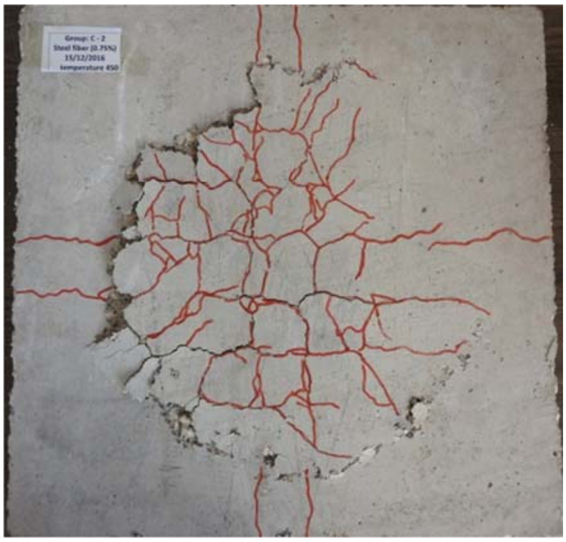

C0.75, SFRC, V_f = 0.75%

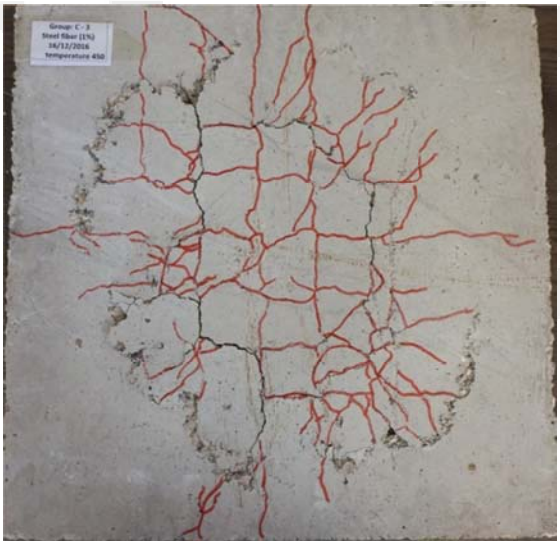

C1, SFRC, V_f = 1.0%

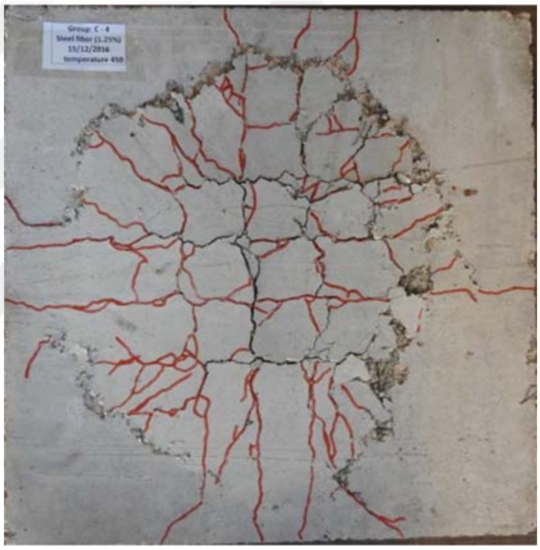

C1.25, SFRC, V_f = 1.25%

Figure 6.20 The failure pattern of slabs in Group C (exposed to 450 ºC)

D0, Normal Concrete

D0.75, SFRC, V_f = 0.75%

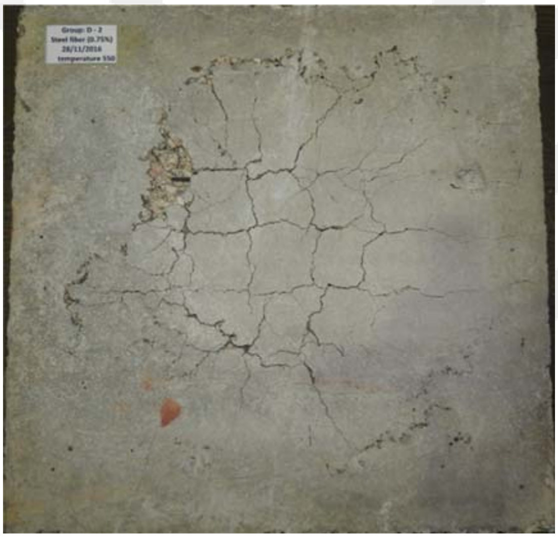

D1, SFRC, V_f = 1.0%

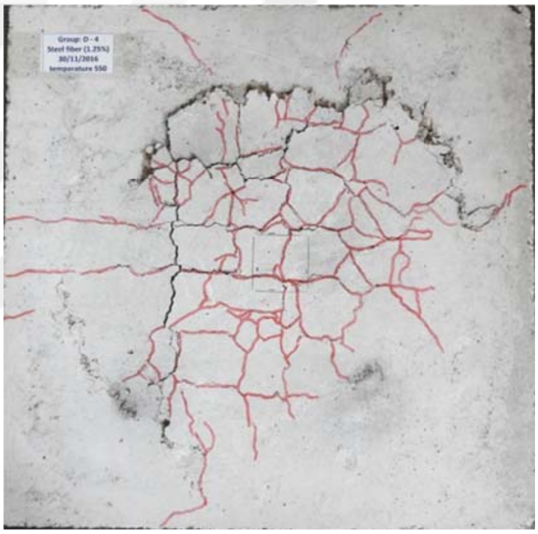

D1.25, SFRC, V_f = 1.25%

Figure 6.21 The failure pattern of slabs in Group D (exposed to 550 ºC)

CHAPTER 7

FINITE ELEMENTS MODELING, THEORY, AND INPUT PARAMETERS

7.1 Introduction

It is apparent that, concrete structures usually do not behave in a way consistent with the assumptions of classical continuum mechanics [121]. Therefore, the classical techniques of strength of materials could not describe the concrete behavior adequately. As an example of this problem is, in a tension field, the stress at the tip of a crack tends to infinity if the material is assumed elastic. Since no material can sustain infinite stress, a region of inelastic behavior must therefore surround the crack tip. Therefore, a correct analysis of many concrete structures must include the ideas of fracture mechanics [121].

Two basic approaches can recognize to model the phenomena of cracking or concrete fracture, namely the discrete fracture and smeared cracking approaches, in the former model, the crack were presented by means of severity and separation between element edges, while in the latter approach, the simulation of distribution of micro cracks as a defect under strain softening formulation of an approach equivalent continuum. There are different methodology using smeared approaches, one that most commonly used is the theory of plasticity. This theory can be a good option if the representation of concrete behavior in macrocracking stages is accurate enough. However, in the microcracking stage, this theory will be difficult to apply. This task can be better solved by using the plastic damage approach.

Fortunately, there were many fracture mechanics approaches have been introduced by FE analysis. The former provide the fundamental of initiation and propagations of cracks, whereas the latter gives the possibility of extending these fundamental to apply it for complex cases. Example of these approaches are, stress intensity factor approach, the energy balance approach, Dugdale model [122], Barenblatt model [123], and fictitious-crack model [124].

In this chapter the model that proposed by Lubliner, et al. [125] and the latter modified by Lee and Fenves [126] are discussed. Parameters that are included in this model are considered in order to match the behavior of concrete under high temperature. Moreover, the choice of the relevant RC mechanical and thermal properties, the geometry and meshing, the modeling of materials under ambient and high temperature conditions, solving technique, and analysis strategy are also presented.

7.2 Concrete Damages Plasticity Model

An irreversible strain in stress-strain behavior of concrete that appears in reality is difficult to be represented in many theories, like, elastic damage and elastic-plastic laws. These difficulties can be seen in the unloading part of the constitutive behavior of concrete, e.g. in the elastic damage approach, there is no residual strain can be captured; however, this strain is overestimated in the elastic-plastic damaged model. Figure 7.1 illustrates the aforementioned argument.

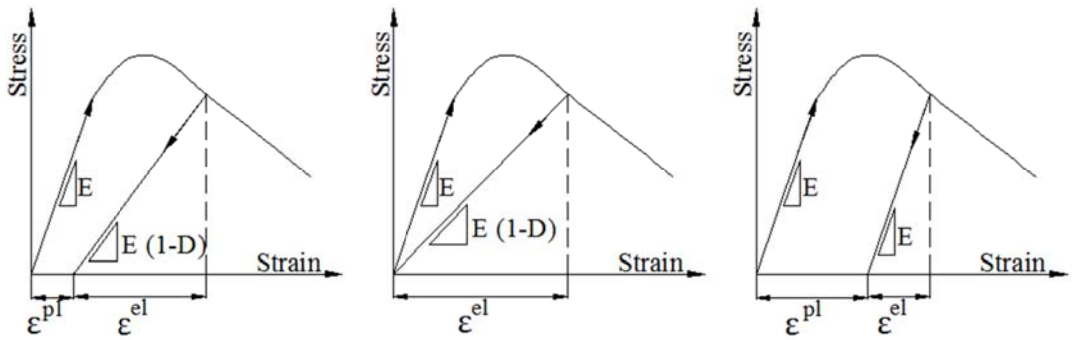

(a) (b) (c)

Figure 7.1 Constitutive behavior of concrete, a) real behavior b) elastic damage c) elastic-plastic law.

Concrete Damages Plasticity (CDP), can be one of the best solutions to represent the concrete behavior in both loading and unloading. Thus solving the aforementioned irreversibility of strains through the incremental plasticity theory, this is formulated in term of three ingredients, hardening, flow rule, and yields surface function. Following subsections provide a brief explanation of the parameters that control these ingredients. Some of these parameters were modified to include the effect of high temperature.

7.2.1 Damaged (hardening) variable

The micro-cracking also causes degradation in the stiffness of the member. Representing this degradation has different forms in the different approaches. Stiffens degradation is modeled from the relationship between stress and effective stress, as in continuum mechanics, or explicitly modeled as in a plasticity model. In the modification of the Lubliner model by Lee, et al., [126], the elastic stiffness degradation is presented through elastic and plastic damage variables, which are corresponding to the hardening in the classical plasticity theory. Two different damage variables are proposed, tensile and compressive damages, which are then being used in estimate variable damage states. These multiple damages are used in the proposed yield function (as will be introduced later).

In order to include the damages in the stress-strain relationship, the following steps are recalled from the incremental theory of plasticity,

$$\sigma = D^{el} \times \varepsilon^{el} \tag{7.1a}$$

$$\varepsilon = \left(\varepsilon^{el} + \varepsilon^{pl}\right) \rightarrow \varepsilon^{el} = \left(\varepsilon - \varepsilon^{pl}\right) \tag{7.1b}$$

$$\sigma = D^{el} \times (\varepsilon - \varepsilon^{pl}) \tag{7.1c}$$

Where ε^{pl} is the plastic strain, and D^{el} is the elastic stiffness that are degraded in term of degradation variable d_x (the ratio of the damaged area to the undamaged area, the subscript x be c for compression damage and t for tension damage) this leads to the following equation,

$$D^{el} = D_o^{el} \times (1 - d_x)$$

For undamaged section $d_x = 0$, hence $D^{el} = D_o^{el}$ (initial elastic stiffness), while for fully damaged section, $d_x = 1$, so that $D^{el} = 0$. In the same manner, if the section is not damaged, i.e. $d_x = 0$, hence, $\sigma = \tilde{\sigma}$, however, if the section is starting to get the damage, the effective stress $\tilde{\sigma}$ becomes more accurate in representing the state.

Therefore, it is convenient to formulate the problem in term of the effective stress, so that Equation 7.1 becomes be as follows,

$$\tilde{\sigma} = (1- d_x)^{-1} \times \sigma \tag{7.2}$$

From the definition of damage variable d, it can be concluded that the values are dissimilar in tension and compression. This is because the areas that effectively carrying the load are different, hence, the cracks in the compression case are parallel to the load direction, whereas, these cracks are transverse to the load direction in tension. Therefore d_x is a function of the effective stress (load per effective area) and the equivalent plastic strain $d_x(\bar{\sigma}, \tilde{\varepsilon}^{pl})$. Both of them are characterized by two hardening variables.

$$\tilde{\varepsilon}^{pl} = \begin{bmatrix} \tilde{\varepsilon}_t^{pl} \\ \tilde{\varepsilon}_c^{pl} \end{bmatrix}$$

These variables are tightly bonded to the dissipation in fracture energy. So that, the microcracking can be represented by increasing the $\tilde{\varepsilon}^{pl}$ value.

The stress-strain relationship in Equation 7.1 can be represented as,

$$\sigma_c = E_o(1- d_c) \times \left(\varepsilon_c - \tilde{\varepsilon}_c^{pl}\right) \tag{7.3a}$$

$$\sigma_t = E_o(1- d_t)\times\left(\varepsilon_t - \tilde{\varepsilon}_t^{pl}\right) \tag{7.3b}$$

Where E_o is the initial elastic stiffens, which is according to [127] equal to,

$$E_o= 21.5 \times 10^3 \times \left(\frac{f_{cm}}{10}\right)^{1/3}$$

The mean compressive strength f_{cm} can be related to the characterize compressive strength f_{ck} as, $f_{cm} = f_{ck} + 8\text{MPa}$

Substitute the Cauchy stress in Equation 7.3, yields,

$$\tilde{\sigma}_c= E_o\times\left(\varepsilon_c - \tilde{\varepsilon}_c^{pl}\right) \tag{7.4a}$$

$$\tilde{\sigma}_t = E_o\times\left(\varepsilon_t- \tilde{\varepsilon}_t^{pl}\right) \tag{7.4b}$$

Rearranging Equation 7.3, the damage variable d can be described in term of the tensile and compressive elastic strains as follows,

$$d_c = 1 - \frac{\sigma_c}{E_o \times \left(\varepsilon_c - \tilde{\varepsilon}_t^{pl}\right)} \tag{7.5a}$$

$$d_t = 1 - \frac{\sigma_t}{E_o \times \left(\varepsilon_t - \tilde{\varepsilon}_t^{pl}\right)} \tag{7.5b}$$

Note, it is worthy to mention here that the stress used in modeling the materials in ABAQUS means the true stress or in well-known (Cauchy stress), which means that the load applied per current area. The strain corresponding to the true stress known as logarithmic strain, calculated by the following integration

$$\varepsilon = \int_{l_o}^{l} \frac{\partial l}{l} = \ln l - \ln l_o = \ln \frac{l}{l_o}$$

In order to convert the nominal stress to true stress for isotropic materials, following equation has to be used;

$$\sigma_{true} = \sigma_{nom}(1 + \varepsilon_{nom})$$
$$\varepsilon_{ln}^{pl} = \ln(1 + \varepsilon_{nom}) - \frac{\sigma_{true}}{E}$$

7.2.2 Flow rule

The flow of the plastic strain (the rate of the plastic strain $\dot{\varepsilon}^{pl}$), is obtained from the flow rule, so that the $\dot{\varepsilon}^{pl}$can be obtained from a scalar plastic potential function that is defined in the effective stress space $\varphi(\bar{\sigma})$, i.e.

$$\dot{\varepsilon}^{pl} = \dot{\lambda} \times \frac{\partial \varphi(\bar{\sigma})}{\partial \bar{\sigma}}$$

The $\dot{\lambda}$ is a positive parameter of proportionality, i.e., it refers to the consistency of the plastic, which is altered for different particles. φ is the Drucker-Prager hyperbolic function,

$$\varphi = \sqrt{(\epsilon \times \sigma_{to} \times \tan \psi)^2 + \tilde{q}^2} - \tilde{p} \tan \psi \tag{7.6}$$

Where, $\tilde{p}$ and $\tilde{q}$ are the effective hydrostatic pressure, and the von-Mises (equivalent effective) stress, respectively, at which,

$$\tilde{p} = -\frac{1}{3}\tilde{\sigma} \times I$$

$$\tilde{q} = \sqrt{\frac{3}{2}\tilde{S} \times \tilde{S}}$$

$$\tilde{S} = \tilde{p}I + \tilde{\sigma}$$

and ϵ is a small value (recommends to assume 0.1) in CDP model, that defines the rate of approach of the plastic potential hyperbola to its asymptote, in other words, the eccentricity (ϵ) is the length of the portion (along the hydrostatic axis in $\tilde{p} - \tilde{q}$) and the vertex of the hyperbola, as shown in Figure 7.2a. when $\epsilon \approx 0$ the flow potential tends to straightening (such as in Durcker-prager hypothesis), and ψ is the dilatation angle of the material that interpreted as the internal friction angle, which is refers to the slop of failure surface toward $\tilde{p}$ on $\tilde{p} - \tilde{q}$ diagram (see Figure7.2a), mostly ranging between 36° and 40°.

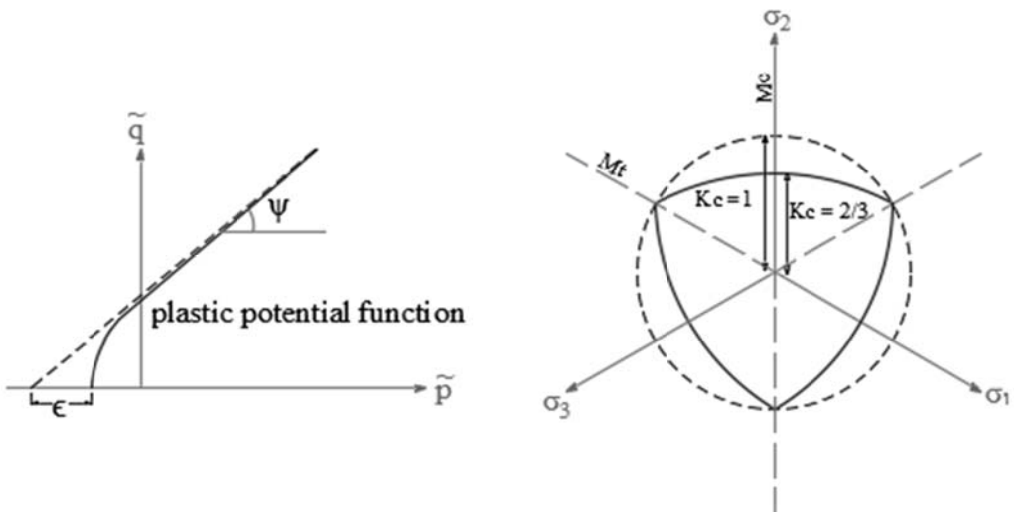

(a) (b)

Figure 7.2 (a) Eccentricity and dilation angle in the meridian plane (b) Yield surfaces in the deviatory plane

7.2.3 Yield function

The CDP can be considered as a modification of the Drucker-Prager model, based on the so-called Lubliner [125] or Barcelona model, in which the yield function for concrete as friction material is assumed related to cohesion.

$$\bar{F}(\sigma) = c \tag{7.7}$$

Where, c is the cohesion with its initial value c_o equals the initial yield under uniaxial compressive stress f_{co}, while $\bar{F}$ is a scalar function of the stress tensor invariants.

Adapting the second invariant of the stress deviator J_2, and the stress first invariant I_1, Lubliner and his coworkers collected all failure data into Equation 7.7 in order to produce the yield surface as follows,

$$\bar{F}(\sigma) = \frac{1}{1-\alpha}\left[\sqrt{3J_2} + \alpha I_1 + \beta\langle\sigma_{max}\rangle - \gamma\langle -\sigma_{max}\rangle\right] \tag{7.8}$$

According to Lubliner, the three parameters α, β, and γ in Equation 7.8, are constant and dimensionless, based on the concrete independent strength test state (uniaxial, biaxial, and triaxial yield compressive and tensile stress in initial state), in which,

$$\alpha = \frac{f_{bo}/f_{co} - 1}{(2 \times f_{bo}/f_{co}) - 1} \tag{7.9}$$

Where, f_{bo}/f_{co} is the comparison of the initial biaxial with the uniaxial yield stresses under compression, Kupfer, et al. [127] observed that this value ranges from 1 to 1.27 based on the percentage of the applied principle stresses (σ_1 / σ_2). In the case of applying equal stresses in both of the two principal directions (σ_1 / σ_2 = 1) and in no restraining to the third direction, the f_{bo}/f_{co} = 1.16. Moreover, Lubliner, et al. [125] limited these percentages between 1.10 and 1.16.

A few data are available regarding the effect of high temperature on the f_{bo}/f_{co}, Kordina and his coworkers [128] found that the f_{bo}/f_{co} under high temperature is greater than its amount under ambient conditions. The details of adopting the Kordina's data are considered with the assumption the proportion of the biaxial compression to the uniaxial compression is varied under high temperature condition, not as constant. Discussion of this modification is presented in Section 5.3.3

(concrete behavior under biaxial stresses). Hence, α will be temperature dependence, i.e

$$\alpha(T) = \frac{f_{bo}(T)/f_{co}(T) - 1}{[2 \times f_{bo}(T)/f_{co}(T)] - 1} \tag{7.10}$$

For the second parameter of Equation 7.8, β can be determined from α, and the initial uniaxial compressive f_{co} and tensile yield stresses f_{to}, so that,

$$\beta = \left[(\alpha - 1) \times \left(\frac{f_{bo}}{f_{co}}\right)\right] - (1 + \alpha) \tag{7. 11}$$

In spite of Equation 7.7 gives good agreement when modeling concrete members under monotonic loading, there still a part of this member behaves as unloaded when the crack initiates (see Figure 7.1a). Lee, et al., [126] have modified Equation 7.7 by assuming two cohesion variables (through damaged variable d_c and d_t), based on the assumption that the concrete was only represented in Equation 7.6 by cohesion c. Therefore the two mentioned variables will be defined by β so that $\bar{F}(\sigma) = c(\tilde{\varepsilon}^{pl})$ and $\beta = \beta(\tilde{\varepsilon}^{pl})$, i.e.

$$\beta(\tilde{\varepsilon}^{pl}) = \left[(1 - \alpha) \times \left(\frac{f_{bo}(\tilde{\varepsilon}_c^{pl})}{f_{co}(\tilde{\varepsilon}_t^{pl})}\right)\right] - (1 + \alpha) \tag{7. 12}$$

The effect of high temperature will be implicitly included in $\beta(\tilde{\varepsilon}^{pl})$ in terms of α, and can be represented as a function of temperature in addition to the damages variable.

The third parameter γ is defined as the shape of the yield surface, it is a constant parameter in term of strength ratio of concrete K_c under axial stress with equal lateral compressive stresses (equal biaxial to triaxial compressive stresses), which is used in yield function for the triaxial compression only when the effective maximum stress is negative. This parameter is found in the comparison between the yielding along the meridians for both tensile and compressive Mt and Mc respectively. At which, the maximum effective stress laying on the points, where $\hat{\sigma}_1 > \hat{\sigma}_2 = \hat{\sigma}_3$ for Mt and $\hat{\sigma}_3 < \hat{\sigma}_1 = \hat{\sigma}_2$ for Mc, where $\hat{\sigma}_3$,$\hat{\sigma}_1$, and $\hat{\sigma}_2$ are the eigenvalue of an effective stress tensor. Physically, K_c can be defined through the deviatoric cross section, as the ratio of the distance between the origin of the hydrostatic axes and the compression and tension meridian as shown in Figure 7.2b. Ottesen, [129] showed that K_c is not constant and is varied from 0.5 to 1. Lubliner, et al. [125] used K_c as a constant parameter equal to 0.667 but it is not supported by experimental data. Therefore, when $K_c = 1$ leads to $\gamma = 0$. In this case the yield surface becomes the same as of Drucker-Prager.

It becomes easy to find the maximum effective stress $\hat{\sigma}_{max}$ on the meridian of the tensile and compressive stresses from the definition of the effective hydrostatic pressure $\tilde{p}$, and Mises equivalent effective stress $\tilde{q}$ that were introduced above. The relationship between them is as follows,

$$(\hat{\sigma}_{max})_{Mt} = \frac{2}{3}\tilde{q} - \tilde{p} \tag{7.13a}$$

$$(\hat{\sigma}_{max})_{Mc} = \frac{1}{3}\tilde{q} - \tilde{p} \tag{7.13b}$$

Now, for $\hat{\sigma}_{max} < 0$ the yielding is governed by the following equations at Mt and Mc meridians,

for tensile meridian, $\left[\left(\frac{2\gamma}{3} + 1\right) \times \tilde{q}\right] - (\gamma + 3\alpha) \times \tilde{p} = (1 - \alpha)\, \hat{\sigma}_c$

for compressive meridian, $\left[\left(\frac{\gamma}{3} + 1\right) \times \tilde{q}\right] - (\gamma + 3\alpha) \times \tilde{p} = (1 - \alpha)\, \hat{\sigma}_c$

let $K_c = \frac{\tilde{q}_{(Mt)}}{\tilde{q}_{(Mc)}}$, thus, for any value of $\tilde{p}$ with negative maximum effective compressive stress, K_c becomes,

$$K_c = \frac{\gamma + 3}{2 \times \gamma + 1}$$

For the right term in Equation 7.7, the cohesion c is also introduced in term of damage variables for both tensile cohesion $c_t = \tilde{f}_{to}(\tilde{\varepsilon}^{pl})$ and compressive cohesion $c_c = -\tilde{f}_{co}(\tilde{\varepsilon}^{pl})$. Moreover, the invariants are represented in terms of effective stress. The yield function of Equation 7.8 becomes a function of the damage variable and the effective stress as shown,

$$F(\bar{\sigma}, \tilde{\varepsilon}^{pl}) = \frac{1}{1-\alpha}\left[\sqrt{3J_2} + \alpha I_1 + \beta(\tilde{\varepsilon}^{pl})\langle\hat{\bar{\sigma}}_{max}\rangle - \gamma\left(-\hat{\bar{\sigma}}_{max}\right)\right] - \hat{\bar{\sigma}}_{co}(\tilde{\varepsilon}^{pl}) \quad (7.14)$$

It can be clearly seen that in case of biaxial compression $\hat{\bar{\sigma}}_{max} = 0$, Equation 7.14 becomes the Durker-Prager criterion, with only α parameter.

7.3 Modeling of Reinforced Concrete Materials

Concrete shows a significantly different behavior in tension than in compression. The compression initial yield stress σ_{co} is significantly higher than that of tension σ_{to} (approximately 10 times). The tension softening is opposite to the compression hardening direction, the stress-strain relationship were presented through scalar damaged elasticity (1 - d) as illustrated above considering the degradation of elastic stiffness at the early stage.

7.4 Concrete Uniaxial Compression Behavior

Generally, three stages can be recognized in the constitutive curves of the behavior of concrete under uniaxial compressive stress and high temperature for each specified temperature. These are, the linear elastic stage, the strain hardening due to the participation of reinforcement, and finally the strain softening until reaching the ultimate level as illustrated in Figure 7.3 for slab P0.

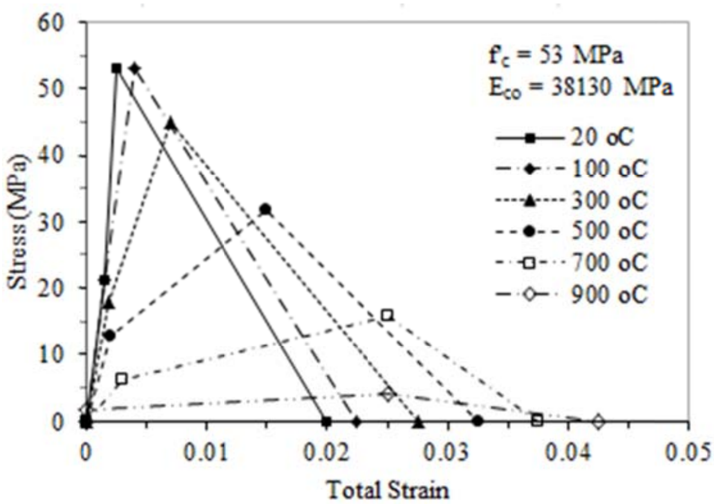

Figure 7.3 Typical concrete stress-strain relationship in uniaxial compression for specimen P0.

For the first stage, the strain related to ascending stress in a linear elastic relationship with a slope equal to E_o, until reaching a threshold of inelastic stage, the limit supposed to be proportional to the amount of compressive strength f'_c. Kmiecik el al. [130] showed that the elastic limit can be specified as,

$$k = 1 - \mathrm{Exp}\left(\frac{-f'_c}{80}\right)$$

In the current work, the plain concrete was preferred to use the limit that is introduced by Eurocode 2 (k = 0.4), which is corresponding to ε_{co} in case of ignoring the effect of high temperature on modulus of elasticity, because it is already included in the compressive stress and strain. As shown in Figure 7.4, this lead to the identifying of elastic modulus in all curves, such that,

$$E_{co},(20) = E_{co},(100) = \ldots. = E_{co},(T)$$

corresponded ε_{co} in Eurocode 2 seems to be governed by the following equation,

$$\varepsilon_c,(T) = (-0.000002 \times T) + 0.0019$$

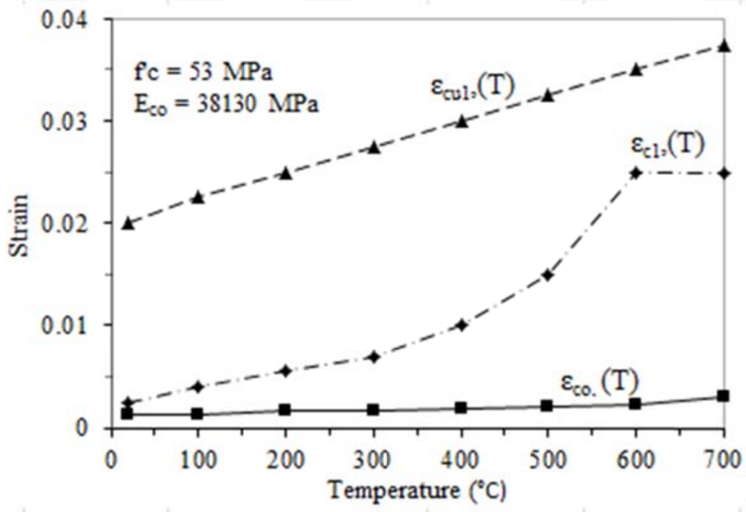

Figure 7.4 Variations of concrete strain $\varepsilon_{co}(T)$, $\varepsilon_{c1}(T)$, and $\varepsilon_{cu1}(T)$ that are corresponding to the elastic limit, 0.4 f 'c, and zero stresses respectively, under rising temperature according to [31] for slab P0.

In the second phase, the concrete exhibiting a strain hardening beyond ($\sigma_{c1} = 0.4\ f'_c$) until the concrete stress reaches the peak value of f'_c, which is corresponding to the $\varepsilon_{c1},(T)$. It is worth to mention here, that $\varepsilon_{c1},(T)$ are increasing smoothly and dramatically with temperature increments up to 600 °C. Above this temperature, the $\varepsilon_{c1},(T)$ is assumed unaffected by the temperature as shown in Figure 7.4. It seems that $\varepsilon_{c1},(T)$ under high temperature is governed by an exponential equation as follows,

$$\varepsilon_{c1},(T) = 0.0025\ e^{(0.0037 \times T)} \quad 20 \leq T \leq 600$$

At the final stage, the load capacity of the concrete is decreasing and shows strain softening until reaching the ultimate strain $\varepsilon_{cu},(T)$. Eurocode 2 accepts to use either linear or nonlinear descending branch to represent the strain softening. From Figure 7.4, the increasing in the ultimate strain under high temperature is linear and is governed by the following equation,

$$\varepsilon_{cu1},(T) = (0.00003 \times T) + 0.0198$$

The compressive strength of SFRC is enhanced by the addition of SF, in turn, improve the compressive strain (ε_{cof}) corresponding to the maximum f'_c and ultimate compressive strain (ε_{cuf}). The SFRC compressive stress-strain relationship considered in current work is based on the proposed formula by Abdul-Razzak and Ali [131] as follows,

$$\varepsilon_{cof} = 0.00072 f_{cf}^{0.32} + 0.00096\ F^{1.77} \tag{7.15}$$

$$\varepsilon_{cuf} = \left(1.229 \times 10^{12} \times f_{cf}^{-8.05}\right) + 0.005\ F^{0.4} \tag{7.16}$$

where F is the index the fibers

$$F = V_f \frac{l_f}{d_f}$$

and, the stress-strain relationship, according to Abdul-Razzak and Ali [131] that used for the current work is as follows,

$$\sigma = -\ a\ f_{cf} \left(\frac{\varepsilon}{\varepsilon_{cof}}\right) \left[\left(\frac{b\varepsilon}{\varepsilon_{cof}}\right) - 2\right] \tag{7.17}$$

where

$$a = 0.63 + 1.11F^2 - 0.997F^3$$

$b = 0.345 + 2.498F^2 - 2.275F^3$

7.4.1 Concrete uniaxial tensile behavior

When a slab is subjected to uniaxial stress, tensile stress becomes more important than compression stress because the tensile strength decreases significantly more than compressive strength [127]. Two states of the RC behavior can be recognized under uniaxial tension (cracked and uncracked stages). In the first stage, concrete carries the applied load and the stress-strain response of concrete in this stage is linear elastic. Then, micro cracks start to initiate as a local damage where the stress concentrates within a limited zone in between the aggregate and the binders. This zone is known as fracture process zone as shown in Figure 7.5. Distributed stress will partition along the member into factitious elements. In the next stage, where the tensile stress reaches 0.9 of the tensile strength, the micro-cracks decreases the stiffness [127], and the deflection of the member is increases. These micro-cracks are localized and connected together in one crack, while the strength of the member is gradually transferred from the concrete to the reinforcement bars. In each stage, the remaining uncracked part of concrete contributes in the member stiffness. This contribution may continue until the reinforcement yields. The contribution of the uncracked parts to the stiffness is known as tension stiffening, this behavior is important to model the load transferring across the crack and then to the rebar.

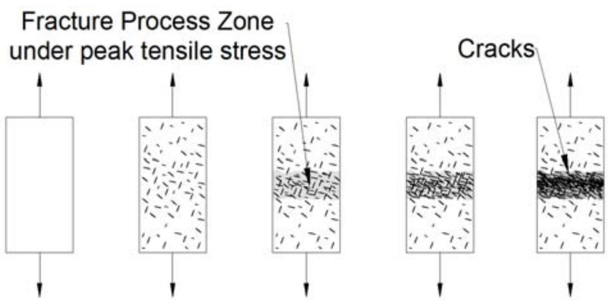

Figure 7.5 Initiation and propagation of micro-cracks in concrete under uniaxial tensile stress.

Tension stiffening can be modeled in three ways, post failure stress-strain relation, stress-displacement, and/or through tensile fracture energy cracking criterion. In order to characterize the brittle behavior of concrete, and to decrease the meshing sensitivity for the elements where no reinforcement is provided, it is preferred to describe the cracking through tensile fracture energy cracking criterion. The fracture energy is the energy required to produce a crack, this property, usually obtained from bending test of notched prism, three points loaded, so that the fracture energy is represents by the area under the softening curve (stress-inelastic crack opening displacement (σ – w) relationship). This relationship is a function of the aforementioned facetious single element effective length l_e, because the crack will occur in that element. Where l_e assumed as the cubic root of element volume [132]. There are many softening models were proposed, varying from single line to nonlinear models, these options discussed below;

- Linear model, in this model the tensile behavior of concrete is based on [133] material model, where the stress-inelastic displacement has a linear descending relationship,

$$\sigma_{ct} = f_{ctm} \left(1 - \frac{w}{w_c}\right) \tag{7.18}$$

In the Figure 7.6, the fracture energy is equal to triangle area that produced of the post peak softening as follow;

$$G_F = 0.5\, f_{ctm} \times w_c \tag{7.19}$$

Where w_c is the maximum opening in fracture zone, $f_{ct}(T)$ is the ultimate tensile stress.

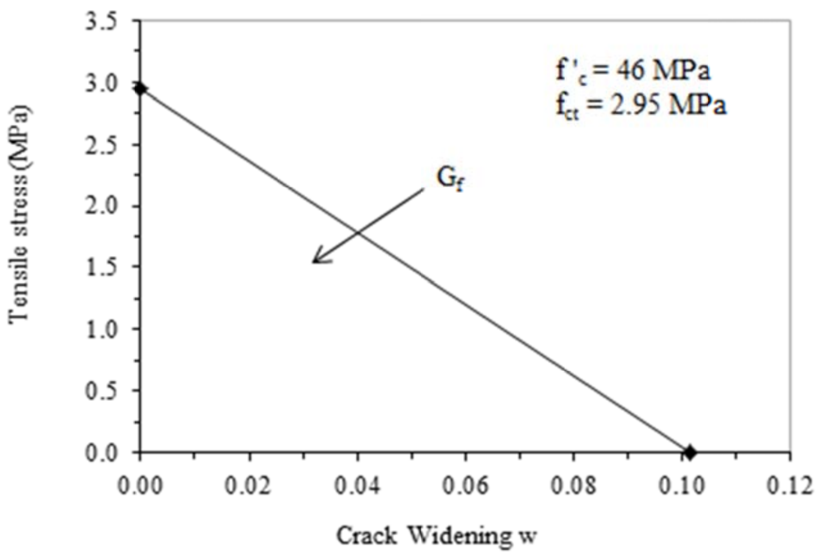

Figure 7.6 Linear softening relationship (stress − inelastic crack opening displacement).

Equation 7.19 can be described in term of plastic tensile strain, this will minimize the localization of the fracture. The plastic strain equal to $\varepsilon_{ct} = w_c / l_e$, where l_e is the element size Figure 7.7, hence, Equation 7.19 can be rewritten as,

$$G_F = 0.5\, f_{ctm} \times \varepsilon_{ctu} \times l_e \tag{7.20}$$

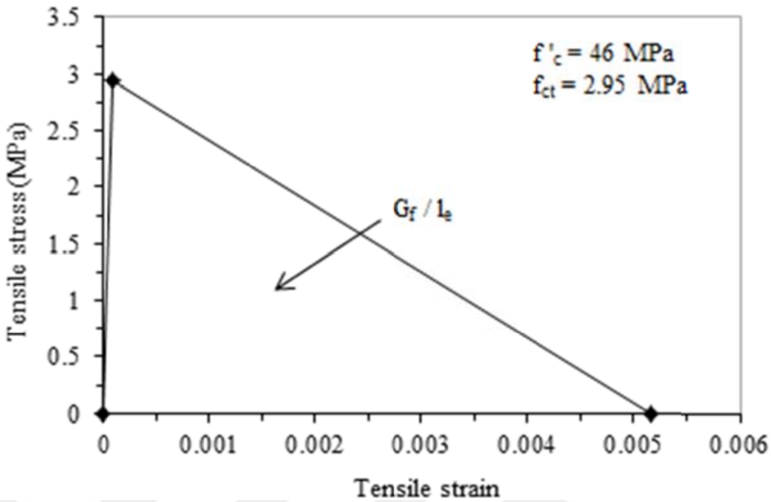

Figure 7.7 Uniaxial tensile stress-strain relationship

where ε_{ctu} is the ultimate tensile strain, which is equal to 0.15‰ [127].

Equation 7.20 can be presented in term of tensile fracture energy at high temperature condition G_F (T) by considering the reduction coefficient $k_{c,t}(T)$ that introduced in Figure 7.8 [31] so that the G_F is equal to,

$$G_F(T) = 0.5 k_{c,t}(T) \times f_{ctm} \times \varepsilon_{ctu} \times l_e \tag{7.21}$$

Where f_{ctm} is the mean tensile strength at ambient condition that equal to,

$f_{ctm} = 0.3 \times (f_{ck})^{2/3}$

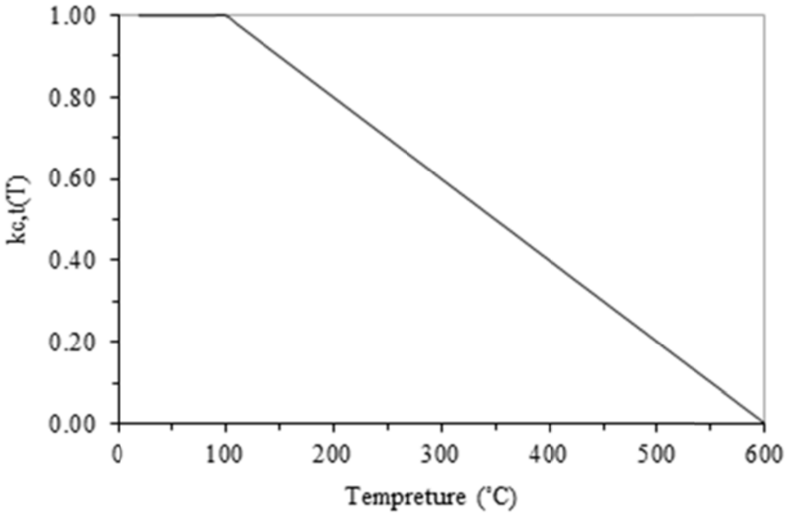

Figure 7.8 Reduction factor to the concrete tensile strength under high temperature condition, according to Eurocode 2. [31]

- Bilinear approach that is supported by the Model Code [97], and used by [132]. In cracked section, the tensile strength degradation is proportional to the increasing in the crack displacement opening in bilinear form as shown in Figure 7.9 and constructed by Equation 7.22a and 7.22b,

$$\sigma_{ct} = f_{ctm} \times \left(1 - 0.8 \times \frac{w}{w_1}\right) \quad \text{for } w \leq w_1 \tag{7.22a}$$

$$\sigma_{ct} = f_{ctm} \times \left(0.25 - 0.05 \times \frac{w}{w_1}\right) \quad \text{for } w_1 < w \leq w_c \tag{7.22b}$$

Where;

$$w_1 = \frac{G_F}{f_{ctm}} \text{ when } \sigma_{ct} = \frac{f_{ctm}}{5}$$

and

$$w_c = \frac{5 \times G_F}{f_{ctm}} \text{ when } \sigma_{ct} = 0$$

The fracture energy G_f can be estimated in term of mean compressive strength f_{cm} [97] as,

$$G_F = 73 \times 10^{-3} \times f_{cm}^{0.18} \quad \text{(N/mm)} \tag{7.23}$$

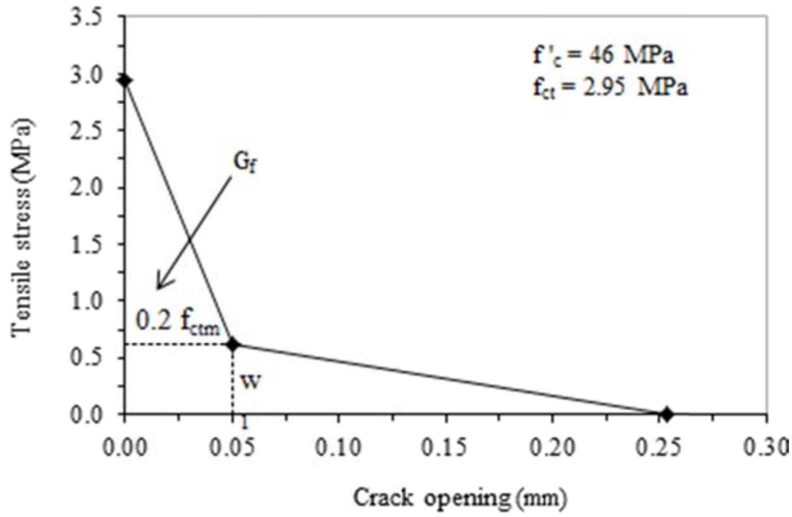

Figure 7.9 Bilinear softening relationship (stress–inelastic crack opening displacement).

Using the same approach of the previous model, the tensile strain can be assumed by dividing the crack displacement (w) by the element size (l_e) [127] (see Figure 7.10), so that the stepwise tensile strains are defined as follow;

$$\varepsilon_{cr} = \frac{f_{ctm}}{E_o}, \quad \varepsilon_1 = \varepsilon_{cr} + \frac{w_1}{l_e}, \quad \text{and} \quad \varepsilon_u = \varepsilon_{cr} + \frac{w_c}{l_e}$$

where, ε_{cr} is the tensile strain at the first cracking stage, ε_1 is the tensile strain when the peak tensile stress is reached and ε_u is the ultimate tensile strain.

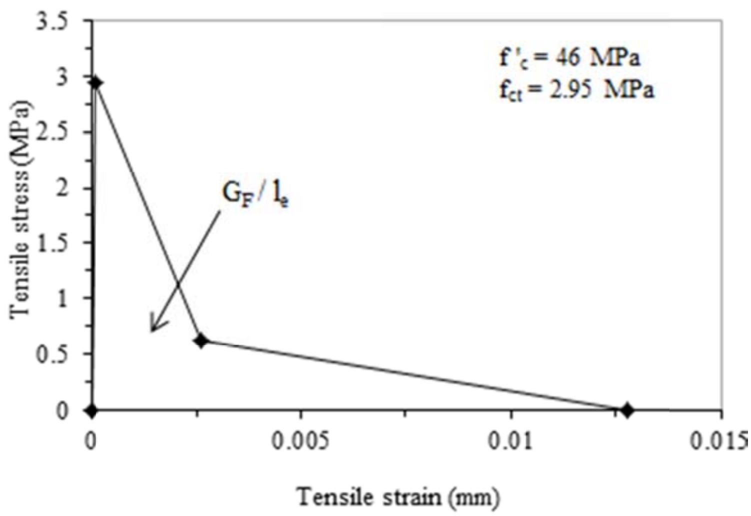

Figure 7.10 Concrete uniaxial tensile stress–strain relationship

- An exponential tension softening response that is introduced by Gopalaratnam et al., [134]. This approach is used by other following researchers [135,112].

In this model, the tensile stress is exponentially related to the crack opening w, as shown in Equation 7.24 and Figure 7.11.

$$\sigma_{ct} = f_{ctm} \times \mathrm{Exp}\left(- w \times \frac{f_{ctm}}{G_F} \right) \tag{7.24}$$

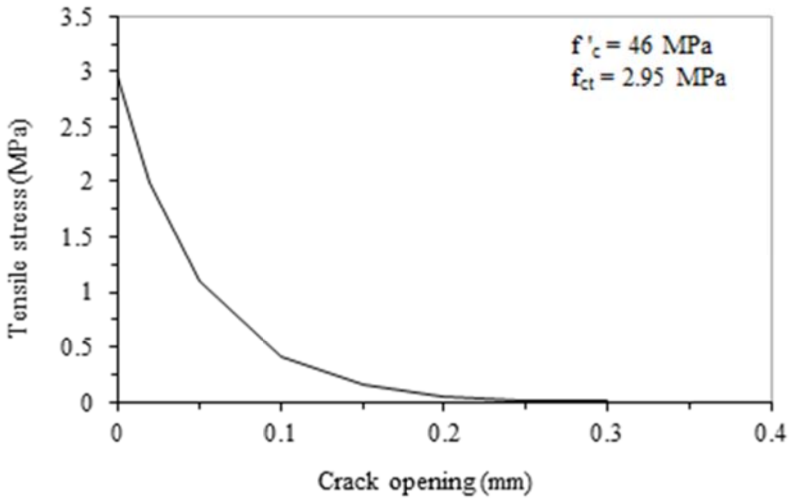

Figure 7.11 Exponential softening relationship (stress–inelastic crack opening displacement).

There are few data on the effect of high temperature on fracture energy G_F. Furthermore, due to different methods used in the different tests and different fire levels and scenarios, the comparison between these experimental data is quite difficult [135]. Nevertheless, it can be said that the fracture energy is slightly increased with increasing the temperature up to 80 °C [97]. Moreover, up to 400 °C the increments are more significant, where the fracture energy G_F increases about 50% compared to the control specimen at ambient condition [135]. This is slightly agreed with Zhang and Bicanic [136] finding for specimens tested after cooling and for the ascending part of the specimens tested in hot condition. However, for hot specimen, Zhang and Bicanic [136] found that G_F decreases about 16% up to 150 °C, this is because of the induced a pressure due to restricted moisture inside the concrete. Beyond 150 °C, different behavior is obtained, where G_F is increasing with the increasing of concrete temperature up to 450 °C with a net increase of 33% compared to ambient conditions.

Related to the present work, most specimens were subjected to high temperature (more than 450 °C) and tested under hot condition. It is suggested to use the bilinear relationship shown in Figure 7.12 that obtained from Zhang and Bicanic, [136] for data up to 450 °C. For the temperatures higher than 450 °C, the $G_F,(T)$ is kept constant at which reached in 450 °C, up to failure temperature, these relations are assumed to be governed by Equation 7.25,

$G_F,(T) = G_F \times [(-0.0012 \times T) + 1.03]$ For $0 \leq T \leq 150$ °C (7.25a)

$G_F,(T) = G_F \times [(0.0017 \times T) + 0.61]$ For $150 < T \leq 450$ °C (7.25b)

$G_F,(T) = G_F \times 1.375$ For $T > 450$ °C (7.25c)

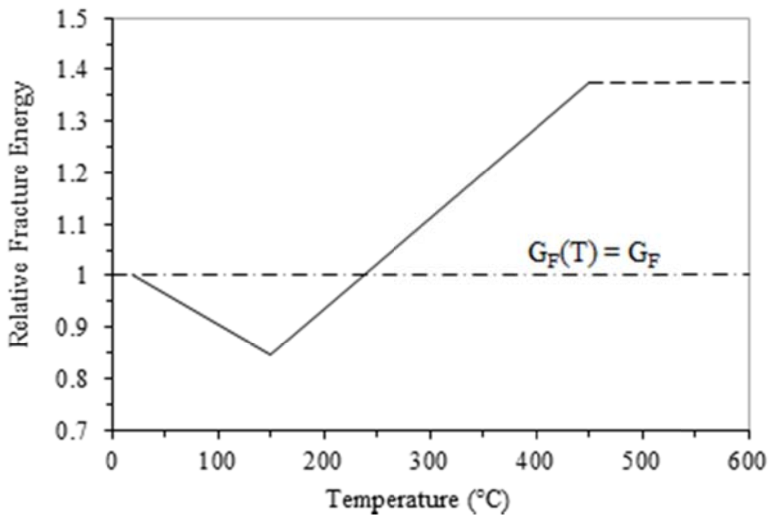

Figure 7.12 Effect of high temperature on concrete fracture energy.

7.4.2 Concrete behavior under biaxial stresses

In the direct vicinity of the column stub of the column-slab joint, triaxial stress states are produced, but, these stresses can be ignored and the biaxial compression is proper to represent the failure criterion [137]. Moreover, the differences between biaxial and the uniaxial tensile strength under ambient condition are small (about 0.013) compared to the differences between the biaxial and the uniaxial compression strength. Experimental data showed that the compressive strength obtained under biaxial compression f_{bo} is greater than that obtained under uniaxial compressive stress f_{co} by about 16%, [125,127,132,112].

Few data can be found in the literature related to the effect of high temperature on the relation of biaxial to uniaxial compressive strength. Both Ehm and Kordina in two different research [128,138], conclude that the biaxial compressive strength under fire condition f_{bo},(T) showed rapidly increasing compared to the f_{co},(20) at ambient condition, even if the σ_2 / σ_{ult} is relatively small compared to σ_1 / σ_{ult}. Moreover, Kordina and his coworker [128] observed that the $f_{bo,}$(T) is also greater than $f_{co,}$(20) in all temperature levels and stress ratios σ_1 / $\sigma_{2.}$ Nevertheless, the f_{bo},(T) / f_{co},(20) are decreasing with increasing in temperature T, this value reach its maximum (1.13) at 20 °C, this fact is illustrated in Figure 7.13a. The same value of $f_{bo,}$(T) compares to the uniaxial compressive strength, but in this case the degradation in the uniaxial concrete strength was considered, i.e. both stress is considered under high temperature. The degradation of uniaxial compressive strength under high temperature f_{co}(T) is adopted according to Eurocode 2 [31] provisions. Figure 7.13b showed that the comparison between the biaxial and uniaxial is oscillating, and have many inflection points, but the highest value reaches 1.4 at 750 °C, because the drop in uniaxial behavior of a concrete at 600 °C showed a rapid drop in its strength for temperature above the 450 °C is about 50% of its value. Whereas, this value is 67% of the biaxial compressive strength.

For the current study, the ratio of f_{bo},(T) / f_{co},(T) is used so that the parameter α in the yield function is also affected by the variation of f_{bo} / f_{co} for both curves in Figure 7.13. These variations of α due to exposing to high temperatures are illustrated in Figure 7.14. From the figure, it can be clearly seen that using the value of α in curve Figure 7.13a is significantly disturbed between 450 °C and 600 °C, while after 600 °C, α exhibits stable decrease. However, in Figure 7.13b, the values of α show discrete intervals of minor increase and decease up to 800 °C. It shows that the temperature above 450 °C is significantly inflected and 600 °C is the active degree. From Figure 7.14 it can be concluded that the variation of α is minimal up to 450 °C. For this reason, the value of f_{bo} / f_{co} up to 450 °C is taken equal to the value at ambient temperature, which equals to 1.16. After 450 °C, a linear decrease is considered up to a value of 0.8 at 800 °C.

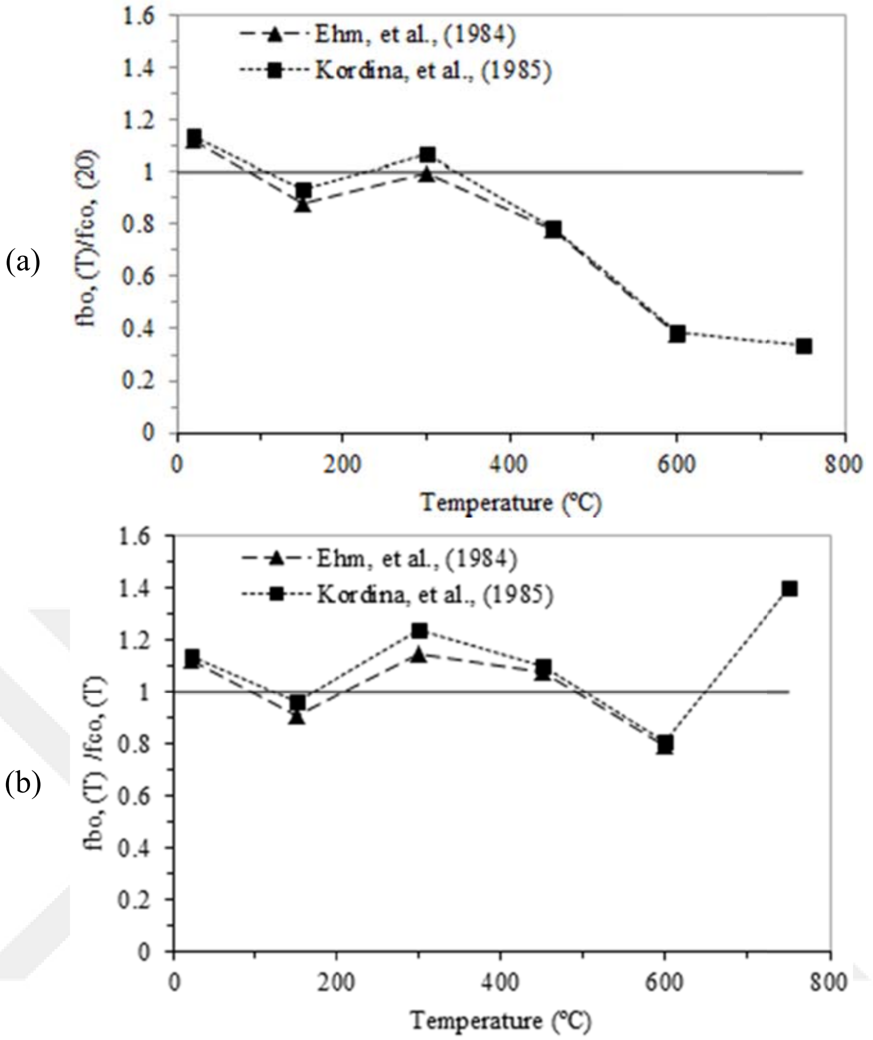

Figure 7.13 The variation of compressive strength of normal concrete at high temperature compared with a) uniaxial compressive strength at ambient condition b) uniaxial compressive strength at high temperature.

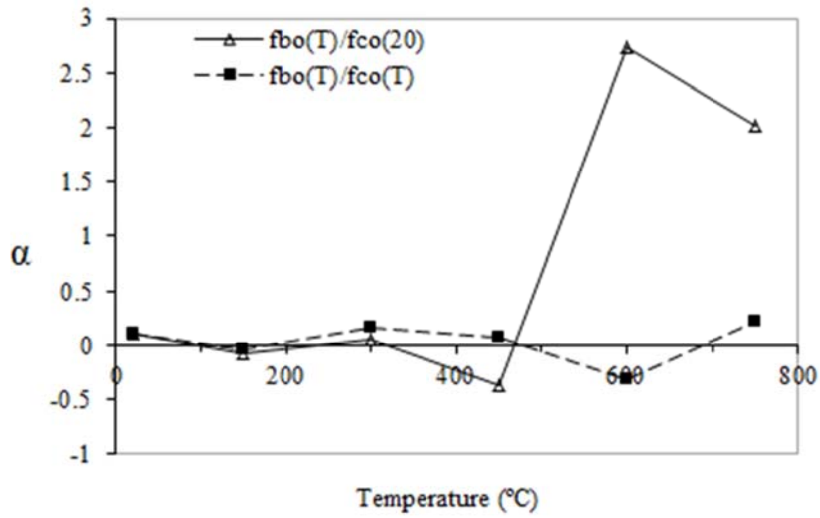

Figure 7.14 The variation of the parameter α of the yield function due to exposing to high temperature.

7.4.3 Concrete strain components

The components of the total strain (ε_{tot}) under the high temperature effect are assumed according to Eurocode 2 [31] as,

$$\varepsilon_{tot} = \varepsilon_{cr}(\sigma, T, t) + \varepsilon_{th}(T) + \varepsilon_{tr}(\sigma, T) + \varepsilon_{\sigma}(\tilde{\sigma}, \sigma, T) \tag{7.26}$$

Where, $\varepsilon_{cr}(\sigma, T, t)$ is the creep strain that is dependent of the mechanical stress σ, the temperature T and the time t. $\varepsilon_{th}(T)$ is the thermal strain, which depends on temperature T, while $\varepsilon_{\sigma}(\tilde{\sigma}, \sigma, T)$ is the load-induce thermal strain that varies with temperature T. Finally, $\varepsilon_{tr}(\sigma, T)$ is the transient state of strain that depends on both the stress σ and the temperature T.

All the selected specimens used in modeling were subjected to short time monotonic loading, hence, the effect of creep strain was neglected, whereas the thermal strain ε_{th} significantly changes up to 700 °C and 805 °C for concrete with siliceous and calcareous aggregates, respectively as shown in Figure 7.15. Then after, the strain keeps constant above the mentioned two temperatures [31].

The transient state strain ε_{tr} is irrecoverable strain, and its temperature dependence is similar to that of thermal strain ε_{th}. Thus, it shows a linear relation under constant stress [139]. The transient state strain can be considered as the most important relation in building fires [140]; Equation 7.27 calculates the transient strain according to Anderberg, et al [139].

$$\varepsilon_{tr} = 2.35\, \varepsilon_{th} \times \frac{\sigma_c}{f_{ck}} \tag{7.27}$$

Figure 7.16 illustrates the behavior of the stress versus transient creep, the compressive strength used for slab P0.

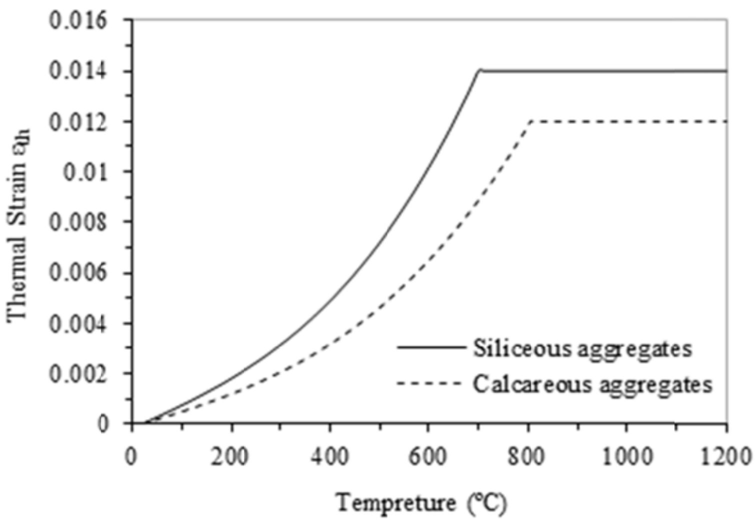

Figure 7.15 Thermal strain in concrete according to Eurocode 2 [31].

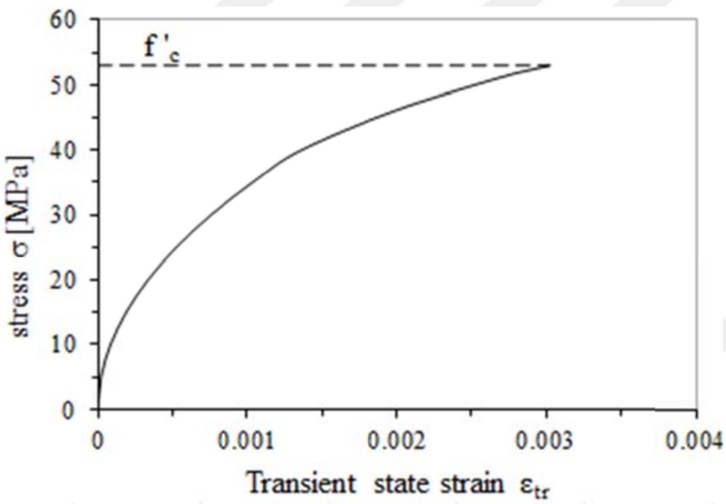

Figure 7.16 Stress-transient state strain relationship for specimen P0

7.5 Reinforce Behavior under Uniaxial Stresses

Reinforced steel bars are commonly assumed to carry uniaxial stress, i.e. such as truss members. One-dimensional elements are satisfactory to represent the behavior of steel bars under tension and compression load. In order to construct the stress-strain relationship of reinforcement bars it is better to start from the effect of high temperature on yield stress. Reinforcement steel is sensitive to temperature exposure, Exposing to high temperature reduces the yield stress of reinforcement in spite of the strength gaining at low temperature [141]. However, the contribution of the reinforcement to the thermal response of the slab can be neglected [31]. Thus, the variation of steel thermal properties is just used in the analysis of the mechanical behavior in the sequential coupling analysis strategy. For fully coupled and thermal stresses, the yield stress of the reinforcement bars kept as its initial condition. Among few available models in the literature, the one proposed by Lie [142] and shown in Equation 7.28 gives good accuracy and easy to representation for the degradation of yield stress in finite element,

$$f_{y'}(T) = f_y \times \left[1 + \frac{T}{900 \times \ln\left(\frac{T}{1750}\right)}\right] \qquad \text{for } 0 \leq T \leq 600\ ℃ \qquad (7.28a)$$

$$f_{y'}(T) = f_y \times \left[\frac{340 - (0.34 \times T)}{T - 240}\right] \qquad \text{for } 600 < T \leq 1000\ ℃ \qquad (7.28b)$$

Figure 7.17 illustrates the comparison between the model of Lie [142] and Eurocode 2. The data in Figure 7.17 has been applied for specimen with f_{ck} = 53 MPa. In addition, the elastic modulus was taken as E_s = 200,000 MPa, and Poisson's ratio was taken as υ = 0.3. The stress-strain relationship of reinforcement bars was modeled according to Eurocode 2 [31] as shows in Figure 7.18. Moreover, the reinforcement thermal elongation is also affected by the increasing of the temperature. Eurocode 2 proposed that the thermal strain $\varepsilon_s(T)$ of the reinforcement bars can be following the increment shows in Figure 7.19 with reference to the length at 20°C.

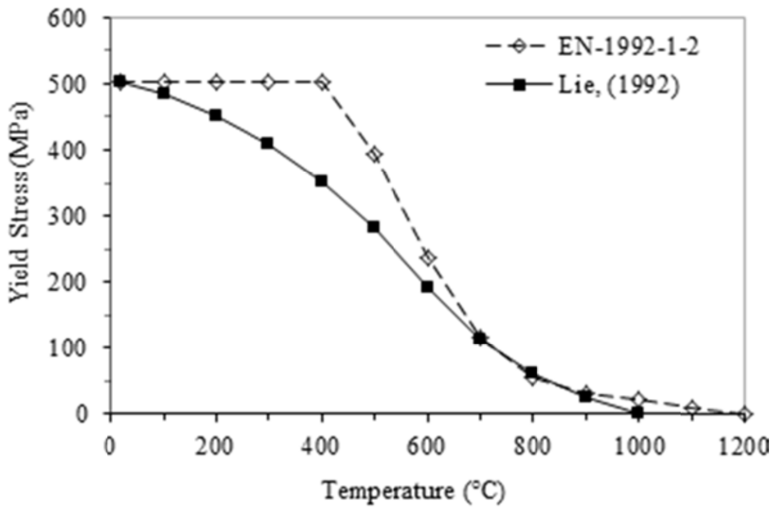

Figure 7.17 Effects of high temperature on yield stress of reinforcement steel.

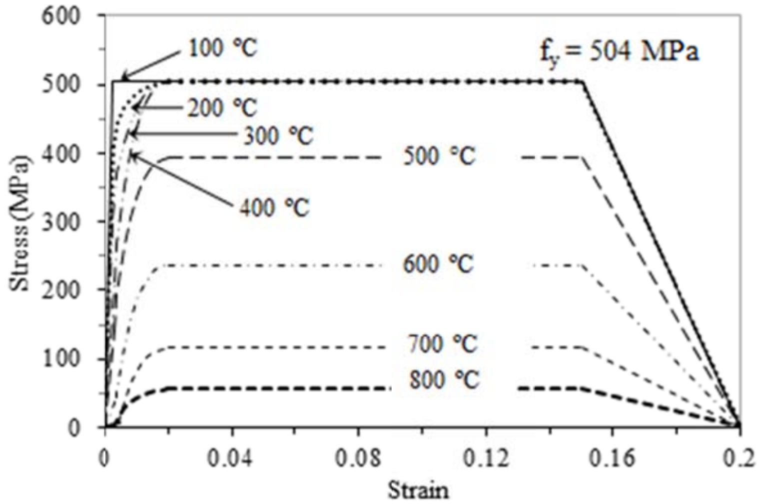

Figure 7.18 Stress-Strain relationship for reinforcement bars according to Eurocode 2 [31] $f_y = 504$ MPa.

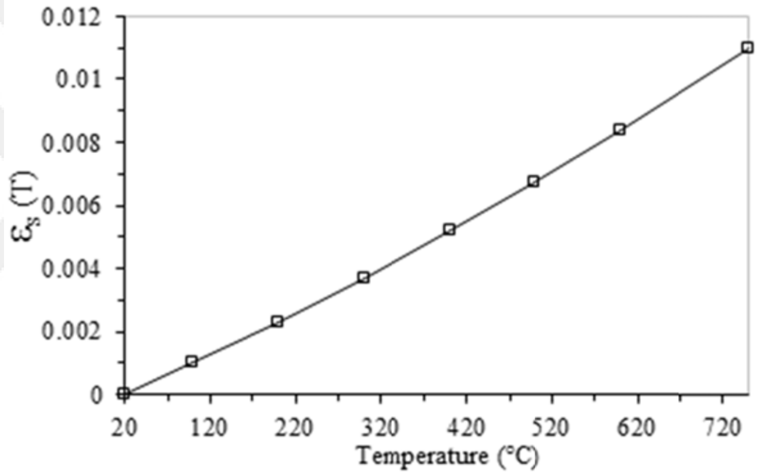

Figure 7.19 Thermal elongation of the reinforcement bars reproduced from Eurocode 2 [31]

7.6 Analysis Procedure

Basically, there are two analytic strategies can be used for thermo-mechanical analysis, fully coupled and sequence analysis, these approaches depend on how to couple the analysis of both thermal and the mechanical solutions.

In the fully coupled strategy, the integration of the temperature takes place using the well-known backward-difference scheme and the newton's method are used to solve the full coupling system. The two techniques can be used in order to construct the matrices, exact and approximate analyses. For the former approach, a no symmetric

Jacobian matrix that couples the systems of thermal and mechanical responses are constructed such as,

$$\begin{bmatrix} K_{uu} & K_{uT} \\ K_{Tu} & K_{TT} \end{bmatrix} \begin{Bmatrix} \Delta u \\ \Delta T \end{Bmatrix} = \begin{Bmatrix} R_u \\ R_T \end{Bmatrix}$$

The subscript u and T refers to the displacement and temperature, respectively. The symbol Δ is the respective corrections, K_{ij} refers to the Jacobian matrix elements in the fully coupled system, and finally R refers to the residual vectors.

The second approach in the analysis strategy is constructed the matrices in a weak coupling. In this case, the diagonal of the coupling matrix is much higher value than the other terms in matrix. If these small terms assumed zero as in the matrix system shown below, the generated equations will be few and saves computational time.

$$\begin{bmatrix} K_{uu} & 0 \\ 0 & K_{TT} \end{bmatrix} \begin{Bmatrix} \Delta u \\ \Delta T \end{Bmatrix} = \begin{Bmatrix} R_u \\ R_T \end{Bmatrix}$$

Solving this system of equations requires the use of the unsymmetrical matrix storage and solution scheme.

In sequentially analysis process, the thermal and mechanical analysis are uncoupled so that U = U(T), the basic energy balance is according to Equation 7.29, in other words, it is assumed that the thermo-mechanical analysis is strongly dependent on the heat transfer, however, the contrary is not.

$$\int_{V^e} \rho c_p \frac{\partial T}{\partial t} \, dV^e = -\int_{s} \vec{q} \times dS \tag{7.29}$$

Therefore, two models are assumed, the first model is a heat transfer analysis and the second was a mechanical analysis model. In the heat transfer model the resultant nodal temperature is stored at a nodal temperature, then these temperatures are used in the next model as a predefined temperature field model. It is worthy to mention here that the meshing and numbering of elements should be the same for both the analysis models.

The time consuming for this analysis strategy is less than that required for the fully coupled one, however the results accuracy is less. This is because of that the effect of the mechanical stress and deflection are ignored in the heat transfer model, this fact are produced by ACI122, 2002 [143], where the degradation of the concrete mechanical properties for the tested specimens under 0.4 f'_c showed less influencing by temperature than that unstressed specimen. This degradation in mechanical properties will affect the temperature distributed along the slab thickness the. On the other hand, when the specimen is deflected due to mechanical effects, all elements will be changing its position, this lead to disturbing the temperature distribution for a moment and then the temperature tends to equalize.

In current work, a different strategy was conducted, because the temperature affects the mechanical properties of the concrete only, whereas there are no thermal stress and strain due to the heating process are remain after cooling. i.e. the analysis in mechanical step is the same of that specimen under ambient condition but with decayed material properties.

7.7 Verification of Finite Element Analysis

7.7.1 Geometry and meshing

By considering the symmetry of the slabs, one quarter of the slab was simulated as shown in Figure 7.20. The planes of symmetry were X-Y and Z-Y planes, so that the Uz = URx = URy = 0 and Ux = URz = URy = 0 respectively. This type of symmetry boundary allows to reduce the size of the modeled slab without affecting the accuracy, however, the symmetry planes assumes adiabatic. Whole specimens were discretized in a finite element of maximum size of 20 mm, as depicted in Figure 7.20, it is worth to mention here that the effect of element size was investigated, and different size can be found in Section 7.7.4. Twelve brick element was used through the slab thickness, which provided accurate behavior for both thermal and mechanical models, more element size- thickness ratio was used by other researchers [112,132] that also gave good results, i.e. the element size could be increased. The total numbers of element were 1350, with 1792 nodes this includes the column plate and half ball's supports.

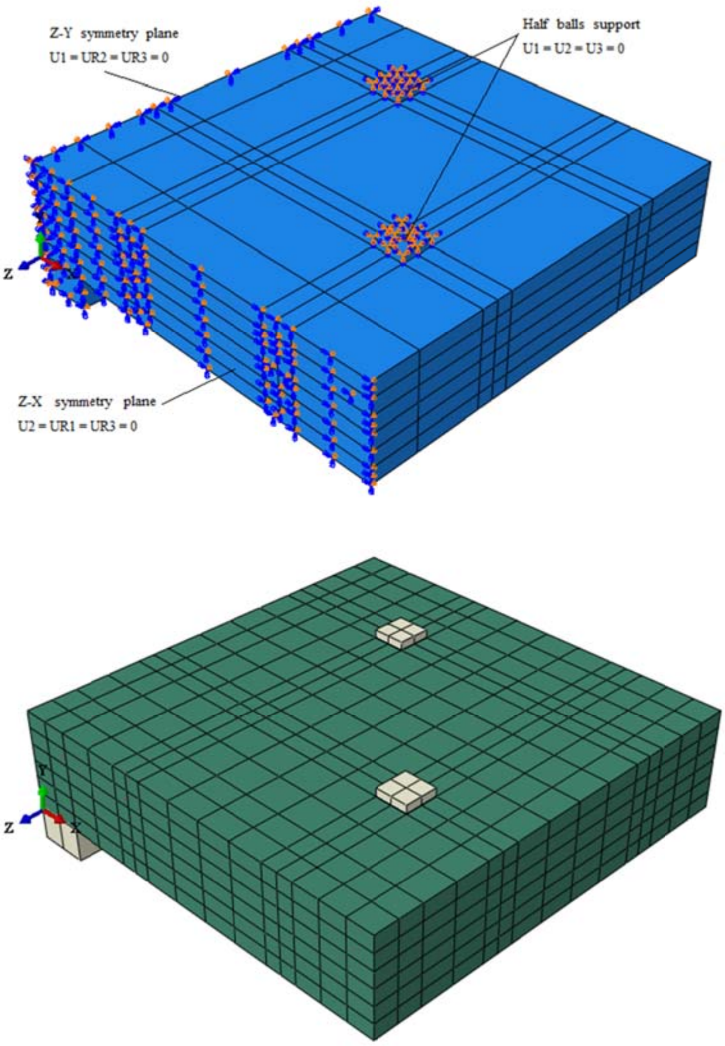

Figure 7.20 Geometry, meshing, and axes of symmetry of simulated slab-column connection

The three-dimensional hexahedral element is widely used and recommended by researchers whenever it is possible, in spite of its difficulty and less versatile for complex geometry and/or for simple geometry that decomposition by partitioning techniques such that used in the present work. The element type used in this stage differed from that used in heat transfer, C3D8R of a 3-D hexahedral solid element (tri-linear displacement brick) of eight nodes was used for concrete. A lower integration order (reduced integration) was chosen to solve the element stiffens and mass matrix, in order to reduce the calculation time with acceptable accuracy, moreover, prevent the shear locking as shown in Figure 7.21a. Moreover, a quadratic element (second order) interpolation was providing, which is good capturing the stress in the varying neutral axis [132], at the area vicinity the column in slab-column assembly, such interpolation is recommended by many researchers for specimen controlled by bending. This is because of the element with first order interpolation and of reduced integration has one integration point, this may deform the element such that all the strains in this integration point may be zero, which in turn, causes uncontrolled mesh deformation, this problem known as hourglassing that is illustrated in Figure 7.21b.

Although the reinforcement bars have a low effect on the heat transfer, but it is important to model in heat transfer model for initial predefined fields of mechanical analysis (numbering and discretizing purposes of the whole reinforced slab) 1-D truss elements (T3D2) of two nodes were used. The truss elements assumed to be embedded (perfectly glued) in the concrete elements. The truss element designed to carry axial load only, which is lying parallel to one of the axis of the solid element. The line truss element can be located anywhere in the 3-D elements, with curvilinear coordinate $\xi = \eta = \zeta = \pm 1$, but in the current work the reinforcement rebars are discretize so that the truss nodes are located at the center of an element, in order to decease the calculation efforts.

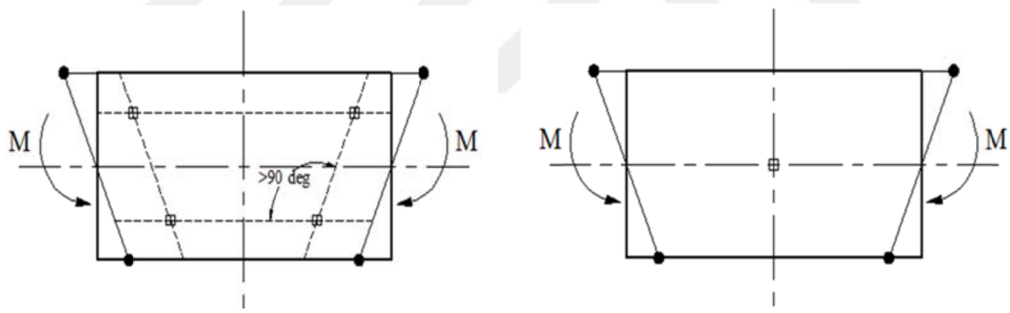

(a) (b)

Figure 7.21 Problem associated with meshing a) shear locking for quadrilateral elements and b) Hourglassing

7.7.2 Boundary condition

The slab was supported by the iron half balls, and therefor the slab could rotate and slip over these half balls, the model aimed to reflect this condition. The top face of the half balls was restrained against plane displacement, while the rotation kept free (i.e. U1 = U2 = U3 = 0) as shown in Figure 7.20, this means that the balls will rotate with the slab which is not the real behavior but not affected the result. The load was applied through controlling the displacement of the steel plate (column stub), so that the amount of increment periods determined to produce 0.4 mm/min, to be consistent with the experimental loading rate. The summation of the reaction forces at the bottom face of the column, where the applied displacement is calculated as slab resistance, this can be done through coupling the degree of freedom of the displaced node with those remaining nodes at the column face. The top column face and bottom face of the half ball's support were perfectly tied to the slab portion that introduced from partitioning, so that the column be the master and the contact slab portion was the slave, however, the contact slab portion was the master and the support was the slave, to avoid the the local damages, the element under the support where defined as linear elastic, such a technic was used by Ozbolt and Vocke [154].

7.7.3 Analysis step

Two types of analyses are available for this type of model, the static and the quasi-static analysis in ABAQUS/Standard and ABAQUS/Explicit, respectively, the former can be done with low rate loading and the viscosity have to be regulated, Genikomsou [132] investigate two viscosity parameter (0.00001 and 0.00005), he found that the static analysis with 0.00001 viscosity and quasi-static result in good agreement. The viscosity is related to the time increments by 15% [132], this will provide good results but with high costs. It is worth mentioning here, that the viscosity parameter is a numerical trick to allow for mass scaling that is speeding up the calculation time, moreover, this parameter is used for suppressing the instabilities where there is a convergence problem. The viscosity parameter is ignored in ABAQUS/Explisit, therefore, it is assumed zero in the current simulation, because quasi-static analysis was considered, which is suitable for nonlinear case that followed by stiffness reduction such as in punching shear.

7.7.4 Simulation results and comparison

7.7.4.1 Slab P60-10B

Specimen P60-10B of normal concrete that constructed and tested under ambient condition was used as control specimen. CDP parameters were investigated through specimen P60-10B. The material properties used in this model are as recorded from experimental work. The stress-strain relationship adopted by EC2 (see Figure 7.22) found to be more ductile than the tested specimen, particularly at elastic branch, and the plastic strain shows lower than elastic strain, for this reason the damage parameters for both compression and tension are not considered, in this case both elastic and plastic strains are equal. Ignoring the damage parameters may underestimate the load resistance, this assumption is accepted by Genikomsou and Polak [132].

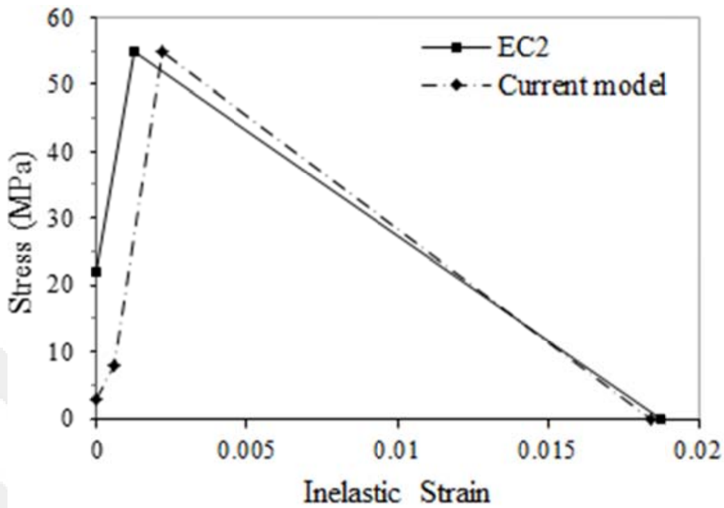

Figure 7.22 Comparison between the stress-inelastic strain adopted in the current work with that proposed by EC2

The concrete as brittle materials sustain the volume changes (known as dilatancy) that induced from the inelastic strain, this parameter can be represented in CDP as the dilation angle that can be considered as a material parameter [126]. As mentioned in the Section 7.2.2, ψ is represented in $\tilde{p} - \tilde{q}$ plane (see Figure 7.2). Figure 7.23 shows the load-deflection curves for different values of ψ, it shows that ψ affected the maximum load, but the significant effect is on the post peak behavior, where increasing ψ is decreasing the brittleness behavior of the slab. The accepted ψ was 30 degrees, which is used for the other slabs.

Figure 7.24 shows the comparison between the experimental load-deflection curve and the FE simulation for different values of K_c, these values are ranging between 0.5 and 1.0, the default value in ABAQUS is 0.667, from the investigated values it shows that increasing the Kc lead to increasing the ductility of the curve, where the Kc = 1.0 that is the Drucker–Prager proposed failure function was the more ductile behavior of the curve. There was a slight effect on the ultimate resistance and deflection, this finding is disagreed with Genikomsou and Polak [132].

The default value of the flow potential eccentricity (ϵ) is 0.1, increasing the value of ϵ to 0.4 was affected the analysis curve at failure stage. Figure 7.25 shows the analysis curves for different values of ϵ.

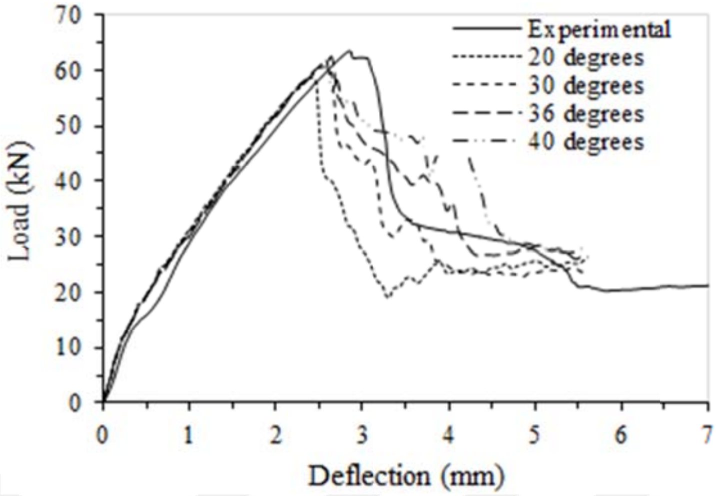

Figure 7.23 Load deflection curves of slab P60-10B for different values of ψ

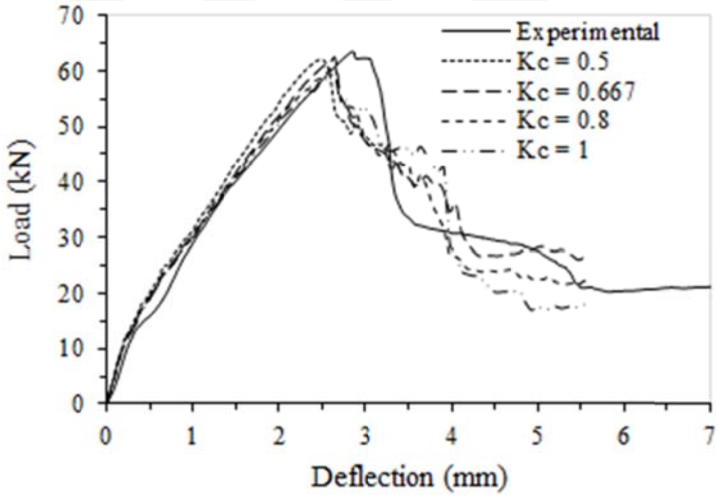

Figure 7.24 Load deflection curves of slab P60-10B for different values of K_c

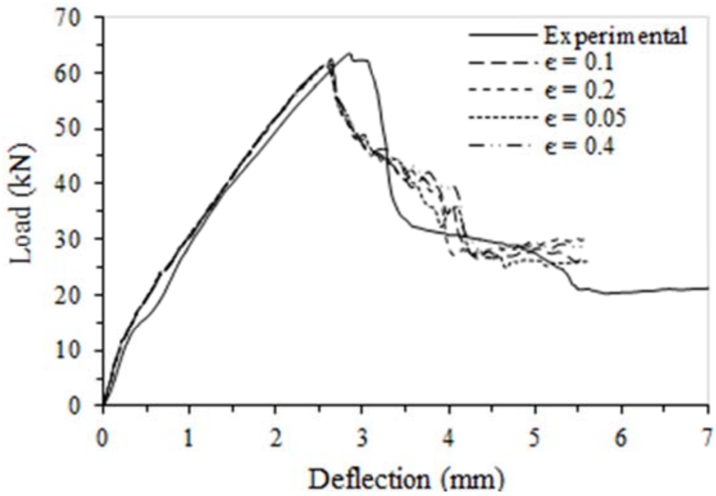

Figure 7.25 Load deflection curves of slab P60-10B for different values of flow potential eccentricities (ϵ)

As aforementioned in Section 7.4.2, there are few data available on the proportion of biaxial to uniaxial compressive strength (f_{bo} / f_{co}) under high temperature condition. The available data shows that f_{bo} / f_{co} is ranging between 1.4 and 0.8 for specimens exposed to temperature up to 750 degrees (see Figure 7.13b). In addition to ABAQUS default value (1.16) further values were investigated (1.4, 1.1, and 0.8). Figure 7.26 shows that f_{bo} / f_{co} is influencing the analysis result on stages beyond the elastic zone, particularly when the proportion equal to 0.8 are used. the other value is not showing up that is 0.5, because the result was unreasonable where the maximum load was increased dozens of times.

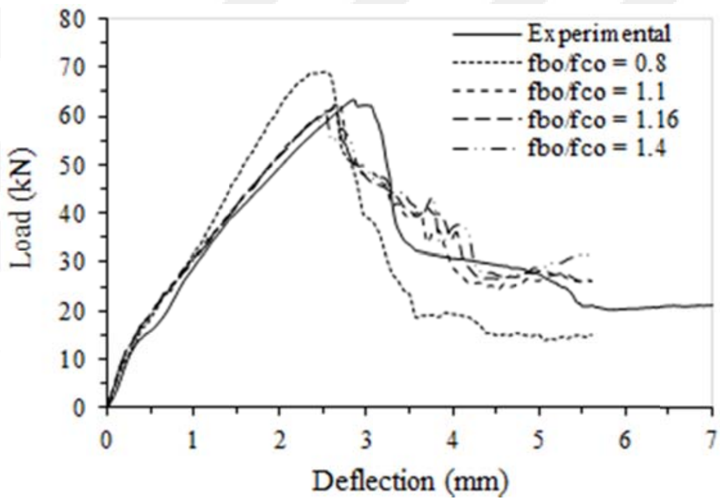

Figure 7.26 Load deflection curves of slab P60-10B for different values of f_{bo}/f_{co}

Genikomsou and Polak [132] shows that, such a model is the mesh size dependent, which is not surprising thing, because it is expected in the most plasticity based problems that shows the strain softening. The sensitivity comes from the maximum size of aggregate that affected the rotation of the slab, for this reason, the element size supposes to be larger than the aggregate size nor too coarse, to avoid the hourglassing problem (see Section 7.7.1) that expected from element C3D8R. Four different element size was conducted in this model, three were of equal length and depth (10, 15, and 20), while the fourth was of 20×10mm that is giving best behavior. Figure 7.27 shows the history of the load deflection curves for the four element size.

In spite of that, both experimental and numerical was carried out displacement controlled, however, the numerical analysis shows the more ductile behavior in the descending branch for all cases that been investigated, this may be due to the difficulties in solution convergence in the post-peak part.

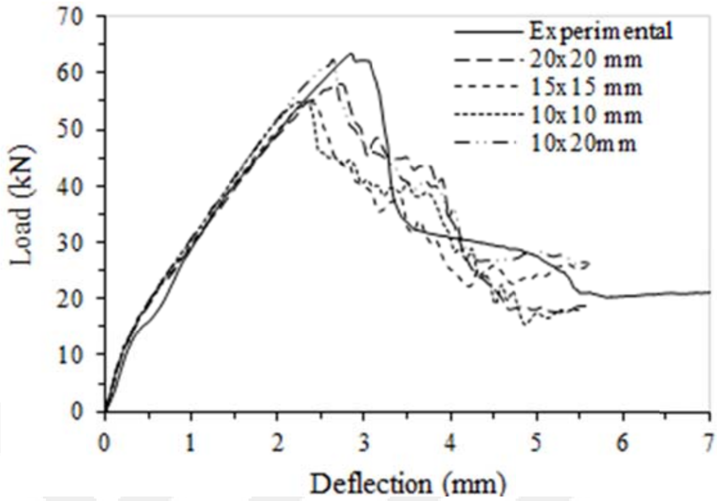

Figure 7.27 Load deflection curves of slab P60-10B for different element size

The crack development can be better represented by introducing the maximum principal plastic strain, this is because the CDP model assumes that the crack is initiated when the maximum principal plastic strain is positive [132] as shown in Figure 7.28a. It can find that the cracks at the tension face are propagated radially from the center of the slab toward the half balls, moreover other cracks are propagated from the bottom of the half balls toward the center of the slab. The punching shear cone is visible due to the sudden opening of the cracks.

The judgment of the agreement of the model is based on the load deflection history. Figure 7.28b shows the displacement isoplane for slab P60_10B, In addition to the central deflection, the displacement of the corner and the center of the edge were also compared with that recorded in experimental work, Figure 7.29 shows a comparison between the model and the recorded displacement from the two dial gages that attached to the corner and the center of the edge, it is clearly can be seen that the differences between the experimental and the model recorded displacement is small particularly in the maximum load.

Figure 7.28c shows the stress of the reinforcement bars, the high stress was developed at bars above the column, the yield stress is reached at slightly before the maximum load was reached.

(a)

(b)

(c)

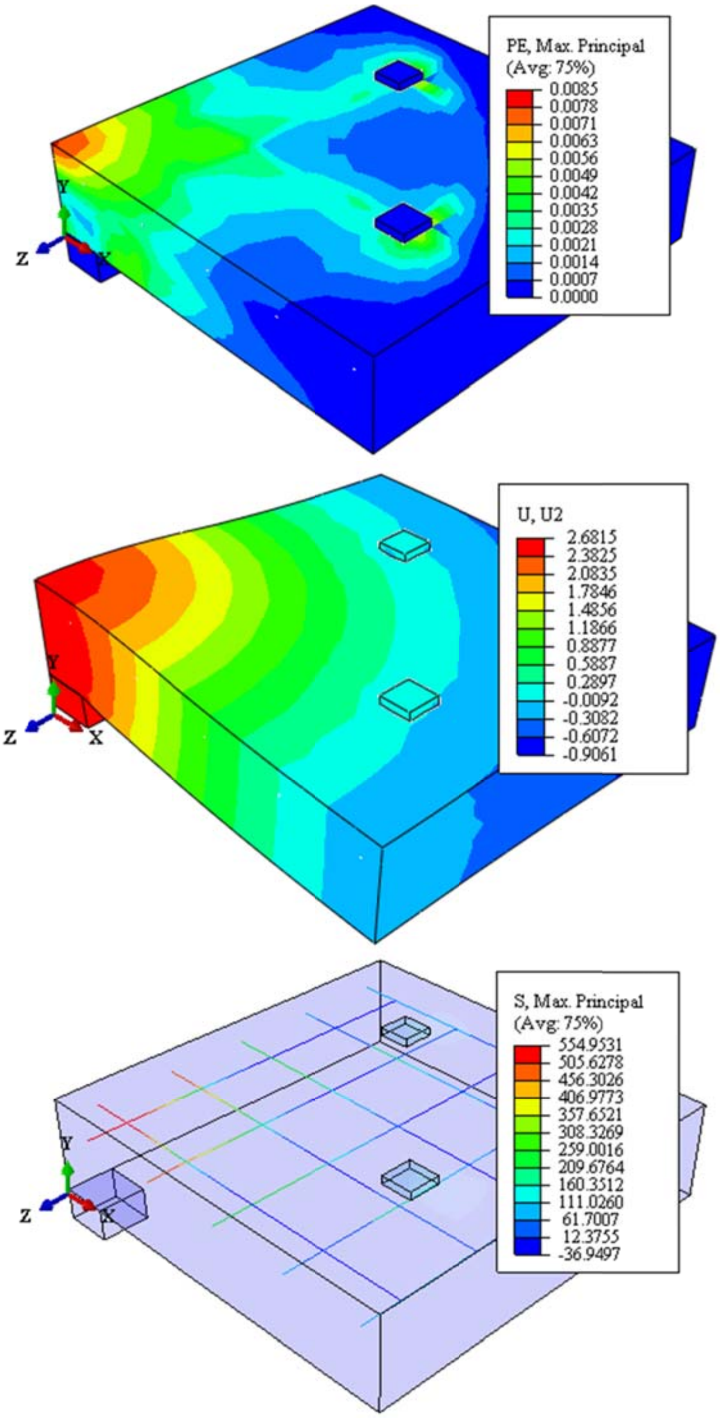

Figure 7.28 Elected output database at maximum load for slab P60-10B (a) maximum principal strain (b) vertical displacement (c) maximum principal stress

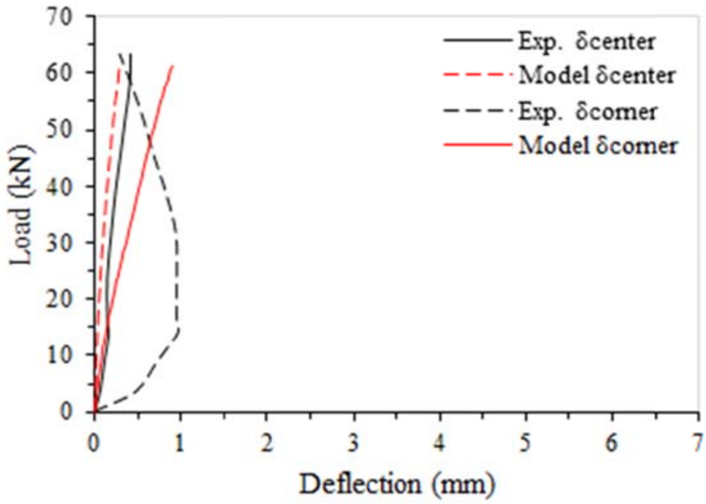

Figure 7.29 Elected output database at maximum load for slab P60-10B (a) maximum principal strain (b) maximum principal stress (c) vertical displacement for different element size

CHAPTER 8

CONCLUSIONS AND RECOMMENDATION

8.1 General

This thesis aimed to discuss the behavior of slab-column connection reinforced by different types and percentages of fibers in addition to the conventional flexural reinforcement. The fibrous concrete mixtures with best behaviors were exposed to fire in order to investigate the residual strength of concrete slabs. Small experimental models were designed to fail in punching shear. The design was conducted based on the whole structural analysis under virtual design load, while the size of the structure and the reinforcement ratio were selected to meet the available tests in literature. Five available mechanical models were presented, discussed, and compared. Moreover, nine code's provisions were presented and discussed through 174 test specimens collected from literature, which were all tested under ambient conditions. On the other hand, two mechanical models for slab-column assembly under fire conditions were presented.

The test results of forty one slab specimens, including twenty five specimens at ambient conditions and sixteen specimens exposed to four levels of temperature, were used to investigate the behavior of slab-column connections both under ambient and high temperature conditions. Among the forty one specimens, some specimens were cast with both ECC and conventional concrete. Such case of composite slabs was not found in the literature. Moreover, no previous experimental research that deals with the residual strength of slabs having similar support configuration was found in literature.

The most important conclusion remarks drawn from the experimental work of this study can be categorized into two main parts as follows,

8.2 Slab-Column Connection under Ambient Conditions

From the twenty one slab specimens tested under ambient conditions, the following conclusions can be drawn:

- All elected codes underestimated the ultimate load resistance of the tested slabs. The Indian standards were the most conservative code, particularly with the small thickness slab, while the remaining elected codes gave almost same predictions.

- None of the elected codes captured the effect of the varying of the reinforcement ratio. The results showed that increase of the reinforcement ratio by 33% increases the ultimate load by 27%. Moreover, conservative estimation of the size effect was noticed for the codes that considers this parameter .

- The variation in the slab thickness showed significant decreasing in punching shear stress in terms of $(1/d)^{1/4}$. This agrees with the other researchers' findings. However, the ductility is decreasing with increasing the slab thickness.

- With all fiber types used in the current work, the behavior of flat plate-column connection shows significant improvement compared with those slabs made from plain concrete. Compared to their corresoponding plain concrete specimens, the ultimate load resistance was increased and the total deformation was decreased for fibrous slab specimens at all loading stages.

- The results showed that the slab reinforced with steel fiber of 1% provided the highest load resistance among all tested slabs of the same dimensions. For this slab, the percentage of the improvement was 76% compared to the normal concrete slab. However, If the normalized load resistance with the square root of the compressive strength is considered, the normal concrete slab made with NM-ECC (at the critical area) and the slab made completely of NM-ECC showed the highest normalized load resistance improvement of about 29% compared to normal concrete slab, while the normalized improvement of SFRC slab was only 7.7%.

- The addition of the steel fiber more than 1% did not provide a significant change to the load resistance, hence, the 1% of steel fiber was found to be the optimum steel fiber content.

- The use of steel fibers and NM-ECC with the tested slabs not only increased the punching shear strength, but also transformed the brittle punching shear failure to a ductile flexural and/or shear failure, which is attributed to the multiple cracking behavior that improved the post maximum load cracking.

- Fiber length has a significant impact on the degree of improvement in ECC properties. Among the four fiber types used in ECC slabs, the highest load resistance was obtained from PVA-ECC of 6 mm fiber that was 46% higher compared to the normal concrete slab, while the NM-ECC improvement reached 30% only. On the other hand, the use of PVA and PP fibers with a fiber length of 12 mm led to almost similar load resistance of normal concrete slabs.

- The effect of Nylon-monofilament content in ECC mix is decreasing in presence of the conventional reinforcement. Increasing the fiber from 0.5 to 2% increased the load resistance of the slabs by 32% for reinforced slabs, while this improvement was 57% for non-reinforced slab. Moreover, it was found that the reinforced specimens sustained 2.5 times higher load resistance than the slabs without conventional reinforcement.

- The multi-cracking behavior in fibrous concrete slab column connectiosn improves the ductility and the energy absorption substantially. For the post-maximum load stage, the ductility and the energy absorption capacity of the slab made from NM-ECC with 2% of fiber were increased by 166 and 588%, respectively. Lower ductility and energy absorption were obtained when the NM-ECC was located at the critical punching shear zone.

- The residual load resistance due to the tensile membrane action of plain concrete was higher than those found in literature. Furthermore, the fibrous concrete in slab-column connection shows significant increase in the residual strength due to membrane action. The highest value was obtained from the SFRC slabs, which was about 88 to 92%. Similar values were recorded for the slabs with NM-ECC and plain concrete, while 72 to 77% of the maximum load was retained for slabs with full NM-ECC. These values decreased for slabs containing polypropylene (PP) and polyvinyl alcohol (PVA) to 37 and 49%, respectively.

- Comparing with the crack pattern found in the literature for plain concrete slabs, the current mix design allowed to produce of an extensive non uniform diagonal cracking. Moreover, the steel fibers delayed the initiation of the cracks, but with more extensive cracking at failure compared to the slab of plain concrete.

- Different crack patterns were shown in slabs made from ECC. The extensive diagonal cracking in PVA-ECC slabs did not extend beyond the punching shear crack, while the cracking in the NM-ECC and PP-ECC extended to the edges of the slab.

8.3 Residual Slab Strength Due to Exposing to High Temperatures

The followings are the main key points that were concluded from the investigation of the residual strength of SFRC slabs due to exposing to high temperatures.

- Using high percentage of fine aggregate increases the contact area with the binder, which improves the stress flow and increases the rate of the reaction process of the components. This positive effect was noticed for temperatures up to 300 ºC for SFRC in the current work.

- The decay in compressive strength of the SFRC is less than that in the plain concrete . The test results showed also that the 0.75% volume fraction of steel fiber led to less decay rate than the those of 1.0 and 1.25%. The percentage reduction in compressive strength for plain concrete specimens exposed to temperatures between 300 and 550 ºC was in the range of 4 to 54% compared to unheated specimens, while for specimens reinforced with 0.75, 1.0, and

1.25% steel fiber and exposed to 450 and 550 ºC, the percentage reductions were in the ranges of 10 to 23%, 22 to 47%, and 17 to 49 %, respectively.

- The highest residual compressive and tensile strengths at 550 °C were 78% and 64%, respectively, compared to the associated specimens of plain concrete. This improvement was obtained from SFRC reinforced by the low percentage of steel fiber (V_f = 0.75 %).

- Exposing to high temperatures increases the SFRC mechanical properties at 150 °C and 300 °C, where the compressive strength was improved by 18% with less improvement in tensile strength. For temperatures above 300 °C, all the mechanical properties are decaying in low rates compared to the plain concrete. The residual compressive and tensile strengths of SFRC with 0.75 % at 550 °C were 76% and 73%, respectively, of their corresponding values at ambient conditions.

- Based on tests on standard cylinders under different levels of high temperature, it was found that the standard cylinder specimens are not suitable to represent the residual strength of concrete exposed to temperatures higher than 300 ^{o}C. This can be attributed to the isoplane produced from thermal gradients. The thermal gradient decreases with increasing the soak time, hence the compressive strength of a specimen exposed to temperatures above 300 ºC significantly differs when the test is conducted after the heating process directly than that conducted after long soak time.

- The finite element thermal analysis of concrete specimens showed that the thermal conductivity of the normal concrete made from high fine aggregate percentages is close to that for SFRC.

- The decay of the tensile strength for concrete reinforced by steel fibers due to exposing to high temperatures is well represented by a polynomial relation with the cubic root of compressive strength. However, for the plain concrete, square root of compressive strength can be related to concrete tensile strength in linear relations.

- Inclusion of steel fibers in flat slabs subjected to concentric loading and high temperatures reduces the displacement at the ultimate load stage. Moreover, it enhances the failure load, which is followed by increasing the diagonal cracking.

- Comparisons between the specimens cracking after failure showed that the use of steel fiber has no significant influence on the failure type and cracking patterns. On the other hand, the level of temperature to which the specimens are exposed does matter.

8.4 Finite Element Analysis

From the presented comparison between the experimental result and the FE simulation can be concluded that the finite element is a good tool to predict the slab load resistance and load-deflection relationship. For the current slab mixture, the stress-strain relationship that adopted by EC2 can be considered with small modification at maximum load, however, the decay in stress-strain that adopted by EC2 for heated slabs was not proper to represent the behavior of the slab.

The default values of ABAQUS for Kc, ϵ, and f_{bo}/f_{co} can be used, while, 30 degrees are preferred for angle of dilation and the damages parameter for both compressive and tensile can be ignored. All mentioned parameters are affected the post-peak behavior. The model is the mesh size dependent, which is not surprising thing, because it is expected in the most plasticity based problems that shows the strain softening. During the trials, it shows that the compressive strength has small influence, while the tensile strength and the fracture energy a dominant influence on the slab's resistance capacity.

8.5 Recommendations for Future Works

Generally, it was found that there are few experimental works regarding the residual strength of slab-column connections exposed to high temperatures. There are different factors affecting the behavior of this structural element, which make the mission of the separation and quantifying of the effect of the various factors is quite complex. The investigation of fibrous concrete slab column assemblies with different slab thicknesses, conventional reinforcement ratios, support conditions, and different relations between column and slab thicknesses may yield better understanding of the main influencing factors. The research can be extended to investigate the behavior of fibrous concrete slabs under different fire scenarios .

The use of various fiber contents and the concentration of these fibers in specific areas in the current work allow for future development of mechanical models. Furthermore, the results obtained from the residual strength can be used to modify the existing mechanical models of the 500 ºC isotherm, where the exposing of the two faces of the slab would eliminate the exterior layers of these faces.

The proposed mix proportions used in the current work are recommended for further works. The threshold of the percentages of fine to coarse aggregates can be investigated through mechanical and structural tests. Moreover, the numerical simulation based on experimental data obtained from many sensors can provide more understanding. This may allow to extend the size effect law proposed by Bazant where the cylinder test is required. Otherwise, the standard cube test is highly recommended for the investigation of concrete structural behavior under fire conditions. This should be tested with suitable soak time. The relation between the standard cube test and the cylinder exposed to high temperatures is a required future work. The proposed equations for predicting the load resistance of slabs exposed to high temperatures should be calibrated for other mix proportions.

REFERENCES

[1] ACICT-13, ACI Concrete Terminology. Farmington Hills: American Concrete Institute, 2013.

[2] P. V. P. Sacramento, M. P. Ferreira, D. R. C. Oliveira, and G. S. S. A. Melo, "Punching Strength of Reinforced Concrete Flat Slabs," *IBRACON Structures and Materials Journal*, **5 (5)**, pp. 659-674, Oct 2012.

[3] C.E. Ospina, G. Birkle, and Widianto, "Databank of Concentric Punching Shear Tests of Two-way Concrete Slabs without Shear Reinforcement at Interior Supports," **2**, 2012.

[4] S Kinnunen and H. Nylander, "Punching of Concrete Slabs without Shear Reinforcement," Royal Institute of Technology, **158**, p. 112, 1960.

[5] J.S. Kuang and C.T. Morley, "Punching shear behavior of restrained reinforced concrete slabs.," *ACI Structural Journal*, **89**, pp. 13-19, 1992.

[6] E. Annerel et al., "Thermo-Mechanical Analysis of an Underground Car Park Structure Exposed to Fire," *Fire Safety Journal*, **57**, pp. 96-106, 2013a.

[7] P. Bamonte, M.F. Ruiz, and A. Muttoni, "Punching Shear Strength of R/C Slab Subjected to Fire," in 7th International Conference on Structure in Fire, Zurich, 2012, pp. 689-698.

[8] P.J. Moss, R.P. Dhakal, G. Wang, and A.H. Buchanan, "The Fire Behaviour of Multi-bay, two-way Reinforced Concrete Slabs," *Engineering Structures*, **30**, pp. 3566-3573, 2008.

[9] P. Bamonte and R. Felicetti, "Fire Scenario and Structural Behaviour of Underground Parking Lots Exposed to Fire," in Proceeding of International Conferance

Applications of structural Fire Engineering, session 2 Fire Modelling, Prague, 19-20 Februari 2009, pp. 60-65.

[10] K. Kordina, "Über das Brandverhalten Punktgestützter Stahlbetonplatten. (on the Fire Behavior of Reinforced Concrete Flat Slabs)," Berlin, Heft 479 1997.

[11] K.E. Ramdane, "Punching Shear of High Performance Concrete Slabs," in 4th International Symposium on Utilization of High-strength/High-performance concrete, Paris, 1996.

[12] H. Gesund and Y. P. Kaushik, "Analysis of Punching Shear Failures in Slabs," *International Association for Bridge and Structural Engineering*, **30** (1), pp. 41-60, 1970.

[13] J. Moe, "Shearing Strength of Reinforced Concrete Slab and Footing under Concentrated Loads," April 1961.

[14] C.S. Whitney, "Ultimate Shear Strength of Reinforced Concrete Flat Slabs, Footings, Beams, and Frame Members Without Shear Reinforcement," *Journal of the American Concrete Institute*, **29** (4), pp. 256-298, Oct. 1957.

[15] R.C. Elstner and E. Hognestad, "Shearing Strength of Reinforced Concrete Slabs," *ACI Journal*, Proceedings, **53**, (1), pp. 29-58, Jan 1956.

[16] F.E. Richart, "Reinforced Concrete Wall and Column Footings," *Journal of the Amarican Concrete Institute*, **20**, (2), pp. 97-127, July 1948.

[17] I. Shehata, "Simplified model for estimating the punching resistance of reinforced concrete slabs," *Materials and Structures/Materiaux et Constructions*, **5** (23), pp. 364-371, 1990.

[18] C. E. Broms, "Concrete flat slabs and footings Design method for punching and detailing for ductility," Royal Institute of Technology, Stockholm, Ph.D Thesis 2005.

[19] ACI318-14, "Building Code Requirements for Structural Concrete (ACI 318M-14) and Commentary (ACI 318RM-14)," American Concrete Institute, Farmington Hills, MI, ACI 318, 2014.

[20] S.D.B. Alexander and Sidney H. Simmonds, "Bond Model for Concentric Punching Shear," *ACI Structural Journal*, **89** (3), pp. 325-334, May-June 1992b.

[21] D.D Theodorkapoulos and R.N.Sawmy, "Ultimate Punching Shear Strength Analysis of Slab-Column Connections," *Cement and Concrete Composites*, pp. 509-521, 2002.

[22] A. Muttoni, "Punching Shear Strength of Reinforced Concrete Slabs Without Transverse Reinforcement," *ACI Structural Journal*, **105** (4), pp. 440-450, 2008a.

[23] A. Muttoni and M. F. Ruiz, "Shear Strength of Members without Transverse Reinforcement as Function of Critical Shear Crack Width," *ACI Structural Journal*, **105** (2), pp. 163-172, March-April 2008b.

[24] A. Muttoni and J. Schwartz, "Behaviour of Beams and Punching in Slabs without Shear Reinforcement," *IABSE Colloquium*, **62**, pp. 703-708, 1991.

[25] A. Muttoni, "Shear and Punching Strength of Slabs without Shear," *Beton- und Stahlbetonbau*, **98** (2), pp. 74-84, 2003.

[26] R. Guidotti, "Poinçonnement des planchers-dalles avec colonnes superposées fortement sollicitées", 2010.

[27] S.D.B. Alexander and S.H. Simmonds, "Tests of Column-Flat Plate Connections," *ACI Structural Joumal*, **89 (5)**, pp. 496-502, September-October 1992a.

[28] P. Tolf, "Plattjocklekens Inverkan Pa Betongplattors Hallfasthet vid Genornstansning.," Institutionen for Byggnadsstatik, KTH, Stockholm, Forsok med cikulara plattor. TRITA-BST Bull. 146, TRITA-BST Bull. 146 1988.

[29] M. Hallgren, "Punching shear capacity of reinforced high strength concrete slabs," Stockholm, Doctoral Thesis. TRITA-BKN. Bull.23 1996.

[30] N Brushlinsky, Marty Ahrens, Sergei Sokolov, and Peter Wagner, "World Fire Statistics," Center of Fire Statistics of CTIF, International Association of Fire and Rescue Services, 2015.

[31] EN1992-1-2, "Eurocode2: Design of Concrete Structures- Part 1-2: General Rules—Structural Fire Design," CEN, Brussels, 2004.

[32] PD7974-7, "Application of fire safety engineering principles to the design of buildings", 2003.

[33] EN1991-1-2, Part 1-2: General actions — Actions on structures exposed to fire, 2002.

[34] P. Bamonte, R. Felicetti, and P.G. Gambarova, "Punching Shear in Fire-Damaged Reinforced Concrete Slabs," *ACI special publ*, SP265-16 (2009a) 345-366.

[35] Milan Dj. Blagojevic' and Dušica J. PEŠIC', "A New Curve for Temperature-Time Relationship in Compartment Fire," *Thermal Science*, **15 (2)**, pp. 339-352, 2011.

[36] M. Law, "A Relationship between Fire Grading and Building Design and Contents," Environment and Fire Offices, Fire Research Station, 1971.

[37] O. Pettersson, Sven-Erik Mangnusson, and Jorgn Thor, Fire Engineering Design of Steel Structures. Stockholm: Swidish Institute of Steel Construction, 1976.

[38] D. Drysdale, An Introduction to Fire Dynamics.: A John Wiley & Sons, Ltd., Publication, 2011, Third Edition.

[39] G.C. Thomas, A.H. Buchanan, and C.M. Fleischmann, "Structural Fire Design: The Role of Time Equivalence," in International Association for Fire Safty Science, Fifth international symposium, Melbourne, 1997, pp. 607-618.

[40] J.H. Lienhard IV and J.H. Lienhard, A Heat Transfere Textbook. Cambidge Massachusetts: Phlogiston Press, 2011.

[41] ASCE, "Structural Fire Protection," ASCE Committee on Fire Protection, Structural Division, American Society of Civil Engineers, New York, Manual (78) Manual 1992.

[42] X.F. Hu, T.T. Lie, G.M. Polomark, and J.W. MacLaurin, "Thermal Properties of Building Materials at Elevated Temperatures," Institute for Research in Construction, Canada, Internal Report (643) 1993.

[43] V. Kodur, "Properties of Concrete at Elevated Temperatures," 2014.

[44] T. Z. Harmathy, "Thermal properties of concrete at elevated temperatures," *Journal of Materials,JMLSA*, **5** (1), pp. 47-74, March 1970.

[45] J.B. De Hanai and K.M.A. Holanda, "Similarities Between Punching and Shear Strength of Steel Fiber Reinforced Concrete (SFRC) Slabs and Beams," *Structures and Materials Journal*, **1 (1)**, pp. 1-16, 2008.

[46] ACI216R-89, "Guide for Determining the Fire Endurance of Concrete Elements," American Concrete Institute, Farmington Hills, MI, ACI 216, Reapproved 1994.

[47] M. Bastami, F. Aslani, and M. E. Omaran, "High-Temperature Mechanical Properties of Concrete," *International Journal of Civil Engineerng*, **8 (4)**, pp. 337-351, 2010.

[48] D.J. Naus, "A Compilation of Elevated Temperature Concrete Material Property Data and Information for Use in Assessments of Nuclear Power Plant Reinforced Concrete Structures," Office of Nuclear Regulatory Research, U.S.National Nuclear Regulatory Commission, Washington, DC, NUREG/CR-7031 2010.

[49] L.Y. Li and J. Purkiss, "Stress–strain constitutive equations of concrete material at elevated temperatures," *Fire Safety Journal*, **40 (7)**, pp. 669-686, 2005.

[50] K. Willam, Y. Xi, K. Lee, and B. Kim, "Thermal Response of Reinforced Concrete Structures in Nuclear Power Plants," Department of Civil, Environmental,and Architectural Engineering/ College of Engineering/ University of Colorado at Boulder, SESM No. 02 2009.

[51] D. J. Naus, "The Effect of Elevated Temperature on Concrete Materials and Structures—A Literature Review," Office of Nuclear Regulatory Research, U.S. Nuclear Regulatory Commission, Washington, DC, NUREG/CR-6900 2006.

[52] E. Annerel and L. Taerwe, "Design Considerations for Shear Failure of Flat Concrete Slabs Exposed to Fire," *in Concrete- Innovation and Design*, fib Symposium, Copenhagen, 2015, pp. 1-13.

[53] EN1992-1-1, "Eurocode 2: Design of concrete structures - Part 1-1: General rules and rules for buildings," CEN, Brussels, 2004.

[54] H.K.M. Smith, B. T. Stratford, and L. Bisby, "Punching Shear of Reinforced Concrete Slabs under Fire Conditions: Experiment vs. Design," in The First International Conference on Structural, CONFAB 2015, The University of Edinburgh, 2015.

[55] W. Dilger, G. Birkle, and D. Mitchell, "Effect of Flexural Reinforcement on Punching Shear Resistance," *SP-232*, pp. 57–74, 2005.

[56] J.M. Yang, Y.S. Yoon, W.D. Cook, and D. Mitchell, "Punching Shear Behavior of Two-Way Slabs Reinforced with High-Strength Steel," *ACI structural Journal*, **107** (4), pp. 468–475, 2010.

[57] I. Fletcher, S. Welch, J. Torero, R. Carvel, and A. Usmani, "Behavior of concrete structures in fire," *Thermal Science*, 11 (2), pp. 37-52, 2007.

[58] E. Annerel, L. Lu, and L. Taerwe, "Punching Shear Tests on Flat Concrete Slabs Exposed to Fire," *Fire Safety J.*, **57**, pp. 83-95, 2013b.

[59] M. Ghoreishi, A. Bagchi, and M.A. Sultan, "Punching Shear Behavior of Concrete Flat Slabs in Elevated Temperature and Fire," *Advances in Structural Engineering*, 18 (5), pp. 659-674, 2015.

[60] J.S. Liao, F.P. Cheng, and C.C. Chen, "Fire Resistance of Concrete Slabs in Punching Shear," American Society of Civil Engineers, ASCE, *Journal of Structural Engineering*, Jan 2013.

[61] H. Salem, H. Issa, H. Gheith, and A. Farahat, "Punching Shear Strength of Reinforced Concrete Flat Slabs Subjected to Fire on their Tension Side," *HBRC Journal,* **8 (1)**, pp. 67-80, April 2012.

[62] H.K.M. Smith, T.J. Stratford, and L.A. Bisby, "Punching Shear of Restrained Reinforced Concrete Slabs Under Fire Conditions," in 8th International Conference on Structures in Fire, Shanghai, China, 2014.

[63] ISO834-1, "Fire-Resistance Tests — Elements of Building Construction — Part 1:General Requirements," International Organization for Standardization, CH-1211 Genève 20, Switzerland, ISO834-1, 1999(E).

[64] ASTM E119, "Standard Test Methods for Fire Tests of Building Construction and Materials," ASTM International, West Conshohocken, PA 19428-2959, An American National Standard 2000.

[65] R.H (discussion by Armer) Wood, "The Reinforcement of Slabs in Accordance with a Pre-Determined Field," Concrete, **2 (2)**, pp. 69-76, 1968.

[66] CSA A23.3, Design of concrete structures.: Canadian Standards Association, 2004.

[67] N. Yermak, P. Pliya, A. L. Beaucour, A. Simon, and A. Noumowé, "Influence of Steel and/or Polypropylene Fibres on the Behaviour of Concrete at High Temperature: Spalling, Transfer and Mechanical Properties," *Construction and Building Materials*, **132**, pp. 240-250, 2017.

[68] J. Michels, D. Waldmann, S. Maas, and A. Zürbes, "Steel Fibers as Only Reinforcement for Flat Slab Construction – Experimenta Investigation and Design," *Construction and Building Materials*, **26**, pp. 145-155, 2012.

[69] R.N. Swamy and S.A.R. Ali, "Punching Shear Behavior of Reinforced Slab-Column Connections Made with Steel Fiber Concrete," *ACI Journal*, pp. 392-406, 1982.

[70] A.M. Shaaban and H. Gesund, "Splitting Tensile Strength of Steel Fiber Reinforced Concrete Cylinders Consolidated by Rodding or Vibrating," *ACI Materials Journal*, **90 (4)**, pp. 366-369, 1993.

[71] R. Serrano, A. Cobo, M.I. Prieto, and M.de las Nieves González, "Analysis of Fire Resistance of Concrete with Polypropylene or Steel Fibers," *Construction and Building Materials*, **122**, pp. 302-309, 2016.

[72] ASCE-07-10, "Minimum Design Loads for Buildings and Other Structures," p. 608, 2010.

[73] S. Ahmad, B.M. Irons, and O.C. Zienkiewicz, "Analysis of Thick and Thin Shell Structures by Curved Finite Elements," *International Journal for Numerical Methods in Engineering*, **2**, pp. 419-451, 1970.

[74] J. Einpaul, M.F. Ruiz, and A. Muttoni, "Influence of Moment Redistribution and Compressive Membrane Action on Punching Strength of Flat Slabs," *Engineering Structures*, **86**, pp. 43–57, 2015.

[75] M.A. Ghoneim and M.T. El-Mihilmy, Design of Reinforced Concrete Structures, 2nd ed.: Cairo University, 2008, **2**.

[76] E.S. Bernard and M. Pircher, "The Influence of Thickness on Performance of Fiber-Reinforced Concrete in a Round Determinate Panel Test," *Cement, Concrete, and Aggregates*, CCAGDP, **23 (1)**, pp. 27-33, 2001.

[77] Ø. Bjøntegaard, "Energy Absorption Capacity for Fibre Reinforced Sprayed Concrete Effect of Friction in Round and Square Panel Tests with Continuous Support (Series 4)," Technology Department, Norwegian Public Roads Administration, TECHNOLOGY REPORT No. 2534 2009.

[78] P.E. Regan and M.W. Braestrup, "Punching Shear in Reinforced Concrete-A State-of-the-Art," Lausanne, 1985.

[79] G.N.J. Kani, "The Riddle of Shear Failure and its Solution," *ACI Journal*, April, **61 (4)**, pp. 441-465, 1964.

[80] N. J. Gardner, "Relationship of the Punching Shear Capacity of Reinforced Concrete Slabs with Concrete Strength," *ACI Structural Journal*, **87 (1)**, pp. 66-71, January-February 1990.

[81] TS500, Requirements for Design and Construction of Reinforced Concrete Structures. Ankara: TUBITAK, 2000 English version, vol. TS500.

[82] M.H. Harajli, D. Maalouf, and H. Khatib, "Effect of Fibers on the Punching Shear Strength of Slab-Column Connections," *Cement & Concrete Composites*, **7**, pp. 161-170, 1995.

[83] S. Guandalini, O.L. Burdet, and A. Muttoni, "Punching Tests of Slabs with Low Reinforcement Ratios," *ACI Structural Journal*, **106 (1)**, pp. 87-95, January-February 2009.

[84] A.M. Shaaban and H. Gesund, "Punching Shear Strength of Steel Fiber Reinforced Concrete Flat Plates," *ACI Structural Journal*, 91(3), pp. 406-414, 1994.

[85] R. Felicetti and P.G. Gambarova, "Effects of High Temperature on the-Residual Compressive Strength of High-Strength Siliceous Concretes," *ACI Materials Journal*, **95 (4)**, 1998.

[86] B. Zhang, N. Bicanic, C.J. Pearce, G. Balabanic, and J.A. Purkiss, "Discussion: Residual Fracture Properties of Normal- and High-Strength Concrete Subject to Elevated Temperatures," *Magazine of Concrete Research*, **52, (2)**, pp. 123-136, 2000. [Online]. https://doi.org/10.1680/macr.2001.53.3.221

[87] J.A. Purkiss, "Steel fibre Reinforced Concrete at Elevated Temperature," *The International Journal of Cement Composites and Lightweight Concrete*, **6 (3)**, pp. 170-184, 1984.

[88] G.M. Chen, Y.H. He, H. Yang, J.F. Chen, and Y.C. Guo, "Compressive Behavior of Steel Fiber Reinforced Recycled Aggregate Concrete after Exposure to Elevated Temperatures," *Construction and Building Materials*, **71**, pp. 1-15, 2014.

[89] C.S. Poon, Z.H. Shui, and L. Lam, "Compressive Behavior of Fiber Reinforced High-Performance Concrete Subjected to Elevated Temperatures," *Cement and Concrete Research*, **34**, pp. 2215–2222, 2004.

[90] J.R. Lawson, T. Phanl, and F. Davis, "Mechanical Properties of High Performance Concrete after Exposure to Elevated Temperatures," National Institute of Standard and Technology, Gaithersburg, NISTIR 6475 2000.

[91] Y. Li and M. J. Spearpoint, "Analysis of Vehicle Fire Statistics in New Zealand Parking Buildings," *Fire Technology*, **43 (2)**, pp. 93-106, 2007.

[92] S.D.B Alexander and H. Simmonds, "Shear-Moment Transfer in Column-Slab Connections," *Civil Engineering*, University of Alberta, SEI-Rep No.141 1986.

[93] DIN1045-2, Concrete, reinforced and prestressed concrete structures- Part 1: Design and construction, August 2008.

[94] AS3600, Concrete Structures. Sydney, Australia: Standards Australian Limited, 2009.

[95] IS456, Plain and Reinforced Code of Practice, 2000.

[96] SNIP2.03.01-84, Concrete and Reinforced Concrete Structures. Russia: National Building Codes Of Russia, 1997 Edition, vol. SNIP2.03.01-84.

[97] MC2010 CEB-FIB, Model Code 2010, 6566th ed. Lausanne: International Federation for Structural Concrete (fib), 2012, **1**.

[98] BS EN1992-1-1, design of concrete structures. Part 1-1: general rules and rules for buildings. Brussels: Eurocode 2,European Committee for Standardization, 2004.

[99] Widianto, O. Bayrak, and J.O. Jirsa, "Two-Way Shear Strength of Slab-Column Connections: Reexamination of ACI 318 Provisions," *ACI Structural Journal*, **106 (2)**, pp. 160-170, March-April 2009.

[100] C.E. Ospina and N.M. Hawkins, "Addressing Punching Failure," *Structure Magazine*, pp. 14-17, 2013.

[101] N.J. Gardner, "ACI 318-05, CSA A23.3-04, Eurocode 2 (2003), DIN 1045-1 (2001), BS 8110-97 and CEB-FIP MC 90 Provisions for Punching Shear of Reinforced Concrete Flat Slabs," *American Concrete Institute*, SP232, pp. 1-22, 2005.

[102] P. E. Regan, "Behaviour of Reinforced Concrete Flat Slabs," London, 1981.

[103] G. Brikle and W.H.Dilger, "Influence of Slab Thickness on Punching Shear Strength," *ACI Structural Journal*, **105 (2)**, pp. 180-188, Mar-Apr 2008.

[104] Z.P. Bazant and Z. Cao, "Size Effect in Punching Shear Failure of Slabs," *ACI Structural Journal*, pp. 44-53, January-February 1987.

[105] K-H. Tan and P. Paramasivam, "Punching Shear Strength of Steel Fiber Reinforced Concrete Slabs," *Journal of Materials in Civil Engineering*, **6 (2)**, pp. 240-253, 1994.

[106] M.E. Criswell, "Strength and Behavior of Reinforced Concrete Slab-Column Connections Subjected to Static and Dynamic Loadings," Vicksburg, Technical Report No. N-70-I 1970.

[107] A. Pan and J.P. Moehle, "Lateral Displacement Ductility of Reinforced Concrete Flat Plates," *ACI Structural Journal*, **86 (3)**, pp. 250-258, 1989.

[108] M.A. Polak, "Ductility of Reinforced Concrete Flat Slab-Column Connections," *Computer-Aided Civil and Infrastructure Engineering*, **20**, pp. 184–193, 2005.

[109] A.E. Green and P.M. Naghdi, "A Re-Examination of the Basic Postulates of Thermomechanics," *in Mathematical and Physical Sciences*, **432**, London, 1991, pp. 171-194.

[110] G.A. Khoury, "Effect of Fire on Concrete and Concrete Structures," *Prog. Struct. Engng Mater*, **2**, pp. 429-447, 2000.

[111] T.T. Lie and V.K.R. Kodur, "Thermal and mechanical properties of steel-fibre-reinforced concrete at elevated temperatures," *Can. J. Civ. Eng.*, **23**, pp. 511 - 517, 1996.

[112] J.V. Aguado, V. Albero, A. Espinos, A. Hospitaler, and M.L. Romero, "A 3D Finite Element Model for Predicting the Fire Behavior of Hollow-Core Slabs," *Engineering Structures*, pp. 1-60, 2016.

[113] Z.P. Bazant and Y. Xiang, "Size Effect in Compression Fracture: Splitting Crack Band Propagation," *Journal of Engineering Mechanics*, **123 (2)**, pp. 162-172, 1997.

[114] Z.P. Bazant and J. Ozbolt, "Compression Failure Of Quasibrittle Material: Nonlocal Microplane Model," Journal of Engineering Mechanics, **118 (3)**, pp. 540-556, 1992.

[115] O. Düğenci and T. Haktanir, "Experimental Research for the Effect of High Temperature on the Mechanical Properties of Steel Fiber-Reinforced Concrete," *Construction and Building Materials*, **75**, pp. 82-88, 2015.

[116] S. Yazıcı, G. Inan, and V. Tabak, "Effect of Aspect Ratio and Volume Fraction of Steel Fiber on the Mechanical Properties of SFRC," *Construction and Building Materials*, **21**, pp. 1250–1253, 2007.

[117] M. Di Prisco and R. Felicetti, "Some Results on Punching Shear in Plain and Fibre-Reinforced Micro-Concrete Slabs," *Magazine of Concrete Research*, **49** (180), pp. 201-219, 1997.

[118] F.I. Faiyadh and M.A. Al-Ausi, "Effect of Elevated Temperature on Splitting Tensile Strength of Fibre Concrete," *The Intemational Journal of Cement Composites and Lightweight Concrete*, **11 (3)**, pp. 175-178, 1989.

[119] R. Narayanan and I.Y.S. Darwish, "Punching Shear Tests on Steel-Fibre-Reinforced Micro-Concrete Slabs," *Magazine of Concrete Research*, **39 (138)**, pp. 42-50, 1987.

[120] A. Abadel, T. Almusallam, Y. Al-Salloum, and H. Abbas, "Punching Shear Strength of Steel Fiber Reinforced High Strength Concrete," in Proc. of the Second Intl. Conf. on Advances In Civil, Structural and Environmental Engineering-ACSEE, USA, 2014, pp. 236-239.

[121] ACI446.3, "Finite Element Analysis of Fracture inConcrete Structures," American Concrete Institute, Standard ACI446.3, 1997.

[122] D.S. Dugdale, "Yielding of Steel Sheets Containing Slits," *J. Mech. Phys. Solids*, **8**, pp. 100-104, 1960.

[123] G.I. Barenblatt, "The Mathematical Theory of Equilibrium Cracks in Brittle Fracture," pp. 62-132, 1962.

[124] A. Hillerborg, M. Modeer, and P-E Petersson, "Analysis of Crack Formation and Crack Growth in Concrete by Means of Fracture Mechanics and Finite Elements," *Cement and Concrete Research*, **6 (6)**, pp. 773-782, 1976.

[125] J. Lubliner, J. Oliver, S. Oller, and E. Onate, "A Plastic Damage Model for Concrete," *International Journal of Solids and Structures*, **25 (3)**, pp. 299-326, 1989.

[126] J. Lee and G.L. Fenves, "Plastic-Damage for Cyclic Loading of Concrete Structures," *Journal of Engineering Mechanics*, **124 (8)**, pp. 892-900, 1998.

[127] H. Kupfer, H.K. Hilsdorf, and H. Rusch, "Behavior of Concrete Under Biaxial Stresses," *ACI Journal Proceedings*, **66 (8)**, pp. 656-666, 1969.

[128] K. Kordina, C Ehm, and U. Schneider, "Effects of Biaxial Loading on the High Temperature Behaviour of Concrete," in Fire Safety Science-Proceedings of the First International Symposium, 1985, pp. 281-290.

[129] N.S. Ottosen, "A Failure Criterion for Concrete," *Journal of Engineering Mechanics Devision*, **103 (EM4)**, pp. 527-535, Aug. 1977.

[130] P. Kmiecik and M. Kamiński, "Modelling of Reinforced Concrete Structures and Composite Structures with Concrete Strength Degradation Taken into Consideration," *Archives of Civil and Mechanical Engineering*, **6 (3)**, pp. 623-636, 2011.

[131] A.A. Abdul-Razzak and A.A.M. Ali, "Modelling and Numerical Simulation of High Strength Fibre Reinforced Concrete Corbels," *Applied Mathematical Modelling*, **35**, pp. 2901–2915, (2011).

[132] A.S. Genikomsou and M.A. Polak, "Finite Element Analysis of Punching Shear of Concrete Slabs Using Damaged Plasticity Model in ABAQUS," *Engineering Structures*, **98**, pp. 38-48, 2015.

[133] P.E. Petersson, "Crack Growth and Development of Fracture Zones in Plain Concrete and Similar Materials," Division of Building Materials, Lund Institute of Technology, LUND, REPORT TVBM-1006 1981.

[134] V.S. Gopalaratnam and S.P. Shah, "Softening Response of Plain Concrete in Direct Tension," *ACI Journal*, **82 (3)**, pp. 310-323, 1985.

[135] C.V. Nielsen and N. Bičanič, "Residual Fracture Energy of High-Performance and Normal Concrete Subject to High Temperatures," *Materials and Structures / Matèriaux et Constructions*, **36**, pp. 515-521, 2003.

[136] B. Zhang and N. Bicanic, "Fracture energy of high-performance concrete at high temperatures up to 450 C: the effects of heating temperatures and testing conditions (hot and cold)," *Magazine of Concrete Research*, **58** (5), pp. 277–288, 2006.

[137] A.E. Long and D. Bond, "Punching failure of reinforced concrete slabs," Proceedings of the Institute of Civil Engineers, **37** (1), pp. 109–135, 1967.

[138] C. Ehm, U. Schneider, and K. Kordina, "Fracture of Concrete Under Biaxial High Temperature Tests," in Fracture 84. Proceedings of the 6th International Conference on Fracture (ICF6), New Delhi, India, 1985, pp. 2795-2800.

[139] Y. Anderberg and S. Thelandersson, "Stress and Deformation Characteristics of Concrete at High Temperatures. 2. Experimental Investigation and Material Behaviour Model," Bulletin of Division of Structural Mechanics and Concrete Construction, Bulletin 54, 1976.

[140] U. Schneider, "Concrete at High Temperatures -- A General Review," *Fire Safety Journal*, **13**, pp. 55 - 68, 1988.

[141] J.A. Purkiss and Long-yuan Li, "Fire Safety Engineering Design of Structures", 3rd ed. Boca Raton: CRC Press, Taylor & Francis Group, 2013.

[142] T. T. Lie, "Structural Fire Protection," Structural Division, ASCE Committee on Fire Protection, New York, Manual 1992.

[143] ACI122R-02, "Guide to Thermal Properties of Concrete and Masonry Systems," American Concrete Institute, Farmington Hills, MI, ACI 122, 2002.

[144] A. Ibrahim, Salah E.E. El-Metwally, Hamed H. Asker, and Mohamed A. El Zareef, "Effect of Mid-Thickness Rebar Mesh on the Behavior and Punching Shear Strength of Interior Slab–Column Connection," *HBRC Journal*, pp. 1-12, 2015.

[145] A. K.M. Jahangir Alam, Khan Mahmud Amanat, and Salek M. Seraj, "Experimental Investigation of Edge Restraint on Punching Shear Behaviour of RC Slab," *The IES Journal Part A: Civil & Structural Engineering*, **2** (1), 2009.

[146] A. Tomaszewicz, "Punching Shear Capacity," *SINTEF Structures and Concrete*, Trondheim, SP2. 2.3 STF70 A93082, 1993.

[147] H. Marzouk and A. Hussein, "Experimental Investigation on the Behavior of High-Strength Concrete Slabs," *ACI Structural Journal*, **88 (6)**, pp. 701-713, 1991.

[148] J. Lovrovich and D. McLean, "Punching Shear Behaviour of Slabs with Varying Span Depth Ratios," *ACI Structructural Journal*, **87**, pp. 507-511, 1990.

[149] P. Regan, "Symmetric punching ofreinforced concrete slabs.," *Magazine of Concrete Research*, **38**, pp. 115-128, 1986.

[150] U. Schaefers, "Konstruktion, Bemessung und Sicherheit gegen Durchstanzen von balkenlosen Stalbetondecken im Bereich der Innensttitzen," Beuth-Verlag, Berlin, DafStb Heft 357 1984.

[151] M. Ladner, "EinfluB der MaBstabgroBe bei Durchstanzversuchen - Ableitung eines begrUndeten Obertragunggesetzes," *Material und Technik*, pp. 60-68, 1973.

[152] G. Corley and N.M. Hawkins, "Shear head reinforcement for slabs," *ACI Journal*, **65 (10),** pp. 811-824, 1968.

[153] M. Manterola, "Poinconnement de dalles sans armature d'effort tranchant," Comite Europeen du Beton (Hrsg.); Dalles, Structures planes, Paris, CEB-Bull. dlnformation (58), 1966.

[154] J. Ozbolt and H. Vocke "Three-dimensional Numerical Analysis of Punching Failure," p.71-78 in: CEB-Bull. (12), fédération internationale du béton (fib), Lausanne, Switzerland, 2001.

APPENDIX A

Table A-1 lists the available experimental literature on punching shear behavior under high temperatures, while Table A-2 summarized the exposure duration, preloading amount, slab ultimate resistance, deflection and the residual strength of the tested slabs that listed in Table A -1.

Table A -1 Available experimental literature data on punching shear under high temperatures

<table>
<tr><th>Reference</th><th>Slab code</th><th>Scenario</th><th>Exposed face</th><th>Shape (1)</th><th>Slab size (mm)</th><th>Col. size (mm)</th><th>ρ (%)</th><th>f_c' (3) (MPa)</th><th>f_y (MPa)</th></tr>
<tr><td rowspan="8">Smith et al. (2015) [54]</td><td>hu50-0.8</td><td>500 °C</td><td rowspan="8">Compression</td><td rowspan="4">Case 3</td><td rowspan="8">1400×1400 h = (50,75, 100)</td><td rowspan="8">120</td><td>0.8</td><td rowspan="8">51</td><td>549.6</td></tr>
<tr><td>hu75-0.8</td><td>480 °C</td><td>0.8</td><td>549.6</td></tr>
<tr><td>hu100-0.8</td><td>130 °C</td><td>0.8</td><td>549.6</td></tr>
<tr><td>hu100-1.5</td><td>208 °C</td><td>1.5</td><td>571</td></tr>
<tr><td>hr 50-0.8</td><td>630 °C</td><td rowspan="4">Case 3(2)</td><td>0.8</td><td>549.6</td></tr>
<tr><td>hr 75-0.8</td><td>560 °C</td><td>0.8</td><td>549.6</td></tr>
<tr><td>hr100-0.8</td><td>435 °C</td><td>0.8</td><td>549.6</td></tr>
<tr><td>hr100-1.5</td><td>510 °C</td><td>1.5</td><td>571</td></tr>
<tr><td rowspan="3">Ghoreishi et al. (2015) [59]</td><td>AT</td><td>249 °C</td><td rowspan="3">Compression</td><td rowspan="3">Case 3</td><td rowspan="3">1000×1000 h = 120</td><td rowspan="3">150</td><td>1.474</td><td rowspan="3">40</td><td rowspan="3">400</td></tr>
<tr><td>BT</td><td>319 °C</td><td>1.158</td></tr>
<tr><td>CT</td><td>278 °C</td><td>0.632</td></tr>
<tr><td rowspan="4">Annerel et al. (2013) [58]</td><td>S0_fire</td><td rowspan="4">ISO 834</td><td rowspan="4">Compression</td><td rowspan="4">Case 2</td><td rowspan="4">3200×3200 h = 250</td><td rowspan="4">300</td><td rowspan="4">0.51</td><td>32.9</td><td rowspan="4">500</td></tr>
<tr><td>S1_fire</td><td>32.9</td></tr>
<tr><td>S2_fire</td><td>31.3</td></tr>
<tr><td>S5_fire</td><td>31.3</td></tr>
</table>

(1) These cases are related to the specimen's shape and configuration, according to Figure 2.17.
(2) Four edges are clamped.
(3) A standard 150×300-mm cylinder, converting from Fcu to f 'c, was according to Eurocode 2 [31].

Table A-1 …. Continued from previous page.

Reference	**Slab code**	**Scenario**	**Exposed face**	**Shape** (1)	**Slab size** (mm)	**Col. size** (mm)	**ρ** (%)	$\mathbf{f'_c}$ (3) (MPa)	$\mathbf{f_y}$ (MPa)
Liao et al. (2013) [60]	CS-R1-C1	ASTME119	Compression	Case 4	1220×1220 h = 120	180	0.92	32	420
	CS-R2-C2						0.43	58	
	TS-R1-C1		Tension		1800×1800 h = 120		0.92	32	
	TS-R2-C1						0.43	32	
	TS-R1-C2						0.92	58	
	TS-R2-C2						0.43	58	
Salem et al. (2012) [61]	S1	233 ^oC	Tension	Case 5	1100×1100 h = 100	150	1.2	22	410
	S2	332 ^oC							
	S3	420 ^oC							
	S4	233 ^oC							
	S5	332 ^oC							
	S6	420 ^oC							
	S7	128 ^oC					1.0		
	S8	188 ^oC							
	S9	260 ^oC							
	S10	128 ^oC							
	S11	188 ^oC							
	S12	260 ^oC							

(1) These cases are related to the specimen's shape and configuration, according to Figure 2.17.
(2) Four edges are clamped.
(3) A standard 150×300-mm cylinder, converting from Fcu to f 'c, was according to Eurocode 2 [31].

Table A-1 …. Continued from previous page.

Reference	Slab code	Scenario	Exposed face	Shape (1)	Slab size (mm)	Col. size (mm)	ρ (%)	f'_c (3) (MPa)	f_y (MPa)
Kordina (1997) [10] [10]	1	ISO 834	Compression	Case 1	2500×2500 h = 200	250	0.56	46	504
	2						0.56	46	504
	3						1.54	51	590
	4						1.54	51	590
	5						1.54	35	590
	6						1.54	35	590
	7						0.56	52	507
	8						1.54	52	590
	9						0.56	44	555
	10						0.56	44	555
	A				2500×2500 h = 150		0.56	41	565
	B						0.56	41	558
	C						0.56	39	565
	D						0.56	39	558

(1) These cases are related to the specimen’s shape and configuration, according to Figure 2.17.
(2) Four edges are clamped.
(3) A standard 150×300-mm cylinder, converting from Fcu to f 'c, was according to Eurocode 2 [31].

Table A -2 Deflection and reduction in slab strength under different exposure times.

Reference	Specimen code†	Exposure duration (min)	Service load (kN)	Punching strength $V_{(20)}$(kN) [b]	Failure load $V_{(T)}$ (kN)	Residual capacity [kN]	Strength reduction [%]	Mid-span deflection at failure (mm)
Smith et al. [54]	hu50-0.8	120	25.50	54.2	-	55.7	-	40.3
	hu75-0.8	121	83	101.4	-	90.7	-	17.7
	hu100-0.8	11	174.6	226.3	174.8	-	23	30.8
	hu100-1.5	14	234	279.7	237	-	15	28.5
	hr50-0.8	121	26.40	54.2	-	64.4	-	29.4
	hr75-0.8	120	82	101.4	-	115.5	-	20.0
	hr100-0.8	120	166.5	226.3	-	245.1	-	20.7
	hr100-1.5	105	233	279.7	233.2	-	17	21.2
Ghoreishi et al. [59]	AT	240	0	249	235	-	6	7
	BT	340	0	225	200	-	11	7
	CT	303	0	160	141	-	12	10
Annerel et al. [58]	S0_fire	120	270	998	-	588	41	2.3
	S1_fire[a]	120	336	1000	-	627	37	4.8
	S2_fire[a]	20	402	1000	-	-	-	-
	S5_fire[a]	20	420	1050	-	-	-	-

† References and specimen details are listed in Table A-1.

[a] The specimens were reinforced with shear reinforcement, in addition to flexural reinforcement.

[b] The specimens' strengths in ambient conditions were obtained from theoretically calculated or tested equivalent specimens.

‡ Load applied within the first 15 minutes.

⋆ Load applied within the first 30 minutes.

Table A -2 ….. Continued from previous page.

Reference	Specimen code†	Exposure duration (min)	Service load (kN)	Punching strength $V_{(20)}$(kN) [b]	Failure load $V_{(T)}$ (kN)	Residual capacity [kN]	Strength reduction [%]	Mid-span deflection at failure (mm)
Liao et al. [60]	CS-R1-C1	480	120	222	-	-	-	5.03
	CS-R2-C2	480	260	482	-	-	-	6.91
	TS-R1-C1	279	116	216	-	-	-	29.45
	TS-R2-C1	260	140	260	-	-	-	24.13
	TS-R1-C2	240	144	266	-	-	-	21.63
	TS-R2-C2	255	166	307	-	-	-	23.83
Salem et al. [61]	S1	60	0	190	178	-	6	9.2
	S2	120	0	190	165	-	13	10.2
	S3	180	0	190	166	-	13	11.7
	S4	60	0	190	172	-	9	9.4
	S5	120	0	190	162	-	15	10.7
	S6	180	0	190	159	-	16	11.8
	S7	60	0	197	192	-	3	8.8
	S8	120	0	197	179	-	9	9.6
	S9	180	0	197	167	-	15	11
	S10	60	0	197	186	-	6	9
	S11	120	0	197	172	-	13	9.7
	S12	180	0	197	162	-	18	11.2

† References and specimen details are listed in Table A-1.
[a] The specimens were reinforced with shear reinforcement, in addition to flexural reinforcement.
[b] The specimens' strengths in ambient conditions were obtained from theoretically calculated or tested equivalent specimens.
‡ Load applied within the first 15 minutes.
⋆ Load applied within the first 30 minutes.

Table A -2 ….. Continued from previous page.

Reference	**Specimen code†**	**Exposure duration** (min)	**Service load** (kN)	**Punching strength** $V_{(20)}$(kN) [b]	**Failure load** $V_{(T)}$ (kN)	**Residual capacity** [kN]	**Strength reduction** [%]	**Mid-span deflection at failure** (mm)
Kordina [10]	1	120	229	680	492	-	28	12.5
	2[a]	27	372	710	475	-	33	9
	3	90	540‡	1260	550	-	56	3.5
	4[a]	90	810‡	1310	810	-	38	1.5
	5	29	328⋆	950	386	-	59	8
	6	70	300⋆	950	380	-	60	8
	7	90	455‡	780	500	-	36	4.3
	8	14	565⋆	1490	568	-	62	4.5
	9	8	320⋆	667	410	-	39	7
	10[a]	180	430	710	460	-	35	3.2
	A	92	287	530	345	-	35	5
	B	120	287	530	360	-	32	2
	C	27	260	510	-	-	-	16
	D	90	260	510	-	-	-	10

† References and specimen details are listed in Table A-1.
[a] The specimens were reinforced with shear reinforcement, in addition to flexural reinforcement.
[b] The specimens' strengths in ambient conditions were obtained from theoretically calculated or tested equivalent specimens.
‡ Load applied within the first 15 minutes.
⋆ Load applied within the first 30 minutes.

APPENDIX B

Test results of RC slab-column connection tested under monotonic increasing load found in literature, which is used in comparisons in Section 4.3.1.

Table B -1 Available experimental literature data on punching shear of SFRC slabs.

Reference	Spci. No	Geometry	c (mm)	b (mm)	a or r_q (mm)	h (mm)	d (mm)	ρ (%)	f'_c (Mpa)	f_y (Mpa)	P_u (kN)
Smith et al., 2015 [54]	AU50-0.8	Rect.	120	1400	1400	50	35	0.69	51.0	550	54
	AU75-0.8	Rect.	120	1400	1400	75	62	0.68	51.0	550	101
	AU100-0.8	Rect.	120	1400	1400	100	83	0.80	51.0	550	226
	AU100-1.5	Rect.	120	1400	1400	100	81	1.46	51.0	571	280
Ibrahim et al., 2015 [144]	A1(40)	Rect.	160	1200	1000	140	107	0.58	33.1	400	308
	A1(60)	Rect.	160	1200	1000	140	107	0.58	48.8	400	340
Liao, et al., 2013 [60]	TS-R1-C1-0	Rect.	180	1800	1800	120	88	0.93	32.0	420	216
	TS-R2-C1-0	Rect.	180	1800	1800	120	88	1.40	32.0	420	260
	TS-R1-C2-0	Rect.	180	1800	1800	120	88	0.93	58.0	420	266
	TS-R2-C2-0	Rect.	180	1800	1800	120	88	1.40	58.0	420	307
	CS-R1-C1-0	Rect.	180	1220	1220	120	88	0.95	32.0	420	222
	CS-R2-C2-0	Rect.	180	1220	1220	120	88	1.47	58.0	420	482
Widianto, et al., 2009 [99]	G05	Rect.	400	4300	1728	150	130	0.50	31.4	420	311
	G1.0	Rect.	400	4300	1728	150	130	1.00	31.4	420	401

Table B -1 …. Continued from previous page.

Reference	Spci. No	Geometry	c (mm)	b (mm)	a or r_q (mm)	h (mm)	d (mm)	ρ (%)	f 'c (Mpa)	f_y (Mpa)	P_u (kN)
Guandalini, et al., 2009 [83]	PG1	Circ.	260	3000	1500	250	210	1.50	27.6	573	1023
	PG-2b	Circ.	260	3000	1500	250	210	0.25	40.5	552	440
	PG-4	Circ.	260	3000	1500	250	210	0.25	32.2	541	408
	PG-5	Circ.	260	3000	1500	250	210	0.34	29.3	555	550
	PG-10	Circ.	260	3000	1500	250	210	0.34	28.5	577	540
	PG-11	Circ.	260	3000	1500	250	210	0.75	31.5	570	763
	PG-3	Circ.	520	6000	2850	500	456	0.33	32.4	520	2153
	PG-6	Circ.	130	1500	752	125	96	1.50	34.7	526	238
	PG-7	Circ.	130	1500	752	125	100	0.73	34.7	550	241
	PG-8	Circ.	130	1500	752	130	117	0.29	34.7	525	140
	PG-9	Circ.	130	1500	752	130	117	0.23	34.7	525	115

Table B -1 …. Continued from previous page.

Reference	Spci. No	Geometry	c (mm)	b (mm)	a or r_q (mm)	h (mm)	d (mm)	ρ (%)	f'_c (Mpa)	f_y (Mpa)	P_u (kN)
Alam et al., 2009 [145]	slab1	Rect.	120	1445	1200	80	64	0.50	38.5	421	225
	slab2	Rect.	120	1445	1200	80	64	1.00	37.4	421	242
	slab3	Rect.	120	1445	1200	80	60	1.50	28.2	421	143
	slab4	Rect.	120	1445	1200	60	44	0.50	38.2	421	138
	slab5	Rect.	120	1445	1200	60	44	1.00	36.6	421	148
	slab6	Rect.	120	1445	1200	60	44	1.50	42.0	421	131
	slab7	Rect.	120	1375	1200	80	64	1.00	32.5	421	182
	slab8	Rect.	120	1375	1200	60	44	0.50	41.3	421	133
	slab9	Rect.	120	1375	1200	60	44	1.00	33.1	421	116
	slab10	Rect.	120	1305	1200	80	64	1.00	37.5	421	189
	slab11	Rect.	120	1305	1200	60	44	0.50	40.4	421	113
	slab12	Rect.	120	1305	1200	60	44	1.00	37.0	421	116
	slab13	Rect.	120	_	1200	80	64	1.00	37.7	421	172
	slab14	Rect.	120	_	1200	60	44	0.50	34.7	421	85
	slab15	Rect.	120	_	1200	60	44	1.00	33.0	421	92
Birkle et al., 2008 [103]	1.00	Circ.	250	_	1000	160	124	1.54	36.2	488	438
	7.00	Circ.	300	_	1500	230	190	1.30	35.0	531	825
	10.00	Circ.	350	_	1900	300	260	1.10	31.4	524	1046

Table B -1 …. Continued from previous page.

Reference	Spci. No	Geometry	c (mm)	b (mm)	a or r_q (mm)	h (mm)	d (mm)	ρ (%)	f 'c (Mpa)	f_y (Mpa)	P_u (kN)
Hallgeen,1996 [29]	HSC0	Circ.	250	2540	2400	240	200	0.80	93.9	643	965
	HSC1	Circ.	250	2540	2400	245	200	0.80	91.3	627	1021
	HSC2	Circ.	250	2540	2400	240	194	0.80	85.7	620	889
	HSC4	Circ.	250	2540	2400	240	200	1.20	91.6	596	1041
	HSC6	Circ.	250	2540	2400	239	201	0.60	108.8	633	960
	N/HSC8	Circ.	250	2540	2400	242	198	0.80	94.9	631	944
	HSC9	Circ.	250	2540	2400	239	202	0.30	84.1	634	565
Tomaszewicz,1993 [146]	ND65-1-1	Rect.	200	3000	2500	320	275	1.50	64.3	500	2050
	ND65-2-1	Rect.	150	2600	2200	240	200	1.70	70.2	500	1200
	ND95-1-1	Rect.	200	3000	2500	320	275	1.50	83.7	500	2250
	ND95-1-3	Rect.	200	3000	2500	320	275	2.50	89.9	500	2400
	ND95-2-1	Rect.	150	2600	2200	240	200	1.70	88.2	500	1100
	ND95-2-1D	Rect.	150	2600	2200	240	200	1.70	86.7	500	1300
	ND95-2-3	Rect.	150	2600	2200	240	200	2.60	89.5	500	1450
	ND95-2-3D	Rect.	150	2600	2500	240	200	2.60	80.3	500	1250
	ND95-2-3D+	Rect.	150	2600	2500	240	200	2.60	98.0	500	1450
	ND95-3-1	Rect.	100	1500	1100	120	88	1.80	85.1	500	330
	ND115-1-1	Rect.	200	3000	2500	320	275	1.50	112.1	500	2450
	ND115-2-1	Rect.	150	2600	2200	240	200	1.70	117.1	500	1400
	ND115-2-3	Rect.	150	2600	2200	240	200	2.60	111.3	500	1550

Table B -1 …. Continued from previous page.

Reference	Spci. No	Geometry	c (mm)	b (mm)	a or r_q (mm)	h (mm)	d (mm)	ρ (%)	f '$_c$ (Mpa)	f_y (Mpa)	P_u (kN)
Ramdane, 1993 [11]	1.00	Circ.	150	1700	1372	125	98	0.58	103.5	550	224
	2.00	Circ.	150	1700	1372	125	98	0.58	57.0	550	212
	3.00	Circ.	150	1700	1372	125	98	0.58	27.6	550	169
	4.00	Circ.	150	1700	1372	125	98	0.58	59.0	550	233
	6.00	Circ.	150	1700	1372	125	98	0.58	108.0	550	233
	12.00	Circ.	150	1700	1372	125	98	1.28	60.5	550	319
	13.00	Circ.	150	1700	1372	125	98	1.28	44.5	550	297
	14.00	Circ.	150	1700	1372	125	98	1.28	61.0	550	341
	16.00	Circ.	150	1700	1372	125	98	1.28	105.3	550	362
	21.00	Circ.	150	1700	1372	125	98	1.28	42.4	650	286
	22.00	Circ.	150	1700	1372	125	98	1.28	90.3	650	405
	23.00	Circ.	150	1700	1372	125	100	0.87	57.2	650	341
	25.00	Circ.	150	1700	1372	125	100	1.27	32.6	650	244
	26.00	Circ.	150	1700	1372	125	100	1.27	37.0	650	294
	27.00	Circ.	150	1700	1372	125	102	1.03	33.2	650	227

Table B -1 …. Continued from previous page.

Reference	Spci. No	Geometry	c (mm)	b (mm)	a or r_q (mm)	h (mm)	d (mm)	ρ (%)	f '$_c$ (Mpa)	f_y (Mpa)	P_u (kN)
Marzouk and Hussein, 1991 [147]	I.HS1	Rect.	150	1700	1500	120	95	0.40	67.0	490	178
	I.HS2	Rect.	150	1700	1500	120	95	0.70	70.0	490	249
	I.HS3	Rect.	150	1700	1500	120	95	1.20	69.0	490	356
	I.HS4	Rect.	150	1700	1500	120	90	2.10	66.0	490	418
	I.HS7	Rect.	150	1700	1500	120	95	0.90	74.0	490	356
	II.HS5	Rect.	150	1700	1500	150	125	0.50	68.0	490	365
	II.HS6	Rect.	150	1700	1500	150	120	0.50	70.0	490	489
	II.HS8	Rect.	150	1700	1500	150	120	1.00	69.0	490	436
	II.HS9	Rect.	150	1700	1500	150	120	1.50	74.0	490	543
	II.HS10	Rect.	150	1700	1500	150	120	2.10	80.0	490	645
	III.HS11	Rect.	150	1700	1500	90	70	0.70	70.0	490	196
	III.HS12	Rect.	150	1700	1500	90	70	1.20	75.0	490	258
	III.HS13	Rect.	150	1700	1500	90	70	1.60	68.0	490	267
	IV.HS14	Rect.	150	1700	1500	120	95	1.20	72.0	490	498
	IV.HS15	Rect.	150	1700	1500	120	95	1.20	71.0	490	560
	I.NS1	Rect.	150	1700	1500	120	95	1.20	42.0	490	320
	II.NS2	Rect.	150	1700	1500	150	120	0.50	30.0	490	396
Lovrovich and McLean, 1990 [148]	F1	Circ.	100	500	200	100	83	1.70	39.3	531	480
	F2	Circ.	100	700	400	100	83	1.70	39.3	531	204
	F3	Circ.	100	900	600	100	83	1.70	39.3	531	149
	F4	Circ.	100	1100	800	100	83	1.70	39.3	531	129
	F5	Circ.	100	1500	1200	100	83	1.70	39.3	531	139

Table B -1 …. Continued from previous page.

Reference	Spci. No	Geometry	c (mm)	b (mm)	a or r_q (mm)	h (mm)	d (mm)	ρ (%)	f '$_c$ (Mpa)	f_y (Mpa)	P_u (kN)
Tolf,1988 [28]	S2-1	Circ.	250	2540	2378	240	200	0.80	25.2	657	603
	S2-2	Circ.	250	2540	2378	240	199	0.80	23.6	670	600
	S2-3	Circ.	250	2540	2378	2040	200	0.45	26.2	665	489
	S2-4	Circ.	250	2540	2378	2040	197	0.45	25.1	664	444
	S1-1	Circ.	125	1270	1189	120	100	0.80	29.1	706	216
	S1-2	Circ.	125	1270	1189	120	99	0.80	23.6	701	194
	S1-3	Circ.	125	1270	1189	120	98	0.40	27.4	720	145
	S1-4	Circ.	125	1270	1189	120	99	0.40	26.0	712	148
Regan, 1986 [149]	I/1	Rect.	200	2000	1830	100	77	1.39	26.6	500	194
	I/2	Rect.	200	2000	1830	100	77	1.20	24.3	500	176
	I/3	Rect.	200	2000	1830	100	77	0.92	28.1	500	194
	I/4	Rect.	200	2000	1830	100	77	1.20	32.1	500	194
	I/5	Rect.	200	2000	1830	100	79	2.74	28.7	480	165
	I/6	Rect.	200	2000	1830	100	79	0.80	22.4	480	165
	I/7	Rect.	200	2000	1830	100	79	0.80	30.6	480	186
Swamy&Ali,1982 [69]	S1	Rect.	150	1800	1690	125	100	0.60	40.1	462	198
	S7	Rect.	150	1800	1690	125	100	0.59	37.4	462	222

Table B -1 …. Continued from previous page.

Reference	Spci. No	Geometry	c (mm)	b (mm)	a or r_q (mm)	h (mm)	d (mm)	ρ (%)	f ′$_c$ (Mpa)	f_y (Mpa)	P_u (kN)
Schaefers, 1984 [150]	0.00	Circ.	210	1960	1680	143	113	0.80	23.1	420	280
	3.00	Circ.	210	1960	1680	200	170	0.60	23.3	450	460
Ladner, 1973 [152]	P1	Circ.	500	2900	1056	280	240	1.30	28.9	544	1662
	M1	Circ.	226	1400	2650	226	240	1.20	31.7	541	362
Corley and Hawkins, 1968 [152]	an-1	Rect.	254	2135	1820	146	111	1.50	44.4	404	334
	an-2	Rect.	203	2135	1820	146	111	1.00	44.4	444	266
Manterola, 1966 [153]	P1-S1	Rect.	100	3250	3000	125	107	1.10	25.6	304	216
	P2-S1	Rect.	250	3250	3000	125	107	1.10	33.8	304	257
	P3-S1	Rect.	450	3250	3000	125	107	1.10	29.7	304	301
	P1-S2	Rect.	100	3250	3000	125	107	1.10	24.2	324	196
	P2-S2	Rect.	250	3250	3000	125	107	1.10	33.1	324	283
	P3-S2	Rect.	450	3250	3000	125	107	1.10	31.9	324	397
	P1-S3	Rect.	100	3250	3000	125	107	1.10	39.7	324	184
	P2-S3	Rect.	100	3250	3000	125	107	1.40	35.8	324	211
	P3-S3	Rect.	100	3250	3000	125	107	0.50	39.2	324	165
	P1-S4	Rect.	100	3250	3000	125	107	0.50	26.4	451	175
	P2-S4	Rect.	250	3250	3000	125	107	0.50	31.3	451	246
	P3-S4	Rect.	450	3250	3000	125	107	0.50	34.2	451	294

Table B -1 …. Continued from previous page.

Reference	Spci. No	Geometry	c (mm)	b (mm)	a or r_q (mm)	h (mm)	d (mm)	ρ (%)	f'_c (Mpa)	f_y (Mpa)	P_u (kN)
Moe, 1961 [13]	S1-60	Rect.	254	1830	1780	152	114	1.10	23.3	399	389
	S2-60	Rect.	254	1830	1780	152	114	0.67	22.1	399	356
	S3-60	Rect.	254	1830	1780	152	114	0.77	22.6	399	364
	S4-60	Rect.	254	1830	1780	152	114	0.88	23.8	399	334
	S1-70	Rect.	254	1830	1780	152	114	1.10	24.5	483	393
	S3-70	Rect.	254	1830	1780	152	114	0.77	25.4	483	378
	S4-70	Rect.	254	1830	1780	152	114	0.88	35.2	483	374
	S4-70A	Rect.	254	1830	1780	152	114	0.88	20.5	483	312
	S5-60	Rect.	203	1830	1780	152	114	1.10	22.2	399	343
	S5-70	Rect.	203	1830	1780	152	114	1.10	23.0	483	378
	R1	Rect.	152	1830	1780	152	114	1.40	26.6	328	312
	H1	Rect.	264	1830	1780	152	114	1.10	26.1	328	372
	M1A	Rect.	305	1830	1780	152	114	1.50	20.8	481	433
Kinn./Nyl.,1960 [4]	IA15a-5	Circular	150	1840	1710	149	117	0.80	28.5	441	255
	IA15a-6	Circular	150	1840	1710	151	118	0.80	26.6	454	275
	IA30a-24	Circular	300	1840	1710	158	128	1.00	26.7	456	430
	IA30a-25	Circular	300	1840	1710	154	124	1.10	25.6	451	408
	IA30d-32	Circular	300	1840	1710	155	123	0.50	26.6	448	258
	IA30d-33	Circular	300	1840	1710	156	125	0.50	26.9	462	258

Table B -1 …. Continued from previous page.

Reference	Spci. No	Geometry	c (mm)	b (mm)	a or r_q (mm)	h (mm)	d (mm)	ρ (%)	f'_c (Mpa)	f_y (Mpa)	P_u (kN)
Elst./Hog.,1956 [15]	A-1b	Rect.	254	1830	1780	152	118	1.20	20.2	332	365
	A-1c	Rect.	254	1830	1780	152	118	1.20	24.0	332	356
	A-1d	Rect.	254	1830	1780	152	118	1.20	29.9	332	351
	A-2c	Rect.	254	1830	1780	152	114	2.50	30.3	321	467
	A-7b	Rect.	254	1830	1780	152	114	2.50	22.6	321	512
	A-3c	Rect.	254	1830	1780	152	114	3.70	21.5	321	534
	A-3d	Rect.	254	1830	1780	152	114	3.70	28.2	321	547
	A-4	Rect.	356	1830	1780	152	118	1.20	21.1	332	400
	A-5	Rect.	356	1830	1780	152	114	2.50	22.8	321	534
	A-9	Rect.	254	1830	1780	152	114	3.42	24.9	321	445
	A-10	Rect.	356	1830	1780	152	114	3.42	24.7	321	489
	A-13	Rect.	356	1830	1780	152	121	0.50	21.2	294	236
	B-2	Rect.	254	1830	1780	152	114	0.50	37.6	321	200
	B-4	Rect.	254	1830	1780	152	114	0.90	37.7	303	334
	B-9	Rect.	254	1830	1780	152	114	2.00	34.6	341	505
	B-14	Rect.	254	1830	1780	152	114	3.00	40.5	325	578

APPENDIX C

Test results of SFRC slabs used in comparisons in Figure 6.14.

Table C -1 Available experimental literature data on punching shear of SFRC slabs.

Reference	**Slab code**	$\mathbf{V_f}$ (%)	l_f/D_f	**Cov.** mm).	**c** (mm)	**b** (mm)	**h** (mm)	**a** or $\mathbf{r_q}$ (mm)	**d** (mm)	**ρ** (%)	**f 'c** (Mpa)	$\mathbf{P_u}$ (kN)
Abadel et al., [120]	M1(1)	0	80	15	50	600	90	500	67	0.75	64.5	78.10
	M2(1)	1.2									73.5	104.60
	M3(1)	1.4									74.7	105.10
De Hania and Holanda, [45]	L1	0	55	10	80	1160	100	–	75	1.57	23.1	137.20
	L2	1									24.4	139.55
	L3	2									28.1	163.62
	L4	0									57	192.86
	L5	1									59.7	215.14
	L6	2									52.4	236.17
	L7	0.75	48	10	80	1160	100	–	75	1.57	36.6	182.85
	L8	1.5									46.1	210.90

(1) Two- edges are clamped.
(2) A standard 150×300 mm cylinder, converting from Fcu to f 'c was according to Eurocode 2 [31].

Table C-1 …. Continued from previous page.

Reference	**Slab code**	**V$_f$** (%)	***l$_f$/D$_f$***	**Cov.** mm).	**c** (mm)	**b** (mm)	**h** (mm)	**a** or **r$_q$** (mm)	**d** (mm)	**ρ** (%)	**f '$_c$** (Mpa)	**P$_u$** (kN)
Harajli et al., [82]	A1	0	0	6	100	650	55	400	39	1.55	29.6	62.53
	A2	0.45	100								30	67.70
	A3	0.8	100								31.4	77.77
	A4	1	60								24.6	68.83
	A5	2	60								20	62.06
	B1	0	0	10	100	650	75	400	55	1.55	31.4	99.36
	B2	0.45	100								31.4	114.65
	B3	0.8	100								31.8	117.30
	B4	1	60								29.1	117.73
	B5	2	60								29.2	145.57
Narayanan and Darwish, [119]	S1	0			100		60		45	1.84	43.3	86.50
	S2	0.25									52.1	93.40
	S3	0.5									44.7	102.00
	S4	0.75									46	107.50
	S5	1									53	113.60
	S6	1.25									53	122.20
Swamy and Ali, [69]	S-1	0	100	20	150	1800	125	1690	100	0.56	37.8	197.70
	S-2	0.6									39	243.60
	S-3	0.9									37.8	262.90
	S-4	1.2									36.9	281.00

VITA

Name and Surname	Farid H. Arna'ot
Nationality	Iraqi
Birth Place and Date	Kirkuk-Iraq-1967
Marital Status	Married
Phone Number	0096477098703042
E-mail	farnaot@gmail.com

EDUCATION

Doctor of Philosophy (Ph.D) in Structural Engineering, Gaziantep University, Turkey, 2017

Master (M.Sc.) in Structural Engineering and Construction, University Putra Malaysia, Malaysia, 2011.

Higher Diploma (H.D) in building and construction, Quality Control on Building Materials, University of Technology, Iraq, 2003.

Bachelor B.Sc. in Civil Engineering, University of Al-Mustanserya, Iraq, 1998.

Technical Diploma in building and construction, Baghdad technical institute, 1986.

PUBLICATIONS

A. International Journals

Farid H. Arna'ot, Sallal R. Abid, Mustafa Özakça, and Nildem Tayşi, "Review of Concrete Flat Plate-Column Assemblies under Fire Conditions," Fire Safety Journal, vol. 93, pp. 39-52, 2017.

Farid H. Arna'ot, Ahmmad A. Abbass, Ahmed A. Abualtemen, Sallal R. Abid, and Mustafa Özakça, "Residual Strength of High Strength Concentric Column-SFRC Flat Plate Exposed to High Temperatures," Construction and Building Materials, vol. 154, pp. 204-218, 2017.

Farid H. Arna'ot, Ahmmad A. Abbass, Ahmed A. Abualtemen, and Mustafa Özakça, "Punching Shear Behavior of Small SFRC Flat Plate," E. J. Engineering Sciences and Technology, vol. 2, pp. 19-30, 2017.

Ali K.H. Alhussainawe, Farid H. Arna'ot, Ahmmad A. Abbass, and Mustafa Özakça, "Size Effect on Punching Shear Behavior of Slab-Column Assembly Made from Engineering Cementitious Composite Materials with Polyvinyl Alcohol Fibers," The International Journal of Energy and Engineering Sciences, vol. 2 no.2, pp. 32-41, 2017.

Hayder K. Ali, Farid H. Arnao't, and Mustafa Özakça, "Nonlinear Three Dimensional Finite Element Analysis of Reinforced Concrete Hollow Beam," International Journal Of Innovative Research In Management, Engineering And Technology, vol. 1, no. 10, pp. 1-10, 2016.

B. International Conference

Israa S. Abbas, Farid H. Arna'ot, Ahmmad A. Abbass, and Mustafa Özakça, "Two-Way Shear Behavior of Concrete Slabs Reinforced with Polypropylene Fibers," in 20. Ulusal Mekanik Kongresi, Bursa, Turkey, 2017.

Ali K.H. Alhussainawe, Farid H. Arna'ot, Ahmmad A. Abbass, and Mustafa Özakça, "Size Effect on Punching Shear Behavior of Slab-Column Assembly Made from Engineering Cementitious Composite Materials with Polyvinyl Alcohol Fibers," in 2nd International Energy & Engineering Conference, Gaziantep, Turkey, 2017, pp. 1110-1118.

A.A. Abo Altemen, F.H. Arnaot, A.A. Abbass, and M. Ozakca, "Punching Shear Behavior of Small SFRC Flate Plate," in Proceeding ICOCEE Cappadocia 2017-2nd International Conference on Civil and Environmental Engineering, Nevsehir, TURKEY, 2017, pp. 891-901.

Raad A. Alameri, Ahmmad A. Abbass, Farid H. Arna'ot, and Mustafa Özakça, "Response of Steel Fiber Concrete Hollow Beams under Four Points Test," in 2nd International Energy & Engineering Conference, Gaziantep, Turkey, 2017, pp. 1119-1129.

Rasool D. Mohsin, Farid H. Arna'ot, Ahmmad A. Abbass, and Mustafa Özakça, "Investigation of the Fracture Energy of Concrete Strengthened by Nylon-Monofilament and Steel Fiber," in 2nd International Energy & Engineering Conference, Gaziantep, Turkey, 2017, pp. 656-663.

Nildem Tayşi, Mukhtar H. Abed, Ahmmad A. Abbass, and Farid H. Arna'ot, "Investigation of Ductility of PVA Fibre Reinforced Beams," in 20. Ulusal Mekanik Kongresi, Bursa, Turkey, 2017.